Local Structure Variation, Phase Stability and Electrocatalytic Activity in Rocksalt and Spinel based Multi-Component (CoCuMgNiZn)-Oxide and its Derivatives

Thesis submitted in partial fulfilment for the

Award of Degree

DOCTOR OF PHILOSOPHY

By

SAPTARSHI MUKHERJEE

Department of Metallurgical Engineering

Indian Institute of Technology

Banaras Hindu University (BHU)

Varanasi – 221005

UP, India

Roll No. 17141502

2024

CERTIFICATE

It is certified that the work contained in the thesis titled **"Local Structure Variation, Phase Stability and Electrocatalytic Activity in Rocksalt and Spinel based MultiComponent (CoCuMgNiZn)-Oxide and its Derivatives"** by Saptarshi Mukherjee has been carried out under my supervision and that this work has not been submitted elsewhere for a degree.

It is further certified that the student has fulfilled all the requirements of Comprehensive, Candidacy and SOTA for the award of Ph.D. degree.

PROF. JOYSURYA BASU

(Supervisor)

Professor

PROF. N. K. MUKHOPADHYAY

(Co-supervisor)

Professor

Department of Metallurgical Engineering

Indian Institute of Technology

(Banaras Hindu University)

Varanasi

DECLARATION BY THE CANDIDATE

I, **Saptarshi Mukherjee,** certify that the work embodied in this Ph.D. thesis is my own bonafide work carried out under the joint-supervision of **Dr. Joysurya Basu** and **Prof. N.K. Mukhopadhyay** for a period from **January 2018 (Registration: December 27, 2017)** to **December 27, 2024** at the **Department of Metallurgical Engineering, Indian Institute of Technology (BHU),** Varanasi, India. The subject matter embodied in this Ph.D. thesis has not been submitted elsewhere for the award of any other degree/diploma. I declare that I have faithfully acknowledged and given credits to the researchers wherever their works have been cited in my work in this thesis. I further declare that I have not wilfully copied any other's work, paragraphs, text, data, results, etc., reported in journals, books, magazines, reports, dissertations, thesis, etc., or available at websites and have not included them in this thesis and have not cited as my own work.

Date: December 27, 2024

Saptarshi Mukherjee

Place: Varanasi **(SAPTARSHI MUKHERJEE)**

CERTIFICATE BY SUPERVISORS

This is to certify that the above statement made by the candidate is correct to the best of my knowledge.

Joysurya Basu

Prof. JOYSURYA BASU
(Supervisor)

N. K. Mukhopadhyay

Prof. N.K. MUKHOPADHYAY
(Co-supervisor)

HEAD OF THE DEPARTMENT

COPYRIGHT TRANSFER CERTIFICATE

Title of the Thesis: Local Structure Variation, Phase Stability and Electrocatalytic Activity in Rocksalt and Spinel based Multi-Component (CoCuMgNiZn)-Oxide and its Derivatives

Candidate's Name: Saptarshi Mukherjee

COPYRIGHT TRANSFER

The undersigned hereby assigns to the Indian Institute of Technology (Banaras Hindu University), Varanasi all rights under copyright that may exist in and for the above thesis submitted for the award of ***Doctor of Philosophy***.

Date: December 27, 2024

Saptarshi Mukherjee

Place: Varanasi **(SAPTARSHI MUKHERJEE)**

Note: However, the author may reproduce or authorize others to reproduce materials extracted verbatim from the thesis or derivative of the thesis for author's personal use provided that the source and the Institute's copyright notice are indicated.

Acknowledgement

"The known is finite, the unknown infinite; intellectually we stand on an islet in the midst of an illimitable ocean of inexplicability. Our business in every generation is to reclaim a little more land…" **-T. H. Huxley**

I must begin by trying to express my lifelong indebtedness towards my thesis supervisor Prof. Joysurya Basu, who also happens to be my friend, philosopher and guide. My greatest accomplishment by far, during this long arduous journey of earning my Ph.D. degree, is to come into correspondence with him. His scientific idiosyncrasies, thought provoking acumen and the sheer zeal to leave significant footprints in the profession, is unparalleled. I am most lucky to have gotten the chance to learn innumerable things from him, which is non-perishable and does not have a scope of decaying with time. The amount of guidance as well as free-hand extended by him in order for me to produce all the work pertaining to this thesis, has sculpted the researcher within me. His bold and fearless approach has inculcated a confidence in me to explore unchartered territories in the fascinating field of materials science and electron microscopy. Furthermore, his empathy and most amicable nature has helped me to grow both professionally and personally. I most sincerely take the pledge of walking down the roads of righteousness, discipline and honesty, which has been constantly and tirelessly advocated by him.

Prof. N. K. Mukhopadhyay, being my thesis co-supervisor, has been a fixed source of motivation and guidance, starting from my post-graduate journey. He is the first person who has introduced me to the nuances of physical metallurgy, which has consequently steered my scientific interests and career path. His classroom lectures on the subjects of materials characterization and intermetallics has immensely helped me throughout this tenure. I must also convey my deepest gratitude for the kindness extended by him during the tough times of lockdown and COVID aftermath. His financial support greatly helped me to attend several national and international conferences. I shall forever be indebted to him.

I sincerely thank my RPEC members, Dr. Imteyaz Ahmad and Dr. A.K. Mondal for their continuous constructive criticisms in the spirit of science, throughout these years. They have also highly facilitated the processing of every single official document during my Ph.D. span, despite all odds.

I cannot miss this opportunity to express my heartfelt thanks to Prof. R.K. Mandal, for being the epitome of support so that I may carry out research activities unperturbed. He is an academician par excellence and I am blessed to have learnt many things during my long association with him as his TA in several courses. Moreover, I am grateful to all the faculty members, present and past HoDs of our department for upholding a conducive research atmosphere in the department.

I take this scope of deeply thanking retired and emeritus faculties of our department Prof. S. Lele, Prof. G.V.S. Sastry, Prof. A.K. Ghose, Prof. S.N. Ojha, Prof. V. Singh among others. It is because of their teachings and encouragement that I have attempted to stand on the shoulder of giants in the field!

It is my good fortune that I got the prestigious opportunity to closely interact with Prof. D. Banerjee (IISc, Bangalore), Dr. P. Ghosal (DMRL, Hyderabad), Dr. K. Muraleedharan (CSIR-CGCRI), Dr. S. Bysakh (CSIR-CGCRI) and Prof. R. Ranjan (IISc, Bangalore) in matters of science and career advice.

I must acknowledge the tremendous faith put in me by faculties of my Alma Mater, Prof. P.P. Chattopadhyay, Prof. A. Basu Mallick, Prof. S. Chatterjee, Prof. S. Sadhukhan, Prof. S. Ghosh, Dr. D. Das, Dr. S.K. Ghosh, Dr. S. Kundu and Dr. T. Mandal of IIEST, Shibpur. In this regard, I also thank my teachers from school (BGKV, Kolkata), who laid the foundation stone of instilling a rational thinker in me.

I would like to take this opportunity to convey my thanks to all the lab staffs Ashok ji, Anjani ji, Ramashware ji, Kamlesh ji, Kamlaprasad ji, Chhotelal ji and Rajendra ji of this department for putting their best-efforts during times of serious crisis. I especially thank Lalit ji for maintaining the most sophisticated characterization facility of our department. I thank our department office staffs Patel ji, Rana ji, Aamir ji, Arun ji and Aftab ji, for handling and processing of all the required paperwork. I also sincerely thank staffs of CIFC of our institute, especially Anirban ji for his tremendous support during tough times.

I would also like to take this moment to thank all my department seniors Dr. M. Singh, Dr. V. Shivam, Dr. V.K. Pandey, Dr. V. Pandey, Dr. Y. Shadangi, Dr. A. Singh, Dr. A.S. Pal, Dr. A.K.L. Das, Dr. H. Jain among others. I sincerely thank my department colleagues and batchmates Soham, Satyam, Purnendu, Dr. R. Tandon, Dr. D. Bhuiyan, Dr. M.D. Rao for making my stay really cherishable. I am also thankful to my department juniors Rajdeep, Sai, Swarnendu, Latha, Snehita, Ashrita, Ravleen, Shivank, Urwashi, Priyatosh, Rajat, Ritwick, Anurag, Deep, Chayon and many others for a fond and memorable experience.

I will forever be grateful to almighty for bestowing me with the fortune of having several friends in my life, who are also my lifelines. They have immensely enriched my life.

Last but most importantly, I would like express my deepest gratitude towards all my family members for being constant motivators. I lost my grandparents when I was quite young, although I carry them in my heart and mind every single day. They have inculcated strong moral principles and values in me long back, which is continuously being germinated as I tread forward in life. Mr. Bimalendu Lahiri, being the brother of my maternal grandmother, has been a constant source of motivation and inspiration. My parents Dr. Pinaki and Mrs. Purabi Mukherjee are God-like figures in my life, for they have sacrificed on several fronts to make a good human being out of me. I just cannot thank them enough. I am also greatly indebted to them for finding my better-half while I was busy earning my Ph.D. degree. I must thank my gorgeous wife Megha for the unwavering support provided by her during a very tough phase. Her cheerful company always kept me focussed and determined. I thank my sister-in-law Alakta, my dearest nephew and best friend Bihan, my cousins Shovan, Sayan and my entire joint family for their relentless warmth and affection. Furthermore, I seek blessings from my late elder brother Debarshi, who in my most regretful opinion made the ultimate sacrifice so that I may shine perhaps. I terribly miss you and forever will……

To conclude, I take immense pride in remarking that my very existence thus far, has been shaped by the sum total of each and every contribution made by all the individuals mentioned above, the list of which is far from exhaustive.

TABLE OF CONTENTS

θ_B : Bragg angle

λ : Wavelength

G : Gibbs free energy

H : Enthalpy } *General Thermodynamics*

S : Entropy (total)

G_{mix} : Gibbs free energy of mixing

H_{mix} : Enthalpy of mixing } *Solution Thermodynamics*

S_{mix} : Entropy of mixing (configurational)

U : Internal Energy

P : Pressure

V : Volume

a : Lattice parameter

d : Inter-planar spacing

RS : Rocksalt

SP : Spinel

TEM : Transmission Electron Microscopy

SEM : Scanning Electron Microscopy

XRD : X-Ray Diffraction

SAED : Selected Area Diffraction Pattern

BF : Bright Field

CDF : Centered Dark Field

XEDS : X-ray Energy Dispersive Spectroscopy

LSV : Linear Sweep Voltammetry

CV : Cyclic Voltammetry

EIS : Electrochemical Impendence Spectroscopy

HEO : High Entropy Oxide

MCO : Multi Component Oxide

ESO : Entropy Stabilized Oxide

List of Figures

Figure 3.4: SEM-XEDS area map with Ca-K, Co-K, Fe-K, Mg-K and Ni-K in quinary equimolar (CaCoFeMgNi)-oxide after (A) sintering at 1523 K for 10 h and (B) sintering at 1523 K for 100 h followed by water quenching. (a) is the zoomed-in version of the area marked in (A) and (b) in the zoomed-in version of the area marked in (B). The XEDS maps are generated from the areas shown in (a) and in (b). In both the samples, two chemically segregated regions, one rich in Co, Mg, Ni ions and other rich in Ca and Fe ions can be observed

Figure 3.5: (a) Back scattered electron (BSE) image and X-ray energy dispersive spectrum (XEDS) from the points marked by s1-s6. Compositional contrast is observed in the BSE image. All the point XEDS from s1-s6 show the presence of all the elements, however in varying quantities. Compositions as obtained from XEDS are tabulated in the table below. It is again reconfirmed that Ca and Fe ion rich regions are relatively lean in Co, Mg and Ni ions and vice-versa. However, all the elements are present in all the phases. Based on the composition the predominant phase in different regions have been identified and their volume fraction as computed from the X-ray diffraction peak analysis is given in the table at the bottom of the figure

Figure 3.6: TEM (a, c) BF images and corresponding (b, d) single crystal diffraction patterns from z = [001] and z = [103] respectively in quinary equimolar (CaCoFeMgNi)-oxide after sintering at 1523 K for 10 h followed by water quenching. Thickness fringes in (a) and mottled contrast in (b) can be observed. The diffraction patterns in (b) and (d) are sharply defined. TEM (e, g) BF images and corresponding (f, h) single crystal diffraction patterns from z = [001] and z = [103] respectively in quinary equimolar (CaCoFeMgNi)-oxide after sintering at 1523 K for 100 h followed by water quenching. In the BF images in (e) and (g) fringe contrast within the mottled regions (marked with arrows) can be observed. In the diffraction patterns in (f) and in (h) arcs with modulated intensities can be observed

Figure 3.7: Selected area diffraction patterns from the quinary equimolar (CaCoFeMgNi)-oxide after sintering at 1523 K for (a) 10 h (b) 100 h followed by water quenching. In (a) experimentally observed d-spacings and their angular relationships are depicted. In (b) zone axis geometries are depicted. In (a) and (b) the data related to the cubic rocksalt phase, cubic spinel phase and the hexagonal phase are marked in green, yellow and white respectively. The cubic rocksalt phase, cubic spinel phase and hexagonal phase are oriented along z = $[\bar{1}11]$, z = $[\bar{1}11]$ and z = $[2\bar{1}\bar{1}0]$ respectively. Their orientation relationships are $[\bar{1}11]_{RS} \parallel [\bar{1}11]_S$ and $(220)_{RS} \parallel (2\bar{2}4)_S$; $[2\bar{1}\bar{1}0]_H \parallel [\bar{1}11]_{RS}$ and $(0002)_H \parallel (\bar{2}02)_{RS}$; and $[2\bar{1}\bar{1}0]_H \parallel [\bar{1}11]_S$ and $(0002)_H \parallel (\bar{4}\bar{2}2)_S$ (RS: Rocksalt, S: Spinel; H: Hexagonal phase)

Figure 3.8: TEM (a) BF image and (b) corresponding rotationally aligned selected area diffraction pattern and (c) DF image using the superlattice reflection at ½[0002] (given at the inset in (c)) from the quinary equimolar (CaCoFeMgNi)-oxide after sintering at 1523 K for 10 h followed by water quenching. Linear fringes in (a) are from the twins and the

curvilinear contrast in (c) is from the APBs. The diffraction pattern in (b) indicates that the twins in (a) are compound deformation twins with s = $(2\bar{1}\bar{1}0)$, $K_1 = (0002)$, $\eta_1 = [0\bar{1}10]$, $K_2 = [10\bar{1}0]$ and $\eta_2 = [01\bar{1}1]$ as twin variants. (d) BF image (e) corresponding rotationally aligned diffraction pattern and (f) DF image from the quinary equimolar (CaCoFeMgNi)-oxide after sintering at 1523 K for 100 h followed by water quenching. The diffraction pattern in (e) is little off from the zone axis as shown in (b). All the spots perpendicular to the row of spots marked in cyan are split. The twins in (d) and in (f) are widely spaced

Figure 3.9: (a) Schematic representation of the mutually rotated domains in the intergrown helical arrangement with cubic rocksalt structure stacked along [001] direction. Possible composition modulation in each domain is marked with different colours. (b) $[2\bar{1}\bar{1}0]$ orthographic projection of the hexagonal phase with 2/3rd octahedral voids filled up. Cation ordering with vacancies along [0001] is depicted

Figure 3.10: (a) Schematic (202) || (422) interface between cubic rocksalt and cubic spinel phase. The interface is coherent. (b) schematic representation of (202) || (0002) interface between the cubic rocksalt phase with the hexagonal phase. The interface in semicoherent with quite minimal incoherency strain. The schematic diagrams are developed from the experimentally observed orientation relationships and the calculated crystallographic data from the diffraction patterns

Figure 4.1: (a) X-ray diffraction (XRD) patterns of (CoCuMgNiZn) ESO after sintering at 1323 K for 10 h followed by water quenching. The diffraction pattern in pink is from the sintered and quenched pellet and the pattern in blue is from its crushed powder. (b) Deconvolution of the XRD peaks from the crushed powder and (c) deconvolution of the XRD peaks from the pellet. Deconvoluted peaks can be matched with CoO, MgO and NiO.

Figure 4.2: (a) X-ray diffraction patterns (XRD) of (CoCuMgNiZn) ESO pellet after sintering at 1323 K for 10 h followed by water quenching (red), after sintering at 1323 K for 100 h followed by water quenching (pink) and after sintering at 1323 K for 10 h followed by furnace cooling (brown). (b) Superimposition of XRD peaks after three different thermal treatments. Long h of exposure at high temperature leads to a systematic left shift coupled with broadening and reduction in total integrated intensity

Figure 4.3: Scanning electron microscope (SEM) image and XEDS chemical maps of Co, Cu, Mg, Ni, Zn and the composite map of (CoCuMgNiZn) ESO pellet after (a) sintering at 1323 K for 10 h and (b) 1323 K for 100 h followed by water quenching. Fine scale segregation of Cu and Mg ions is evident in the maps. It is marked with arrows and delineated with dotted boundaries

Figure 4.4: Sintered and quenched equimolar quinary (CoCuMgNiZn)ESO exhibiting (a) Polycrystalline electron diffraction pattern with spotty rings which can be indexed to a FCC phase with a~4.23 Å lattice parameter whereas (b) and (c) are the corresponding BF-DF pair showing nano-crystallites of the rocksalt phase. It was recorded from the periphery of

the sample after ion-milling, making it necessary to revisit and optimize the electron thinning parameters to avoid such process-induced particle size refinement

Figure 4.5: (a-d) Electron diffraction patterns of (CoCuMgNiZn) ESO after sintering at 1323 K for 10 h followed by water quenching. The electron diffraction patterns are from (a) z=[012], (b) z=[$\bar{1}$14], (c) z=[$\bar{1}$23], (d) z=[$\bar{1}$12]. In the bright field image in (e) tweed contrast within the grain body and fringe contrast at the grain boundaries is observed. (f) Magnified image of the region marked with dotted square in (e). Tweed free region is marked with yellow lines

Figure 4.6: (a-d) Electron diffraction patterns, bright and dark field images of (CoCuMgNiZn) ESO after sintering at 1323 K for 10 h followed by water quenching. The diffraction pattern in (a) corresponds to z=[$\bar{1}$00] zone axis pattern of a cubic rocksalt structure. Diffused scattering, streaking and shape evolution (inset) of 02$\bar{2}$ type spot is observed. Extreme ends of the modulated spots are joined together to reveal the mutually rotated symmetry shapes. In the dark field image in (b) mutually intersecting non-orthogonal tweeds are observed. The electron diffraction pattern in (c) is from z=[011] zone axis of the same grain, where streaking and diffused intensity of the spots is observed. The bright field image in (d) shows the inter-penetrating tweeds

Figure 4.7: (a) Mutually rotated symmetry shapes as obtained from the electron diffraction pattern in Figure 5(a). The symmetry shapes may be separated into two groups with mutual relative rotation and with different c/a ratios. (b) Principal vectors from the symmetry shapes in (a) are plotted to reveal their relative rotation. (c) Mutually rotated symmetry shapes in (a) are superimposed to schematically generate the electron diffraction pattern in Figure 4.5(a)

Figure 4.8 (a-d): Electron diffraction patterns and TEM bright field images of (CoCuMgNiZn) ESO after sintering at 1323 K for 10 h followed by water quenching. Arcing in (a) z=[$\bar{1}$00] and (c) z=[$\bar{1}$12] electron diffraction patterns is associated with the mutual in-plane and out-of-plane rotation of domains. Intensity modulated arcs in each of the diffraction patterns are connected with dotted lines to reveal the symmetry shapes of the corresponding zone axes. Fringe contrast is observed in corresponding bright field images in (b) and (d). The fringes are marked with arrows

Figure 4.9: XRD patterns of (CoCuMgNiZn) ESO after sintering at 1323 K for 10 h followed by water quenching (in red) and after sintering at 1323 K for 10 h followed by ageing at 723 K for 120 h followed by water quenching (in blue). Anomalous intensity distribution and broadening of diffraction peaks after ageing is evident in the ESO

Figure 4.10: (a) z=[$\bar{1}$00] electron diffraction pattern, TEM (b-c) bright field images and (d) dark field image of (CoCuMgNiZn) ESO after sintering at 1323 K for 10 h, subsequent ageing at 723 K for 120 h followed by water quenching. In the diffraction pattern in (a),

asymmetrical diffused streaking of spots, splitting of spots is observed. In the bright field images (b-c) domain like structure with domain wall boundaries are observed. The domain wall boundaries are lightened up in the dark field image in (d) with g=020 diffraction spot

Figure 4.11: (a-b) Electron diffraction patterns from a different region of (CoCuMgNiZn) ESO after sintering at 1323 K for 10 h, subsequent ageing at 723 K for 120 h followed by water quenching. The diffraction pattern in (a) is inverted with respect to the diffraction pattern in (b). The patterns may be indexed with co-existent rocksalt phase and a spinel phase with a definite orientation relationship. The d-spacings, angular relationships and ratio of principal vectors are marked in (a). In (b) the diffraction spots corresponding to a rocksalt phase (green) and a spinel phase (yellow) are marked with different colours. The diffraction spots are connected with differently coloured dotted lines to bring out the zone axes symmetry shapes

Figure 4.12: (a) Schematic representation of structurally modulated domains in 2D and in 3D in the (CoCuMgNiZn) ESO. Structural modulation may be initiated with the chemical modulation in individual domains, which are represented with different colours. Structural modulation in 3D makes the ESO appear uniform in chemistry due to the overlap of domains with different chemistry. (b) Schematic representation of oriented growth of rocksalt phase and a spinel phase as obtained from the experimental diffraction patterns in Figure 10. The interface is coherent

Figure 5.1: (a) X-ray diffraction (XRD) patterns of equimolar (CoMgNi)-oxide powder in the as-mixed condition and after 5h, 15h, 40h of ball milling. (b) Simulated XRD pattern of cubic rocksalt (a ~ 4.2 Å) in red and cubic spinel (a ~ 8.1 Å) in blue respectively. (c) Magnified view of 311 peak of cubic spinel and 111 peak of cubic rocksalt in as-mixed condition and after 5h, 15h and 40h of ball milling (d) Magnified view of the evolution of 200 peak of cubic rocksalt phase in the as-mixed condition and after 5h, 15h and 40h of ball milling

Figure 5.2: X-ray diffraction (XRD) patterns of equimolar binary (MgNi)-oxide, (CoNi)-oxide and ternary (CoMgNi)-oxide powder after sintering at 1473 K for 10h followed by water quenching. In all three compositions cubic rocksalt phase forms as the major phase, however, with varying intensity ratios of 111 and 200 diffraction peaks

Figure 5.3: (a) X-ray diffraction (XRD) patterns of equimolar ternary (CoMgNi)-oxide powder (light green) and pellet (dark green) after sintering at 1473 K for 10h followed by water quenching. In the pellet, signature of cubic spinel phase is observed, which is absent in the powder. (b) Normalized intensity plots from the experimental XRD patterns of the powder (light green) and pellet (dark green). Compton modified scattering background is represented as bands with respective colours. Compton modified background for the powder being high, the low intensity spinel peak gets suppressed in the powder

Figure 5.4: (a-d) Bright field image and selected area diffraction patterns along z=[011], z=[125] and z=[013] zone axes from ternary equimolar (CoMgNi)-oxide after sintering at

1473 K for 10 h followed by water quenching. The diffraction patterns may be indexed to a cubic rocksalt phase (a ~ 4.2 Å) with diffuseness and occasional spot splitting. Mottled contrast associated with strain fields is observed in the bright field image. (e) Centred dark field image and complementary bright field image (inset) from the same ternary equimolar (CoMgNi)-oxide after sintering at 1473 K for 10 h followed by ageing at 723 K for 120 h, in which parallel fringe with alternating contrast is observed. (f) Magnified bright field image of (e) showing multiply oriented fringes with ~1.5-3.5 nm spacing between them

Figure 5.5: (a) Selected area electron diffraction pattern along z=[001] zone axis of (CoMgNi)-oxide after sintering at 1473 K for 10h followed by water quenching. Onset of splitting in the higher order spots (marked by dotted circles) is observed. (i-iv) Intensity distribution plots of 200 and 220 type spots are almost symmetrical. (b) Selected area electron diffraction pattern along z=[001] zone axis of (CoMgNi)-oxide after sintering at 1473 K for 10h, ageing at 723 K for 120h followed by water quenching. The diffraction spots are split and arced with modulation of intensity distribution. (v-viii) Intensity distribution plots of 200 and 220 type spots are not symmetrical with several maxima

Figure 5.6: X-ray diffraction (XRD) patterns of (CoMgNi)-oxide with systematic addition of Fe- and Mn-ions after sintering at 1473 K for 10h followed by water quenching. With systematic addition of Fe- and Mn-ions the major phase in the equimolar multicomponent oxide changes from cubic rocksalt phase to cubic spinel phase

Figure 5.7: (a, c) Selected area electron diffraction patterns along z=[001] and z=[$\bar{1}$14] zone axes respectively and (b, d) bright field images of the multicomponent equimolar (CoFeMgMnNi)-oxide after sintering at 1473 K for 10h followed by water quenching. Electron diffraction patterns are indexed to a cubic spinel phase (a~8.38 Å). In the bright field images mottled contrast with occasional fringe contrast (Figure 7d (inset)) is observed

Figure 5.8: Selected area electron diffraction patterns and bright field images of (CoFeMgMnNi)-oxide after sintering at 1473 K for 100h followed by water quenching.

The diffraction pattern in (a) is indexed to a cubic spinel phase, z=[$\bar{1}$14] zone axis along with a coexistent rocksalt phase, z=[001] zone axis. Indices of the diffraction spots, their angular relationships and ratios of principal vectors are given in (b), which is inverted with respect to (a). In the corresponding bright field image in (c), extensive fringe contrast (marked by arrows) within the mottled contrast is observed. The diffraction pattern in (e) is indexed to the same cubic spinel phase, z=[012] zone axis along with the coexistent cubic rocksalt phase, z=[013] zone axis. Indices of the diffraction spots, their angular relationships and the ratios of the principal vectors are given in (f), which is inverted with respect to (e). The corresponding bright field image in (d) shows domain like structure along with fringe contrast. Orientation relationship between the cubic spinel phase and the cubic rocksalt phase is evident

Figure 5.9: X-ray diffraction (XRD) patterns of (CoFeMgMnNi)-oxide and (CoCrFeMnNi)-oxide after sintering at 1473 K for 10h followed by water quenching. In

both of the multicomponent oxides cubic spinel phase is observed to be the predominant phase with systematic peak splitting and shouldering

Figure 5.10: (a-f) Bright field, centred dark field and selected area electron diffraction patterns of (CoCrFeMnNi)-oxide after sintering at 1473 K for 10h followed by water quenching. The diffraction pattern in (c) is indexed to a cubic spinel phase, z=[001] zone axis. The diffraction spots are diffused with streaking along mutually perpendicular 220 type directions (marked with arrows). In the bright field image in (a) and corresponding centred dark field image in (b) modulation and formation of nanodomains are observed (marked with arrows). In two-beam bright field image in (e) and in (f) modulation along 220 direction is observed. Corresponding two beam diffraction pattern is given in the inset of (e). Cross penetration of modulation leading to the formation of domains is shown in the high magnification image in (d)

Figure 5.11 (a-b): Projected interface structure diagram between cubic spinel phase and cubic rocksalt phase. The interface structure diagram has been developed based on the experimentally observed orientation relationship between the cubic spinel phase and the cubic rocksalt phase. The interfaces are semi-coherent in nature

Figure 6.1: LSV plots recording the current density as a function of applied voltage, calibrated against reduced hydrogen electrode. The response from each oxide is colour coded. The inset compares the electrocatalytic response from (CoCuMgNiZn)-oxide and its derivative (CoMgNi)-oxide after sintering and ageing heat treatments

Figure 6.2: Experimental XRD patterns from sintered and quenched equimolar, ternary (CoMgNi)-oxide (green), quaternary (CoMgMnNi0-oxide (purple), quinary (CoFeMgMnNi)-oxide (blue), (CaCoFeMgNi)-oxide (orange) and (CoCuMgNiZn)-oxide (magenta). Respective phases have been marked with different coloured symbols

Figure 6.3: SEM-SE micrographs, selected area diffraction pattern and TEM bright field/dark field images from sintered and quenched (a1-a3) (CaCoFeMgNi)-oxide, (b1-b3) (CoFeMgMnNi)-oxide, (c1-c3) (CoCuMgNiZn) ESO and (d1-d3) (CoCrFeMnNi) HEO respectively. The microstructural features are marked with arrows and indexing of diffraction patterns have been done employing different colour schemes

Figue 6.4: SEM-XEDS chemical mapping from (a1) sintered and quenched (CoMgNi)-oxide, (a2) sintered, aged and quenched (CoMgNi)-oxide, (b1) sintered and quenched (CoCuMgNiZn) ESO and (b2) sintered, aged and quenched (CoCuMgNiZn) ESO respectively. The quantification of the cation weight % has been provided in coloured boxes adjacent to the respective maps

Figure 6.5: (a) LSV response from sintered and quenched equimolar (CoMgMnNi)-oxide, (b) CV plots from the same oxide under varying scan rates and (c) schematic representing possible mechanism behind enhanced electrocatalytic activity in the same dual-phase oxide

Figure 6.6: (a) Overpotential plots for all the respective multicomponent oxides at 5 mA/cm^2 and (b) Tafel slopes for the same oxides. The histogram is accompanied with computed overpotential values at 1 mA/cm^2 (in white) and at 10 mA/cm^2 (in black). The Tafel slopes are marked over each oxide

Figure 7.1: Sintered and quenched pellet of equimolar ternary (CoMgNi)-oxide placed on an alumina tray filled with a mixture of alumina and graphite powder (a) before ageing treatment and (b) after ageing treatment. The obvious change in colour of the powder bed may easily be discerned

Figure A.1: Single-crystal spot electron diffraction patterns from several zone axis of a FCC structure ($u^2+v^2+w^2<22$). The patterns have been simulated with the help of JEMS software. The respective zone axis directions are marked with "ZA" on top of each pattern. The ratio of the principal vectors along with the interplanar angles are marked in the respective patterns.

Synopsis

Continuously diminishing fossil fuel resources, growing environmental concerns and changing geo-political scenario has incentivized the search for new energy resources and technologies. It has been well understood that future sustainable and green energy innovations will be mostly driven by the synthesis of new materials. Multicomponent high entropy oxides (HEOs) are perceived to serve as candidate materials in the field of catalysis, electro-chemical energy conversion and storage, electronic devices, thermal barrier coatings among many others. HEOs may be looked at as a recent vintage of the high entropy alloys (HEAs). They were brought into existence by innovative thinking with a dash of serendipity by Cantor and Yeh during 2004-05. HEOs were invented following the lineage of HEAs, however much later. The first HEO was reported in 2015 in CoCuMgNiZn-oxide by Rost et al. and was categorized as entropy stabilized oxide (ESO). Following this, a number of HEO systems have been reported. HEOs are slightly different than the HEAs as in HEOs there are more than one cation and anion sublattice and substitution may happen in either of them. The calculation of configurational entropy is also different in these systems. In addition, these systems are sensitive to environment in order to sustain their defect equilibria and electrical neutrality. It has been believed so far that all HEOs are single phase solid solutions with little or no reference to their stability.

The research work reported in this thesis has derived motivation to understand the formation of single-phase in rocksalt-, spinel-based HEOs and its derivatives, their stability and microstructural evolution. The thesis has been organized in seven chapters. **Chapter 1** introduces the basic concepts of designing HEOs, its similarities and differences with traditional dilute alloys, HEAs, bulk metallic glasses (BMGs) and their applications in the fields of catalysis, electrochemical energy storage and conversion. **Chapter 2** describes the

precursor metal oxides, heat treatment procedures for solid-state synthesis of multicomponent metal oxides and the working principles of the characterization techniques used.

Synthesis, phase evolution, composition modulation, local structural variation and their stability in multi-component equimolar (CaCoFeMgNi)-oxide and its ternary and quaternary derivatives have been reported in **Chapter 3**. The rationale behind synthesizing and characterizing the above material system as a starting point is the isostructuralism of all the constituent binary oxides in their +2 oxidation states. The empirical rules initially put forth for the formation of ESOs/HEOs by Rost et al., later by Sarkar and co-workers harp on non-isostructuralism of at least one constituent oxide, otherwise the 5-component mixture (HEO) shall inevitably end up being phase-pure with the same crystal structure as its constituent binary oxides. However, transition metals in their ionic states are known to display multiple oxidation states. Oxygen partial pressure is also known to alter the oxygen stoichiometry in metallic oxides leading to an anion deficient or excess composition, which in turn produces various kinds of defect microstructures. It was found out that the ternary equimolar (CoMgNi)-oxide exhibited single-phase signature from X-ray diffraction (XRD) experiments, while quaternary equimolar (CaCoMgNi)-oxide produced a two-phase mixture, both having the cubic rocksalt structure, however one rich in Co-, Mg-, Ni-ions (major phase, ~62%, a=4.15Å) and the other rich in Ca-ions (minor phase, ~38%, a=4.83Å). The equimolar (CaCoFeMgNi) multicomponent oxide (MCO) showed a complex diffraction pattern which could be indexed to the presence of at least four phases. The major rocksalt phase enriched in (Co,Mg,Ni), forms almost 50% of the phase fraction while Fe-enriched ordered hexagonal phase forms ~35% and the remaining Ca-enriched regions form a rocksalt phase (a=4.83Å) as well as a spinel phase (a=8.32Å), with combined phase fraction of around 15%. SEM-XEDS chemical mapping clearly brings

about large-scale chemical segregation of Ca- and Fe-ions, however, maintaining the presence of all five cations in all the phases but to varying extents. Transmission electron microscopy (TEM) results throw insight into the phase formation, its stability and microstructural evolution after sintering at 1473K for 10h as well as for 100h followed by water quenching. The system tries to reduce the lattice strain arising out of the major phase (Co, Mg, Ni enriched rocksalt) by systematic mutual in-plane and out-of-plane rotation amongst the structural domains forming a helical structure. This leads to the appearance of linear fringes having alternating contrast with 2-5 nm width in diffraction contrast imaging along with extensive spot-splitting and arcing of spots in the single crystal diffraction patterns. The Fe-rich hexagonal phase on the other hand undergoes structural ordering with cations and vacancies producing anti-phase domain boundaries in the process, along with array of fine twin-related planar faults which grows significantly with prolonged exposure at high temperatures. Furthermore, there are also some regions within the MCO where three phases having cubic rocksalt, cubic spinel and ordered hexagonal structures are found to co-exist. They possess a definite orientation relationship among them with coherent/semi-coherent interphase interfaces.

The first ever reported (CoCuMgNiZn) ESO has been taken up as the model system, and the exploration of its physical metallurgy is given in **Chapter 4**. X-ray diffraction (XRD) studies indicate that the HEO is single phase with cubic rocksalt structure on average. However, XRD pattern obtained from the sintered pellets and powder shows systematic shoulders associated with all the fundamental peaks of rocksalt phase (a~4.23Å) along with a reversal of intensities of the first two peaks having non-ideal intensity ratio. Upon peak deconvolution, signatures from constituent oxides of CoO, MgO and NiO brings out an excellent match with the reported d-spacings. In the hyperspectral chemical mapping (SEM-XEDS), fine-scale segregation of Mg- and Cu-ions could be discerned, which

becomes more prominent with prolonged exposure at elevated temperature. TEM BF-CDF imaging along with corresponding SAED pattern from z=[100] zone axis of the sintered and quenched quinary HEO exhibit wavy domain like structure of alternating contrast with diffused interfaces oriented along the <002> directions of the cubic rocksalt structure. Moreover, geometric shape evolution of the diffraction spots could be discerned along with diffuse streaking between it. Such a diffraction pattern translates into mutually rotated cubic domains, occasionally with a hint of tetragonality, that prefers to grow along the c-axis of the FCC crystal structure in 3-D. The tweed morphology as viewed from the four-fold axis of the cubic rocksalt structure, appears as discontinuous jagged steps of alternating contrast from the z=[011] zone axis. The tweeds, with minor chemical fluctuations, may act as template for enhanced phase separation to produce a self-assembled microstructure, provided sufficient stimulus is applied to overcome its kinetics of solid-state phase transformation. The HEO was subsequently aged at an intermediate temperature of 723K for 120h to understand its phase stability and microstructural evolution. Although the quinary HEO maintains its global average rocksalt structure, as understood from the XRD pattern, however with major peak broadening and highly non-ideal peak ratios. This observation is counterintuitive as the system gets more time to relieve its residual strain. TEM imaging clearly reveals grown domain structure, however not grown to a large extent, in-line with the anticipated sluggish kinetics of the material system. The domain interior is of lighter contrast while the domain walls are of darker contrast, with occasional appearance of δ-fringe contrast. These evidences point to the metastability in the time-temperature space of the phase-pure quinary composition with respect to systematic structural modulation accompanied by minor composition fluctuation. Furthermore, in a bid to release its volumetric strain, apart from lattice strain, arising from the multi-cationic sublattice, a cubic spinel phase (double the lattice parameter) is found to coexist with cubic

rocksalt phase having a definite orientation relationship and sharing perfectly coherent interfaces. To the best of knowledge of the author, such direct observations and inferences have not been reported in literature during the last decade, following the discovery of the first HEO having rocksalt crystal structure in 2015.

Chapter 5 encompasses the effect of systematic partial substitution of cations in equimolar ratio on the phase evolution, its stability and microstructural formation. Equimolar ternary (CoMgNi)-oxide, common to both the previous chapters, has been explored thoroughly. The as-mixed mixture produced signatures from both rocksalt (CoO, MgO, NiO) and spinel (Co_3O_4) phase. However, with the advent of progressive high-energy ball-milling, a competition between the two phases could be seen in the form of peak mergers. Apart from that, the shift of peaks with higher h of milling was found to be non-unidirectional, which is counterintuitive. The competing shifts of the peaks may be attributed to combined phenomenon of build-up of varying amount of vacancy concentration in both the phases upon milling, with refinement of particle size and concomitant increase in lattice strain. Upon sintering and quenching, the equimolar ternary composition exhibits phase-pure signature of a disordered rocksalt phase (a~4.2Å). However, the sintered pellet shows a sharp (220) peak of a spinel phase (a=8.36Å), which was only seen as a hump for the sintered powder. It becomes evident after analysis that the crushing action of the sintered pellet (owing to the brittle nature of ceramics) increases the strain in the material, which in turn raises the Compton modified background, enabling it to mask low intensity peaks from structurally correlated phases having low phase fractions. TEM observations could not find conclusive evidence for coexisting spinel phase owing to its rather small volume fraction. However, upon ageing the sintered (CoMgNi)-oxide at intermediate temperature for long h, extensive fringe contrast of 1.5-3.5 nm width could be seen in the micrographs along with major spot-splitting and arcing in the corresponding diffraction patterns. Several

intensity maxima could be deconvoluted from each principle spot of the z=[001] zone axis pattern, which could be systematically joined to obtain several four-fold symmetry shapes that are rotated with respect to each other. Partial substitution by Mn- and Fe-ions in equimolar (CoMgNi)-oxide resulted in phase-pure spinel (a~8.38Å) signature from the sintered and quenched quinary (CoFeMgMnNi)-oxide. This HEO forming composition has not been reported before. However, the peaks in the XRD pattern are finitely broad with non-uniform intensity ratios along with shoulders and splits, especially in the peaks of (222), (400) and (440). It could simultaneously be indexed to (111), (200) and (220) planes of a rocksalt phase with half the lattice parameter. This single-phase spinel-forming composition was further sintered at elevated temperature for prolonged time to check the phase stability, which resulted in a very similar diffraction pattern as the sintered and quenched one. However, electron diffraction and TEM imaging points at a nuanced picture in the energy landscape of the HEO, which was previously unanticipated. Systematic presence of fringe contrast along with domain-like morphology from two major zone-axes of the spinel structure reveal systematic presence of other spots. Those spots may be indexed to a rocksalt phase of exactly half the lattice parameter of the spinel phase, which are found to be have definite orientation relationships with each other. The interface structure is mostly semi-coherent. It may be inferred that rocksalt domains grow locally inside the major spinel phase, and vice-versa as proved in the previous chapter, all in a bid to relieve the geometric frustration in the lattice. Furthermore, Mg- was replaced by Cr-ions to synthesize (CoCrFeMnNi)-oxide, the first reported spinel forming HEO. Although the XRD pattern brings out a high degree of one-to-one correspondence as obtained from (CoFeMgMnNi)-oxide, however with peak broadening and excessive shouldering. TEM BF-CDF imaging interestingly reveals interweaved domain-like morphology of 5nmx5nm with alternate dark and bright contrast. Corresponding electron diffraction pattern from

z=[001] zone axis exhibits continuous diffuse streaking along mutually perpendicular <220> directions. This points to coordinated local structural modulation assisted phase separation event, although at the nascent stage in the spinel HEO, which was unanticipated since its discovery.

Chapter 6 documents structure-property correlation of all the MCOs/ESOs/HEOs explored in the previous experimental chapters. Since this class of materials have multi-faceted areas of application owing to its favourable functional properties in general, the performance of them as catalysts for efficient evolution of oxygen and hydrogen from electrochemical water-splitting experiments has been carried out. Using a three-electrode setup, all the equimolar ternary, quaternary and quinary MCO/ESO/HEO compositions were tested against linear sweep voltammetry (LSV), cyclic voltammetry (CV) and electrochemical impedance spectroscopy (EIS) tests. It was found out for apparent phase-pure compositions, the catalytic performance drops consistently with ageing in the all the cases. Such an observation could be attributed to the fine-scale segregation of redox active Co-, Cu-, Fe- Ni-, Mn-ions as observed from SEM-XEDS chemical mapping. Moreover, multi-phasic (CaCoFeMgNi)-oxide produces the least promising dataset, while the two-phase mixture of rocksalt and spinel phases in equimolar (CoMgMnNi)-oxide outperforms all the other compositions, with the lowest overpotential of 390 mV at a current density of 10mA/cm^2 and lowest Taffel slope of ~74.6 mV/dec. Such an observation hints to enhanced electrocatalytic performance where reversible inter-conversion between two related phases may occur during oxidation and reduction cycles of the water-splitting process. It further validates the school of thought put forth by Zhai et al., on the use of poly-cationic oxides (PCOs) for efficient two-step thermochemical water-splitting.

Chapter 7 discusses the major conclusions arising from the research work carried out throughout this thesis as a whole, along with a few points for future scope of exploration.

Dedicated to my parents,

My late grandparents

&

In regretful memory of

My elder brother

(2nd September 1984 – 23rd April, 2024)

Chapter – 1
Introduction

1.1. Brief history of materials design

Growing environmental concerns, continuous depletion of fossil fuel reserves and changing geo-political scenario has incentivized the search for new energy resources and technologies [1-5]. It has been well understood that future sustainable and green energy revolutions will be driven by the innovations of materials [4-7]. Modern day civilization relies heavily on the production and processing of numerous materials at very large scales for a plethora of applications. This includes bulk production of innumerable kinds of materials for manufacturing familiar daily life objects to components for critical engineering applications [8,9]. India alone produces over 100 MT of crude steel every year for its use in construction, automobile and allied industries, whereas Taiwan on its own produces more than 15 million semiconductor wafer microchips per year for application in the fields of physical and biological sciences, sports and entertainment alike [10,11]. Interestingly, our ancestors from prehistoric times too depended on various materials, however on a much more modest scale. Weapons, tools, ornaments and artworks were forged from simple materials which would help in protecting themselves (survival of the fittest) while at the same time hunt effectively and migrate efficiently. A schematic representing the chronological evolution of materials along with the human race is presented in Figure 1.1. Since time immemorial, stone and wood were extensively used to perform miraculous things of the time, lighting fire and making wheels. After a few thousand centuries of stone age and crudities of our neolithic ancestors, the chalcolithic period saw man using native metals like copper, tin, lead and arsenic for the first time [12]. In this era of early metallurgists, people quickly realized how to extract metals from their relatively pure naturally occurring mineral ores and once extracted they could be hardened by repeated hammering (forging). Gold and silver also caught attention due to their luster but were too soft to be used in anything apart from ornamentation and craft. However, the

importance of gold as a precious metal led to the dishonest mixing of other elements in small quantities and thus the art of alloying was brewed for the first time. This led to the explosion from copper age to bronze age. People soon realized that alloying makes a material stronger and easier to cast into various shapes than their monolithic counterparts. Alloying, which started as an accidental malpractice ~5000 years ago, soon became a quintessential practice and continues to thrive to this day [13]. The historical milestone of the industrial revolution and renaissance in many parts of the world may directly be attributed to the age-old cumulative understanding of metallurgy and materials, which then started to bloom as a young subject of science [14]. It is now one of the most fascinating interdisciplinary branches of science today. Thus, metallurgy and materials knowledge evolved from rudimentary art to state-of-the-art science over thousands of years, with incremental progress until recently. Current advances in science and technology have brought us at the forefronts of materials exploration [4-9].

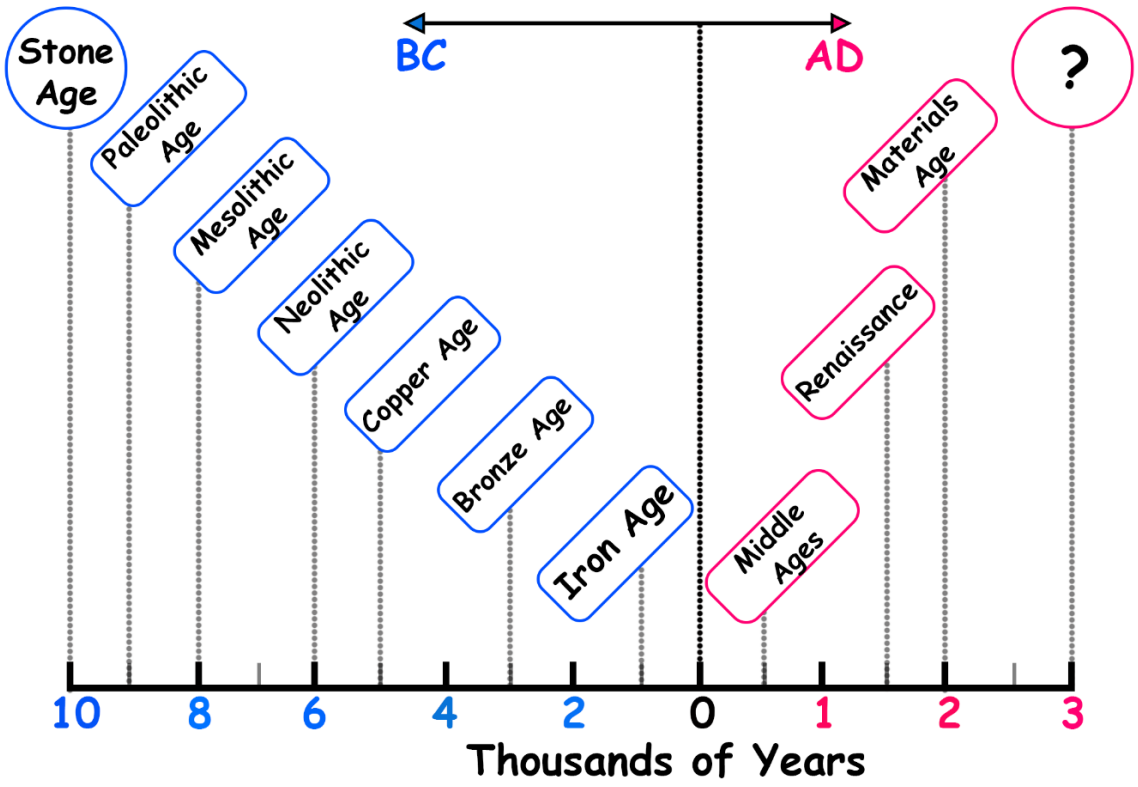

Figure 1.1: Schematic representing the long arduous journey of pre-historic humans in relationship with materials, which in turn holds huge promise for the future.

Materials design encompasses a broad knowledge-based approach in discovering and/or synthesizing materials with a desired combination of properties. Traditionally, there was no well laid principle to arrive at a particular composition with a specific structure and specific set of properties. Empiricism-based heuristic approach has led traditional metallurgists to design alloys/materials for various applications. This approach demands observing a large number of material systems so as to decipher underlying patterns and it heavily relies on the researcher's experience, grasp over the subject, intuition-driven trial-and-error and serendipity [15,16]. Hume-Rothery rules for solid-solution formation, Inoue's criteria for glass formation, Pettifor structure maps for synthesis of intermetallic compounds and Pauling's rules for formation of ionic materials are some of the notable achievements of the age-old heuristic approach [17-20]. However, this approach is not being able to keep pace with the modern-day scenario where there is an ever-increasing demand for materials. In the field of engineering alone, more than 1000 different types of metallic alloys are being used daily [21]. Regardless, this is a miniscule fraction of the possible number of alloys that can be synthesized [22]. In this context, inverse-heuristic approach is gaining momentum with the advent of data mining and machine learning. The new-age materials design adopts a forward or "function follows form" approach. It involves several descriptors namely atomic identity, chemistry and structure (ACS) as input parameters to ensue specific material output properties. However, with the advancement in computational prowess, a contrary approach where the desired target properties are used as an input to determine the ACS which in turn can reveal the material composition space, is being explored. This is the "form follows function" inverse-heuristic design philosophy [23,24]. In the author's opinion, old-fashioned heuristic approach is irreplaceable, although clubbed with data mining, modelling and simulation is bound to make newer materials exploration more exciting. A brief review of materials design philosophy over the last

century and a paradigm shift in it are presented in this chapter. The chapter culminates with identifying the scientific bottlenecks in the field thus far and formulate problem statements which shall serve as the objectives of the thesis.

1.2. Metallic alloys and compounds

1.2.1. Traditional multicomponent alloys

The early 19th century witnessed the birth of inductive reasoning and observation-based empiricism and its father is widely regarded as Francis Bacon. Soon, most of the demand for robust alloys were propelled by core manufacturing industries of automobile, electrical and construction sectors [14]. Development of grain-oriented texture in Fe-Si alloy, along with other minor alloying elements, by controlled heat-treatment schedule for transformer core laminations was one of the first concise alloy design strategies to be adopted successfully at industrial scales [25]. In this context, seminal works of Sorby (birth of metallography), Matthiessen (conductivity in alloys), Bozorth (Invar), Barrett (silicon-iron), Seebeck (thermoelectricity), Graham and Sieverts (gas occlusions in metals), Zackay (TRIP steel), Bauschinger (deformation of metals), Buerger (deformation micromechanics) are worth mentioning [15]. The discovery of x-rays by Roentgen during beginning of the 20th century followed by the invention of Transmission Electron Microscope by Ruska and Knolls shortly after, completely transformed the dimensions of the subject [26,27]. This led eminent scientists such as Bragg and Bragg, Von Laue, Ewald, Otto Müller and others to directly investigate the microstructure at unprecedented resolution and indirectly explore the crystal structure of crystalline materials [28,29]. On top of that, seminal works on equilibrium constitutional diagrams for binary alloys during this period made alloy design a very conscious strategy for several varied applications [30]. In this regard, the traditional alloys were mainly composed of one element (in principal amount) alloyed with several

elements in non-major proportions. They were commonly referred to as “dilute alloys” or X-based alloys (X: element in principal amount). A list of note-worthy dilute alloys is mentioned in Figure 1.2. along with their rough timeline of development.

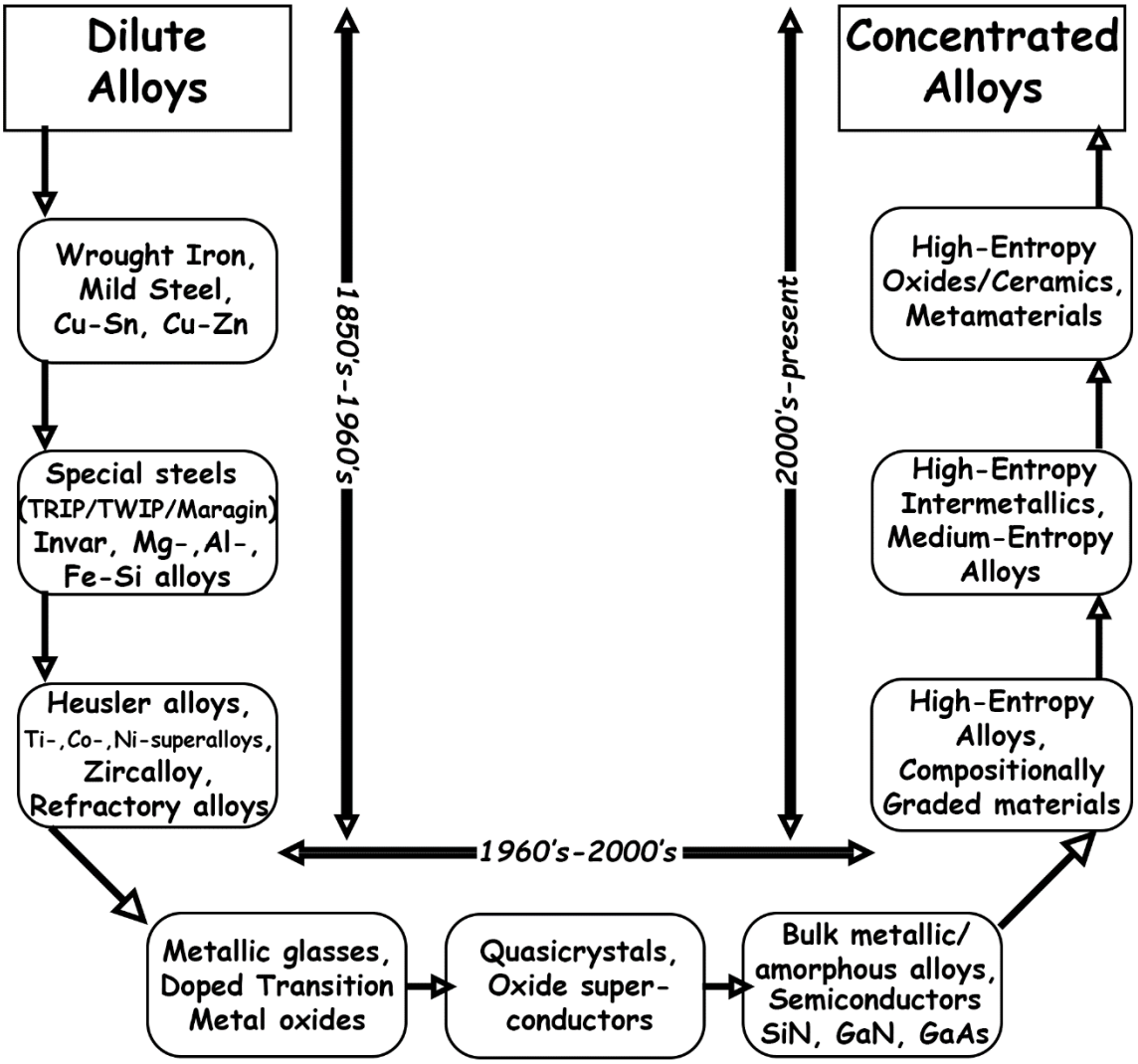

Figure 1.2: Broad categorization of profound engineering materials based on their alloy design strategy and their estimated timeline of evolution during the last two centuries.

The most notable dilute alloy is steel with 40-85 wt% Fe, 0.08-2 wt% C and balance other alloying elements, which in itself is a broad subject of study owing to its versatility, diversity and relevancy even to this day [31-33]. A typical microstructure of steel usually consists of multiple phases predicted by Gibbs phase rule from Fe-$C_{equivalent}$ constitution

diagram (in case of near equilibrium processing) or from TTT/CCT diagrams (for non-equilibrium processing). It then becomes possible to engineer the second phase(s) in terms of shape, size, distribution, volume fraction to achieve strength-ductility tradeoff, a common performance barrier well-documented in steel literature [34]. Expanding to non-ferrous alloys, it was systematically reported that several multi-phase dilute alloys often yield good combination of properties while many do not. The Ni-based superalloy may be cited as one such example where the γ/γ' dual-phase microstructure with shape-controlled ordered domains within the matrix phase provides excellent properties even at elevated temperatures [35,36]. Additionally, Ti-6Al-4V is an (α+β)-Ti alloy and is commonly regarded as Ti-superalloy [37]. On the other hand however, most β-Ti alloys suffer from poor combination of properties due to ω-phase transformation products [38,39]. It is because of the heavy mismatch of active slip systems in the BCC matrix of β-Ti when compared to hexagonal (complete-collapse) or trigonal (partially-collapse) ω nano-domains, that crack generation and propagation gets favoured along the interphase interfaces, causing embrittlement and premature failure of structural components [40,41]. A quintessential strategy in alloy development, after a general composition is ball-parked, is to seek explanations to fundamental root causes of failure or poor performance and how to favourably engineer them. This helps to develop better structure-property-performance co-relationships and strategies to make existing alloys better. Hence tremendous efforts have been put over several decades in the areas of material processing and heat-treatment induced strengthening mechanisms so as to improve the performance of the existing dilute alloys [31-41].

During this period, Hume-Rothery postulated few empirical rules for extensive solid-solubility considering the atomic size, electronegativity and crystal structure of individual elements, which is useful to this day [42]. These rules could predict, barring a few

exceptions, simple isomorphous (complete miscibility across entire composition range) systems from that of limited solubility systems coupled with one or more invariant reactions. This qualitative approach in tandem with thermodynamic descriptors and advanced metallographic techniques of the time proved to be a great combination in designing and processing newer alloys of both ferrous and non-ferrous nature with huge success [43,44].

1.2.2. Bulk metallic glasses

Turnbull and Duwez demonstrated for the first time a rapid solidification technique which was able to produce cooling rates as high as 10^6 K/second in their seminal work during late 1950's [45,46]. The first liquid alloy to be vitrified by cooling from the molten state was Au-Si alloy [47]. Decades after this discovery, dozens of ferrous and non-ferrous alloy systems were found to form glasses over a wide range of composition [46]. There is usually no recalescence process associated with glass formation and thus it is categorized as a 2^{nd}-order phase transformation under Landau scheme of phase transitions. The characteristic microstructural feature is the amorphous structure of the alloy with electron diffraction revealing diffuse-ring pattern [48-50]. Amorphization of an alloy essentially involves the kinetic suppression of nucleation and growth from its undercooled melt. Initially, the glassy state was understood from Kauzmann's paradox of undercooling [51]. It depicts a scenario where the entropy of molten liquid (above the melting point) when extrapolated backwards under the action of undercooling, becomes lower than the entropy of the solid phase of the same composition, which is absurd. To avoid this absurdity, the system chooses to be in a glassy-state without crystallizing. However, such high cooling rates posed a practical difficulty in the dimensions of the rapidly cooled alloy, often restricting specimen geometry to thin foils, ribbons or powder [47]. Metallurgists of the time started dreaming of newer alloys that could form glasses at much lower cooling rates like their silicate glass

counterpart, which would realize their production in bulk form as well as in bulk quantities. After almost thirty years of research in the field of metallic glasses, pioneering work by Inoue during late 1980's and Johnson a decade later, catapulted the emerging field to new heights and bulk metallic glasses (BMG's) were born [52,53]. A number of La-, Mg-, Zr-, Ti-, Pd-, Fe-, Al-, and Ni-bearing glass formers were identified which could be vitrified with cooling rates as low as 0.1 K/second [53-55]. They could also be cast into 12mm diameter rods [55]. This development directly extended the opportunity to understand long-standing problems in solidification science and the structure of the liquid phase of the alloys. Extensive research in BMG's often captured precipitation of nano crystals/quasicrystals upon cooling, establishing a link with possible short-range order (SRO) in the liquid state, which is proven to be a statement of fact with advancement of electron microscopy [56-59].

Several empirical criteria for formation of BMG's were proposed by Inoue which later became synonymous with inverse Hume-Rothery criteria for solid-solution formation [49]. Inoue argued that multicomponent alloys with large atomic radii mismatch between constituent elements and highly negative heats of mixing between each pair of binaries should favour glass formation [52]. This is why constitution diagrams with deep eutectics and intermetallics are prone to glass formation [53-55]. It is envisaged that geometric frustration in the lattice, if allowed to exceed beyond a certain threshold can structurally destabilize the lattice from crystallizing and hence solidify in a glassy-state.

1.2.3. Multiprincipal elemental alloys

High entropy alloys (HEAs) were brought into existence by innovative thinking coupled with a dash of serendipity by Cantor and Yeh, independently during 2004-05 [60,61]. They argued in favour of little or no data on ternary, quaternary, quinary and subsequent higher-

order constitution diagrams which has confined traditional metallurgists to explore alloys based on one or two components in principal amounts only. Although this approach has enriched the database of alloys pertaining to the corners/edges of the binary and to some extent ternary constitution diagrams, it also has led to the center composition-space of higher-order equilibrium diagrams practically unexplored [60].

In binary or ternary dilute alloys, physical metallurgists are primarily concerned about solid-solution phases and invariant reaction products at the terminal ends of the diagram. This is usually because of the formation of hard and brittle topologically packed intermetallic and vacancy-ordered phase(s) at the centers of the phase diagram, most prominent example being the Al-Ni phase diagram [62,63]. Linearly extrapolating the argument to the center composition-space of higher order systems, predict several secondary phases in accordance to the Gibbs phase rule. However, it is counterintuitive to find one or two simple solid-solution phase(s) when a large number of elements (≥5) are mixed in principal (equiatomic or near-equiatomic) amounts [61]. This has been coined as the "High Entropy" effect which constitutes one of the four core effects in concentrated alloys, apart from "sluggish diffusion", "lattice distortion" and "cocktail effect" which are well documented in literature [64-67]. The birth of such concentrated alloys of 5-6 or more elements in equiatomic or near equiatomic ratio exponentially increased the number of alloys that could be formed and studied, which was previously unanticipated. A simple palette of 40 elements from the periodic table if alloyed in equiatomic or near equiatomic proportions offers a possibility of $\sim 10^{10}$ multiprincipal elemental alloys [22]. An explosion of materials research based on the newly formulated alloy design technique yielded several novel classes of materials which is summarized in Figure 1.3 [68-71].

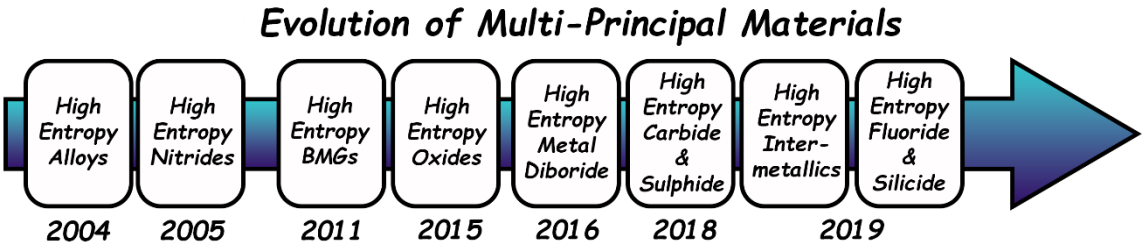

Figure 1.3: Fruits of concentrated alloy design strategy.

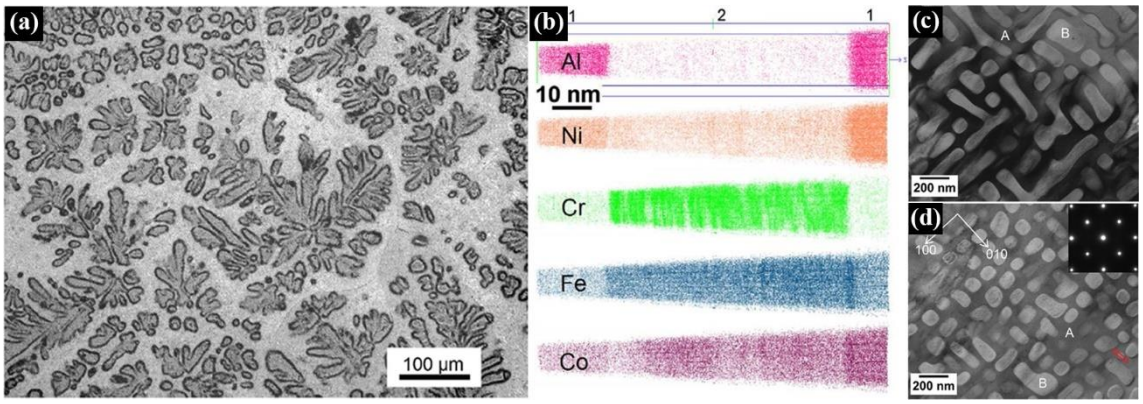

Figure 1.4: As-cast AlCoCrFeNi HEA (a) optical micrograph showing dendritic solidification, (b) 3D reconstruction of Al, Co, Cr, Fe and Ni atoms from APT experiment and (c,d) TEM BF images of dendritic and interdendritic phase with definite morphology. The dark contrast matrix phase (marked as A) is Al-Ni rich while the bright precipitate phase (marked as B) is Cr-Fe rich [77].

The high entropy effect has been attributed to the overwhelming dominance of configurational entropy of mixing (ΔS_{mix}), which would always offset enthalpy of mixing (ΔH_{mix}) term in the free energy equation and consequently in the energy landscape of the alloy [72]. Hence, it was believed that such a thermodynamic mandate holds the clue to simple solid-solution phase formation, with randomly distributed motifs in the disordered lattice. However, it was a matter of time before the scientific community found out through careful experimentation that almost all the HEAs were not phase pure [73,74]. Even if in rare instances some of them like CoCrFeMnNi Cantor alloy were established to be single-phase, it was later found to be metastable with respect to time-temperature assisted phase separation events [75,76]. Thus, what started out as clean microstructures composed of

simple solid-solution phase, turned out to be highly complex in due course of research. One such example of microstructural evolution from AlCoCrFeNi HEA processed via solid-state route and consolidated by spark plasma sintering is shown in Figure 1.4 [77]. It depicts a two-phase mixture of sub-micron sized ordered BCC second phase decorating a disordered BCC matrix phase. Furthermore, transmission electron microscopy in conjunction with spectroscopy has revealed nanoprecipitates, ordered solid-solution phases, intermetallic phases, amorphous phases and short-range order domains in numerous alloys. These observations essentially hint at the shortcomings of the oversimplified model for entropic stabilization in multiprincipal elemental alloys [22, 73-77].

1.3. High entropy oxides

This class of materials were conceived following the lines of high entropy alloys by Maria and Rost in 2015 [78]. The model high entropy oxide (HEO) system is the equimolar mixture of Co^{+2}, Cu^{+2}, Mg^{+2}, Ni^{+2} and Zn^{+2} which forms a phase-pure solid-solution phase with the cubic rocksalt (MO) structure. Their work demonstrated entropic reversibility i.e. transformation of multi-phase to single-phase above a threshold sintering temperature and back to multi-phase on lowering the temperature [78,79]. This was achieved by in-situ heating XRD experiment. STEM-EDS too revealed random distribution of cations in the ordered oxygen sub-lattice ion columns. These observations convinced the scientific community to promote this particular composition of HEO as entropy stabilized oxide (ESO) with homogeneous single-phase structure, which is a subset of HEO and in turn of multiprincipal materials. This has been depicted in Figure 1.5. With the discovery of high entropy oxide, a host of several classes of high entropy oxides based on different crystal structures evolved. A comprehensive list is shown in Figure 1.6, which is far from exhaustive since novel oxides are continuously being synthesized [80-82].

Although the material design premise of HEOs is an extension to the principles of HEAs, there are certain fundamental distinctions between the two. A HEO has two separate sublattices for cation and anion compared to a single lattice framework for HEA [78]. However, that is just one scenario.

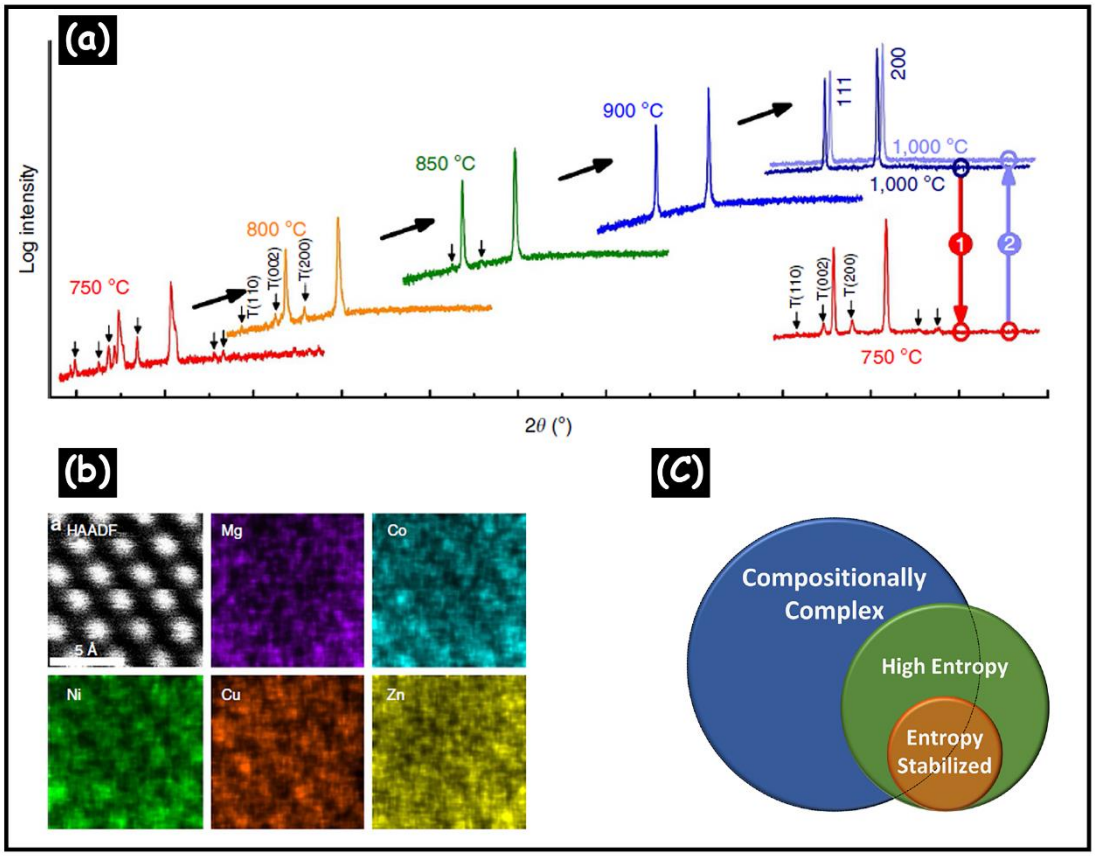

Figure 1.5: (a) Entropy driven reversible transition from multiphase to single phase (b) corresponding STEM-HAADF-EDS mapping of rocksalt HEO and (c) Venn diagram of concentrated materials [78,79].

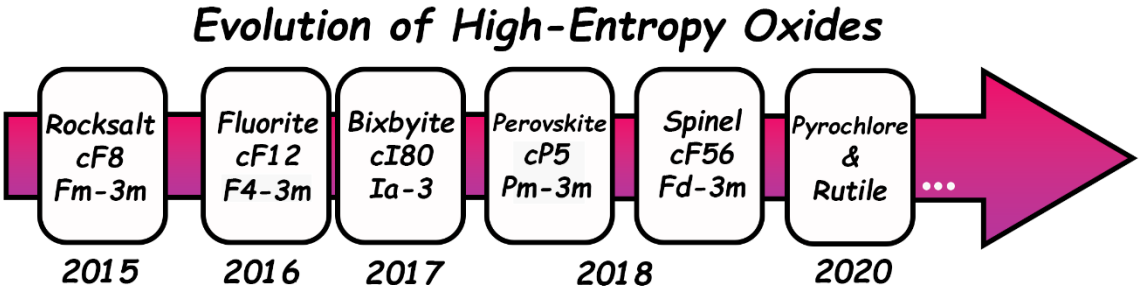

Figure 1.6: Various sub-class of HEOs with their space group and Pearson symbol.

They can have multiple sublattices for either cation or anion or both and substitution may occur in either of them, which makes calculation of configurational entropy of the system much more robust.

In addition, any ceramic system is governed majorly by ionic bonding in contrast to metallic bonding in HEAs. This makes such systems sensitive to environment and processing conditions in order to sustain their defect equilibria and net charge neutrality. Despite challenges, empirical criteria for formation of ESOs highlight the importance of similar cationic radii at specific oxidation state and coordination number, along with non-isostructuralism in at least one precursor oxide coupled with immiscibility in at least one pair of constituent binary oxides [78,83]. It is further believed that in HEOs, the presence of ordered anion-sublattice accommodates the non-stoichiometry and possible defect structure in the cation-sublattice during processing. This helps to preserve the complete disorder in the multi-cationic sublattice, allowing the formation of a homogeneous single-phase solid-solution [78-84].

1.3.1. Thermodynamics

The desire to come up with “new” and “exotic” materials is envisaged to outrun basic thermodynamic considerations for designing future HEOs [22,85]. Ideal mixing dictates that the number of components in a solid-solution does not affect the solubility of an additional component, but such systems are rare-most, if not hypothetical. In real systems, the type and nature of the additional component, its structural transformations and its pair-wise non-ideal interactions with other components determine the solubility limit. Due to ionic-covalent bonding in ceramics, long-range or short-range (LRO/SRO) ordering is believed to be the norm producing homologous series of compounds, which in turn decreases the overall configurational entropy [85,86]. Moreover, synthesis of

nanocrystalline HEOs can have huge impact arising out of contributions of surface energy to the overall free energy, which may shift the phase boundaries stabilizing certain polymorphs or altering the solubility-limit [87]. Proponents of entropic stabilization in multicomponent oxides over that of multi-principal elemental alloys, often argue in favour of the omnipresent ordered anion-sublattice, in the interstitial voids of which cations populate in a random disordered fashion and forms their own cation-sublattice [78]. The ordered oxygen-sublattice is thought to accommodate any defects arising out of pairwise interactions in the multi-cation sub-lattice. It is believed that ordered anion-sublattice framework protects the randomness or disorder in the cation sub-lattice, provided mixing (configurational) entropy is maximized by incorporating 5 or more cation species in equimolar or near equimolar proportions [82-84]. However, the physical picture might not be as straight forward as previously reasoned. This is so because there are families of oxides where the cation builds the lattice framework and anion goes to the interstitial voids instead; the most technologically relevant system is that of ceria (CeO_2) and other lanthanide-based oxides [88]. The relative size of anion and cation at a specific oxidation state and coordination environment determines their site specificity in the lattice [89]. Apart from that, there could be more than one cation and/or anion sublattices dictated by order, disorder or both. Processing conditions, especially partial pressure of the gas being purged can significantly alter the local defect structure in either of the sublattice along with enriched/deficient sub-lattice in order to maintain net charge neutrality [89]. This introduces complexity in the already oversimplified entropy of mixing term in the free energy equation, which is frequently overlooked. In the literature of CoCuMgNiZn HEO, there are few reports on the possible co-existence of allied spinel phase in minor fraction apart from defect microstructure and Jahn-Teller distortions caused by Cu^{+} and/or Co^{3+} ions in the phase evolution process [90-92]. Moreover, in the x-ray diffraction signatures of the

HEO, the intensity ratios do not match with the ideal cF8 (Fm-3m) crystal structure of rocksalt. Apart from that, systematic shoulder peaks at roughly half the intensity of accompanying Bragg peaks could be observed in sintered and quenched HEOs, which has been attributed to $K\alpha_{II}$ excitation [84]. However, this does not appear to be very convincing since wavelengths of the Kα doublets differ in the 3rd place of decimal which results to angular deviation in the second place of decimal of 2θ, but experimentally observed difference in angular disposition are several times higher. Documentation regarding stability of the entropy stabilized single-phase in CoCuMgNiZn ESO as well as other HEOs is quite scarce in literature so far. Although few theoretical modelling and simulation, along with in-situ heating and calorimetry experiments have explored the stability of the phases, however for very limited exposure times, which may not be comparable to the kinetics of such chemically complex multicomponent systems [78-84]. In this context, thermodynamic stability is a pressing issue and it is worth re-visiting this fundamental aspect with the help of Figure 1.7. Assuming the solid in Figure 1.7 to be iron, which can exist in all three solid, liquid and gaseous states, it is known for a fact that enthalpy of liquid iron will always be more than that of solid iron, as entropy too of liquid iron will always be greater than that of its solid. However, below the melting point, a state of matter with lower enthalpy or entropy is more stable, but in transforming to liquid above its melting point makes both the enthalpy and entropy higher. Thus, a generalized statement cannot be made that a phase with lower enthalpy or higher entropy is always stable or shall remain to be stable. Above the melting point, the liquid has lower free energy at all temperatures than the solid, and below the melting point, the solid always has lower free energy. To summarize, solid is always stable below T_m while liquid is always stable above T_m, as both have lower free energy. This is the reason that free energy (G) is the only thermodynamic descriptor that is used as a single stability criterion.

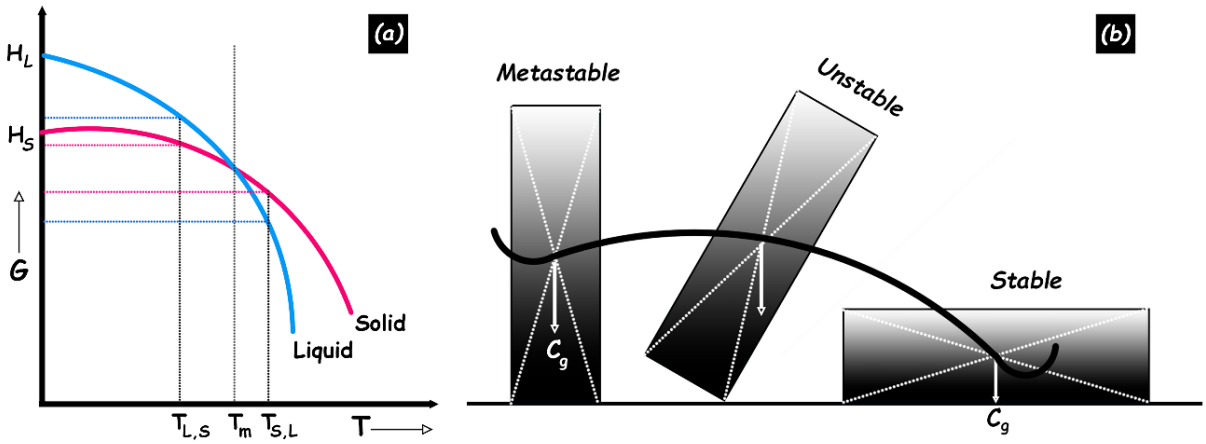

Figure 1.7: (a) G vs T plot of a solid and its liquid at constant pressure, where the slope of the curves gives entropy and its intercept the enthalpy while (b) is the schematic demonstration of local minima separated by activation barrier in the energy landscape of a mechanical object as it falls.

Therefore, a phase with higher configurational entropy but higher free energy is less stable than a phase with lower configurational entropy but lower free energy. The manifestation of enthalpic penalties combined with maximizing randomness in the multi-cationic sublattice in multicomponent oxides shall be demonstrated throughout this thesis.

1.3.2. Structure

Metallurgists are traditionally interested in impure materials, be it alloyed or doped. They are also most interested in deciphering the crystal structure and exploring the microstructure of alloys, compounds and composites. It is well established that composition is profoundly co-related with both microstructure and crystal structure of any material and vice-versa, which in turn dictates the material properties [93,94]. Hence, understanding the crystal and microstructure paves the path for engineering them to extract better material performance, consequently innovating materials design in general. Majority of ceramic crystal structures are based on either FCC or HCP close-packing of one type of ion(s) while the other type of ion(s) occupies specific sets of interstitial sites. The rocksalt (MO) crystal structure, having NaCl as the prototype, forms by mutual interpenetration of multiple cubic

sub-lattices. This results in the bigger Cl^- ions to build up the lattice framework with motifs at (0,0,0), (1/2,1/2,0), (1/2,0,1/2), (0,1/2,1/2) and the smaller Na^+ ions to fit in the octahedrally located voids at (1/2,1/2,1/2), (0,0,1/2), (0,1/2,0), (1/2,0,0) [93,94]. The space group becomes Fm-3m and Pearson symbol cF8. Between any two close-packed layers of anions, a hexagonal array of cations with identical periodicity can be visualized. A model structure with edge-sharing MO_6 octahedra is shown in Figure 1.8, with inset depicting the maximum radius of the ionic species occupying the octahedral voids without any distortion. For FCC close-packed systems, the motifs when approximated as hard spheres touch along the close-packed directions i.e. <110> resulting in:

$$\mathbf{4r = \sqrt{2}a} \qquad \textbf{(i)}$$

$$\mathbf{^{max}R_v = (\sqrt{2}-1)r} \qquad \textbf{(ii)}$$

Where 'a' depicts the lattice parameter of the cubic structure, 'r' is the ionic radius of Cl^- at six-fold coordination and '^{max}Rv' is the maximum ionic radius of the smaller Na^+ ions that can snugly fit in the octahedral void. Solving equations (i) and (ii) yields:

$$\mathbf{^{max}R_v = 0.146a} \qquad \textbf{(iii)}$$

Since the formation and stability of all ionic compounds are governed by Pauling's rules, it demands that the radius ratio (r_c/r_a) must lie between 0.414-0.732 for a rocksalt structure [20]. Transitioning to spinel crystal structure, it is a 2x2x2 supercell where anions decorate the overall FCC lattice framework while cations partially fill up both the octahedral and tetrahedral voids. Spinels have general formula of AB_2O_4 where cations in +2 oxidation states prefer filling half of the octahedral voids whereas cations in +3 oxidation states prefer to fill out one-eighth of the tetrahedral voids [93-95]. There could be inverse spinel structure with different site-specificity of the cations or there could be mixed spinel with random occupation of cations.

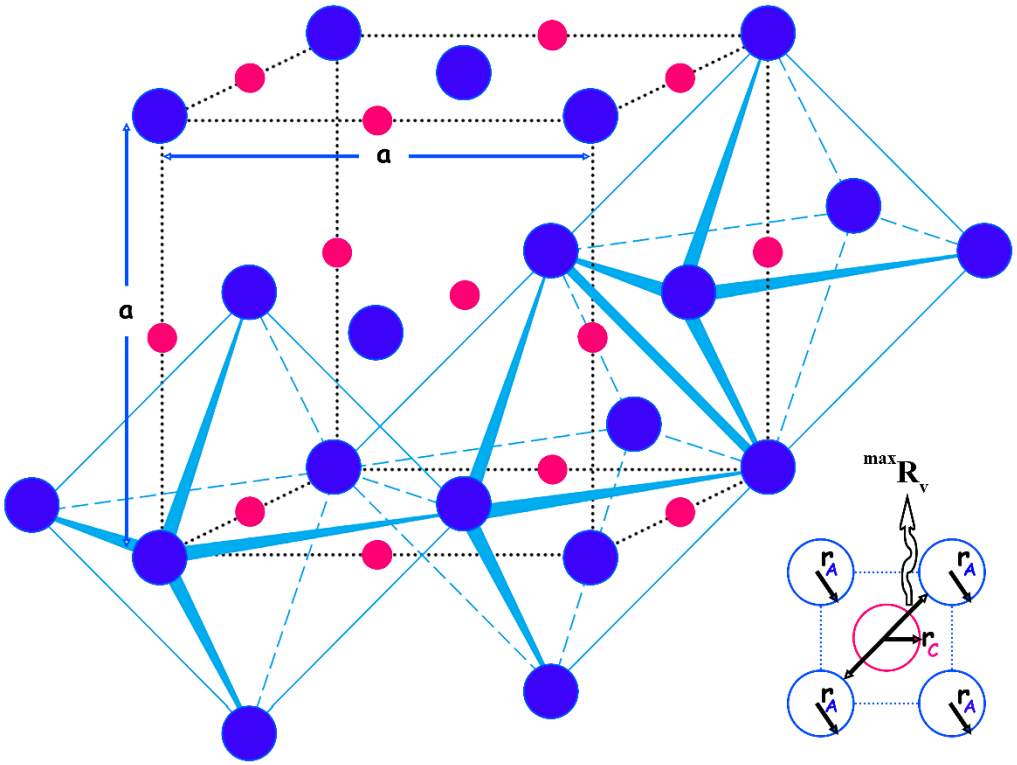

Figure 1.8: A typical rocksalt prototype structure with anions (marked in blue) decorating the fcc lattice positions and cations (marked in red) occupying the octahedral voids. Three edge-sharing six-fold coordination polyhedras are depicted for clarity.

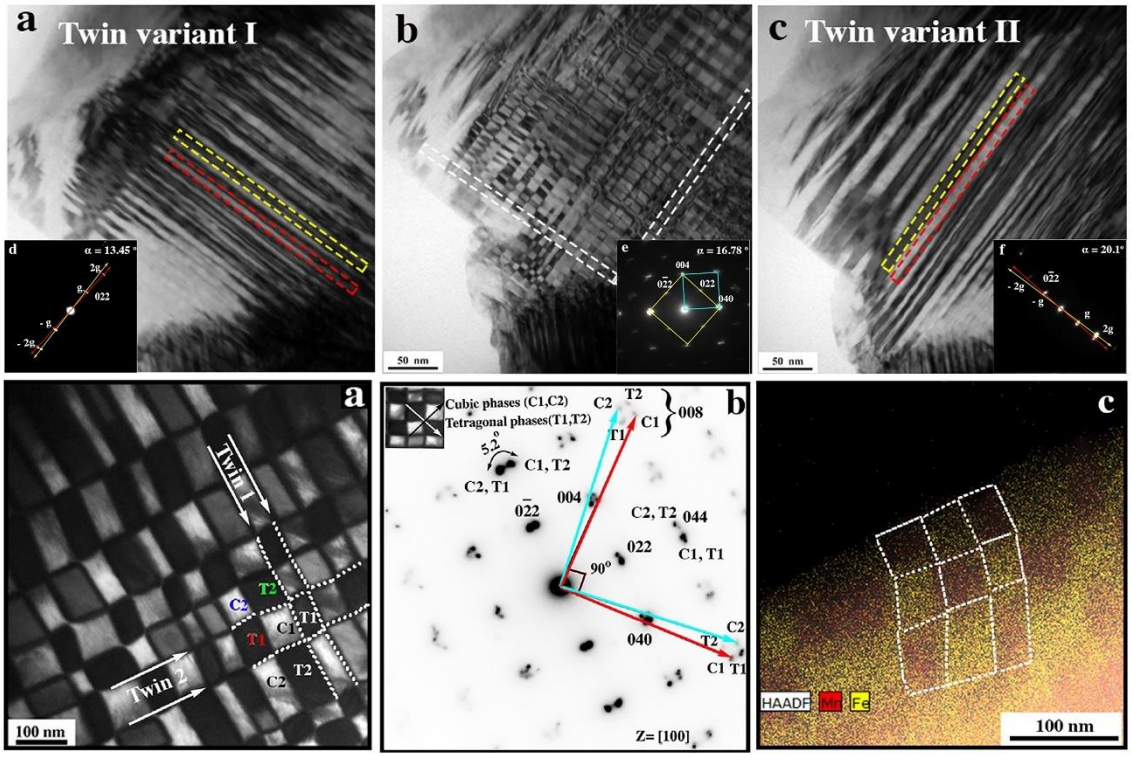

Figure 1.9: Recurrent compositional phase separation leading to a chessboard-like microstructure in CoFeMn medium entropy oxide characterized by spinel structure [103].

The cubic spinel is designated by Fd-3m space group and cF56 Pearson symbol. This is the highest symmetry group of cubic spinel, while other polymorphs of the phase have lower symmetry elements [95]. Apart from that, both cubic rocksalt and cubic spinel are amenable to distortions in the cubic crystal structure leading to tetragonal, orthorhombic, rhombohedral and even monoclinic variants [96-99]. It is perhaps important to further realize that the spinel mineral ($MgAl_2O_4$) is a highly ordered normal spinel which forms under extreme heat and pressure over geological time spans. Thus, lab or industry synthesized $MgAl_2O_4$ will always be disordered to certain degree, which holds good for most of the spinel forming materials that has been synthesized or ever will be [94].

Polytypism is another well documented phenomenon closely related to polymorphism in ceramics, although the variants of a particular structure only differ with respect to the stacking sequence of intermediate 2-D layers [94]. Complex disposition of anti-phase boundaries (APBs) has been witnessed in simple parent structure types [97]. Moreover, phase separation within monophasic transition metal oxides has been well explored by Rao and his co-workers [100,101]. They are mostly driven by the competition between charge localization and delocalization which has contrasting magnetic and electric properties. Such kinds of phase separation were mostly recorded during early 2000's in cuprates and manganates with length scale of phase separation lying anywhere between 1-200 nm [100-102]. Couple of decades later, Pal et. al successfully demonstrated chessboard-like (CB) microstructure in multicomponent CoFeMn and CoFeGaMnZn spinel oxide through recurrent compositional phase separation and cross-penetration of twin variants, shown in Figure 1.9 [103,104]. The sequence of phase transformation events leading to nano CB microstructure has been explained in light of twinning-induced, pseudo-spinodal segregation of ionic species. Crystallographic model of evolution of CB microstructure based on irregular octahedra's face-sharing with one another along elastically soft <022>

directions has also been put forth. During the same time, Singh et al. reported type-I and type-II rhombohedral distortions in layered rocksalt structured Li(Ni,Mn)O cathode material [105]. Non-cubic distortions to binary/ternary cubic rocksalt and cubic spinel is also reported [110]. Apart from chemical modulation, phase separation and ordering, early works of Tilley, Anderson and Hyde during 1970's reveal extensive planar fault mediated exotic structures in various metal oxides [106-109]. Earlier it was believed that non-stoichiometry in metal oxides is structurally accommodated by point defects like in $Fe_{1-n}O$, $TiO_{1\pm n}$, $VO_{1\pm n}$ among others [110]. Later it was found that most often than not, such changes due to anion/cation ratio is accommodated by planar faults or intergrowth structures like in reduced WO_3, TiO_2, Nb_2O_5 and many others [106-109].

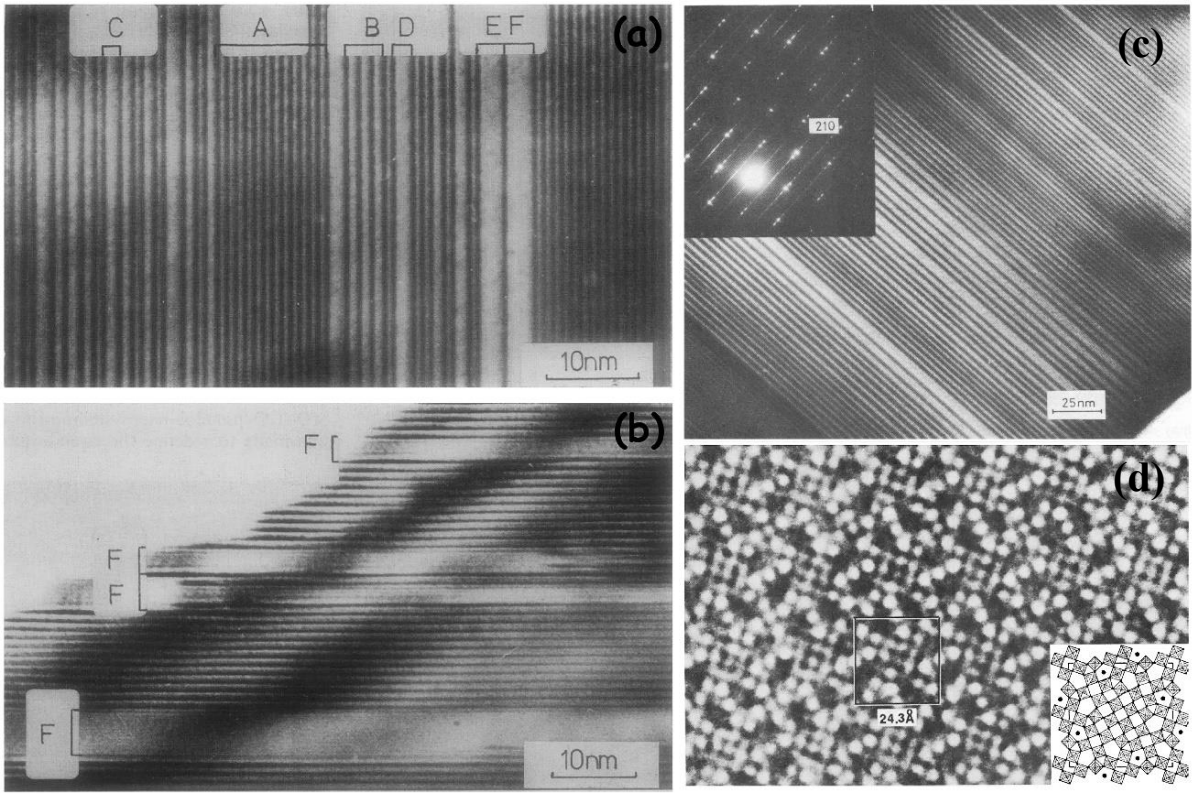

Figure 1.10: (a) Disordered $Sr_3Ti_2O_7$ crystal with phase intergrowths from varying stoichiometries, (b) intergrowth of stable $SrTiO_3$ (c) TEM BF image of disordered faults on (210) planes of doped TiO_2 with corresponding electron diffraction pattern at the inset and (d) phase-contrast image of $2Nb_2O_5$, $7WO_3$ [108,109].

They also demonstrated special tiling structures at atomic scale due to mutual rotation between domains in geometrically frustrated spinels, perovskites and spinelloids such as $CaFe_2O_4$, $BaFe_{12}O_{19}$, $SrTi_2O_3$ among others [106-109,111]. The process of interaction of planar defects leading to ordering, clustering or elimination of point defects is known as "crystallographic shear" (CS) and the trace of such planes are termed CS planes. The micrographs of such extensive faulted structures have been depicted in Figure 1.10 along with corresponding streaked electron diffraction pattern and high-resolution phase-contrast image [108,109].

1.3.3. Properties

1.3.3.1. Mechanical properties

Extensive research on HEOs in less than a decade has made them a popular choice for its use in several applications along with scope for further enhancement. The rutile (TiO_2 prototype) structure exhibits highest hardness and elastic modulus among all the HEO family of structures [112]. The fluorite (CaF_2 prototype) HEOs generally show greater hardness than pyrochlore HEOs [113]. Due to the inherent oxidation and corrosion resistance, HEOs are also being fabricated in thick and thin films for environmental and abrasive coatings in structural components. Al_2(CoCrCuFeNi)O and (AlCrTaTiZr)O have shown the highest hardness in all of the existing oxide coatings at ~22 and ~20 GPa respectively [114]. Low thermal conductivity coupled with sluggish grain-growth kinetics have made HEOs viable options for refractory applications as well as thermal barrier coatings (TBCs) for aero-engines and gas-turbines [112]. Moreover, there remains tremendous scope for engineering the composition, phase and microstructure of such HEOs in order to explore materials with very low or negative thermal expansion coefficients [112-114].

1.3.3.2. Functional properties

Transition metal oxides have long been explored for their favourable polarization and charge-lattice coupling response [115]. Chemical modulation has been intrinsically linked with the phase stability for desirable ferroelectric, dielectric and piezoelectric response [115]. In this context, MCOs/ESOs/HEOs have emerged as attractive candidates for enhanced properties owing to the entropic stabilization of disordered solid-solution phase(s) in them [112-114]. It is believed that global-scale disorder in materials may give rise to polar nanoregions (PNR) and its coupling with lattice phonons propels the property as a relaxor ferroelectric material [112]. Additionally, geometric frustration may induce local distortions which enhances dielectric and piezoelectric response [114]. Few research groups have shown that (CoCuMgNiZn) rocksalt ESO exhibit structural tunability upon varying the composition, owing to Jahn-Teller distortions induced by Cu- and/or Co-ions, which results in high dielectric constants and favourable catalytic activity [92,116]. It has also been demonstrated to possess superior lithium-storage properties due to tunable pseudocapacitive contributions [117]. Relaxor-like characteristics have been reported for Ba(ZrSnTiHfNb) perovskite HEO [112]. (LaPrNdSmEu)NiO_3 HEO have been found to go through a low temperature metal-insulator transition, attributed to geometric distortions arising out of coordinated octahedra tilting [80]. Fluorite (CeLaPrSmY)O_2 have demonstrated that the band gap and crystal structure can be tuned via oxygen stoichiometry due to the hybridization of oxygen and rare earth elements, which in turn may be developed for scintillator and laser applications [81]. Furthermore, double-exchange and super-exchange phenomena renders HEOs with tunable properties like ferro-/anti-ferro-, ferri-/anti-ferri- and diamagnetism [118]. Ferrite based spinel HEO like (CoCuMgNiZn)Fe_2O_4 have shown soft magnetic character with coercive field of ~100 Oe, whereas, chromite-based spinel HEOs like (CoCuFeMgNi)Cr_2O_4 have recorded coercive field as high as 1 T

[112]. HEO ferrites are also promising candidates as magnetic insulators with good quality surface for its application in spintronics and nonvolatile memory devices [112-114].

1.3.4. Fields of application

The field of high entropy ceramics (HECs) blossomed since the first ever reported HEO in 2015 [78,80]. They mainly caught attention of researchers because of their remarkable properties, apart from debatable schools of thought so far their phase formation, stability and microstructural evolution is concerned [81, 85-87]. Focusing on the properties, HEOs have been reported to be promising candidates in various fields of application, an overall schematic of which is given in Figure 1.11. Understanding and engineering charge transport mechanisms in HEOs offer promising avenues for exploring enhanced properties, especially as electrode material for secondary-ion batteries and fuel cells [112-114].

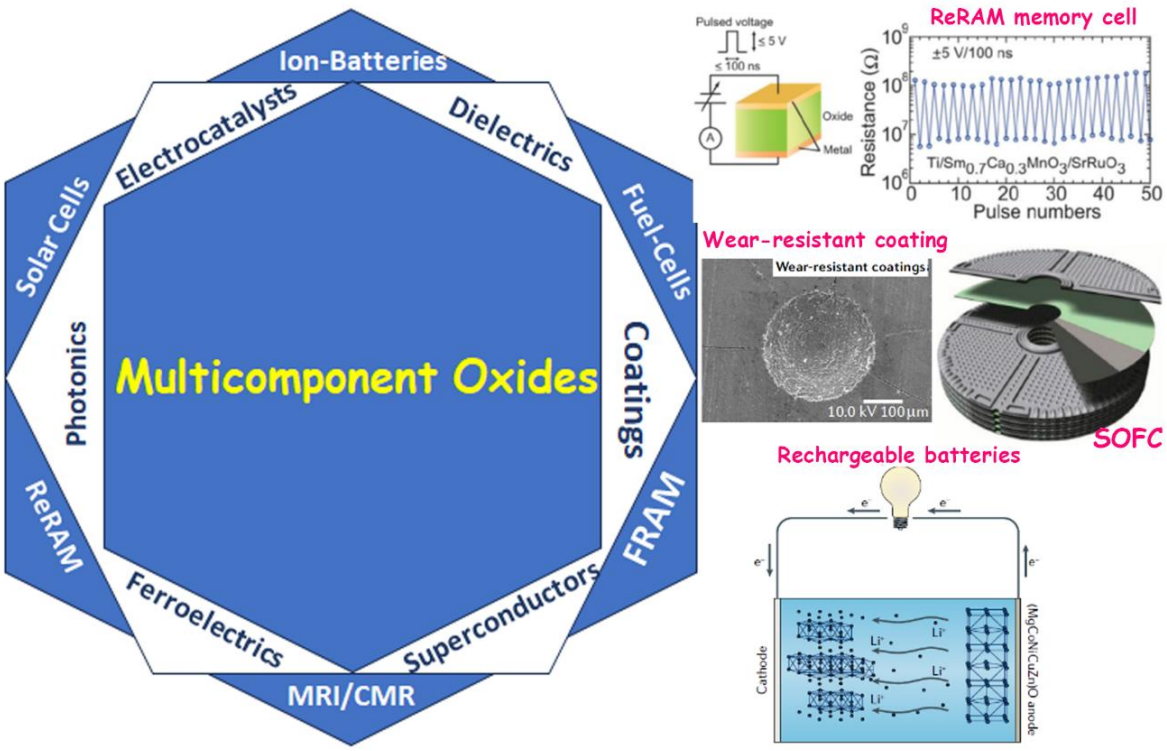

Figure 1.11: Fields of application for HEOs reported so far.

HEOs have already become promising candidates as anode material, cathode material as well as solid-state electrolyte for Li-ion batteries [119,120]. Soon after the first HEO was successfully synthesized, Berardan and coworkers reported room temperature superionic conductivity of Li-ions (> 10^{-3} S/cm) and fast mobility of Na-ions (> 10^{-6} S/cm) in $(MgCoNiCuZn)_{1-x-y}Ga_yA_x$ (where A=Li, Na, K) HEO, significantly exceeding the generally used lithium phosphorous oxy-nitride solid-state electrolyte [117]. They also reported colossal dielectric constant for doped rocksalt-based HEOs, which have the potential to serve as high-*k* dielectric materials [116].

(MgCoNiCuZn) HEO has also demonstrated good charge cycling response and very high specific capacities. The currently favoured anode material is graphite with a capacity of ~360 mAh/g [112]. Rocksalt type high entropy oxyfluorides have also been explored as cathode material for Li-ion batteries and they have delivered specific energies up to ~307 mAh/g, with scope for further improvement [119]. An equimolar hexanary HEO has been reported to show ~40% increase in capacity and energy density as cathode material than its constituent lower-order oxides [112]. Coin cells fabricated with (MgCoCuNiZn)O as polysulfide anchor show competitive reversible capacity, excellent cycling stability and low-capacity decay for its use in lithium-sulfur batteries [120].

Multi-cationic HEOs have compositional freedom which translates to substantial electronic structure and coordination environment tunability, that makes them ideal candidates as catalysts [121]. (FeNiCoCrMn)-layered glycerate HEO have shown rapid transport of reactants to the material while providing additional catalytic active sites [121]. The use of $(FeMgCoNi)O_{1.2}$ poly-cationic oxide (PCO) has demonstrated a significant reduction of temperature under which efficient hydrogen evolution reaction occurs via two-step thermochemical water-splitting [122]. HEOs have also shown promise as catalytic booster for oxidative desulphurization of diesel [112]. Mesoporous $(MgCoNiCuFe)_x$-Al_2O_3 have

reported against CO oxidation and CO_2 hydrogenation and have showed negligible degradation after 48h along with superior sulfur tolerance to CuO-Al_2O_3 [113]. Spinel-based HEOs are further being exploited for efficient oxygen evolution reaction (OER) and hydrogen evolution medium (HER) from electrochemical water-splitting [123]. Rocksalt-based HEOs on the other hand have been found to exhibit long-range antiferromagnetic ordering below Neel temperature of ~113 K, suitable for its use in memory devices [124,125].

It has been demonstrated that local disorder in ionic charge can further reduce the thermal conductivity of HEOs without compromising on the mechanical stiffness. Equimolar (MgNiCoCuZnSb) HEO has shown the lowest conductivity of ~1.4 W/mK among similar class of materials [126]. Perovskite-based (BaCaLaPbSr)TiO_3 HEO have shown ~5 times reduction in thermal conductivity compared to $SrTiO_3$, with figure of merit over 0.2 [112]. Thin films of hexanary Ba(ZrSnTiHfNb)O_3 HEO with perovskite structure has recorded thermal conductivity of ~0.55 W/mk, which is an order of magnitude lower than binary or ternary perovskites [114]. High entropy niobates or zirconates have become promising candidates for thermal and environmental protection applications, owing to their very low thermal conductivity along with uncompromised mechanical rigidity [80]. (AlCrTaTiZr) HEO has been reported extremely high hardness values of ~22 GPa as well as exceptional wear resistance [81]. $(LaNdSmEuGd)_2Ti_2O_7$ HEO with pyrochlore structure has been reported to withstand up to 5 times the thermal cycling as $La_2Zr_2O_7$ can withstand [112]. Similar HEOs are also known to have reduced leaching rates compared to its lower-order derivatives, and consequently are being considered for managing nuclear waste [112].

1.4. Objectives of the thesis

- Systematic partial substitution of one or more cationic species with other ones is theoretically known to keep the configurational entropy of the whole equimolar mixture intact [72]. However, this simple logical assumption has been debunked in the recent past in HEA literature [75-77]. Thorough investigations with a clear understanding in this regard is yet to be realized in HEOs and it has been taken up in this research.
- In principle, HEOs should crystallize in a single-phase with random and homogeneous distribution of ions across all length scales [78]. However, that is perhaps not the scenario. The initial goal of the current research has been to synthesize and characterize equimolar binary, ternary, quaternary derivatives of the equimolar quinary rocksalt and spinel HEOs (CoCuMgNiZn)O and $(CoCrFeMnNi)_3O_4$ respectively by systematic partial substitution. The random distribution of multiple cations forming simple solid-solution phase with rocksalt or spinel structure has been explored throughout this thesis, in an attempt to understand the mechanism behind the entropic stabilization in HEOs.
- Thermodynamic stability of HEOs has been a pressing issue since its inception and it has hardly been tackled in literature [85,86]. The consequences of prolonged heat treatments on the phase stability and microstructural evolution in various multicomponent oxides have been examined through systematic diffraction, electron microscopy and spectroscopy experiments. In this regard, XRD, SEM-SE/BSE imaging, SEM-XEDS analytical mapping, TEM imaging and SAED techniques have been exhaustively utilized.
- Another primary objective behind carrying out the current research revolves around the manifestation of lattice strain due to geometric frustration in both the sub-lattices in HEOs. Additionally, the effect of volumetric strain due to competition between multiple cations with non-ideal interactions among them has been explored. There is also a

possibility of interfacial strain build-up due to local structural modulation or intergrowth of correlated second phases, which too has been investigated throughout this research work.

- Presence of secondary phase(s), evolution of defect microstructure, chemical or structural modulation at sub-micron length scales and diffusion-assisted reconstructive phase transformations have been thought of in HEO literature [91,92]. However, direct evidences for such schools of thought are scarce. It has been carefully examined throughout the research work carried out in this thesis.
- HEOs have been reported to outperform its monolithic counterparts by leaps and bounds in several applications so far [112]. The enhanced properties are often attributed to the synergistic effect arising out of high configurational entropy [113,114]. However, a sound picture of structure-property correlation is missing. The research work in this thesis explores the catalytic activities of several multicomponent oxides for efficient evolution of oxygen and hydrogen from electrochemical water-splitting experiments. The properties have been correlated with the crystal structure, its deviation from ideality, relative phase fractions and segregation of redox active species.
- In order to arrive at a holistic picture, the popular 'materials tetrahedron' strategy has been adopted throughout this thesis. It is schematically represented in Figure 1.12. Synthesis and processing of various MCOs/ESOs/HEOs have been characterized at the microstructural and crystal structure length scales, and a correlation is established with the obtained properties. Modeling and simulation techniques have also been employed to validate the experimental findings.

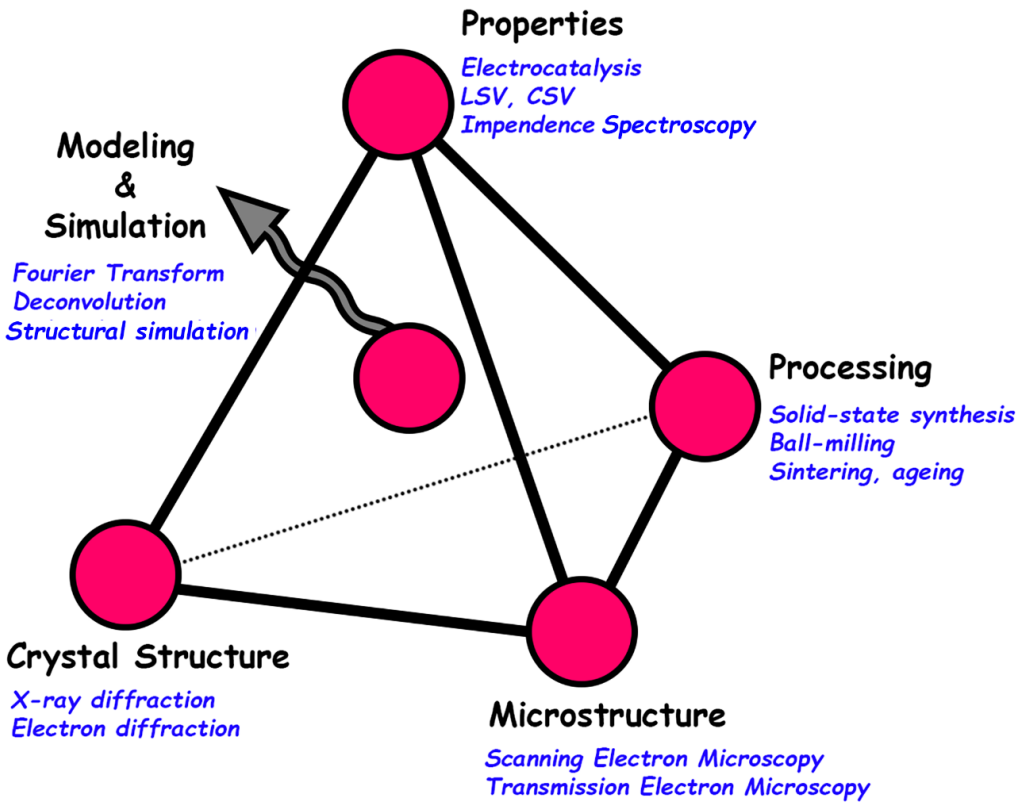

Figure 1.12: Materials tetrahedron describing the correlative interconnection between processing and properties via characterization and computation after a suitable composition is identified. This approach has been followed throughout the thesis and implemented on several multicomponent oxides.

1.5. Reference

1. C. Liu, F. Li, L. P. Ma, H. M. Cheng, Advanced materials for energy storage, Adv. Mater., 2010, 22, E28-E62
2. B. C. H. Steele, A. Heinzel, Materials for fuel-cell technologies, Nature, 2001, Vol. 414, 345-352
3. X. Yu, Z. Tang, D. Sun, L. Ouyang, M. Zhu, Recent advances and remaining challenges of nanostructured materials for hydrogen storage applications, Prog. Mater. Sci., 2017, Vol. 88, 1-48
4. A. S. R. Bati, M. Batmunkh, J. G. Shapter, Emerging 2D layered materials for perovskite solar cells, Adv. Energy Mater., 2019, 1902253 (21 pages)

5. J. Knaster, A. Moeslang, T. Muroga, Materials research for fusion, Nature Physics, 2016, Vol. 12, 424-434
6. Y. Liu, X. Zhang, Metamaterials: a new frontier of science and technology, Chem. Soc. Rev., 2011, Vol. 40, 2494-2507
7. N. I. Zheludev, Y. S. Kivshar, From metamaterials to metadevices, Nature Materials, 2012, Vol. 2, 917-924
8. Sir C. V. Raman, The Indian musical drums, Proc. Ind. Acad. Sci., A, 1934, Vol. 1 (II) (14 pages)
9. S. J. Zinkle, J. T. Busby, Structural materials for fission & fusion energy, Materials Today, 2009, Vol. 12 (11), 12-19
10. K. Kumar, J. Bandi, L. R. Tenneti, The Indian steel industry: Growth, challenges and digital disruption, PwC India, 2019 (28 pages)
11. J. A. Mathews, A Silicon Valley of the East: Creating Taiwan's semiconductor industry, California Management Review, 1997, Vol. 39 (4) (30 pages)
12. A. C. Reardon, Discovering Metals: A historical overview, Metallurgy for Non-Metallurgist, 2011, Vol. 74 (2) (12 pages)
13. R. F. Mehl, A Brief History of the Science of Metals, The Maple Press Company, USA, 1948 (88 pages)
14. B. Cohen, The Eighteenth-Century Origins of the Concept of Scientific Revolution, Journal of the History of Ideas, USA, 2014 (33 pages)
15. R. W. Cahn, Alloy design: a historical perspective, Proc. Indian Acad. Sci., 1980, Vol. 3 (4), 255-260
16. S. Ghosh, J. Basu, D. Ramachandran, E. Mohandas, M. Vijayalakshmi, A unified approach to phase and microstructural stability for Fe-ETM alloys through Miedema's model, Intermetallics, 2012, Vol. 23, 148-157

17. W. H. Rothery, The freezing points, melting points and the solubility limits of the alloys of silver and copper with the elements of B-subgroup, Philosophical Transactions of the Royal Society of London, 1933, Vol. 223
18. A. Inoue, Stabilization of metallic supercooled liquid and bulk amorphous alloys, Acta Mater., 2000, Vol. 48, 279-306
19. D. G. Pettifor, The structure of binary compounds I: Phenomenological structure maps, J. Phys. C: Solid State Physics, 1986, Vol. 19 (3), 285-313
20. L. Pauling, The principles determining the structure of complex ionic crystals, J. Am. Chem. Soc., 1929, Vol. 51 (4), 1010-1026
21. S. P. Pandey, V. Singh, The importance of engineering materials in present world, Int. J. Sci. & Res., 2017, Vol. 6 (3), 433-441
22. W. Steurer, Single-phase high-entropy alloys: A critical update, Materials Characterization, 2020, Vol. 162, 110179
23. T. W. Liao, G. Li, Metaheuristic-based inverse design of materials: A survey, J. Materiomics, 2020, Vol. 6, 414-430
24. C. Y. Lee, C. Y. Jui, A. C. Yeh, Y. J. Chang, W. J. Lee, Inverse design of high entropy alloys using a deep interpretable scheme for materials attribution analysis, J. Alloys Comp., 2024, Vol. 976, 173144 (12 pages)
25. J. Bierman, Science and society in the *New Atlantis* and other renaissance utopias, PMLA, 1963, Vol. 78 (5), 492-500
26. W. R. Nitske, The Life of Wilhelm Conrad Rontgen, Discoverer of the X-ray, University of Arizona Press, 1971 (355 pages)
27. E. Ruska, The development of the electron microscope and of electron microscopy, Reviews of Modern Physics, 1987, Vol. 59 (3) (24 pages)

28. P. W. Hawkes, J. C. H. Spence, Science of Microscopy, Vol. I, Springer, USA, 2008, 98765432
29. D. B. Williams, C. B. Carter, Transmission Electron Microscopy: A Textbook for Materials Science, Springer, USA, 2009, Edition 2, Vol. I-IV (779 pages)
30. H. Okamoto, T. B. Massalski, Guidelines for binary phase diagram assessment, J. Phase Equilibria, 1993, Vol. 14 (3), 316-335
31. R. Kanno, M. Tsujii, K. Hanya, K. Matsuoka, T. Tominaga, F. Ozaki, Steels, Steel Products and Steel Structures Sustaining Growth of Society (Infrastructure Field), Nippon Steel Technical Report, No. 101, 2012, 57-67
32. L. Gardner, The use of stainless steel in structures, Prog. Struct. Eng. Mater., 2005, Vol. 7, 45-55
33. H. K. D. H. Bhadeshia, Steels for bearings, Progress in Materials Science, 2012, Vol. 57, 268-435
34. Y. Wei, Y. Li, L. Zhu, Y. Liu, X. Lei, G. Wang, Y. Wu, Z. Mi, J. Liu, H. Wang, H. Gao, Evading the strength-ductility trade-off dilemma in steel through gradient hierarchical nanotwins, Nat. Commun., 2014, Vol. 5, 3580, 1-8
35. J. Rosler, O. Nath, S. Jager, F. Schmitz, D. Mukherji, Fabrication of nanoporous Ni-based superalloy membranes, Acta Mater., 2005, Vol. 53, 1397-1406
36. H. Choe, D. C. Dunand, Synthesis, structure, and mechanical properties of Ni-Al and Ni-Cr-Al superalloy foams, Acta Mater., 2004, Vol. 52, 1283-1295
37. I. Gurrappa, Characterization of titanium alloy Ti-6Al-4V for chemical, marine and industrial applications, Materials Characterization, 2003, Vol. 51, 131-139
38. K. K. Mccabe, S. L. Sass, The initial stages of the omega phase transformation in Ti-V alloys, Philos. Mag., 1971, Vol. 23, 184, 957-970

39. S. K. Sikka, Y. K. Vohra, R. Chidambaram, Omega phase in materials, Prog. Mater. Sci., 1982, Vol. 27, 245-310
40. C. Ghosh, J. Basu, D. Ramachandran, E. Mohandas, Phase separation and ω transformation binary V-Ti and ternary V-Ti-Cr alloys, Acta Mater., 2016, Vol. 121, 310-324
41. A. Devaraj, S. Nag, R. Srinivasan, R. E. A. Williams, S. Banerjee, R. Banerjee, H. L. Fraser, Experimental evidence of concurrent compositional and structural instabilities leading to ω precipitation in titanium-molybdenum alloys, Acta Mater., 2012, Vol 60, 596-609
42. W. H. Rothery, The Structure of Metals and Alloys, Nature, 1936, Monograph and Report Series No.1, Vol. 38, London Institute of Metals
43. Y. M. Zhang, S. Yang, J. R. G. Evans, Revisiting Hume-Rothery's rules with artificial neural networks, Acta Mater., 2008, Vol. 56, 1094-1105
44. U. Mizutani, H. Sato, T. B. Massalski, The original concepts of the Hume-Rothery rule extended to alloys and compounds whose bonding is metallic, ionic, or covalent, or a changing mixture of these, Prog. Mater. Sci., 2021, Vol. 120, 100719
45. D. Turnbull, Theory of catalysis of nucleation by surface patches, Acta Metallurgica, 1953, Vol. 1 (1), 8-14
46. P. Duwez, Metastable phases obtained by rapid quenching from the liquid state, Progress in Solid State Chemistry, 1967, Vol. 3, 377-400
47. Joysurya Basu, Glass Forming Ability and Stability: Bulk Zr-based and Marginal Al-based Glasses, PhD Thesis, 2004, Indian Institute of Science©, Bangalore, India
48. J. Basu, S. Ranganathan, Crystallisation in Al-ETM-LTM-La metallic glasses, Intermetallics, 2004, Vol. 12, 1045-1050

49. J. Basu, S. Ranganathan, Glass-forming ability and stability of ternary Ni-early transition metal (Ti/Zr/Hf) alloys, Acta Mater., 2008, Vol. 56, 1899-1907
50. J. Basu, D. V. Louzguine, A. Inoue, S. Ranganathan, Synthesis and devitrification of glassy Zr-Ti-Ni and Zr-Hf-Ni ternary alloys, Journal of Non-Crystalline Solids, 2004, Vol. 334&335, 270-275
51. H. Tanaka, Possible resolution of the Kauzmann paradox in supercooled liquids, Physical Review E, 2003, Vol. 68, 011505
52. A. Inoue, Stabilization of metallic supercooled liquid and bulk amorphous alloys, Acta Mater., 2000, Vol. 48, 279-306
53. W. L. Johnson, Thermodynamic and kinetic aspects of the crystal to glass transformation in metallic materials, Prog. Mater. Sci., 1986, Vol. 30, 81-134
54. A. Inoue, Amorphous, nanoquasicrystalline and nanocrystalline alloys in Al-based systems, Prog. Mater. Sci., 1998, Vol. 43, 365-520
55. A. Inoue, A. Takeuchi, Recent development and application products of bulk glassy alloys, Acta Mater., 2011, Vol. 59, 2243-2267
56. G. V. S. Sastry, C. Suryanarayana, A new ordered phase in the Al-Pd system, Mat. Res. Bull., 1978, Vol. 13, 1065-1070
57. G. V. S. Sastry, V. V. Rao, P. Ramachandrarao, T. R. Anantharaman, A new quasi-crystalline phase in rapidly solidified Mg_4CuAl_6, Scripta Metallurgica, 1986, Vol. 20, 191-193
58. N. K. Mukhopadhyay, S. Ranganathan, K. Chattopadhyay, On the short-range order in Al-Mn quasicrystals during low-temperature ageing, Philos. Mag. Lett., 1987, Vol. 56 (4), 121-127

59. N. K. Mukhopadhyay, G. N. Subbanna, S. Ranganathan, K. Chattopadhyay, An electron microscopic study of quasicrystals in a quaternary alloy $Mg_{32}(Al,Zn,Cu)_{49}$, Scripta Metallurgica, 1986, Vol. 20 (4), 525-528

60. B. Cantor, I. T. H. Chang, P. Knight, A. J. B. Vincent, Microstructural development in equiatomic multicomponent alloys, Mat. Sci. Eng. A, 2004, 375-377, 213-218

61. J. W. Yeh, S. K. Chen, S. J. Lin, J. Y. Gan, T. S. Chin, T. T. Shun, C. H. Tsau, S. Y. Chang, Nanostructured high-entropy alloys with multiple principal elements: Novel alloy design concepts and outcomes, Advanced Engineering Materials, 2004, Vol. 6 (5), 299-303

62. I. Ansara, N. Dupin, H. L. Lukas, B. Sundman, Thermodynamic assessment of the Al-Ni system, Journal of Alloys and Compounds, 1997, Vol 247, 20-30

63. J. Q. Guo, K. Ohtera, Microstructures and mechanical properties of rapidly solidified high strength Al-Ni based alloys, Acta Mater., 1998, Vol. 46 (11), 3829-3838

64. N. K. Mukhopadhyay, High entropy alloys: a renaissance in physical metallurgy, Current Science, 2015, Vol. 159 (4), 665-667

65. S. Ranganathan, Alloyed pleasures: Multimetallic cocktails, Current Science, 2003, Vol. 85 (10), 1404-1406

66. F. Otto, Y. Yang, H. Bei, E. P. George, Relative effects of enthalpy and entropy on the phase stability of equiatomic high-entropy alloys, Acta Mater., 2013, Vol. 61, 2628-2638

67. Y. Zhang, T. T. Zuo, Z. Tang, M. C. Gao, K. A. Dahmen, P. K. Liaw, Z. P. Lu, Microstructures and properties of high-entropy alloys, Prog. Mater. Sci., 2014, Vol. 61, 1-93

68. J. M. Torralba, P. Alvaredo, A. G. Junceda, High-entropy alloys fabricated via powder metallurgy: a critical review, Powder Metallurgy, 2019, Vol. 62 (2), 84-114

69. N. Zhou, S. Jiang, T. Huang, M. Qin, T. Hu, J. Luo, Single-phase high-entropy intermetallic compounds (HEICs): Bridging high-entropy alloys and ceramics, Science Bulletin, 2019, Vol. 64, 856-864

70. D. Raabe, C. C. Tasan, H. Springer, M. Bausch, From high-entropy alloys to high-entropy steels, Steel Research Int., 2015, Vol. 86 (10), 1127-1138

71. O. F. Dippo, N. Mesgarzadeh, T. J. Harrington, G. D. Schrader, K. S. Vecchio, Bulk high-entropy nitrides and carbonitrides, Nature Scientific Reports, 2020, Vol. 10, 21288

72. S. Guo, C. T. Liu, Phase stability in high entropy alloys: Formation of solid-sollution phase or amorphous phase, Progress in Natural Science: Materials International, 2011, Vol. 21, 433-446

73. Y. V. Krishna, U. K. Jaiswal, M. R. Rahul, Machine learning approach to predict new multiphase high entropy alloys, Scripta Materialia, 2021, Vol. 197, 113804 (11 pages)

74. L. J. Santodonato, P. K. Liaw, R. R. Unocic, H. Bei, J. R. Morris, Predictive multiphase evolution in Al-containing high-entropy alloys, Nat. Commun., 2018, Vol. 9, 4520 (10 pages)

75. Y. C. Huang, C. S. Tsao, S. K. Wu, C. Lin, C. H. Chen, Nano-precipitates in severely deformed and low-temperature aged CoCrFeMnNi high-entropy alloy studied by synchrotron small-angle X-ray scattering, Intermetallics, 2019, Vol. 105, 146-152

76. K. H. Lee, S. K. Hong, S. I. Hong, Precipitation and decomposition in CoCrFeMnNi high entropy alloy at intermediate temperatures under creep conditions, Materialia, 2019, Vol. 8, 100445 (10 pages)

77. A. Manzoni, H. Daoud, R. Volkl, U. Glatzel, N. Wanderka, Phase separation in equiatomic AlCoCrFeNi high-entropy alloy, Ultramicroscopy, 2013, Vol. 132, 212-215

78. C. M. Rost, E. Sachet, T. Borman, A. Moballegh, E. C. Dickey, D. Hou, J. L. Jones, S. Curtarolo, J. P. Maria, Entropy-stabilized oxides, Nat. Commun., 2015, Vol. 6, 8485 (8 pages)

79. M. Brahlek, M. Gazda, V. Keppens, A. R. Mazza, S. J. McCormack, A. M. Gryn, B. Musico, K. Page, C. M. Rost, S. B. Sinnott, C. Toher, T. Z. Ward, A. Yamamoto, What is in a name: Defining high entropy oxides, APL Mater., 2022, Vol. 10, 110902 (12 pages)

80. B. L. Musico, D. Gilbert, T. Z. Ward, K. Page, E. George, J. Yan, D. Mandrus, V. Keppens, The emergent field of high entropy oxides: Design, prospects, challenges and opportunities for tailoring material properties, APL Mater., 2020, Vol. 8, 040912 (17 pages)

81. S. Akrami, P. Edalati, M. Fuji, K. Edalati, High-entropy ceramics: Review of principles, production and applications, Materials Science & Engineering R, 2021, Vol. 146, 100644 (64 pages)

82. J. Dabrowa, M. Stygar, A. Mikula, A. Knapik, K. Mroczka, W. Tejchman, M. Danielewski, M. Martin, Synthesis and microstructure of the $(Co,Cr,Fe,Mn,Ni)_3O_4$ high entropy oxide characterized by spinel structure, Materials Letters, 2018, Vol. 216, 32-36

83. A. Sarkar, Q. Wang, A. Schiele, M. R. Chellali, S. S. Bhattacharya, D. Wang, T. Brezesinski, H. Hahn, L. Velasco, B. Breitung, High-entropy oxides: Fundamental aspects and electrochemical properties, Adv. Mater., 2019, 1806236 (9 pages)

84. C. M. Rost, Z. Rak, D. W. Brenner, J. P. Maria, Local structure of the $Mg_xNi_xCo_xCu_xZn_xO$ (x=0.2) entropy-stabilized oxide: An EXAFS study, J. Am. Ceram. Soc., 2017, Vol. 100, 2732-2738

85. G. Anand, A. P. Wynn, C. M. Handley, C. L. Freeman, Phase stability and distortion in high-entropy oxides, Acta Mater., 2018, Vol. 146, 119-125

86. S. J. McCormack, A. Navrotsky, Thermodynamics of high entropy oxides, Acta Mater., 2021, Vol. 202, 1-21

87. A. D. Dupuy, X. Wang, J. M. Schoenung, Entropic phase transformation in nanocrystalline high entropy oxides, Mater. Res. Lett., 2019, Vol. 7 (2), 60-67

88. O. Elmutasim, A. G. Hussien, A. Sharan, S. Alkhoori, M. A. Vasiliades, I. M. A. Taha, S. Kim, M. Harfouche, A. H. Emwas, D. H. Anjum, M. Efstathiou, C. T. Yavuz, N. Singh, K. Polychronopoulou, Evolution of oxygen vacancy sites in ceria-based high entopy oxides and their role in N_2 activation, ACS Appl. Mater, Interfaces, 2024, Vol. 16, 23038-23053 (16 pages)

89. L. Pauling, The principles determining the structure of complex ionic crystals, J. Am. Ceram. Soc., 1929, Vol. 51 (4), 1010-1026

90. W. Hong, F. Chen, Q. Shen, Y. H. Han, W. G. Fahrenholtz, L. Zhang, Microstructural evolution and mechanical properties of (Mg,Co,Ni,Cu,Zn)O high-entropy ceramics, J. Am. Ceram. Soc., 2019, Vol. 102, 2228-2237

91. A. D. Dupuy, M. R. Chellali, H. Hahn, J. M. Schoenung, Nucleation and growth behaviour of multicomponent secondary phases in entropy-stabilized oxides, J. Mater. Res., 2023, Vol.38 (1), 198-204

92. D. Berardan, A. K. Meena, S. Franger, C. Herrero, N. Dragoe, Controlled Jahn-Teller distortion in (MgCoNiCuZn)O-based high entropy oxides, Journal of Alloys and Compounds, 2017, Vol. 704, 693-700

93. C. B. Carter, M. G. Norton, Ceramic Materials Science and Engineering, Springer Nature, USA, 2013, Edition 2, XXXIII (766 pages)

94. Y. M. Chiang, D. P. Birnie, W. D. Kingery, Physical Ceramics Principles for Ceramic Science and Engineering, John Wiley & Sons Inc., USA, 1997 (542 pages)

95. K. E. Sickafus, J. M. Wills, N. W. Grimes, Structure of spinel, J. A. Ceram. Soc., 1999, Vol. 82 (12), 3279-3292

96. J. B. Goodenough, A. L. Loeb, Theory of ionic ordering, crystal distortion, and magnetic exchange due to covalent forces in spinels, Physical Review, 1955, Vol. 98 (2) (18 pages)

97. P. E. Vullum, H. L. Lein, M. A. Einarsrud, T. Grande, R. Holmestad, TEM observations of rhombohedral and monoclinic domains in $LaCoO_3$-based ceramics, Philosophical Magazine, 2008, Vol. 88 (8), 1187-1208

98. K. Behnia, Finding merit in dividing neighbors, Science, 2016, Vol. 351, 6269 (2 pages)

99. S. Massidda, M. Posternak, A. Baldereschi, R. Resta, Noncubic behavior of antiferromagnetic transition-metal monoxides with the rocksalt structure, Phys. Rev. Lett., 1999, Vol. 82 (2), 430-433

100. C. N. R. Rao, P. V. Vanitha, A. K. Cheetham, Phase separation in metal oxides, Chem. Eur. J., 2003, Vol. 9 (4), 829-836

101. V. B. Shenoy, D. D. Sarma, C. N. R. Rao, Electronic phase separation in correlated oxides: The phenomenon, its present status and future prospects, Chem. Phys. Chem., 2006, Vol. 7, 2053-2059

102. Y. Horibe, S. Takeyama, S. Mori, Large-scale phase separation with nano-twin domains in manganite spinel $(Co,Fe,Mn)_3O_4$, AIP Conference Proceedings, 2016, 1763, 050005 (6 pages)

103. A. S. Pal, A. K. L. Das, K. Gururaj, M. Sadhasivam, K. M. Knowles, Md. I. Ahmad, K. G. Pradeep, J. Basu, Nanoarchitectonics of self-assembled chessboard-like

structures by recurrent phase separation and coalescence of nano domains in CoFeMn oxide, Acta Mater., 2023, 242, 118423 (12 pages)

104. A. S. Pal, A. K. L. Das, A. Singh, K. M. Knowles, Md. I. Ahmad, J. Basu, Evolution of a self-assembled chessboard nanostructure spinel in a CoFeGaMnZn multicomponent oxide, Philosophical Magazine, 2022, Vol. 102 (12), 1121-1135

105. A. Singh, S. Yasui, A.S. Pal, L.A. Bendersky, I. Takeuchi, R.K. Mandal, J. Basu, Structure and interfaces of compositionally graded $Li(Ni,Mn)_xO_y$ cathodes on (111) Nb-doped $SrTiO_3$, Philosophical Magazine, 2022, 102, 1547-1579

106. B. G. Hyde, A. N. Bagshaw, Some defect structures in crystalline solids, Annu. Rev. Mater. Sci., 1974, Vol. 4, 43-92

107. J. S. Anderson and R. J. D. Tilley, Crystallographic shear in oxygen-deficient rutile: An electron microscopic study, Journal of Solid State Chemistry, 1970, Vol. 2 472-482

108. R. J. D. Tilley, The formation of shear structures in sub-stoichiometric tungsten trioxide, Mat. Res. Bull., 1970, Vol. 5, 813-824

109. R. J. D. Tilley, An electron microscope study of perovskite-related oxides in Sr-Ti-O system, Journal of Solid State Chemistry, 1977, Vol. 21, 293-301

110. A. Schron, C. Rodl, F. Bechstedt, Crystalline and magnetic anisotropy of the 3d-transition metal monoxides MnO, FeO, CoO and NiO, Physical Review B, 2012, Vol. 86, 115134

111. P. K. Davies, M. Akaogi, Phase intergrowths in spinelloids, Nature, 1983, Vol. 305, 788-790

112. C. Oses, C. Toher, S. Curtarolo, High-entropy ceramics, Nat. Rev. Mater., 2020, Vol. 5, 295-309

113. M. Anandkumar, E. Trofimov, Synthesis, properties, and applications of high-entropy oxide ceramics: Current progress and future perspectives, Journal of Alloys and Compounds, 2023, Vol. 960, 170690

114. A. C. Yeh, S. Gorsse, V. Keppens, D. A. Gilbert, Design and development of high entropy materials, APL Materials, 2023, Vol. 11, 030402

115. J. B. Goodenough, Perspective on engineering transition-metal oxides, Chemistry of Materials, 2014, Vol. 26, 820-829

116. D. Berardan, S. Franger, D. Dragoe, A. K. Meena, N. Dragoe, Colossal dielectric constant in high entropy oxides, Phys. Status Solidi RRL, 2016, Vol. 10 (4), 328-333

117. D. Berardan, S. Franger, A. K. Meena, N. Dragoe, Room temperature lithium superionic conductivity in high entropy oxides, J. Mater. Chem. A, 2016, Vol. 4, 9536-9541

118. Z. Y. Liu, Y. Liu, Y. Xu, H. Zhang, Z. Shao, Z. Wang, H. Chen, Novel high-entropy oxides for energy storage and conversion: From fundamentals to practical applications, Green Energy and Environment, 2023, Vol. 8, 1341-1357

119. Z. Lun, B. Ouyang, D. H. Kwon, Y. Ha, E. E. Foley, T. Y. Huang, Z. Cai, H. Kim, M. Balasubramanian, Y. Sun, J. Huang, Y. Tian, H. Kim, B. D. McCloskey, W. Yang, R. J. Clement, H. Ji, G. Ceder, Cation-disordered rocksalt-type high entropy cathodes for Li-ion batteries, Nature Materials, 2021, Vol. 20, 214-221

120. Q. Wang, A. Sarkar, Z. Li, Y. Lu, L. Velasco, S. S. Bhattacharya, T. Brezesinski, H. Hahn, B. Breitung, High entropy oxides as anode material for Li-ion battery applications: A practical approach, Electrochemistry Communications, 2019, Vol. 100, 121-125

121. S. H. Albedwawi, A. Aljaberi, G. N. Haidemenopoulos, K. Polychronopoulou, High entropy oxides-exploring paradigm of promising catalysts: A review, Materials and Design, 2021, Vol. 202, 109534 (27 pages)

122. S. Zhai, J. Rojas, N. Ahlborg, K. Lim, M. F. Toney, H. Jin, W. C. Chueh, A. Majumdar, The use of poly-cation oxides to lower the temperature of two-step thermochemical water splitting, Energy Environ. Sci., 2018, Vol. 11, 2172-2178

123. J. Baek, M. D. Hossain, P. Mukherjee, J. Lee, K. T. Winther, J. Leem, Y. Jiang, W. C. Chueh, M. Bajdich, X. Zheng, Synergistic effects of mixing and strain in high entropy spinel oxides for oxygen evolution reaction, Nat. Commun., 2023, Vol. 14 (5936), 1-11

124. J. Zhang, R. P. Hermann, Long-range antiferromagnetic order in a rocksalt high entropy oxide, Chem. Mater., 2019, Vol. 31, 3705-3711

125. M. P. J. Segura, T. Takayama, D. Berardan, A. Hoser, M. Reehuis, H. Takagi, N. Dragoe, Long-range magnetic ordering in a rocksalt-type high-entropy oxides, Appl. Phys. Lett., 2019, Vol. 114, 122401 (6 pages)

126. J. L. Braun, C. M. Rost, M. Lim, A. Giri, D. H. Olson, G. N. Kotsonis, G. Stan, D. W. Brenner, J. P. Maria, P. E. Hopkins, Charge-induced disorder controls the thermal conductivity of entropy-stabilized oxides, Adv. Mater., 2018, Vol. 30, 1805004 (8 pages)

Chapter – 2

Materials & Methods

2.1. Precursor oxides

The individual metal oxides were procured in powder form with particle size ranging from 40-50 μm (mesh size) from either Alfa Aesar or Sigma Aldrich. The purity of the individual oxides exceeds 99.5 at% for most while it is more than 99.9 % for some of them. An exhaustive list of the precursor oxides, their purity, ionic radii at specific coordination environment along with their preferred crystal structure is given in Table 2.1. The individual oxides were so chosen to understand entropic stabilization in quinary multicomponent oxides through systematic partial substitution. Since HEOs/ESOs show excellent functional properties in most cases than not, it is worth examining the microstructural evolution and phase stability in such chemically complex systems.

2.2. Solid-state synthesis

There are several ways of synthesizing materials through powder metallurgy route classified broadly under two categories i.e. top-down approach and bottom-up approach [1]. Among them, there could be many further classifications based on length-scale (micron, sub-micron, nano), morphology control, processing environment and so on [1-3]. For the research work pertaining to this thesis, solid-state route of top-down approach has been selected mostly because of the relative ease of handling raw materials coupled with high success rate of synthesis. The purity of precursor oxides procured, their molecular weights, ionic radii at specific coordination environment (six-fold coordination unless otherwise mentioned) and their preferred crystal structures have been listed in Table 2.1 [4,5]. The precursor powders have been weighed in equimolar proportions, mixed thoroughly in a mortar and pestle before uniaxially compacting the mix in a hydraulic press under 4T load. The green compacted pellets of ~12 mm diameter and ~4-5 mm thickness were subjected to various sintering heat treatment schedules (Figure 2.1a). Green

compacted pellets of each and every composition have been stacked vertically inside a platinum crucible with the platinum lid on, and the sintered pellets from the centre of the stacks were taken for further examination. This ensured uniform sintering with minimal contamination. The sintering process has been carried out in a high-temperature tube furnace with $MoSi_2$ heating filament and in air atmosphere. The detailed heat treatment cycles are schematically shown in Figure 2.1a. In another set of samples, ball-milling has been adopted to examine the effect of high strain rate processing on phase evolution apart from uniform mixing. High-energy ball-milling was carried out in a Retsch PM-400 planetary mill operating at 200 rpm in dry atmosphere (Figure 2.1b). Zirconia vial and zirconia balls were used for milling, with ball to powder ratio maintained at 10:1. The milling has been carried out for 1 minute at a stretch followed by 30 seconds of idle time which was again followed by a minute of milling and so on. This was carefully controlled so that the local rise in temperature upon continuous ball milling does not induce dynamic recrystallization [6]. Samples were taken out at regular intervals of ball-milling to understand the phase evolution and it was continued for a maximum of 40 h.

Table 2.1: Table of precursor oxides depicting their purity, molecular weight, ionic radii and preferred crystal structure with space group notation and Pearson symbol.

	CaO	Co(II,III)O	Cr(III)O	CuO	Fe(III)O	MgO	Mn(III)O	NiO	ZnO
Purity (%)	99.95	99.8	99.9	99.9	99.8	99.98	99.8	99.9	99.95
Mol. Wt. (a.m.u.)	56.07	240.795	151.989	79.54	159.687	40.304	157.873	74.69	81.37
Ionic Radii (Å)	1 (6)- 1.34 (12)	0.75 (+2) 0.55 (+3)	0.62	0.77 (+1) 0.73 (+2)	0.78 (+2) 0.65 (+3)	0.72 (6) 0.57 (4)	0.72	0.69	0.74
Preferred Crystal structure	Rocksalt Fm-3m, cF8	Rocksalt/Spinel Fm-3m, cF8 / Fd-3m, cF56	Corrundum R-3c hR10	Tenorite C2/c mC8	Corrundum R-3c hR10	Rocksalt Fm-3m cF8	Bixbyite Ia-3, cI80 / Spinel, cF56	Rocksalt Fm-3m cF8	Wurtzite/Zinc Blende $P6_3mc$/F-43m hP4/cF8

During high-energy ball-milling, the powder particles undergo a process of cold welding, repeated fracture and rewelding. For this reason, such processes were coined as Mechanical Alloying (MA) techniques by the International Nickel (INCO) company during the early 1960's. The recognition of MA, from a mixing tool to a potential non-equilibrium

processing technique took place during the early 1980's when it was observed that Ni-Nb system and Y-Co intermetallic compound formed amorphous phase. Further investigations employing MA routes produced a variety of stable and metastable phases including supersaturated solid-solutions, crystalline and quasicrystalline intermediate phases along with amorphous alloys [6]. The use of high-energy ball-milling in the course of this research has been primarily to refine particle size and yield homogeneous inter-mixing of multiple constituent oxides. However, it does bring out another competing phenomenon which will be elucidated in Chapter 5 of the thesis.

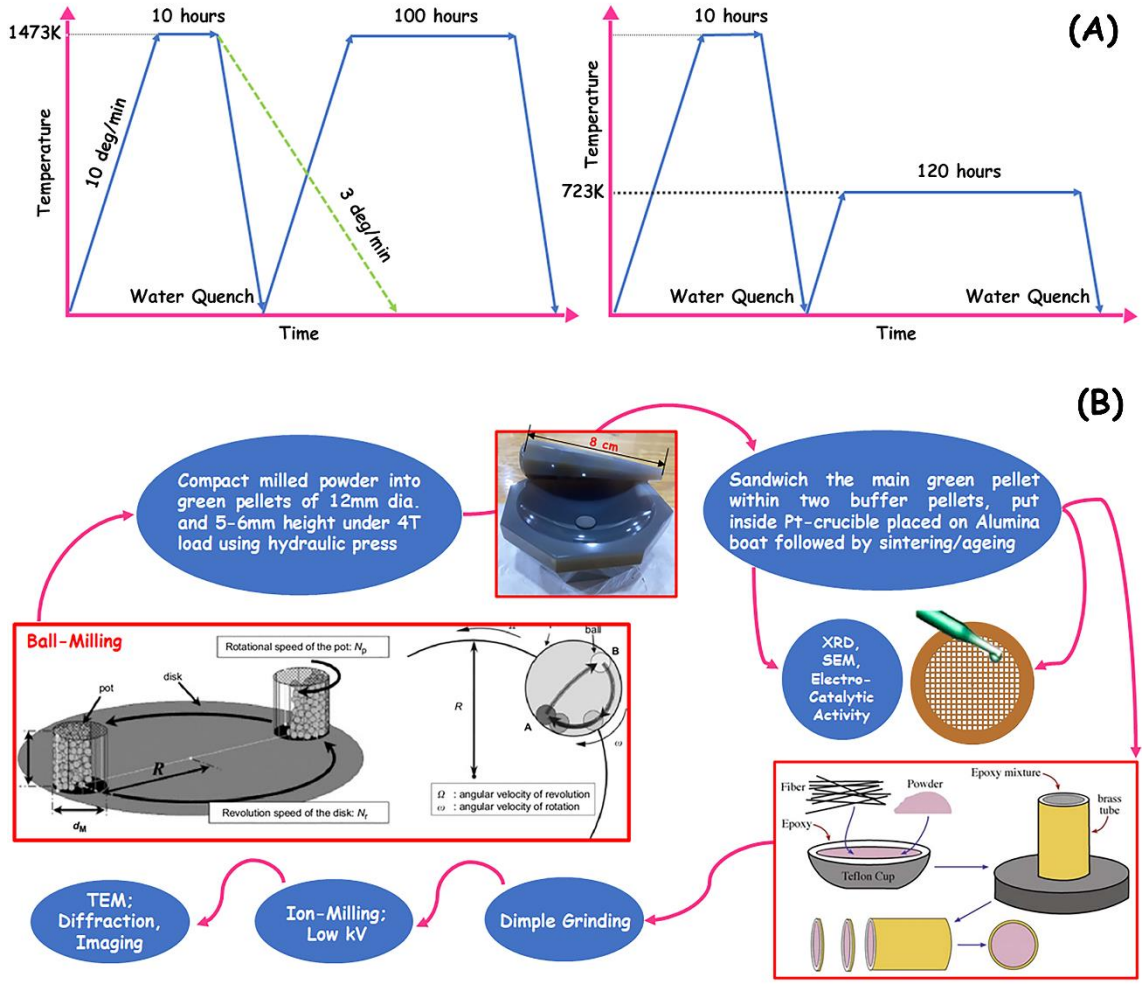

Figure 2.1: (a) Time-temperature diagram showing sintering of consolidated green pellets under various heat treatment schedules, which has been implemented for various multi-cationic compositions throughout the thesis. (b) Schematic showing mixing of powders in definite proportion, their consolidation followed by meticulous sample preparation for extensive characterization.

2.3. X-ray diffraction (XRD)

X-rays were discovered by Roentgen in 1895 after his persistent experimentation with Lenard's tube on C_4BaN_4Pt sample and was named so because of their unknown nature at the time [7]. Little did the German physicist know that this discovery would spark the scientific revolution of the late 19^{th} and early 20^{th} century. Radiography was shortly initiated by physicians and medical personnels to investigate internal organs of patients without precise knowledge of the radiation being used [8,9]. X-rays were subsequently treated as waves in the lines of Huygen's principles and Young's double-slit experiments. Couple of years after its discovery, Thomson demonstrated that X-rays could ionize gas and this led to the discovery of electrons in 1897. However, the most profound work arising out of constant curiosity regarding the very nature of X-rays led Becquerel to accidentally discover radioactivity, before M. Curie and P. Curie advanced our understanding of the subject further by leaps and bounds. Both these imperceptible yet powerful rays imparted new tools to probe almost anything and everything around us while elegantly bringing out the deficiencies in our own senses. Soon, groundbreaking work by Einstein yet again reclaimed the particle nature of X-rays by demonstrating the photoelectric effect in 1905. However, it was not until 1912 that the exact nature of X-rays was established. Due to pioneering works of Ewald and Von Laue, the phenomenon of X-ray diffraction by crystals was discovered [10]. This discovery at one hand proved the wave nature of X-rays and on the other hand provided a new method for investigating the fine structure of matter. It is now understood that X-rays are electromagnetic (EM) radiation of the same nature as light, but of much shorter wavelength. Electromagnetic radiation according to classical mechanics is treated as a wave while it is treated as a stream of particles (quanta or photons) according to quantum mechanics, an extension to the revolutionary concepts put forth by Bohr, de Broglie, Heisenberg, Schrodinger among others. A schematic of the entire EM

spectrum is given in Figure 2.2 with range of energy, frequency and wavelength highlighted on top and bottom. Von Laue worked out the mathematics of diffraction by x-rays from a periodic arrangement of atoms in a 3D crystal which opened up two broad fields i.e. crystal structure determination and spectroscopy related measurement and quantification. The later was dealt by Friedrich and Knipping while W.L. Bragg and W.H. Bragg tackled the first problem and came up with the celebrated Braggs law of crystal diffraction [11].

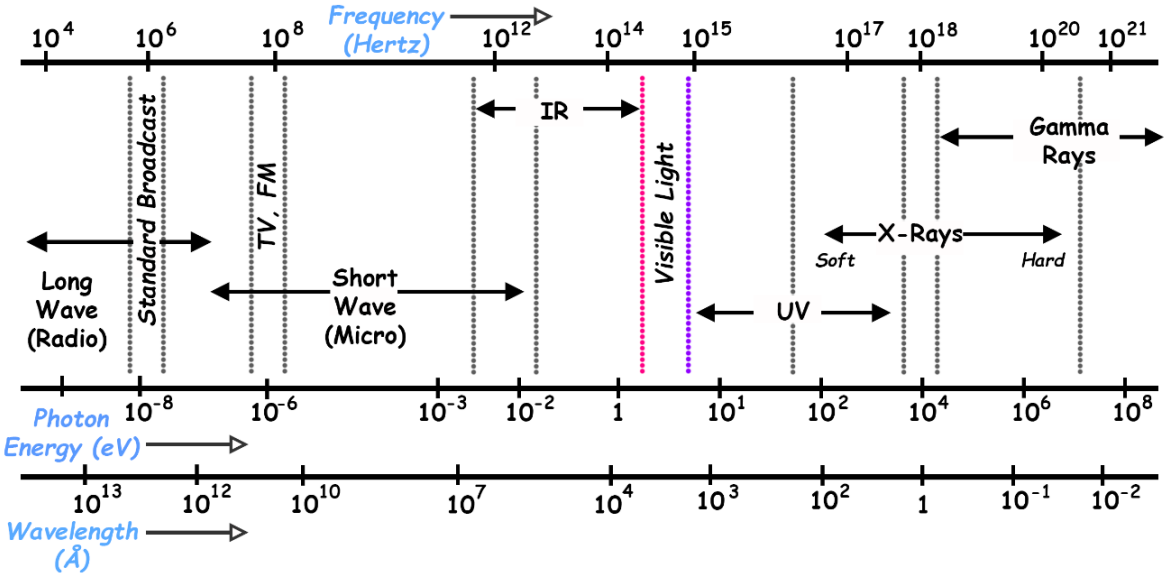

Figure 2.2: Schematic of the electromagnetic (EM) spectrum.

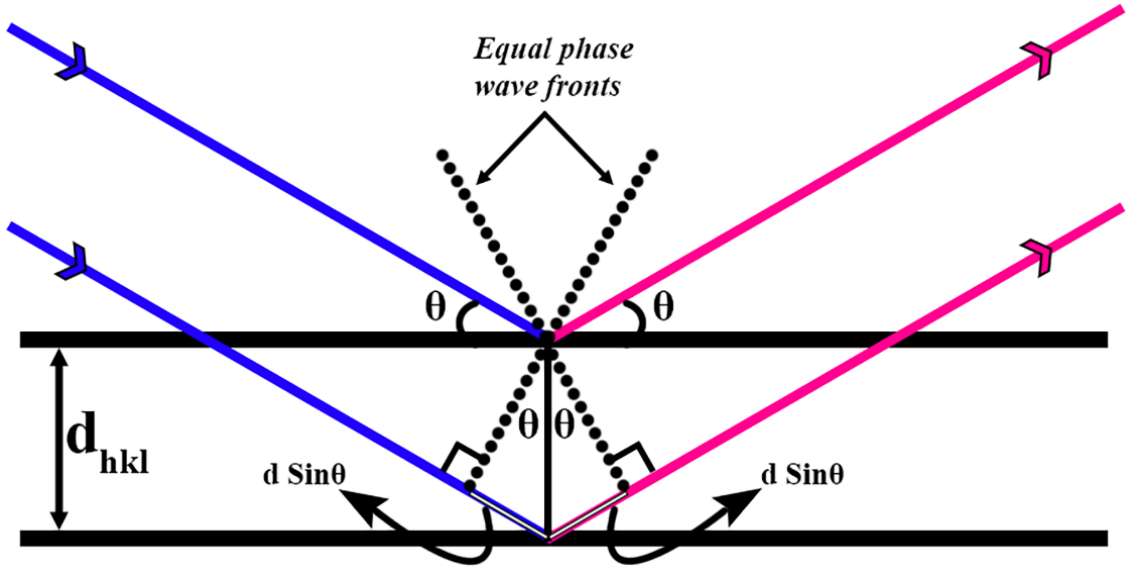

Figure 2.3: Schematic of the Real-space formulation of Braggs law for X-ray diffraction.

XRD experiments for probing internal structure of materials was understood to be essentially reinforced coherent scattering from periodic lattice planes decorated by crystal motifs. Braggs law dictates that the path difference between the top and bottom layer of the same family of crystallographic planes must equal one wavelength for constructive interference, and hence strong diffraction to occur (Figure 2.3). Therefore,

$$\mathbf{d_{hkl}\ sin\theta + d_{hkl}\ sin\theta = \lambda} \qquad \textbf{(i)}$$

$$\mathbf{\lambda = 2d_{hkl}\ sin\theta} \qquad \textbf{(ii)}$$

It is frequently encountered that the LHS of the equation is multiplied by an integer "n" since this also provides prerequisite condition for constructive interference. However, this convention can be circumvented by dividing d_{hkl} by n which gives a more realistic picture of constructive interference from the n^{th} order diffracting planes. It then becomes possible with the help of this simple yet powerful equation to calculate interplanar spacings from a set of diffracting planes and work out the crystal structure of unknown materials. Interestingly, the determination of crystal structures helped to shed light on the nature of chemical bonds in a material when Bragg and Bragg examined NaCl to dismiss the idea of NaCl molecules in favour of positive and negative ions bound by electrostatic forces in ionic bonding [12]. X-ray and matter interaction soon opened up a field of science on its own and X-ray crystallography was born (Figure 2.4). Although the generation of x-rays has electronic origins, it can effectively be used to probe the crystal structure of metals and its alloys, ceramics and its compounds to glasses, amorphous materials and quasicrystals. Depending on the input stimulus and properties of the material to be investigated, several signals carrying a wealth of information may be retrieved upon x-ray and matter interaction. The knocking-off of an electron from the innermost shell of an atom is known to produce characteristic excitation lines (characteristic x-rays) and the filling up process from higher

order shells may give rise to secondary x-rays, fluorescent radiation or Auger electrons [8]. A schematic representing the major signals produced in events of strong x-ray and matter interaction is given in Figure 2.4. Although the very definition of x-ray diffraction demands coherent elastic scattering process, however that is an idealised situation and deviation from ideality is unavoidable. Generally, the signals can broadly be classified under four categories: *elastic coherent*, *inelastic coherent*, *elastic incoherent* and *inelastic incoherent*. Usually, the spectroscopic principles rely on incoherent and inelastic scattering while neutron scattering relies on inelastic coherent scattering [9].

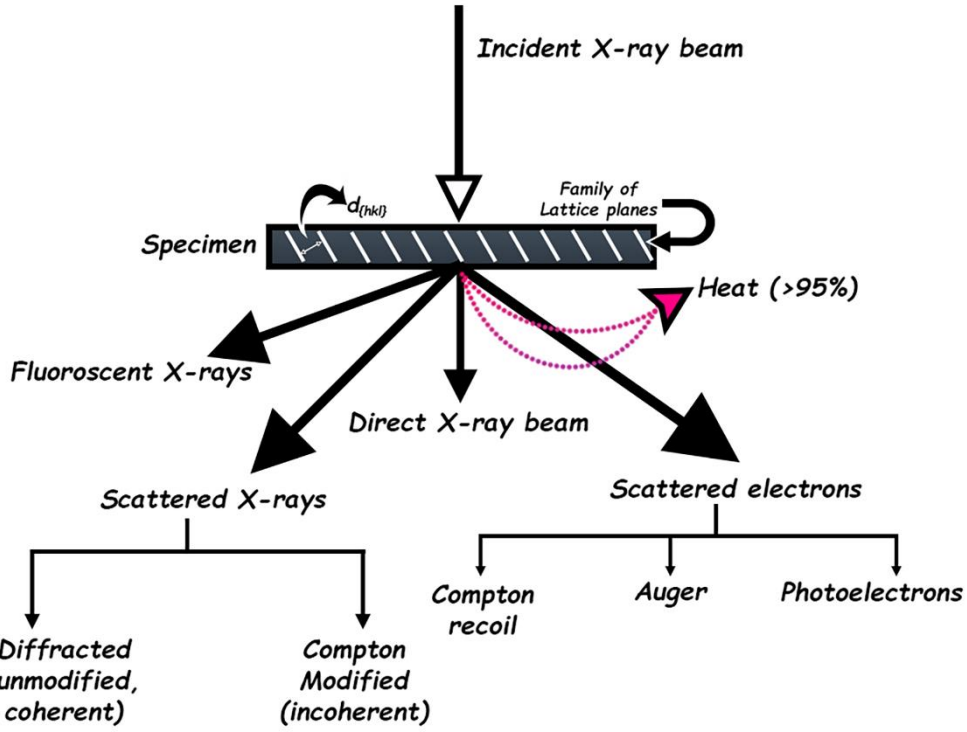

Figure 2.4: Schematic representing various kinds of signal generation on interaction between x-ray and matter.

Determination of crystal structure relies on the fact that the diffraction signature (pattern) is nothing but a Fourier transform of the atomic scattering function distribution of a material [9]. This translates to intensity as a function of 2θ in a systematic pattern of delta functions according to the extinction conditions of a particular type of crystal structure. However, the

finite width in the peaks and its shape evolution is indicative of the contributions from grain/particle size distribution and lattice strain in polycrystalline materials [8]. Further information regarding presence of second phases may be found out by deconvolution of peaks. Ratio of peak intensities is another useful parameter for structural refinement while normalised peak ratios provide approximate phase fractions in multi-phase materials. Thomson scattering on one hand is responsible for the sharp signature peaks while Compton scattering on the other, discovered in 1923, was helpful in demonstrating the particle nature of light after the photoelectric effect [13]. However, it proved to be a nuisance in diffraction work as it contributes to the background noise in diffraction patterns owing to the incoherent and inelastic nature of the radiation. It turns out that since the total integrated intensity of peaks are inversely proportional to both the mass absorption coefficient as well as the cell volume squared, large lattice parameter phase(s) of high molecular weight metallic compounds/ceramics contribute to enhanced Compton modified background than their metallic alloys counterpart. Details of sample preparation, make and model of diffractometers used along with its process parameters are reported in the 'materials and methods' section of each chapter.

2.4. Transmission electron microscopy (TEM)

On one hand XRD was providing indirect signatures so as to decode the crystal structure of a material while optical microscopy (VLM) on the other was able to provide microstructural information, however, the spatial resolution was restricted to the micron or at-best the sub-micron range. In extraordinary circumstances, Ruska and Knoll came up with first prototype of a working TEM during early 1940's, surpassing the resolution limit of visible light [14]. It took almost two decades after their invention, before the first ever commercial TEM was launched, due to the robust engineering challenges associated in assembling such electron microscopes. It has been a journey of no looking back since then,

with continuous and rapid improvement in vacuum technology, high voltage technology, electronics, automation and manufacturing of detectors, electromagnetic lenses along with their aberration correction [15-17]. The resolution limit has gone down from sub-micron to nano to sub-nano and even sub-angstrom length scales with scope for further improvement. Since a TEM image projects the 3D internal structure of materials in a 2D plane at unprecedented resolution and magnification, the human brain generally fails to fathom the richness of information by just looking at it. The humongous contribution by electron microscopy experimentalists and theoreticians alike in the last several decades towards the advancement of the field is filled with richness and its comprehensive accord is beyond the scope of the thesis [18].

Various contrast forming mechanisms occupy the heart of TEM imaging. They may be broadly classified as; (1) Amplitude contrast (special case is diffraction contrast under 2-beam geometry), (2) Z-contrast and (3) Phase contrast [16]. The dynamic coupling of direct and diffracted beams produces diffraction contrast and can be appreciated better with the help of Howie-Whelan equations [15-18]. These simultaneous partial differential equations explain the origin of bend contours and thickness fringes as important imaging artifacts, along with contrast mechanisms arising from various defect structures. The TEM primarily is operated under two modes; one is the conventional parallel illumination setup (CTEM) with activated pre- and post-specimen lenses and the other is the scanning transmission (STEM) mode with only pre-specimen lens and scan coils activated. Theorem of reciprocity along with advanced beam and lens correction has advanced Scanning-TEM techniques like STEM-HAADF and STEM-EDS/EELS under convergent electron probe setup. There are several advantages as well as disadvantages of using parallel or convergent mode for TEM observations, although the nature of the material problem under investigation dictates the reliance of the technique to be used.

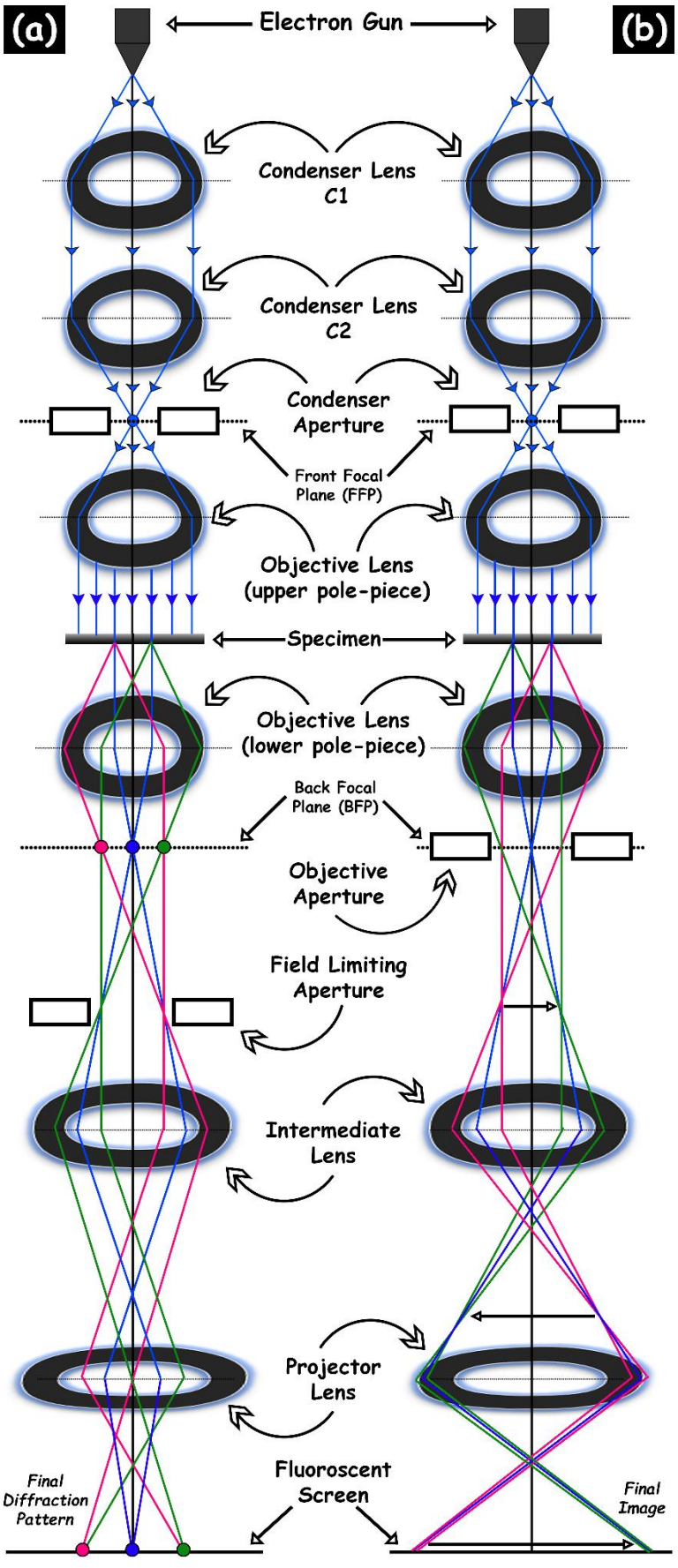

Figure 2.5: Schematic of the TEM under (a) diffraction and (b) imaging mode.

A detailed schematic of TEM under diffraction and imaging mode is given in Figure 2.5. Apart from imaging nanostructures and atom columns, the TEM is a very powerful tool pertaining to single crystal diffraction work. In this context, Bragg's law with respect to real-space formalism is perfectly corroborated with Laue and Ewald's treatment of the reciprocal-space. The symmetry considerations for diffraction geometry demands that the unit vector normal to the diffracting planes be parallel with the diffraction vector i.e.

$\mathbf{\Delta k} \parallel \mathbf{n}$.

The ray diagram of a possible diffraction event in the reciprocal-space formalism is schematically shown in Figure 2.6. The Laue condition of diffraction is satisfied when the diffraction vector ($\mathbf{\Delta k}$) equals the reciprocal lattice vector ($\mathbf{g}$). Under this special condition, the coefficients of the reciprocal lattice vectors take on special integer values corresponding to the miller indices of the allowed set of planes. This results in:

$$\mathbf{\Delta k \cdot a = h;\ \Delta k \cdot b = k;\ \Delta k \cdot c = l} \qquad \textbf{(iii)}$$

Where a, b and c are lattice vectors. Since TEM sample geometry is restricted to a few mm in length and breadth, but only a few tens of nm in its thickness, it lifts off the restriction on the third Laue condition (unlike XRD) and allows for diffraction spots from higher order Laue zones to be simultaneously present in the pattern. This is further facilitated by the fact that the Ewald sphere cuts the reciprocal space with almost zero curvature since radius of the sphere is far greater than the reciprocal lattice vectors and thus allows for collection of data from very small volumes. Moreover, the formation of 1-D rail-rods in place of otherwise 0-D points arising out of the thin foil effect (thickness of electron transparent samples are infinitesimally smaller compared to their surface dimensions) also facilitates much stronger electron-matter interactions at non-exact Bragg angles than x-ray and matter [16].

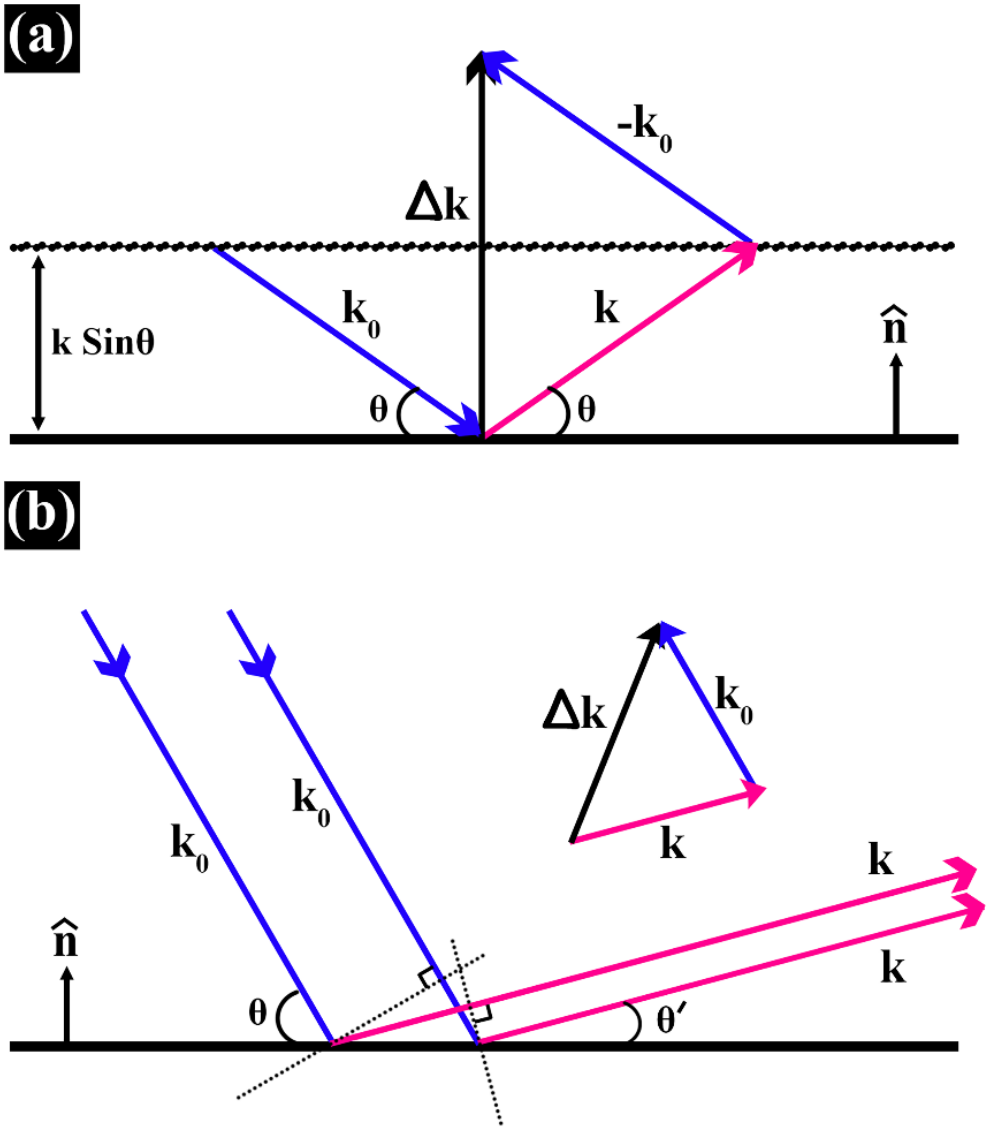

Figure 2.6: Schematic representing the diffraction setup in reciprocal space for (a) proper and (b) improper geometry.

2.5. Scanning electron microscopy (SEM)

Modern science is heavily reliant on microscopy as seeing is believing. The invention of the TEM quickly saw its upgradation to a STEM by retrofitting a pair of scan coils, which was then used to take the first STEM micrograph of a ZnO crystal at 23 kV at ~50 nm resolution [19]. However, the first demonstration of the capabilities of a Scanning Electron Microscope (SEM) for surface characterization came couple of decades later from Smith and Oatley [20]. It was Oatley's students who made incremental progress to the optical

setup and the SEM started to be commercialised with the advent of digital electronics [21,22]. There are no post-specimen lenses in an SEM, since a fine electron-probe falls on the surface of the specimen to scan it in raster manner and generate various signals that are then captured by dedicated detectors. The specimen chamber in an SEM can accommodate multiple samples mounted on metallic stubs. Electrically conducting samples are readily imaged and examined under the SEM, however, gold/carbon coating is required for insulators. Imaging and spectroscopy are the two most commonly used modes in a SEM. However, it also has the capability of performing electron backscattered diffraction (EBSD) which can map the relative orientation of grains or microstructural features [22].

The primary contrast forming mechanism in SEM images include topographical contrast in secondary electron (SE) images and atomic number contrast in backscattered electron (BSE) images. The most pronounced advantage of an SEM as an investigation tool arises from its high depth of field. It may be defined as the ability of the system to image features at differential heights from the surface with negligible loss of resolution. This makes the SEM an ideal choice for non-destructive testing (NDT) and fracture surface analysis [21]. Apart from several contrast mechanisms, lens aberrations significantly affect the quality of the final image. Cranking up the magnification without correcting for the lens defects systematically leads to aberrations in the optical system to blow up further. A schematic representing the major lens defect is presented in Figure 2.8. Since electrons interact much more strongly with matter than the strongest of x-rays (low wavelength high energy), the penetration depth of electrons is usually much smaller. Auger electrons are ejected from a depth of ~ 10 Å from the surface followed by secondary electrons which come out from ~ 50-500 Å while back-scattered electrons and x-rays are emitted from further depths, often restricting the total interaction volume to few tens of a nm in thickness. The types of signals expected from electron-matter interaction is given in Figure 2.7.

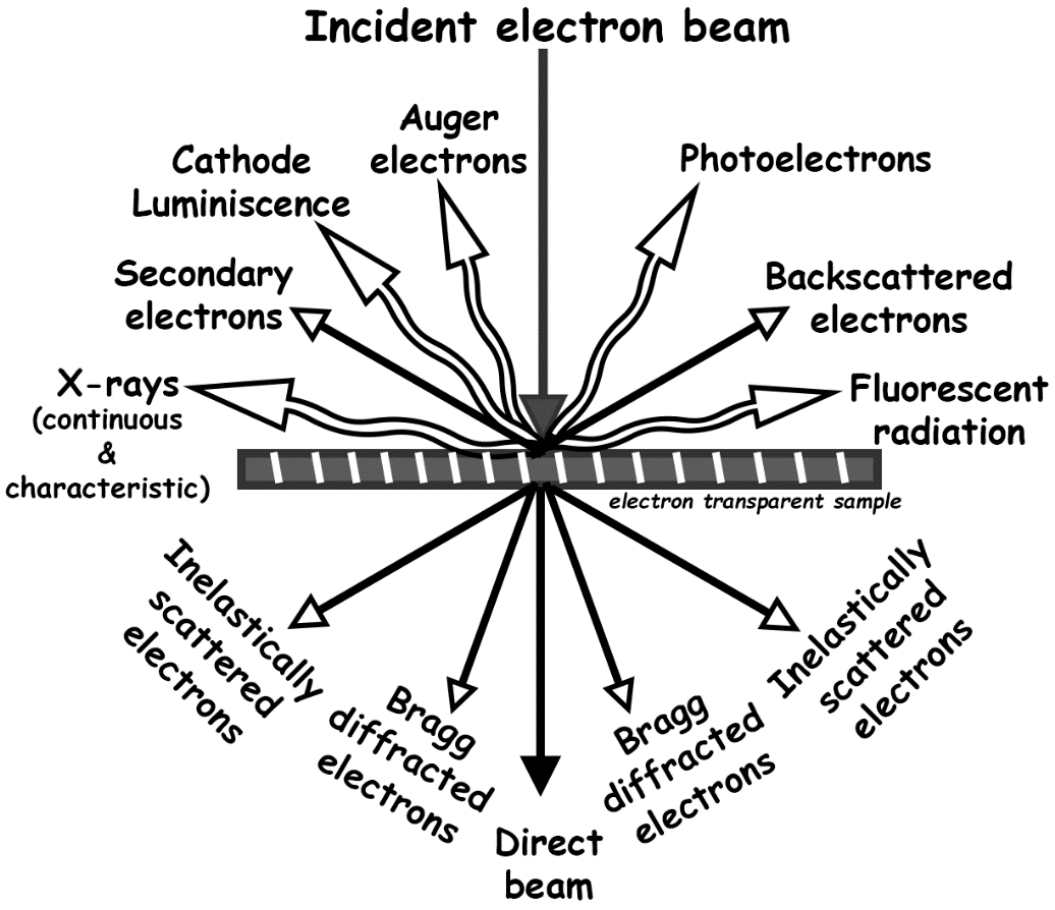

Figure 2.7: Schematic of the various kinds of signals that are produced from typical interactions between electron and matter.

The scattering cross-section at constant energy varies with "Z^2" (atomic number) and the probability of scattering through a given angle varies as "$(Z/E)^2$". It follows from calculations of Murata et al. that the mean free path between scattering events at 30 keV decreases with increasing atomic number from ~528 Å for Al to ~131 Å for Cu and ~50 Å for Au. Since the probability of scattering is low and the mean free path is large for low atomic number elements, there is not much scattering near the surface of the specimen as the electron enters. As the energy of the electrons decreases during passage through the sample, the number of scattering event increases and a state of complete diffusion of electron trajectories can be expected. This results in a pear-shaped interaction volume when

any specimen is examined under the SEM as has been corroborated with Monte-Carlo simulations [22].

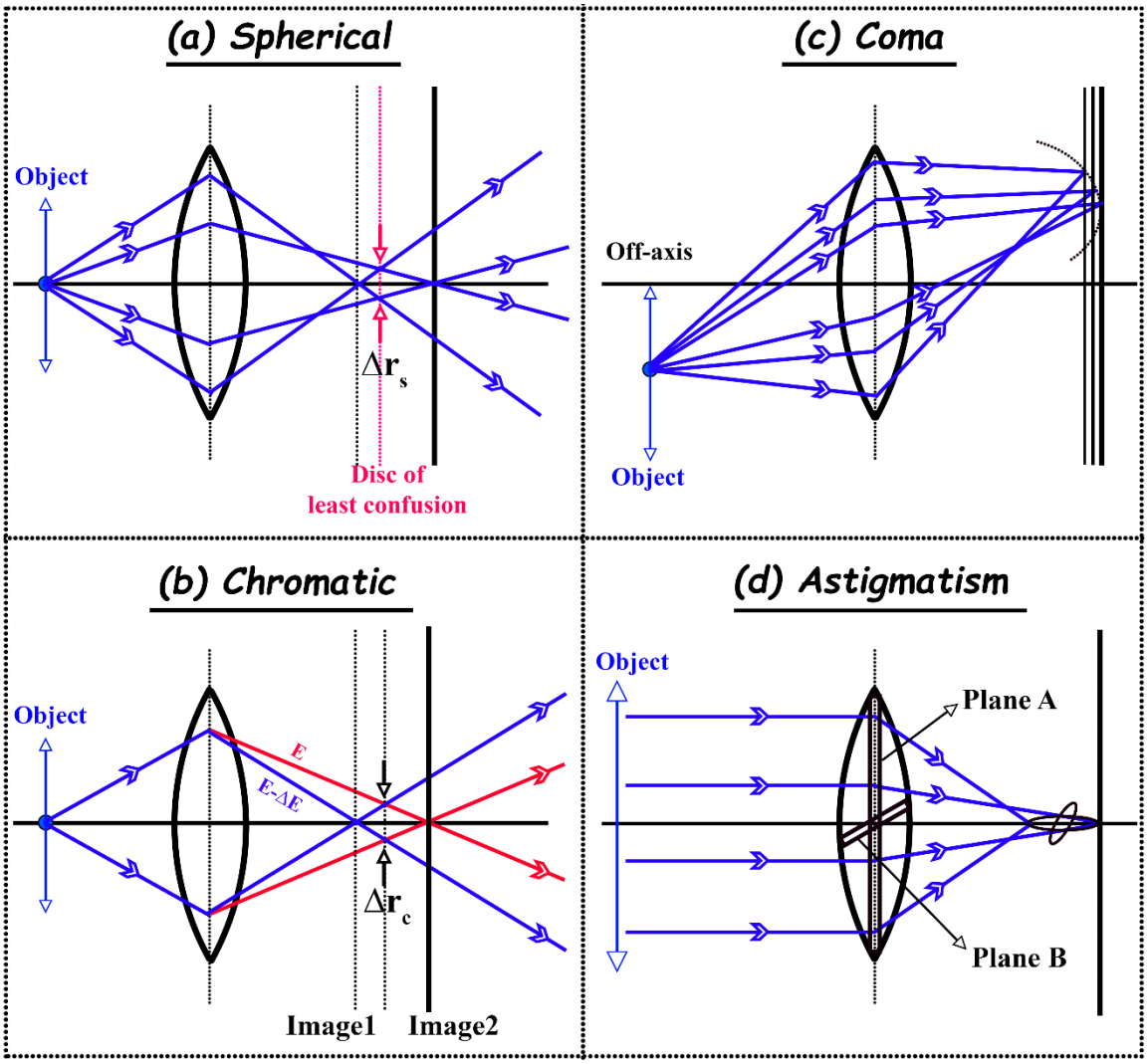

Figure 2.8: Schematic diagram of the four primary electromagnetic lens aberrations.

2.6. Structure Modelling and Simulation

Analysis of results (top-down) pertaining to diffraction or imaging using electrons and even x-rays often require complementary approaches (bottom-up) to arrive at satisfactory conclusions. In this regard, modelling and simulation provides a powerful tool if used cautiously. The research work undertaken throughout the thesis combines experimental evidences with structural modelling and simulation of diffraction patterns. For real-space

3-D structure and interfaces, VESTA^{TM} software has been extensively used. Pearsons's handbook of crystallographic data was referred for the Wyckoff positions of ions in the multicomponent oxides [23]. The anticipated presence of complete disorder in entropy stabilized oxides may be treated with idealized Wyckoff positions, whereas formation of two- or multi-phase with probable short-range order and defect structure can make selection of ionic positions quite complicated. Apart from crystal and interface structures, diffraction signature from x-ray and matter interaction has been simulated through indigenously developed code using MATLAB^{TM}. It uses the combined equation accounting for atomic scattering factor, multiplicity factor, polarization factor, temperature and absorption factor to compute the total integrated intensity of x-ray peaks. Furthermore, JEMS^{TM} software was used extensively for generating standard zone-axis electron diffraction patterns and stereographic projections.

2.7. Electrocatalysis

Production of hydrogen through water electrolysis has emerged as the new energy currency owing to its high energy density and zero carbon emission. However, efficient and clean hydrogen production is dependent on the ease of oxygen production as one half of redox reaction, which is highly energy consuming and rate limiting. Therefore, it becomes essential to develop efficient electrocatalysts for enhancing the efficiency of the oxygen evolution reaction (OER) [24-26].

Electrocatalytic activity for efficient catalysis in water-splitting experiments were carried out on an Electrochemical and Corrosion Studio using the CORRTEST software. A three-electrode setup with glassy carbon as working electrode, Ag/AgCl as reference electrode and carbon black as counter electrode all dipped in an 1M KOH solution as electrolyte was used. The glassy carbon electrode was cleaned thoroughly in a slurry of high purity alumina

before “ink” of each composition was drop-cast onto the inverted tail of the glassy carbon electrode (0.071 cm^2 surface area). For preparing the ink, thin slices were cut from the sintered pellets of various compositions and it was ground into powder by mortar and pestle after which 1 mg of the specimen powder was mixed with 10 µL of 5wt% Nafion solution and 350 µL of ethanol in a vial. The vial was then ultrasonicated for sufficient time before ~ 7 µL of the ink was pipetted out on to the glassy carbon electrode. After the setup was complete, linear sweep voltammetry (LSV), cyclic voltammetry (CV) and electron impedance spectroscopy (EIS) was carried out multiple times on each of the compositions for reproducibility of results. Overpotential plots along with Taffel slopes have been computed for each of the multicomponent oxide compositions and the results have been rationaled with respect to the crystal structure, chemical modulation and phase-fractions.

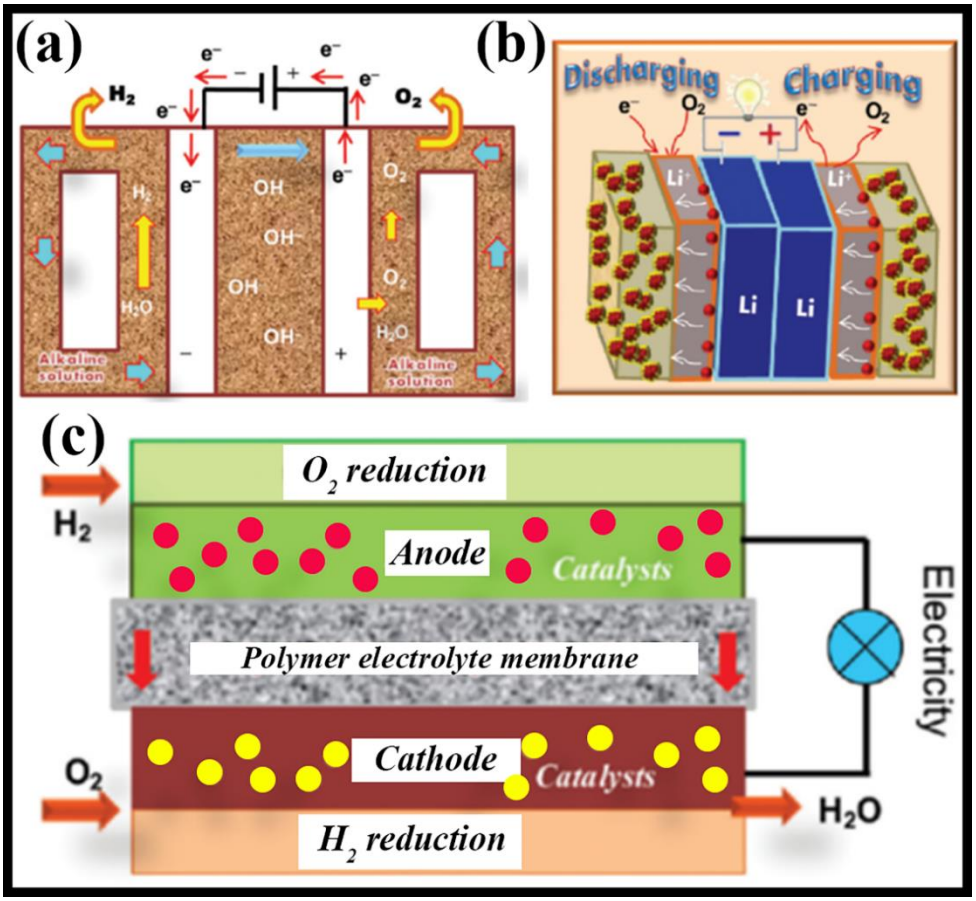

Figure 2.9: Schematic representation of (a) Electrochemical Fuel cell (b) Li-ion battery and (c) Electrocatalysis for water-splitting experimental setup [24,25].

2.8. Reference

1. K. V. Mahesh, S. K. Singh, M. Gulati, A comparative study of top-down and bottom-up approaches for the preparation of nanosuspensions of glipizide, Powder Technology, 2014, Vol. 256, 436-449.
2. B. L. Musico, D. Gilbert, T. Z. Ward, K. Page, E. George, J. Yan, D. Mandrus, V. Keppens, The emergent field of high entropy oxides: Design, prospects, challenges and opportunities for tailoring material properties, APL Mater., 2020, Vol. 8, 040912 (17 pages)
3. L. Lin, K. Wang, R. Azmi, J. Wang, A. Sarkar, M. Botros, S. Najib, Y. Cui, D. Stenzel, P. A. Sukkurji, Q. Wang, H. Hahn, S. Schweidler, B. Breitung, Mechanochemical synthesis: route to novel rock salt structured high-entropy oxides and oxyfluorides, 2020, Vol. 55, 16879-16889.
4. C. B. Carter, M. G. Norton, Ceramic Materials Science and Engineering, Springer Nature, USA, 2013, Edition 2, XXXIII (766 pages)
5. Y. M. Chiang, D. P. Birnie, W. D. Kingery, Physical Ceramics Principles for Ceramic Science and Engineering, John Wiley & Sons Inc., USA, 1997 (542 pages)
6. C. Suryanarayana, Mechanical alloying and milling, Progress in Materials Science, 46, 2001, 1-184
7. M. M. Woolfson, An Introduction to X-ray Crystallography, Cambridge Universty press, UK, Edition 2, 1997 (414 pages)
8. B. D. Cullity, Elements of X-ray Diffraction, Addison-Wesley Publishing Company Inc., USA, Editon 2, 1978 (569 pages)
9. C. Suryanarayana, M. G. Norton, X-ray Diffraction A Practical Approach, Springer Science plus Business Media LLC, USA, 1998 (275 pages)

10. M. Eckert, Max Von Laue and the discovery of x-ray diffraction in 1912: Then and now, Ann. Phys. (Berlin), 524, No. 5, 2012, A83-85
11. W. L. Bragg, The analysis of Crystals by the X-ray Spectrometer, Proceedings of the Royal Society A, 1914, Vol. 89, Issue 613, 469-489
12. W. L. Bragg, The structure of some crystals as indicated by their diffraction of X-rays, Proceedings of the Royal Society A, 1913, Vol. 89, Issue 610 (31 pages)
13. P. Eisenberger, P. M. Platzman, Compton scattering of X-rays from bound electrons, Physical Review A, Vol. 2 (2), 415-423
14. E. Ruska, The development of the electron microscope and of electron microscopy, Reviews of Modern Physics, 1987, Vol. 59 (3) (24 pages)
15. B. Fultz, J. Howe, Transmission Electron Microscopy and Diffractometry of Materials, Springer, Verlag, Berlin, Heidelberg, Edition 3, 2008 (771 pages)
16. D. B. Williams, C. B. Carter, Transmission Electron Microscopy: A Text Book for Materials Science, Springer, New York, USA, Edition 2, 2009, Vol. I-IV (779 pages)
17. J. W. Edington, Practical Electron Microscopy in Materials Science, The McMillan Press, London and Eindhoven, 1974, Vol. I-V (558 pages)
18. Z. L. Wang, New developments in Transmission Electron Microscopy for Nanotechnology, Adv. Mater., 2003, Vol. 15 (18), 1497-1514
19. E. Olsson, L. K. L. Falk, G. L. Dunlop, R. Osterlund, The microstructure of a ZnO varistor material, J. Mat. Sci., 1985, Vol. 20, 4091-98
20. C. W. Oatley, The early history of the scanning electron microscope, J. Appl. Phys., 1982, Vol. 53 (2) (14 pages)
21. N. Tanaka, Scanning Transmission Electron Microscopy of Nanomaterials: Basics of imaging and analysis, Imperial College Press, London, 2014 (616 pages)

22. R. F. Eagerton, Physical Principles of Electron Microscopy: An Introduction to TEM, SEM and AEM, Springer, USA, Edition 2, 2016 (211 pages)
23. P. Villars, L. D. Calvert, Pearson's handbook of crystallographic data for intermetallic phases, American Society of Metals, 1986, Vol. 1-3 (3258 pages)
24. D. Wang, C. Duan, Y. Yu, X. Li, Z. Wang, Y. Liu, C. Liu, Co-regulation of anion-cation in transition metal high entropy oxide for outstanding OER electrocatalytic performance, J. Alloys Comp., 2023, Vol. 967, 171758 (8 pages)
25. Z. Wang, J. You, Y. Zhao, R. Yao, G. Liu, J. Lu, S. Zhao, Research progress on high entropy alloys and high entropy derivatives as OER catalysts, J. Environ. Chem. Eng., 2023, Vol. 11, 109080 (24 pages)
26. J. Baek, Md. D. Hossain, P. Mukherjee, J. Lee, K. T. Winther, J. Leem, Y. Jiang, W. C. Chueh, M. Bajdich, X. Zheng, Synergistic effects of mixing and strain in high entropy spinel oxides for oxygen evolution reaction, Nat. Commun., 2023, Vol. 14, 5936 (11 pages)

Chapter – 3

Composition modulation, strain minimization and oriented growth of phases in equimolar (CaCoFeMgNi) multicomponent oxide

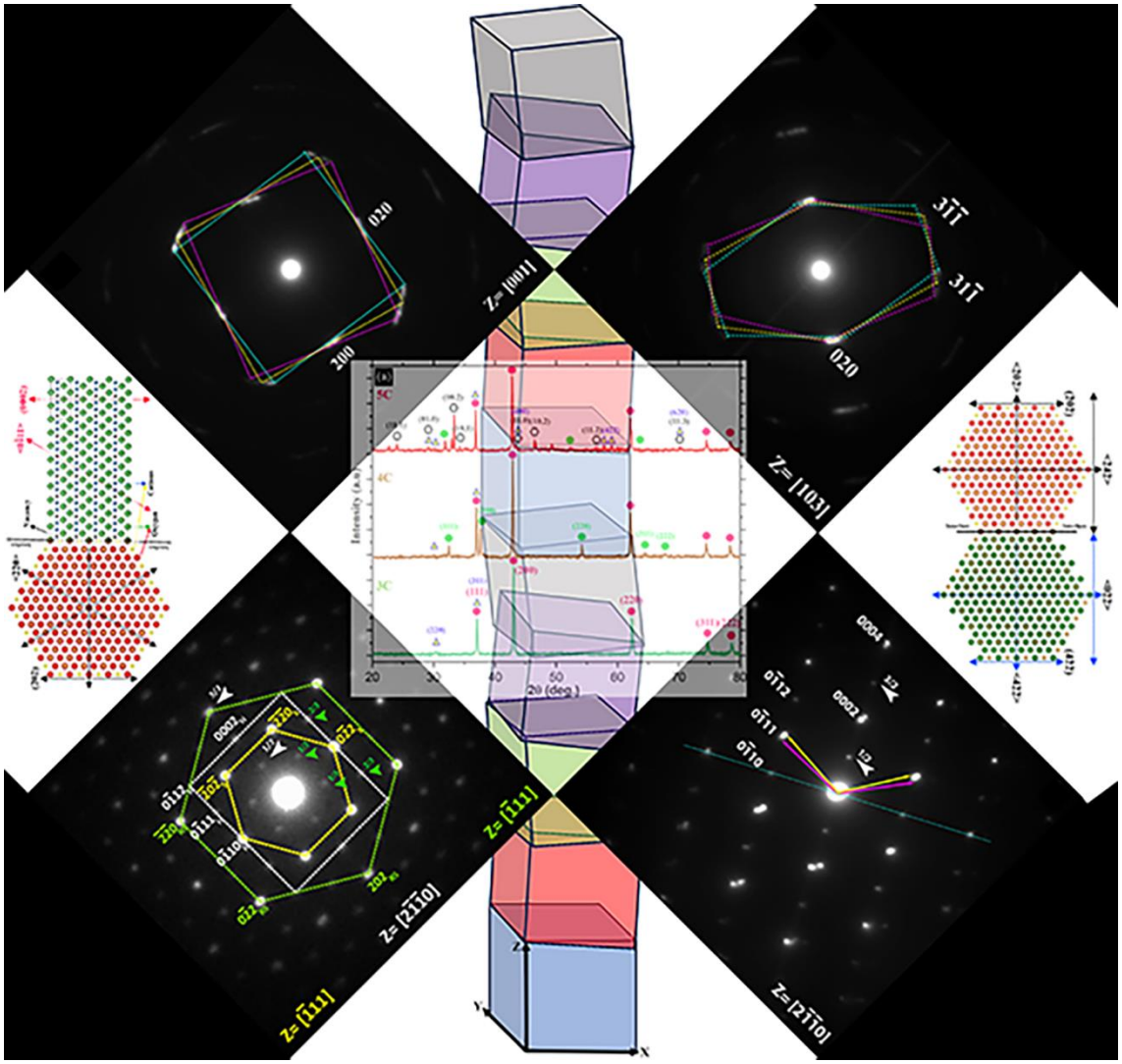

3.1. Introduction

Continuously depleting fossil fuel resources, growing environmental concerns, changing geopolitical scenario and ever-increasing energy needs have incentivized in simulating a fresh search on economically sustainable, environmentally friendly, robust energy harvesting and storage technologies [1-2]. While the operational mechanisms of fundamental principles for energy harvesting and storage are being researched at atomic and nanometer length scales, search for advanced materials, which can provide a suitable platform for efficient exploitation of the fundamental principles at atomic and nanometer length scales has also become an important facet globally [3-5]. High entropy materials (HEMs), especially high entropy ceramics (HECs) has received a lot of attention in the recent past as it is envisaged as a potential candidate material for energy harvesting and storage pertaining to its favorable electrochemical, thermoelectric and catalytic properties [6-8].

Over the last two decades, a considerably good volume of data on design, microstructure evolution, phase stability and properties on high entropy alloys (HEAs) have been documented in scientific literature [9-11]. In comparison to that, high entropy oxides (HEOs) or high entropy ceramics (HECs) are of recent vintage. The scientific literature on these materials is not so much enriched so far, their design principles, microstructure evolution, phase stability and properties are concerned [12]. HEOs/HECs may be considered to be developed in the natural evolutionary process of HEAs [6, 13]. However, there are certain fundamental concepts, e. g. assessment of configurational entropy, that need to be treated differently as the HEOs/HECs are ionic in nature and there are separate sublattices for cations and anions [14]. Initially it was believed that for HEAs with more than or equal to five elements, the configurational entropy was so high that the entropy term always dominated the total free energy of the system [15]. However, of late it is observed

that many of the HEAs are metastable in nature, more than two phases form in the traditional HEAs, which has put a question mark in front of the high configurational entropy concept extended so far in order to explain their microstructure evolution and phase stability [9, 16-17]. It is now proposed that HEA is a misnomer [18] and this kind of alloys should be termed as multi-principal element alloys (MPEAs) or complex concentrated alloys (CCAs) [19-20]. HEOs/HECs are also believed to be entropy stabilized single phase solid solutions. The role of strain energy in the lattice of HEOs/HECs, due to the presence of ions of different sizes, in determining its microstructure evolution and phase stability has remained almost unexplored [21-22].

It is believed that in HEOs, isostructuralism of precursor oxide components that finally builds up the HEO would always favor single phase HEO formation. It may accommodate one or two non-isostructural oxide components. In addition to that negative enthalpy of mixing and low to moderate difference in ionic sizes will favor the formation of single-phase HEOs [14, 23]. The work has been taken up to test the significance of the postulates and to explore the role of strain energy arising out of ionic radii and interface incoherency in a quinary equimolar (CaCoFeMgNi)-oxide. The phase stability and microstructure evolution has been compared with the ternary (CoMgNi)-oxide and quaternary (CaCoMgNi)-oxide derivatives of the original quinary equimolar (CaCoFeMgNi)-oxide. The precursor oxides of the multicomponent quinary oxide are the oxides of Ca, Co, Fe, Mg and Ni, all of which are cubic rocksalt in structure in the +2-oxidation state of the respective cations. The cation sublattice of the quinary multicomponent HEO is likely to be substituted by the ions of Ca, Co, Mg, Fe and Ni. The ionic radii of Co, Mg, Fe and Ni are close to one another. However, the ionic radius of Ca is different from the other cations [24-25] in the same coordination environment. In this work, the role of micro-strain in the lattice induced by different cations and the strain induced by interface incoherency have

been investigated. Finally, it has been established that the quinary oxide is not solely configurational entropy stabilized. However, it's a trade-off between the strain energy and the entropy that eventually determines the phase stability and microstructure evolution in this multicomponent oxide.

3.2. Materials and methods

Phase evolution, composition modulation and oriented structural intergrowth has been studied in equimolar CaCoFeMgNi multicomponent oxide. High purity metal oxide; CaO (>99.95 at%), Co(II, III)O (>99.8 at%), Fe (II, III)O (>99.8 at%), MgO (99.98 at%) and NiO (99.9 at%) were procured from either Sigma Aldrich or Alfa Aesar. Oxides in equimolar proportions were mixed together and were thoroughly ground in a mortar and pestle before they were green compacted in a uniaxial hydraulic press with 4 Ton load. In one set of samples, the mixed metal oxides in equimolar proportions were ball milled for 40 h in dry environment in a zirconia vial with zirconia balls with ball to powder ratio 10:1 before it was green compacted in a uniaxial hydraulic press with 4 Ton load. Green compacted mixed oxide pellets of 12 mm diameter were sintered at 1523 K (1250 ^{o}C) for 10, 25 and 100 h in air atmosphere and the sintered pellets were quenched in water. The sintering was carried out in a platinum crucible with the platinum lid on. Three green compacted pellets of similar composition were vertically stacked in the platinum crucible and the sintered pellet from the center of the stack was taken for further studies in order to avoid contamination during sintering. Sintered pellets were ground and polished from both sides and were studied by a Malvern Panalytical Empyrean high-resolution x-ray diffractometer with Cu-K_{α} radiation operated at 40 kV operating voltage with 40 mA current. Relative volume fraction of the phases was determined by peak ratio method of the x-ray diffraction (XRD) peaks. Microstructure and composition of the sintered pellets were studied in a FEI Quanta 200F scanning electron microscope (SEM) with an accelerating

voltage of 30 kV. For SEM studies the sintered and quenched pellets were metallographically polished and ultrasonicated in ethanol. X-ray energy dispersive spectroscopy (XEDS) mapping of the samples was done at the regions of interest in order to understand the distribution of the ions. The sintered and quenched pellets were studied in a FEI Tecnai G2 T20 transmission electron microscope (TEM) under 200 kV accelerating voltage. For TEM observations, the sintered and quenched samples were sliced by a low-speed saw, ground and polished to optimal thickness and it was ion-beam thinned to electron transparency.

The simulation of x-ray diffraction patterns was done by indigenously developed code and JEMS software was used for simulation of electron diffraction patterns. VESTA^{TM} software was used for development of crystal structure models.

3.3. Results

Phase evolution in equimolar ternary (CoMgNi)-oxide, quaternary (CaCoMgNi)-oxide and quinary (CaCoFeMgNi)-oxide after sintering at 1523 K for 10 h and water quenching has been studied through powder x-ray diffraction. The experimental powder x-ray diffraction pattern from the equimolar sintered and quenched ternary (CoMgNi)-oxide is given in Figure 3.1a-3C. The diffraction peaks are quite sharp with minimal broadening and all of them match with the solid solution phase of CoO, MgO and NiO with cF8 rocksalt structure with ~4.21 Å lattice parameter. There are two peaks, which could be indexed to cF56 (Ni,Mg)Co_2O_4 spinel phase with ~8.41 Å lattice parameter. However, the presence of this phase cannot be confirmed at this stage. Even if it is assumed to be present, its volume fraction is supposed to be very small. The simulated x-ray diffraction pattern corresponding to the CoO, MgO and NiO based solid solution phase with cF8 rocksalt structure (Figure 3.1b, in red) matched quite accurately with the experimental x-ray diffraction pattern.

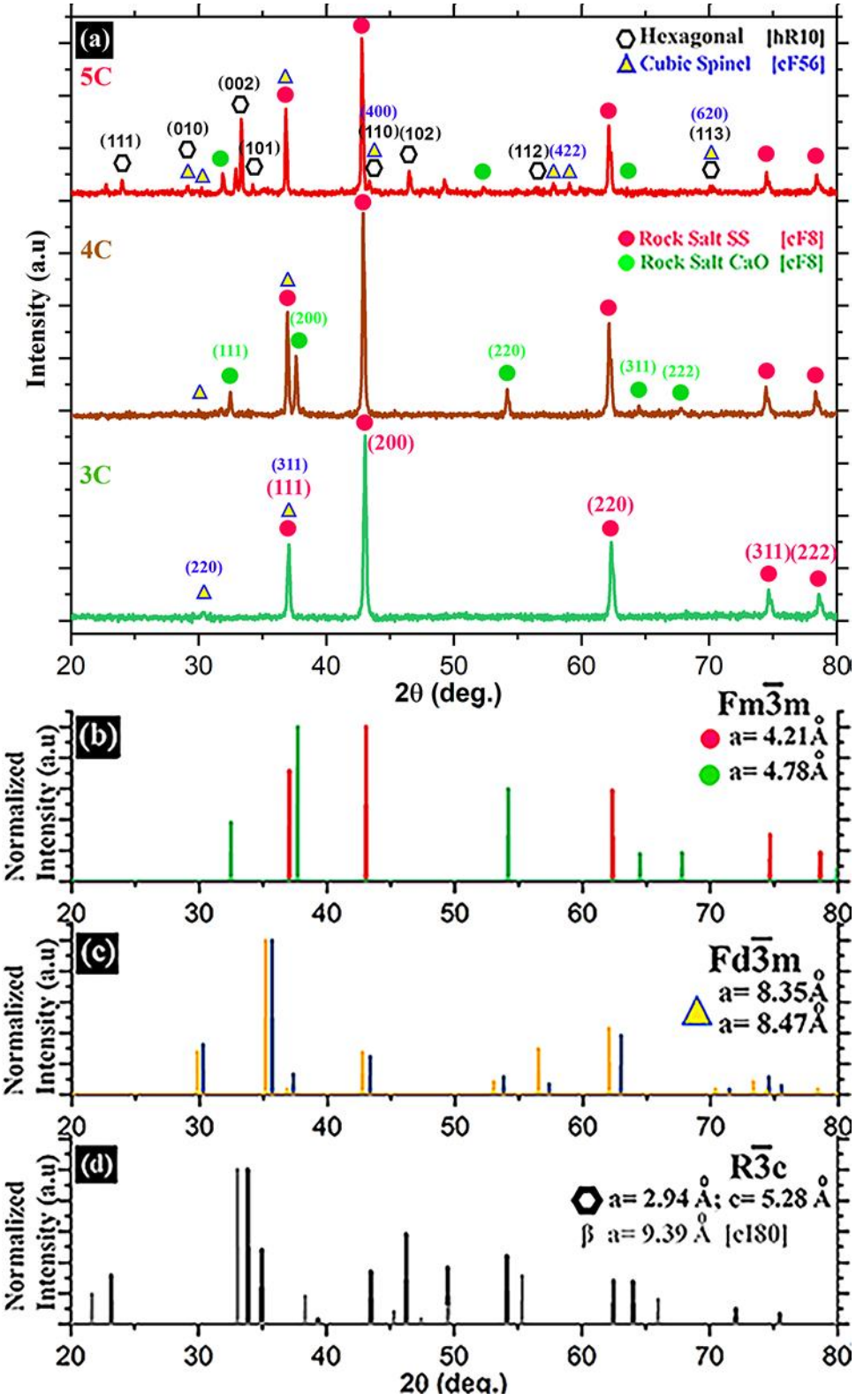

Figure 3.1: Experimentally observed x-ray powder diffraction pattern of (a-3C) ternary (CoMgNi)-oxide (a-4C) quaternary (CaCoMgNi)-oxide (a-5C) quinary (CaCoFeMgNi)-oxide after sintering at 1523 K for 10 h followed by water quenching. Simulated X-ray powder diffraction pattern of (b) cubic rocksalt structure with ~4.21 Å and ~4.78 Å lattice parameters (c) cubic spinel structure with ~8.35 Å and ~8.47 Å lattice parameters and (d) hexagonal phase with a ~2.94 Å, c ~5.28 Å lattice parameter and cubic Fe_2O_3 with ~9.39 Å lattice parameter.

The sharpness of the experimental diffraction peaks indicates that the solid solution phase does not have quenching or solid solutioning induced residual strain in it. However, weak shouldering is observed in the 200, 220, 311 and 222 peaks, which might indicate a possibility of polymorphic transformation of the cubic rocksalt phase to a tetragonal phase. However, it cannot be confirmed at this stage and it would require further investigation. Additional diffraction peaks are observed in the experimental x-ray diffraction pattern from the sintered and quenched equimolar quaternary (CaCoMgNi)-oxide sample (Figure 3.1a-4C). In addition to the solid solution phase of (CoMgNi)-oxide with cubic rocksalt structure with ~4.21 Å lattice parameter, another isostructural solid solution phase based on CaO with ~4.78 Å lattice parameter is observed. The relative volume fractions are ~61.2% and ~38.8% for the (CoMgNi)-oxide and CaO-based oxide SS phases respectively. In this diffraction pattern, the peaks are quite sharp with minimal broadening indicating minimal or almost no solid solutioning or quenching induced residual strain in the sample. However, the shoulders in the diffraction peaks corresponding to the (CoMgNi)-oxide are still observed. The shouldering in the CaO based solid solution phase is also present. However, not so prominent at lower diffraction angles. The simulated polycrystalline x-ray diffraction pattern for the CaO based solid solution phase with rocksalt structure (Figure 3.1b, in green) match quite well with the experimental pattern. It may be concluded from these observations that a solid solution phase with cubic rocksalt structure forms in the equimolar (CoMgNi)-oxide upon sintering at 1523 K for 10 h followed by quenching. However, upon addition of CaO, two isostructural solid solution phases with rocksalt structure and with different lattice parameters are observed. The reason behind such observation would be discussed in the discussion section.

Quite a few additional diffraction peaks are observed in the experimental x-ray diffraction pattern of the equimolar quinary (CaCoFeMgNi)-oxide after sintering at 1523 K for 10 h

followed by quenching (Figure 3.1a-5C). In this diffraction pattern, in addition to the solid solution phases based on (CoMgNi)-oxide with ~4.21 Å lattice parameter, CaO based solid solution phase with ~4.78 Å lattice parameter, a spinel phase with ~8.41 Å lattice parameter is also present. The spinel phase brings out a very good match with the simulated polycrystalline diffraction pattern (Figure 3.1c) of $(Ni,Fe)Co_2O_4$ spinel (in blue) with ~8.35 Å lattice parameter and $(Ca,Fe)_3O_4$ spinel (in yellow) with ~8.47 Å lattice parameter. It is assumed that the experimentally observed spinel phase is a chemical and structural derivative of the two above mentioned spinel phases. In addition to that, a hexagonal phase (hR10) with quite similar symmetry elements to that of Fe_2O_3 is observed. The simulated diffraction pattern of the hexagonal phase (Figure 3.1d) with lattice parameter a ~2.94 Å and c ~5.28 Å matches closely with the experimental diffraction peaks of the hexagonal phase in Figure 3.1a-5C. It is assumed that the hexagonal phase is a derivative of Fe_2O_3 phase. The structural details of this phase will be presented later in this paper through electron diffraction. The relative volume fraction of (CoMgNi)-oxide based SS phase, CaO-based SS phase, spinel phase and the hexagonal phase are ~48.1%, ~11.25%, ~5.12% and ~35.5% respectively. It is important to point out that there is a cubic polymorph (cI80) of Fe_2O_3 phase, the simulated diffraction pattern of which is given in Figure 3.1d (in grey). However, it shows a weak match with the experimental diffraction pattern (Figure 3.1a-5C). It is assumed that the cubic polymorph is not present in the sintered and quenched (CaCoFeMgNi)-oxide. It is observed that multiple phases are formed in the quinary (CaCoFeMgNi)-oxide after sintering at 1523 K for 10 h followed by water quenching. In order to explore the effect of processing route, the as-mixed quinary oxide was ball milled for 40 h and then the milled green compact was sintered at 1523 K for 10 h followed by water quenching.

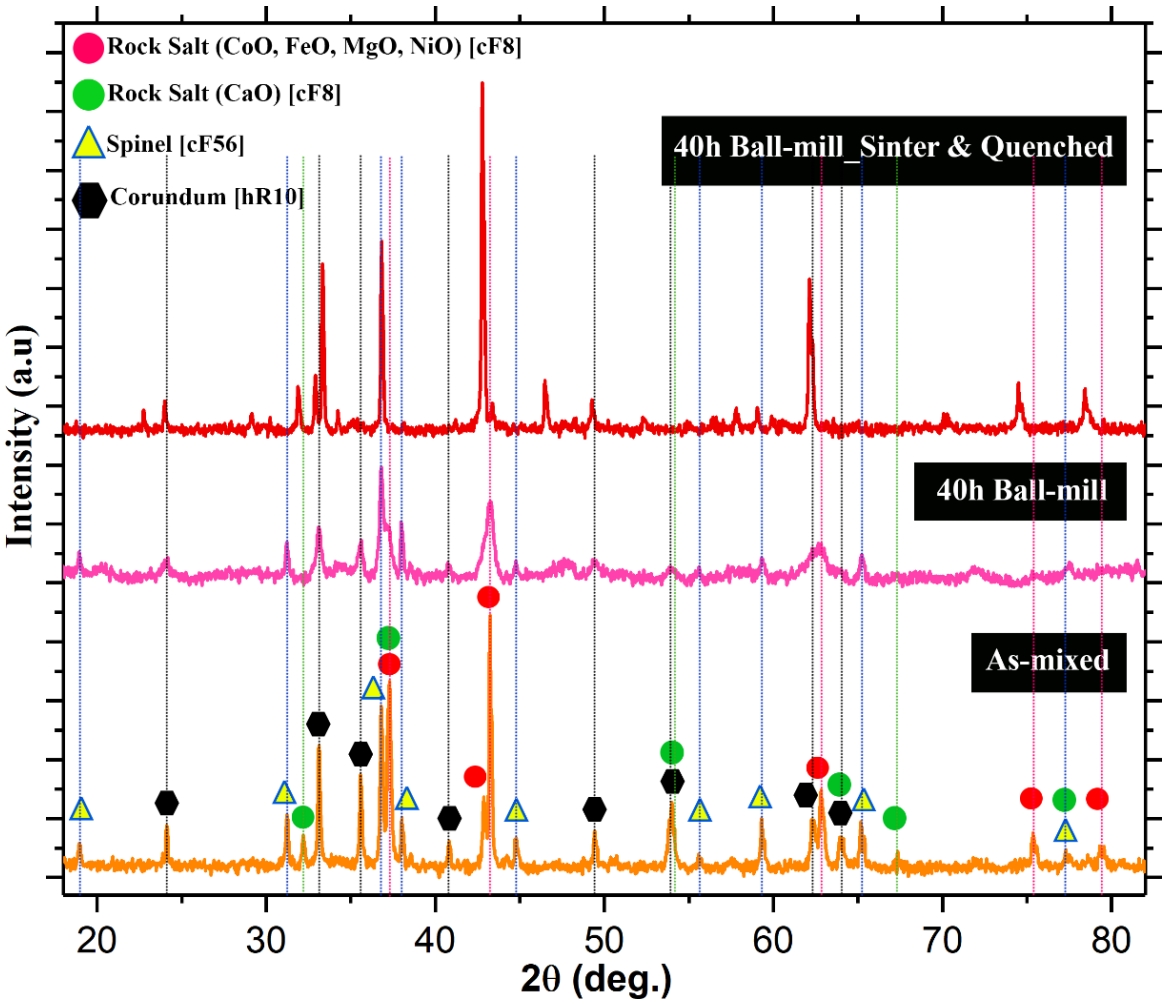

Figure 3.2: Experimentally observed powder x-ray diffraction patterns of as-mixed (CaCoFeMgNi) precursor oxide powders in equimolar ratio (in orange), the same as-mixed powder after dry ball milling for 40 h (in pink) and the pellet after sintering the green compacted ball milled powder at 1523 K for 10 h followed by water quenching (in red). In the sintered pellet cubic rocksalt phase, cubic spinel phase and the hexagonal phase can be indexed.

In the powder x-ray diffraction pattern of the as mixed quinary oxide (Figure 3.2, in orange) all the diffraction peaks corresponding to CaO, CoO, FeO, MgO, NiO, Co_3O_4 / Fe_3O_4 spinel and Fe_2O_3 corundum phases are present. After 40 h of ball milling the diffraction peaks are broadened (Figure 3.2, in pink) with a drop in intensity. The individual oxide phases cannot be distinguished anymore with certainty. This observation may be explained in the light of accumulation of strain and minor solid solutioning of oxide phases during ball milling. However, the as-mixed, ball milled and green compacted pellet after sintering at 1523 K

for 10 h followed by water quenching gives rise to a diffraction pattern (Figure 3.2, in red), which is quite similar to the as-mixed, green compacted, sintered at 1523 K for 10 h and quenched diffraction pattern of the same quinary oxide (Figure 3.1a-5C). It may be easily concluded from this observation that intermediate ball milling does not have any significant influence in the phase evolution in this quinary oxide.

In order to understand the phase and microstructural stability, green compacted equimolar (CaCoFeMgNi)-oxide was sintered at 1523 K for different length of time i. e. for 10, 25, 100 h followed by water quenching.

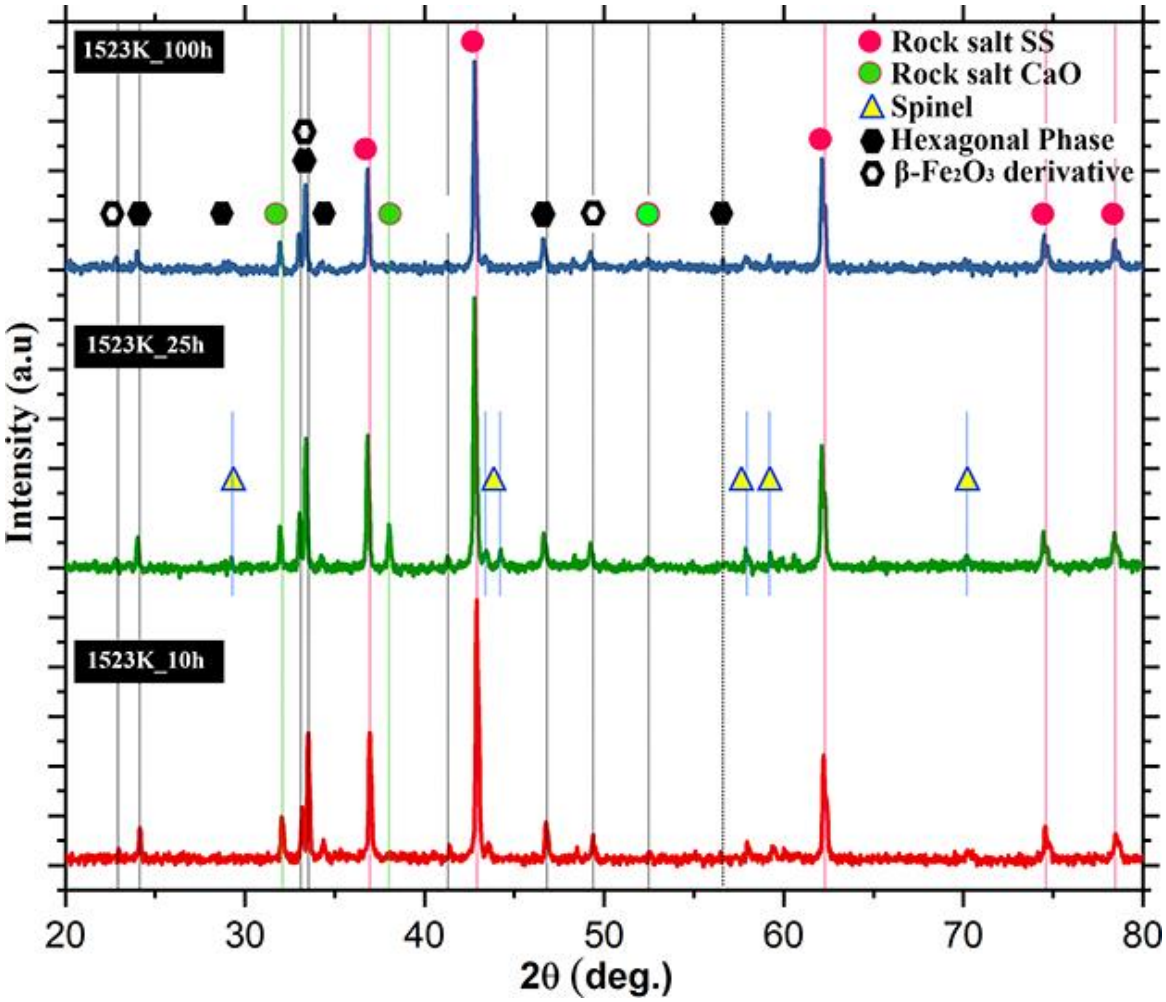

Figure 3.3: Experimentally observed x-ray diffraction patterns of quinary equimolar (CaCoFeMgNi)-oxide pellet after sintering at 1523 K for 10 h (in red), 25 h (in green) and 100 h (in blue). In all the sintered pellets cubic rocksalt phase, cubic spinel phase and the hexagonal phase can be indexed.

The multiple display of x-ray diffraction patterns after sintering for different length of time followed by water quenching is given in Figure 3.3. It is observed that cubic solid solution phase with rocksalt structure, however, based on CaO and (CoMgNi)-O with ~4.78 Å and ~4.21 Å lattice parameters respectively are still present in all of 10 h, 25 h and 100 h sintered samples. The hexagonal phase with a ~2.94 Å and c ~5.28 Å lattice parameter, which is considered to be a chemical and structural derivative of hexagonal Fe_2O_3 is present in all the three sintered samples. The cubic spinel phase with ~8.41 Å lattice parameter, which is assumed to be the chemical derivative of $(Ni,Fe)Co_2O_4$ (a = 8.35 Å) and $(Ca,Fe)_3O_4$ (a = 8.47 Å) is also present in all three sintered samples. However, the signature of the spinel phase is most prominent in the 25 h sintered sample. It may be concluded from this observation that the phases are stable up to 100 h of sintering time. Only the spinel phase becomes most prominent in the 25 h sintered samples and it is not so prominent in the 10 h and 100 h sintered samples. The solid-solution based spinel phase obtained in the present study may be seen to be structurally related with the solid-solution based rocksalt phases in terms of octahedral void filling. The probable structural correlation will be discussed in the discussion section in detail, which will explain the prominent presence and partial disappearance of the spinel phase.

SEM secondary electron micrograph of quinary equimolar (CaCoFeMgNi)-oxide sintered at 1523 K for 10 h followed by water quenching (Figure 3.4A) and its zoomed-in version (Figure 3.4a) shows irregular grain structure in the size range of ~ 5-10 μm. Pores are not observed significantly in the microstructure. The XEDS chemical mapping from the zoomed-in area (Figure 3.4a) clearly indicates chemical segregation during the sintering process. As seen from the maps, Fe and Ca ions get segregated in the grains and the boundary regions are enriched with Co, Mg and Ni ions.

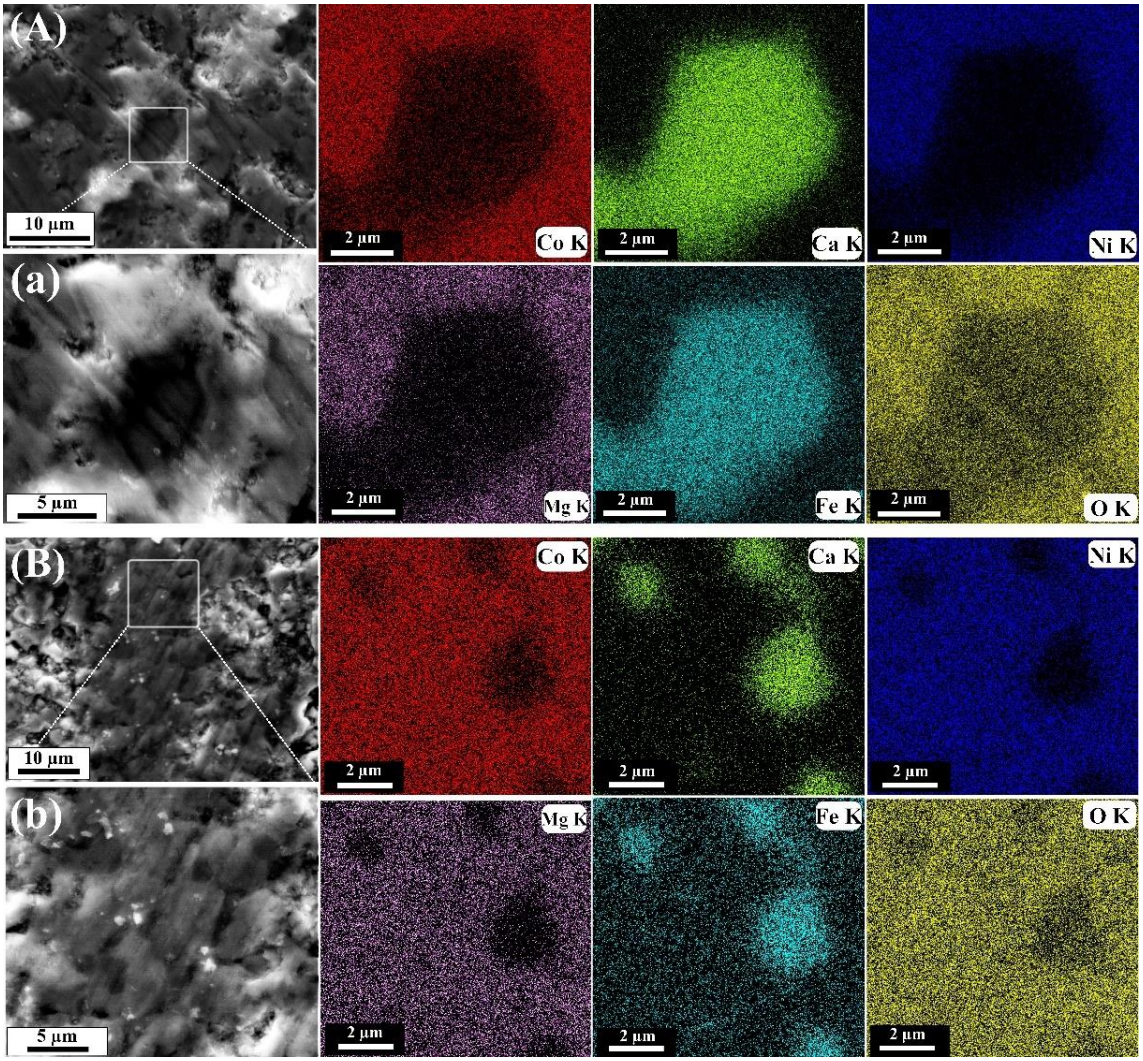

Figure 3.4: SEM-XEDS area map with Ca-K, Co-K, Fe-K, Mg-K and Ni-K in quinary equimolar (CaCoFeMgNi)-oxide after (A) sintering at 1523 K for 10 h and (B) sintering at 1523 K for 100 h followed by water quenching. (a) is the zoomed-in version of the area marked in (A) and (b) in the zoomed-in version of the area marked in (B). The XEDS maps are generated from the areas shown in (a) and in (b). In both the samples, two chemically segregated regions, one rich in Co, Mg, Ni ions and other rich in Ca and Fe ions can be observed.

This observation further reinforces the analytical outcomes of the XRD patterns in Figures 3.1, 3.2 and 3.3, where solid solution phases based on (CoMgNi)-oxide and CaO has been reported. Further, the spinel phase is reported to be a chemical derivative of $(Ni,Fe)Co_2O_4$ and $(Ca,Fe)_3O_4$. It is highly likely that the spinel phase may exist in both the regions. The hexagonal phase, which is assumed to be a chemical derivative of hexagonal Fe_2O_3 is likely to be present in the Ca and Fe enriched areas. It may be concluded that CaO based solid

solution phase, the spinel phase and the hexagonal phase coexist in the Ca and Fe enriched regions, whereas the (CoMgNi)-O based solid solution phase and the spinel coexist in the Co, Mg, Ni enriched regions. Their coexistence behaviour will be reported in the subsequent sections. It is noteworthy at this point that oxygen mapping reveals qualitatively non-uniform distribution of oxygen. It is preferentially enriched in the areas where solid solution phase based on (CoMgNi)-oxide and the spinel phase are present. It is depleted in the regions where CaO based solid solution phase, spinel phase and the hexagonal phase coexist. SEM secondary electron image (Figure 3.4B) and its zoomed-in version (Figure 3.4b) indicates that after 100 h of sintering followed by water quenching there is no significant change in the microstructure. The grains are still irregular in shape with insignificant or almost no grain growth during the elongated sintering process. After 100 h of sintering the grain size is ~ 5-15 μm. In this sample also the porosity remains to be very low. XEDS chemical maps from the zoomed-in area in Figure 3.4b indicates segregation of Ca and Fe with respect to Co, Mg and Ni. Inhomogeneous distribution of oxygen and its preferential segregation in the Co, Mg, Ni enriched regions are also noteworthy. The XEDS chemical map from Figure 4b shows chemical segregation in multiple pockets, which further reinforces the claim that the chemical segregation is characteristic of the sintered microstructure.

SEM-BSE image of sintered and quenched (CaCoFeMgNi)-oxide (1523K, 10h) along with point XEDS spectra and relative composition of the phases from several regions are given in Figure 3.5. The variation in contrast arising out of chemical segregation is clearly evident from the BSE image. Additionally, point EDS has been carried out on regions of interest. Six such regions have been chosen of varying contrast and they have been categorized and clubbed in the table below (Figure 3.5). It is seen that the pair of regions marked as 1,6 have similar chemical distribution while the pair marked as 2,3 in turn have similar

chemical distribution, however different from each other. Similarly, regions marked as 4 and 5 are compositionally different from each other as well as from region pairs 1,6 and 2,3. The relative volume fraction listed in the last column of the table has been deduced from curve profile fitting of the XRD patterns reported in Figures 3.1-3.3, and its subsequent calibration through peak intensity ratio method. It may therefore be concluded from point EDS analysis that in the Co, Mg, Ni rich regions Ca and Fe ions are present in minor quantities and vice-versa, which further reinforces inference drawn from Figure 3.4.

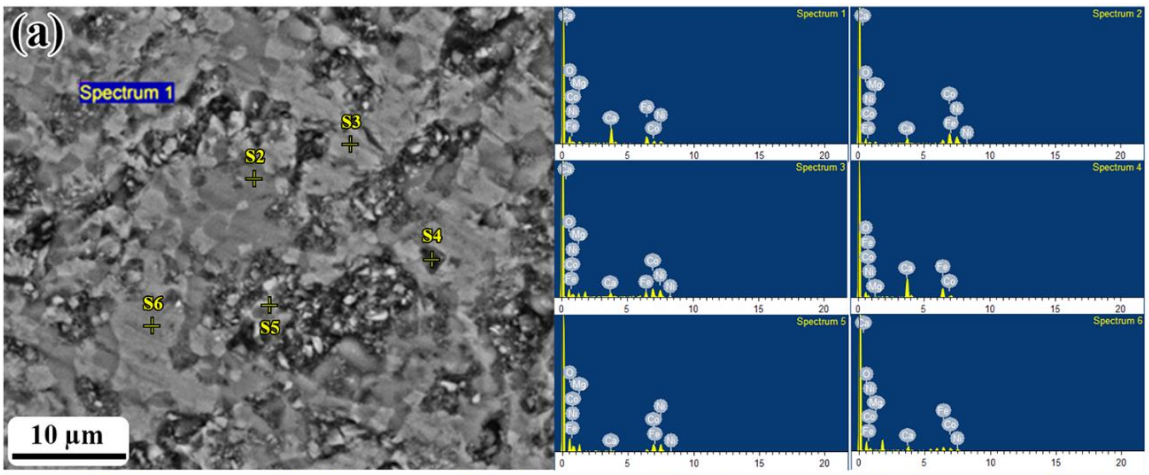

S1	Wt. %	S2	Wt. %	S3	Wt. %	S4	Wt. %	S5	Wt. %	S6	Wt. %
Ca	25.43	Ca	5.52	Ca	4.59	Ca	26.86	Ca	0.38	Ca	17.41
Co	11.7	Co	36.71	Co	29.54	Co	5.25	Co	27.4	Co	10.05
Fe	18.96	Fe	9.59	Fe	11.43	Fe	37.61	Fe	4.92	Fe	15.6
Mg	3.52	Mg	4.06	Mg	6.64	Mg	0.12	Mg	12.33	Mg	3.56
Ni	9.55	Ni	30.94	Ni	30.85	Ni	1.85	Ni	28.1	Ni	13.14

	Chemical distribution	Phase (P)	P. Fraction
Region 1,6	*Rich in Ca, Fe ; Moderate in Co, Ni ; Lean in Mg*	*Cubic Rock salt (a= 4.83 Å)*	~ 11.2%
Region 2,3	*Rich in Co, Ni ; Moderate in Fe, Mg ; Lean in Ca*	*Cubic Spinel (a= 8.32 Å)*	~ 5.1%
Region 4	*Rich in Fe, Ca ; Moderate in Co ; Lean in Mg, Ni*	*Ordered Hexagonal (a=2.94 Å, c=5.28 Å)*	~ 35.5%
Region 5	*Rich in Co, Mg, Ni ; Lean in Ca, Fe (major phase)*	*Cubic Rock salt (a= 4.15 Å)*	~ 48.1%

Figure 3.5: (a) Back scattered electron (BSE) image and X-ray energy dispersive spectrum (XEDS) from the points marked by s1-s6 in (CaCoFeMgNi)-oxide sintered at 1523K for 10h. Compositional contrast is observed in the BSE image. All the point XEDS from s1-s6 show the presence of all the elements, however in varying quantities. Compositions as obtained from XEDS are tabulated in the table below. It is again reconfirmed that Ca and Fe ion rich regions are relatively lean in Co, Mg and Ni ions and vice-versa. However, all the elements are present in all the phases. Based on the composition the predominant phase in different regions have been identified and their volume fraction as computed from the X-ray diffraction peak analysis is given in the table at the bottom of the figure.

TEM bright field images and corresponding electron diffraction patterns for quinary equimolar (CaCoFeMgNi)-oxide after sintering at 1523 K for 10 h followed by water quenching are given in Figure 3.6 (a-d). After sintering for 10 h followed by quenching, polygonal and faceted (Figure 3.6a) grains can be observed in the microstructure. Thickness fringes within the grains indicates that the grains are polyhedral in shape. The corresponding diffraction pattern in Figure 3.6b is a z = [001] zone axis pattern of a cubic phase. The 200 and 220 plane spacings as measured from this diffraction pattern turns out to be ~2.06 Å and ~1.45 Å respectively, which are very close to the same d-spacings of the (CoMgNi)-oxide solid solution phase as obtained from the x-ray diffraction pattern. The calculated lattice parameter for this solid solution phase turns out to be ~4.16 Å, which is within ~2% error range of calculated lattice parameter of the same phase as obtained from the x-ray diffraction pattern. Bright field image from the same 10 h sintered and quenched sample but from a different region is given in Figure 3.6c. In this image also faceted grain is observed. However, within the grain considerable amount of mottled contrast is present, which indicates the presence of micro-strain within the grain body. The corresponding diffraction pattern (Figure 3.6d) is along cubic z = [103] zone axis, which matches with the same cubic solid solution phase of (CoMgNi)-oxide with rocksalt structure with ~4.16 Å lattice parameter. Bright field images from two different regions after sintering at 1523 K for 100 h followed by water quenching are given in Figure 3.6e and Figure 3.6g respectively. In both the images the grains are quite large. However, within the grains strong mottled contrast is observed. A careful look reveals a fringe contrast (pointed with black arrows) within the mottled regions. The origin of the fringe contrast within the mottled regions is not directly interpretable from the images. However, the corresponding diffraction patterns from the respective regions (Figure 3.6f and Figure 3.6h) offer interesting insights about accumulated micro-strain in the lattice, which might be treated as

the origin of fringe contrast in the bright field images and the tendency of the system to minimize it in the process of long-term sintering. The diffraction pattern in Figure 3.6f corresponds to the region in the bright field image in Figure 3.6e. In the diffraction pattern cubic 4-fold symmetry is quite easily discerned. However, the principal reflections are arced instead of being spots with several intensity maxima present in each of them. When the intensity maxima present in each of the arcs are joined geometrically by dotted coloured lines as has been done in Figure 3.6f, presence of several square patterns rotated with respect to one another by a very small angle is observed. However, in this image only three such square patterns are shown for the purpose of clarity.

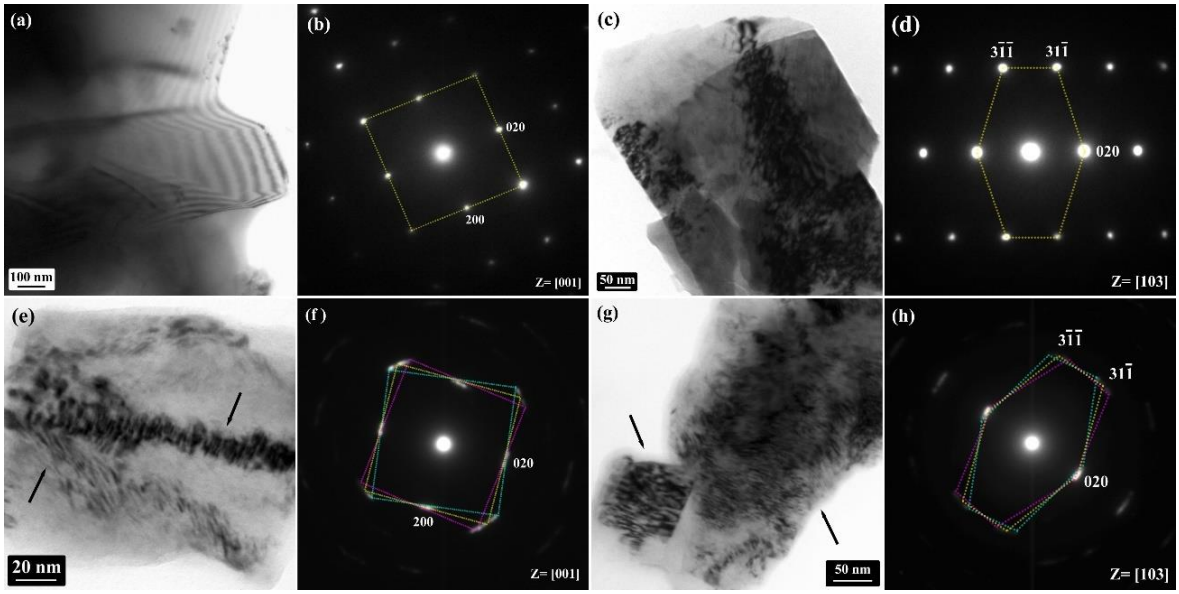

Figure 3.6: TEM (a, c) BF images and corresponding (b, d) single crystal diffraction patterns from z = [001] and z = [103] respectively in quinary equimolar (CaCoFeMgNi)-oxide after sintering at 1523 K for 10 h followed by water quenching. Thickness fringes in (a) and mottled contrast in (b) can be observed. The diffraction patterns in (b) and (d) are sharply defined. TEM (e, g) BF images and corresponding (f, h) single crystal diffraction patterns from z = [001] and z = [103] respectively in quinary equimolar (CaCoFeMgNi)-oxide after sintering at 1523 K for 100 h followed by water quenching. In the BF images in (e) and (g) fringe contrast within the mottled regions (marked with arrows) can be observed. In the diffraction patterns in (f) and in (h) arcs with modulated intensities can be observed.

The diffraction pattern (Figure 3.6h) from the region given in the bright field image in Figure 3.6g also shows similar arcing with several intensity maxima. In this diffraction pattern, when the intensity maxima are geometrically connected by dotted lines, each of the dotted polygons in the shape of distorted hexagons conforms to the z = [103] zone axis pattern of a cubic phase, which matches quite closely with the solid solution phase of (CoMgNi)-oxide with rocksalt structure with ~4.16 Å lattice parameter. In Figure 3.6h three such dotted coloured polygons are shown for the purpose of clarity. The presence of arcs in the diffraction patterns after 100 h of sintering (Figure 3.6f and Figure 3.6h) and simultaneous presence of fringe contrast in the mottled regions in the bright field images (Figure 3.6e and Figure 3.6g) confirms that the (CoMgNi)-oxide solid solution phase with rocksalt structure is rotated with respect to one another successively through a very small angle. The diffraction pattern in Figure 3.6f is along z = [001] and the intensity along any arc is not totally uniform. This indicates that the solid solution phase with rocksalt structure has a successive in-plane small angle rotation when viewed along z= [001]. However, non-uniform intensity distribution indicates to the probability of having an out-of-plane rotation between two successive cubic domains, which can be confirmed from the diffraction pattern in Figure 3.6h with viewing direction as z = [103]. Along this zone axis also, arcing and non-uniform intensity distribution is observed, which necessarily indicates the successive rotation between the cubic domains resulting into an inter-penetration between two consecutive domains in 3-dimension. As the zone axes in Figure 3.6f (z = [001]) and Figure 3.6h (z =[103]) are not mutually perpendicular to one another, arcing in both the diffraction patterns may be treated as the confirmatory evidence of interpenetration of mutually rotated cubic domains in 3-dimension. The detailed structural model and possible mechanism behind the formation of such inter-penetrated domains will be discussed in the discussion section.

Selected area diffraction pattern from another region of the quinary equimolar (CaCoFeMgNi)-oxide after sintering at 1523 K for 10 h and 100 h followed by water quenching is given in Figure 3.7a and Figure 3.7b respectively. In both the diffraction patterns multiple spots with modulation of intensity could be observed. The measured d-spacings from the diffraction pattern are marked in Figure 3.7a, which are similar for Figure 3.7b also. However, the corresponding reciprocal lattice vectors are marked in Figure 3.7b and the indexing holds well for the diffraction pattern given in Figure 3.7a also. A close look at the diffraction patterns in Figure 3.7a and in Figure 3.7b indicates that essentially there is no difference between them in terms of spot position and their intensities. However, the diffraction spots in Figure 3.7b are more sharply defined than the similar spots in Figure 3.7a. It may be inferred from this observation that there is no phase change that takes places while the quinary oxide is sintered for 10 h and for 100 h. The increase in the sharpness of the spots may be related to the strain relaxation in the lattice that takes place during the long hours of sintering process [24,25]. The d-spacings are marked in Figure 3.7a. Very similar d-spacings were observed in x-ray diffraction patterns for similar samples, which may be indexed to the cubic solid solution phase based on CaO with rocksalt structure with a ~4.78 Å lattice parameter, cubic spinel phase with a ~8.41 Å lattice parameter and a hexagonal phase with a ~2.94 Å and c ~5.28 Å lattice parameter (c/a = 1.8) respectively. It is noted that the hexagonal phase is related to the structural and chemical derivative of the Fe_2O_3 based phase as observed in the x-ray diffraction studies. It is further noted that in this diffraction pattern any signature of the cubic solid solution phase of (CoMgNi)-oxide with rocksalt structure and with a ~4.16 Å lattice parameter could not be observed. It is inferred from this observation that the diffraction pattern is from the Ca and Fe ion rich regions of the sample as observed in the SEM-XEDS chemical maps in Figure 3.4. Now it may be explicitly said that the Ca and Fe rich regions consist of CaO based solid solution phase,

cubic spinel phase and the hexagonal phase. The Co, Mg, Ni rich regions consist of mainly the (CoMgNi)-oxide solid solution phase.

The presence of a large number of spots and their modulation in intensities in Figure 3.7(a-b) can be explained only when the simultaneous presence of all the three phases i. e. the CaO based solid solution phase with rocksalt structure, cubic spinel phase and the hexagonal phase and their oriented growth is taken into consideration. The reciprocal lattice vectors specific to the three different phases, their corresponding d-spacings are marked with different colour scheme in Figure 3.7a. Whereas the zone axis patterns and the indices for three different phases are marked with different colour scheme in Figure 3.7b. In both the figures CaO based cubic solid solution phase with rocksalt structure is marked in green, the cubic spinel phase is marked in yellow and the hexagonal phase, which is supposed to be a structural and chemical derivative of Fe_2O_3 is marked in white. In Figure 3.7b, the zone axis pattern marked in yellow, is the z = [$\bar{1}$11] pattern from the cubic spinel phase with a ~8.41 Å lattice parameter. In the same figure, the zone axis pattern marked in green corresponds to the z = [$\bar{1}$11] pattern of the CaO based cubic rocksalt phase with a ~4.78 Å lattice parameter. It is clearly observed that there is an orientation relationship between the CaO based cubic solid solution phase with rocksalt structure and the cubic spinel phase. The orientation relationship is $[\bar{1}11]_{RS} \parallel [\bar{1}11]_S$ and $(220)_{RS} \parallel (2\bar{2}4)_S$ (Rocksalt phase is represented as 'RS' and spinel phase is represented as 'S'). Similarly, the pattern marked in white (Figure 3.7b) is the z = [$2\bar{1}\bar{1}0$] zone axis pattern of the hexagonal phase with a ~2.94 Å and c ~5.28 Å. This pattern also clearly indicates a strong orientation relationship with the cubic rocksalt phase and the cubic spinel phase.

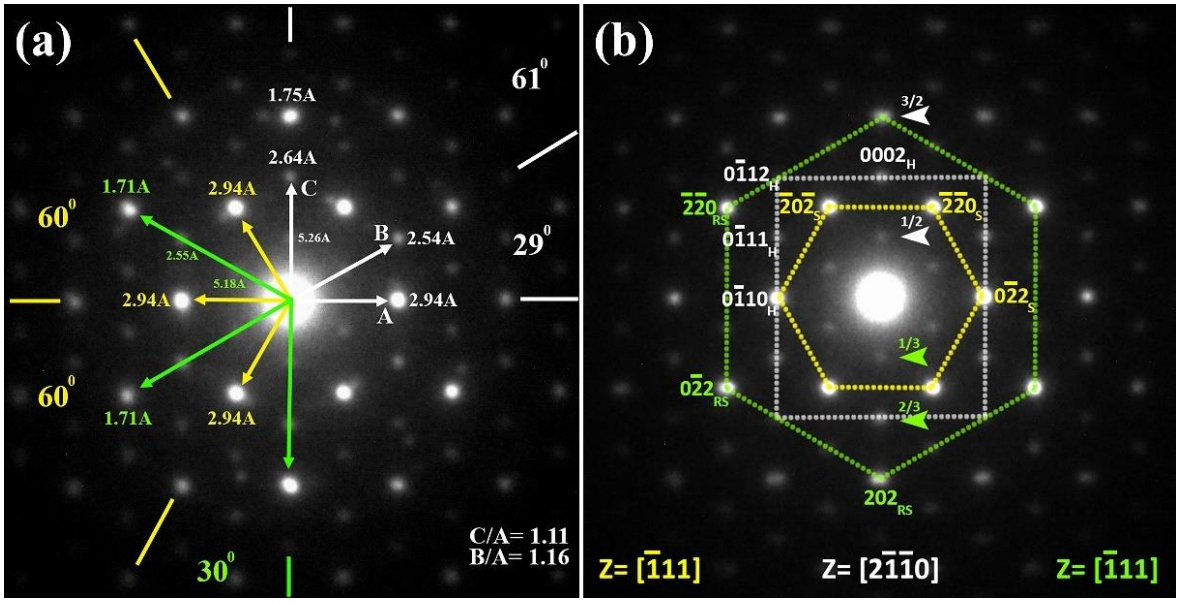

Figure 3.7: Selected area diffraction patterns from the quinary equimolar (CaCoFeMgNi)-oxide after sintering at 1523 K for (a) 10 h (b) 100 h followed by water quenching. In (a) experimentally observed d-spacings and their angular relationships are depicted. In (b) zone axis geometries are depicted. In (a) and (b) the data related to the cubic rocksalt phase, cubic spinel phase and the hexagonal phase are marked in green, yellow and white respectively. The cubic rocksalt phase, cubic spinel phase and hexagonal phase are oriented along z = [$\bar{1}$11], z = [$\bar{1}$11] and z = [2$\bar{1}\bar{1}$0] respectively. Their orientation relationships are [$\bar{1}$11]$_{RS}$ || [$\bar{1}$11]$_S$ and (220)$_{RS}$ || (2$\bar{2}$4)$_S$; [2$\bar{1}\bar{1}$0]$_H$ || [$\bar{1}$11]$_{RS}$ and (0002)$_H$ || ($\bar{2}$02)$_{RS}$; and [2$\bar{1}\bar{1}$0]$_H$ || [$\bar{1}$11]$_S$ and (0002)$_H$ || ($\bar{4}\bar{2}\bar{2}$)$_S$ (RS: Rocksalt, S: Spinel; H: Hexagonal phase).

The orientation relationships are [2$\bar{1}\bar{1}$0]$_H$ || [$\bar{1}$11]$_{RS}$ and (0002)$_H$ || ($\bar{2}$02)$_{RS}$; [2$\bar{1}\bar{1}$0]$_H$ || [$\bar{1}$11]$_S$ and (0002)$_H$ || ($\bar{4}\bar{2}\bar{2}$)$_S$ (Hexagonal phase is represented as 'H'). It is clearly observed that the spots common to any two or more of rocksalt phase, spinel phase or hexagonal phase are more intense than the spots which are unique to either of the three phases. Additionally, ordering induced superlattice reflections are present in Figure 3.7(a-b). The superlattice reflections are marked following the same colour scheme as mentioned earlier (Hexagonal: white, Rocksalt: green). In the hexagonal phase, along 0002 reciprocal lattice vector two superlattice reflections are discerned at ½[0002] and 3/2[0002] (marked with white arrows). Similarly, along the <220> directions of the cubic rocksalt phase, which is also the <0$\bar{1}$11>

direction for the hexagonal phase, superlattice reflections are observed at 1/3<220> and 2/3<220> (marked with green arrows). As the directions are common to both the cubic rocksalt phase and the hexagonal phase, at this moment it cannot be confirmed whether the origin of the superlattice reflections is due to the cubic rocksalt phase or the hexagonal phase. However, in Figure 3.8b, in the zone axis pattern from the hexagonal phase along z = [2$\bar{1}\bar{1}$0] the superlattice reflections are not observed along <0$\bar{1}$11> directions. It can be confirmed from this observation that the additional ordering spots along <220> directions in Figure 3.7(a-b) are due to the cubic rocksalt phase. The physical implications for existence of such superlattice reflections along <0002> directions of the hexagonal phase and <220> directions of the cubic rocksalt phase will be discussed in the discussion section.

TEM bright field images and diffraction patterns from the hexagonal phase reported in the preceding section in the quinary equimolar (CaCoFeMgNi)-oxide after sintering for 10 h and 100 h followed water quenching are given in Figure 3.8(a-c) and Figure 3.8(d-f) respectively. After sintering for 10 h, in the quinary oxide (Figure 3.8a) several parallel fringes (marked with dotted yellow lines) with finite width ~5-10 nm could be observed. The fringes are likely to be originated from a series of planar faults existing within the grain body. The rotationally oriented diffraction pattern (Figure 3.8b) from the same region conforms to the hexagonal phase with a ~2.94 Å and c ~5.28 Å as reported in the preceding section for the same quinary oxide after sintering for 10 h and 100 h (Figure 3.7(a-b)). In the diffraction pattern superlattice reflections at ½[0002] and 3/2[0002] (marked with white arrows) indicating an order along the c-axis of the hexagonal phase is observed. It is to be noted that no superlattice reflection is observed along [0$\bar{1}$11]. Further it is to be noted that the reflections along [0$\bar{1}$10] are not split. However, all other reflections are split into two. It is further observed that a rotation of 180^{o} around 0002 axis leaves the split spots mirror

reflections to one another. This confirms that the parallel fringes in the bright field image in Figure 3.8a are compound deformation twins with shear plane s = $(2\bar{1}\bar{1}0)$, $K_1 = (0002)$, $\eta_1 = [0\bar{1}10]$, $K_2 = [10\bar{1}0]$ and $\eta_2 = [01\bar{1}1]$ as twin variants. The symbols have their usual meaning in twin crystallography.

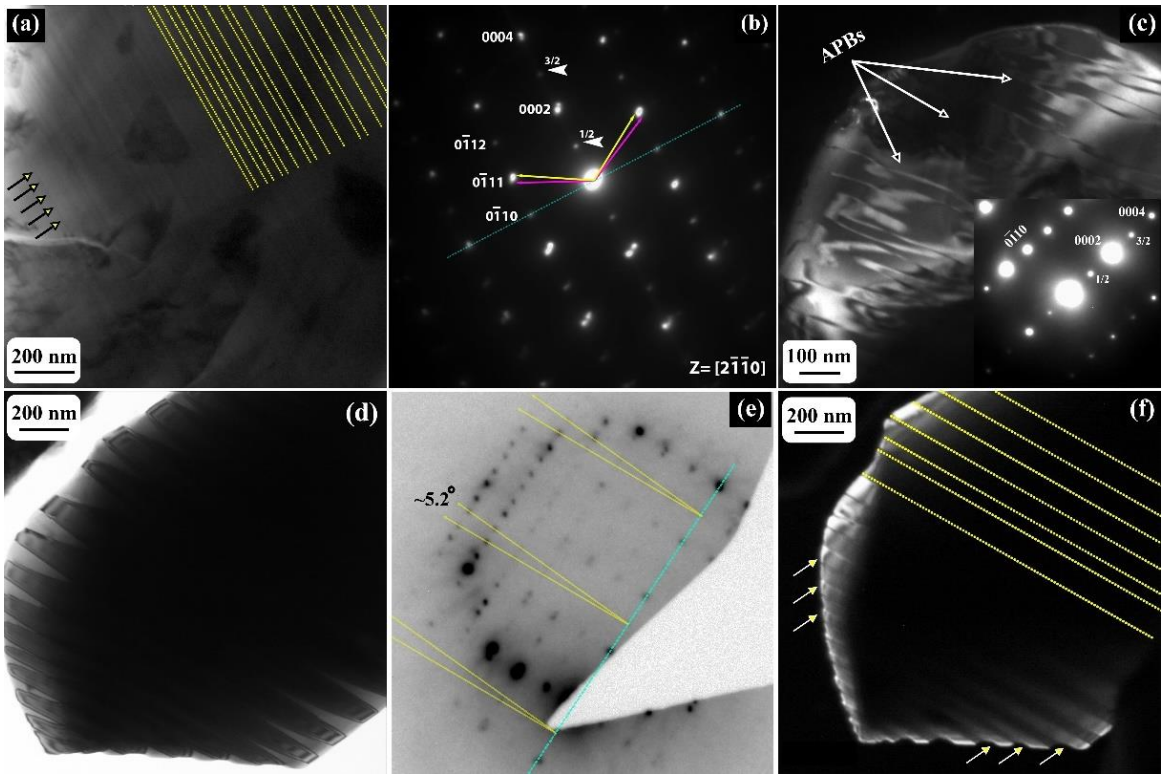

Figure 3.8: TEM (a) BF image and (b) corresponding rotationally aligned selected area diffraction pattern and (c) DF image using the superlattice reflection at ½[0002] (given at the inset in (c)) from the quinary equimolar (CaCoFeMgNi)-oxide after sintering at 1523 K for 10 h followed by water quenching. Linear fringes in (a) are from the twins and the curvilinear contrast in (c) is from the APBs. The diffraction pattern in (b) indicates that the twins in (a) are compound deformation twins with s = $(2\bar{1}\bar{1}0)$, $K_1 = (0002)$, $\eta_1 = [0\bar{1}10]$, $K_2 = [10\bar{1}0]$ and $\eta_2 = [01\bar{1}1]$ as twin variants. (d) BF image (e) corresponding rotationally aligned diffraction pattern and (f) DF image from the quinary equimolar (CaCoFeMgNi)-oxide after sintering at 1523 K for 100 h followed by water quenching. The diffraction pattern in (e) is little off from the zone axis as shown in (b). All the spots perpendicular to the row of spots marked in cyan are split. The twins in (d) and in (f) are widely spaced.

Dark field image from the same 10 h sintered and quenched sample from a different region in Figure 3.8c and its diffraction pattern at the inset shows that in the dark field image

several curved linear contrasts often resulting into a loop are present. The diffraction pattern in the inset (Figure 3.8c) is along z = [$2\bar{1}\bar{1}0$]. In this diffraction pattern spot splitting is not observed. However, the curvilinear contrast in the image may be correlated with the existence of antiphase domains (antiphase domain boundaries: APBs) within the hexagonal phase (marked with white arrows). The origin of antiphase domains and its physical implications will be discussed in the discussion section.

Similar alternate bright and dark fringe contrast, however, grown to a larger extent is observed in the bright field image (Figure 3.8d) and in the dark field image (Figure 3.8f) of the 100 h sintered and quenched sample (marked with arrows in Figure 3.8f). In the rotationally oriented diffraction pattern (Figure 3.8e) from the same region, which is little away from the nearest zone axis, similar spot splitting is observed. In may be inferred from this observation that the compound deformation twins as shown in the 10 h sintered and quenched sample (Figure 3.8a) grow further in the 100 h quenched sample.

3.4. Discussion

(CaCoFeMgNi)-oxide was synthesized through solid state route, in which the green compact was sintered at 1523 K for different lengths of time and they were water quenched. Lower order derivatives of the quinary equimolar oxide i.e. (CoMgNi)-oxide, (CaCoMgNi)-oxide were also synthesized and they were subjected to similar processing conditions in order to compare the phase evolution, microstructural stability against a standard set of conditions. The effect of processing route also has been investigated. A unified look at the results leads to some fundamental understanding about this multicomponent oxide, its phase and structure evolution, their oriented intergrowth, distribution of chemistry and microstructural stability, which will be discussed in the subsequent sections. At the end, an attempt will be made to comment whether entropy is

the only determining factor or there is an interplay of several other factors that ultimately decide its phase, microstructure evolution, its stability and hence, its properties.

3.4.1. Phase and microstructure evolution and its stability

The precursor oxides leading to the formation of quinary equimolar (CaCoFeMgNi)-oxide are CaO, CoO, FeO, MgO and NiO. All the individual oxides are having cubic rocksalt structure [24-25]. CoO, FeO and NiO may exist in other crystal structures as they can exist in several oxidation states and they can switch their oxidation states quite easily [26]. Cubic spinel variant of Co_3O_4 and Fe_3O_4 has also been reported. Fe_2O_3 is the hexagonal/rhombohedral variant that is quite abundantly available in nature. However, there is a structural correlation between the cubic rocksalt phase and the spinel phase. In the cubic rocksalt phase, all the octahedral voids are filled with cations whereas in cubic spinel half of the octahedral voids are filled with cations. In case of hexagonal Fe_2O_3 $2/3^{rd}$ of the available octahedral voids are filled with cations. Their structural relationship will be discussed in detail in the subsequent sections.

It has been widely reported in literature that systematic replacement of ions for a ceramic crystal or atoms for a metallic crystal may lead to the formation of single phase multicomponent solid solution/intermetallic/compound-based materials [20, 22-23, 27-28]. However, systematic replacement should be such that the multicomponent materials become equimolar or almost equimolar. In the present work, all the precursor oxides with cubic rocksalt structure were put together in equimolar proportions with an expectation that they will form single phase solid solution through systematic replacement. Contrary to the expectation, it has been observed that ternary equimolar (CoMgNi)-oxide formed single phase solid solution after sintering and quenching, where under similar processing condition quaternary equimolar (CaCoMgNi)-oxide formed two cubic solid solution phases with rocksalt structure and with two different lattice parameters. One of the solid solution

phases is based on CaO and other one is based on (CoMgNi)-oxide. It may be inferred that Ca^{2+} cations were not completely accepted in the isostructural lattice of the solid solution phase of (CoMgNi)-oxide. Upon addition of Fe^{2+}/Fe^{3+} ions, additional phases with rhombohedral/hexagonal structure and cubic spinel phase are also observed. The cation radii of Ca^{2+}, Co^{2+}, Mg^{2+}, Ni^{2+} and Fe^{2+} are ~ 1 Å, 0.75 Å, 0.72 Å, 0.69 Å and 0.78 Å respectively [24-25]. The cation radii are reported based on their 6-fold coordination environment. It is evident from the cation radii that except for Ca^{2+}, all other cation radii are within ~12% difference. Equimolar addition of CoO with MgO or NiO leads to the partial replacement of cations in the crystal lattice with rocksalt structure and their cation radii being close to one another introduction of micro strain in the lattice is not enough to frustrate and destabilise the original crystal lattice. However, upon addition of CaO, due to the large difference in cation radii of Ca^{2+} ion with the remaining ions, the original rocksalt lattice is strained and it rejects most of the Ca^{2+} ions leading to the formation of another solid solution phase with rocksalt structure but with different lattice parameter. Introduction of lattice strain to frustrate/destabilise a crystal has been reported in metallic systems also and its manifestation in other extreme is the formation of metallic glasses [29-31]. In multicomponent or high entropy materials even though single-phase solid solution or compounds with five or more elements have been reported, their stability is still under investigation due to the presence of strain apart from other thermodynamic factors. It has been reported in multicomponent metallic alloys that composition migration takes place upon ageing [32]. In CoFeGaMnZn multicomponent oxide compositional phase separation has been reported leading to the formation of chessboard-like microstructure [33-34]. The compositional segregation is quite evident in the present study also. As observed from the SEM-XEDS maps (Figure 3.4), in the quinary (CaCoFeMgNi)-oxide, two distinct regions one rich in Ca and Fe ions and other rich in Co, Mg and Ni ions are present. Two different

solid solution phases with rocksalt structures but with different lattice parameters are observed in two compositionally segregated regions. In the Ca and Fe ion rich regions additional ordered hexagonal/rhombohedral phase and spinel phase are observed.

A quick look at the binary phase diagrams of different binary combinations of the quinary oxide under study reveals that many of the phase diagrams are isomorphous, quite a few of them show solid solutioning along with binary invariant reactions. None of them show any immiscibility. However, in the quinary oxide clear composition segregation is observed. This clearly indicates that ternary, quaternary and quinary interactions should also be taken into account in order to predict phase formation and its stability in multicomponent oxides. It has been reported in earlier literature that similar cation radii at a specific oxidation state and coordination environment, presence of immiscibility in at least one pair of components and non-isostructuralism in at least one component are the essential criteria for the formation of single-phase solid solution in multicomponent materials [14, 23]. The quinary oxide studied in the present work does not meet any of the criteria. However, the experimental validation of the postulates should be investigated further. It has also been reported that isostructuralism [23] would anyway promote the formation of single-phase solid solution which is proved to be not valid for the quinary oxide studied in the present work.

3.4.2. Strain minimization and oriented intergrowth of phases

Quinary (CaCoFeMgNi)-oxide upon sintering and quenching forms two chemically segregated regions comprising of mainly two solid solution phases with rocksalt structure along with a spinel phase and an ordered hexagonal phase. The electron diffraction patterns from the same solid solution phase after 10 h of sintering at 1523 K followed by quenching shows well defined diffraction spots (Figure 3.6(a-d)). However, in the bright field image mottled contrast typical of accumulated strain fields are observed. The structure of the same

phase remains to be cubic rocksalt with similar lattice parameter after sintering for 100 h followed by quenching. However, in the electron diffraction patterns and in the bright field images some new features are observed (Figure 3.6 (e-h)). In the diffraction patterns the spots are transformed into arcs with modulation of intensities and in the bright field images fringe contrast (marked by arrows) is observed. When the modulated intensity maxima in the diffraction patterns are connected geometrically, several symmetry shapes corresponding to the cubic zone axis, however, rotated with respect to one another are observed. It clearly indicates that there are domains with cubic crystal structures, which are rotated with respect to one another through a very small angle. The presence of arcs in both the diffraction patterns (Figure 3.6f and Figure 3.6h) confirms that the cubic domains are having in-plane and out-of-plane rotation with respect to one another. A schematic diagram of such rotated cubic domains in 3D is given in Figure 3.9a. It is inferred from the diffraction patterns and from the schematic diagram that during long time sintering, in the cubic solid solution phase of (CoMgNi)-oxide, cubic domains are formed and they are rotated with respect to one another. This observation pertains to the tendency of the solid solution phase to minimize it lattice and interface strain during the long-time sintering. During long-time sintering, in the original solid solution phase of (CoMgNi)-oxide composition modulation develops that helps in reducing the lattice strain by preferentially enriching one domain by one kind of ion. However, in this process, lattice parameter of each domain also changes, even though negligibly. The local change in lattice parameter manifests itself as interfacial strain between different domains. In order to minimize the interfacial strain, the compositionally modulated domains rotate with respect to one another. Each of the compositionally modulated domains are represented by different colours in the schematic diagram in Figure 3.9a. Their rotation in order to reduce the interfacial strain is also observed in the schematic.

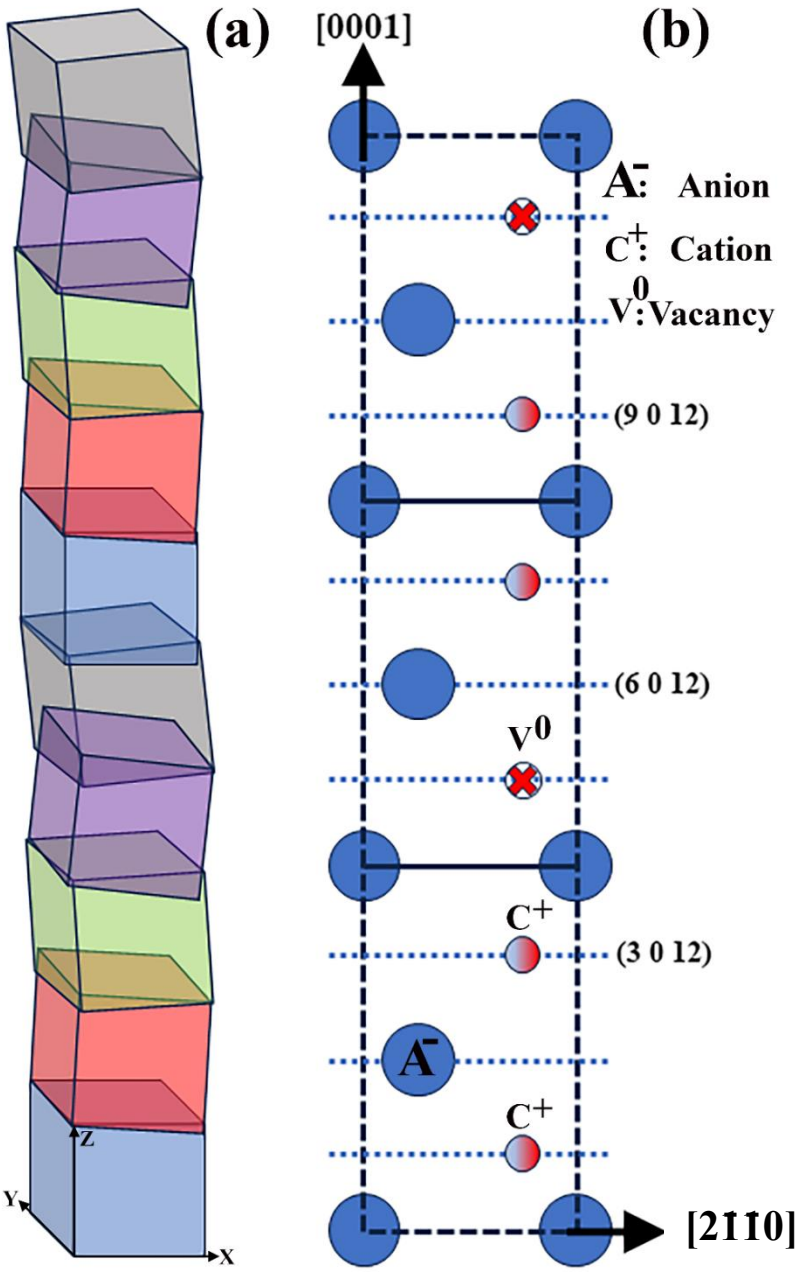

Figure 3.9: (a) Schematic representation of the mutually rotated domains in the intergrown helical arrangement with cubic rocksalt structure stacked along [001] direction. Possible composition modulation in each domain is marked with different colours. (b) [2$\bar{1}\bar{1}$0] orthographic projection of the hexagonal phase with 2/3rd octahedral voids filled up. Cation ordering with vacancies along [0001] is depicted.

Presence of such domains leads to the formation of fringe contrast within the mottled regions in the bright field images (marked with arrows, Figure 3.6e and Figure 3.6g). The width of the fringes may be directly correlated with the size of the compositionally

modulated domains. It has been reported theoretically that such kind of helical structures may form in oxides [35-36]. However, experimental evidence of such rotated helical structures in multicomponent oxide has not been reported before. In the Ca and Fe ion rich regions of the quinary oxide, after sintering at 1523 K for different lengths of time followed by quenching, solid solution phase with cubic rocksalt structure with ~4.78 Å lattice parameter, a spinel phase with ~8.41 Å lattice parameter and a hexagonal phase with a ~2.94 Å, c ~5.28 Å lattice parameter are observed. It is evident from the electron diffraction patterns from these phases after 10 h and 100 h of sintering that the phases grow with a very strong orientation relationship (Figure 3.7a-b). After 10 h of sintering, the diffraction spots (Figure 3.7a) are relatively smeared out, whereas the same diffraction spots become quite sharply defined after 100 h of sintering (Figure 3.7b). This observation clearly indicates that there is no change in orientation relationship among the phases, however, enhancement in sharpness of the diffraction spots may be related to the reduction in strain in the phases. Several orientationally related phases may be indexed from the diffraction patterns (Figure 3.7a-b). They are marked with different colours. The d-spacings are marked in Figure 6a and corresponding reciprocal vectors are marked in Figure 3.7b. From the z = $[2\bar{1}\bar{1}0]$ zone axis pattern of the hexagonal phase, superlattice reflections at 1/2[0002] and 3/2[0002] are observed. This clearly indicates ordering in the hexagonal phase along [0002] and the positions of the superlattice reflections ascertains that the original hexagonal lattice is tripled along [0002] direction due to ordering. The orthographic projection of the hexagonal lattice along $[2\bar{1}\bar{1}0]$ direction is given in Figure 3.9b. It is observed that 2/3rd of the octahedral voids are filled with cations and there is an ordering between the cations and the vacancies, which leads to the origination of the superlattice reflections at 1/2[0002] and 3/2[0002]. Partial occupancy of the tetrahedral voids will also lead to ordering, however, in that case the position of the superlattice reflections will be different. Cation and vacancy

ordering along [0002] direction also makes sure maximum possible separation between the cations, which in turn reduces the energy of the crystal. Development of this order in this crystal may be seen as an attempt by the crystal to reduce its energy by maximizing the separation between the similarly charged cations.

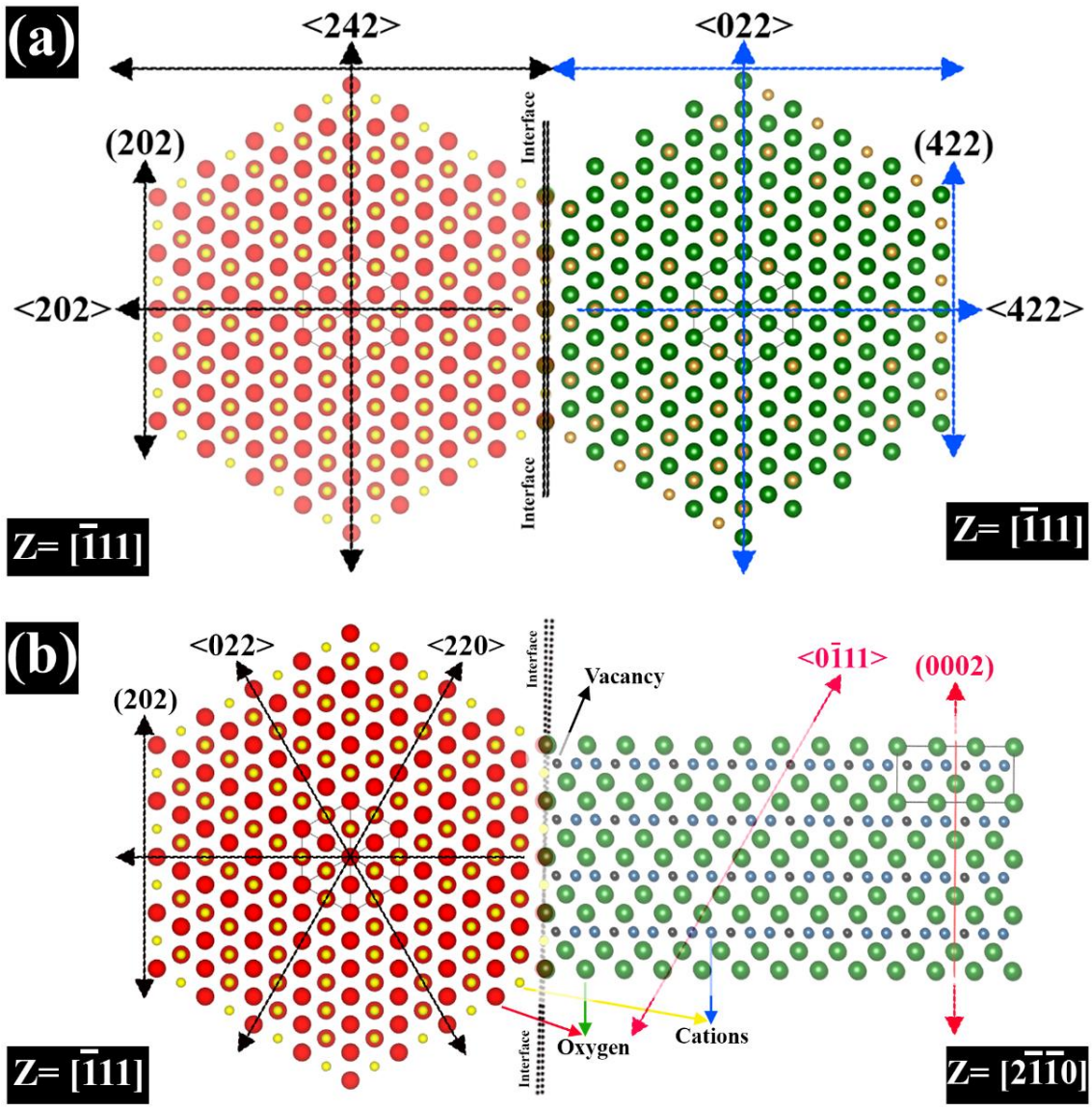

Figure 3.10: (a) Schematic (202) || (422) interface between cubic rocksalt and cubic spinel phase. The interface is coherent. (b) schematic representation of (202) || (0002) interface between the cubic rocksalt phase with the hexagonal phase. The interface in semicoherent with quite minimal incoherency strain. The schematic diagrams are developed from the experimentally observed orientation relationships and the calculated crystallographic data from the diffraction patterns.

It is worth mentioning that existence of such charged cation pairs separated by vacancies may lead to the formation of dipoles [25], which may originate novel properties in such crystals with several cations in the lattice. It is also to be noted that a hexagonal/rhombohedral phase was identified from the x-ray diffraction pattern of this sample (Figure 3.1-5C), which was pointed out to be correlated with hexagonal/rhombohedral Fe_2O_3 phase. It is now evident that the hexagonal phase obtained in the Ca and Fe ion rich regions is indeed a chemical and structural derivative of hexagonal/rhombohedral Fe_2O_3 phase. In both the diffraction patterns in Figure 3.7(a-b), a strong orientation relationship is observed between the cubic solid solution phase with rocksalt structure, cubic spinel phase and the hexagonal phase. In the cubic solid solution phase with rocksalt structure, superlattice reflections at 1/3[220] and 2/3[220] reciprocal lattice vectors are observed. It necessarily means that ordering takes place along <220> directions of the rocksalt phase that triplicates the cubic lattice. The orthographic projection of the solid solution phase with rocksalt structure (Figure 3.10a) along [111] shows that cation order takes place along <220> directions. The cubic spinel phase is oriented with the rocksalt phase such that $[\bar{1}11]_{RS} \parallel [\bar{1}11]_S$ and $(220)_{RS} \parallel (2\bar{2}4)_S$ (Rocksalt phase is represented as 'RS' and spinel phase is represented as 'S'), which necessarily means that the spinel phase is having 30^o in-plane rotation with respect to the rocksalt phase. However, ordering in the spinel phase could not be ascertained. The interface diagram for the cubic rocksalt phase and the spinel phase is shown in Figure 3.10a. The interface is absolutely coherent. This orientation relationship develops in order to minimize the strain energy of the interface. Similar coherent interfaces have been observed between rocksalt and spinel phases before. It is worth mentioning that rocksalt phase might undergo rhombohedral distortion and still may remain coherent with the spinel phase. In the present study, no definite proof for rhombohedral distortion of the rocksalt phase has been observed [37].

Similar orientation relationship is observed between the cubic rocksalt phase and the hexagonal phase. As stated before, the orientation relationship is $[2\bar{1}\bar{1}0]_H \parallel [\bar{1}11]_{RS}$ and $(0002)_H \parallel (\bar{2}0\bar{2})_{RS}$; $[2\bar{1}\bar{1}0]_H \parallel [\bar{1}11]_S$ and $(0002)_H \parallel (\bar{4}\bar{2}\bar{2})_S$ (Hexagonal phase is represented as 'H'). From the interface diagram (Figure 3.10b), it is evident that the interface between cubic rocksalt and the hexagonal phase is semi-coherent. Here again, the tendency of the system to reduce its interface energy is quite evident that leads to oriented intergrowth. Similar, orientation relationship is observed between the cubic spinel phase and the hexagonal phase. The orientation relationship has been stated before. The interface structure is quite similar to the interface between cubic rocksalt phase and the hexagonal phase. It is semi-coherent in nature. In this interface structure also, the tendency of system to reduce its interface energy is strongly evident.

3.4.3. Free energy stabilization through internal energy, strain energy and configurational entropy

Energetics, enthalpy and configurational entropy of multicomponent materials has been discussed since the discovery of metastable materials [38-39]. During rapid solidification or mechanical alloying, formation of metastable phases, extension of solid solubility, bulk metallic glasses (BMGs) or bulk amorphous alloys (BAAs) etc. were reported several decades back [30-31]. Even though BMGs are multicomponent in nature, they are most often not equimolar. They may be treated as dilute multicomponent alloys. Since the discovery of BMGs, the science of glass formation and its alloy design strategies have mostly progressed through empiricism. Presence of more than three elements with widely different atomic sizes frustrates the crystal lattice due to the introduction of unusually large amount of micro-strain in the lattice, that ultimately leads to the glass formation. The structural frustration of the crystal lattice due to presence of micro-strain may be considered as inverse Hume-Rothery rule of solid solution formation. High negative enthalpy of

mixing among the constituent elements favours glass formation. It is famously known as Inoue's criteria of BMG formation. BMG forming alloys discovered so far mostly can be explained in the light of Inoue's criteria of BMG formation.

Multicomponent high entropy alloys (HEAs), which are of recent vintage, have also been dealt with empiricism [10-11]. Presence of multiple elemental species in the same crystal lattice increases the configurational entropy of the system so high that the HEAs are always stabilized by entropy. However, over last two decades, high entropy intermetallic phases have also been reported [27-28], where existence of order essentially will not allow the configurational entropy to be as high as a high entropy solid solution phase. Additionally, many of the HEAs have shown metastability in the temperature-composition space, which necessarily makes the high entropy stabilization concept questionable [32]. Currently it is also believed that the term HEA is a misnomer, rather it should be termed as multi-principal element alloys (MPEAs) or complex concentrated alloys (CCAs) [9, 20].

High entropy oxides (HEOs) or high entropy ceramics (HECs) is of latest vintage and in these materials, the configurational entropy is calculated separately for the cation and anion sublattice before they are added together in order to assess the total entropy [18, 22]. In HEOs/HECs also order may exist, which will not allow the configurational entropy to be as high as a random multicomponent solid solution. However, the stabilization of HEOs/HECs is believed to be entropy driven, i. e. the total entropy of the cation and anion sublattice is so high that the free energy of the phase is always dominated by the high negative value of TS (T: Temperature, S: configurational entropy) term. This has given birth to the term entropy stabilized materials (ESMs) for this class of oxides or ceramics [40]. In the present study, a strong and well-defined tendency of the system to minimize its strain energy has been observed. Ternary (CoMgNi)-oxide, after sintering leads to the formation of single solid solution phase with rocksalt structure. However, upon addition of CaO, the

quaternary (CaCoMgNi)-oxide, after sintering forms two solid solution phases with rocksalt structure, however, with two different lattice parameters. This observation may be explained in the light of their difference in atomic radii, introduction of micro-strain in the lattice and the tendency of the system to reduce its micro-strain further by compositionally separating into two different phases. In quinary equimolar (CaCoFeMgNi)-oxide, after sintering, two compositionally segregated regions are observed in the microstructure. In addition to that, compositionally modulated domains with in-plane and out-of-plane rotation, leading to a helical structure is observed after long time sintering in the (CoMgNi)-oxide solid solution phase. In the Ca and Fe ions rich regions, oriented intergrowth of the solid solution phase, spinel phase and the hexagonal phase is observed. The interface diagram of the three inter grown phases with strong orientation relationship shows that the interfaces are coherent or semi-coherent in nature. In addition, APBs in the hexagonal phase further points towards the tendency of the system to minimize its strain energy, often at the cost of a finite reduction in configurational entropy.

Free energy change (ΔG) may be represented as $\Delta G = \Delta H - T\Delta S$ at constant temperature and pressure, where the symbols have their usual meaning. Again, $\Delta H = \Delta U + P\Delta V$, where $P\Delta V$ represents mechanical energy involved in the process. In condense matter systems, the numerical value of $P\Delta V$ at constant P will not be very high. However, it relates to the strain energy and its physical manifestations are micro strain in the lattice, around the defects and interfaces. The expression of free energy may be written as $\Delta G = \Delta U + P\Delta V - T\Delta S$. Configurational entropy (ΔS) being always positive, the term $T\Delta S$ is always positive. The mechanical energy term $P\Delta V$ is always positive. The internal energy (ΔU) is an intrinsic property of the system. Now the trade-off between the mechanical strain energy $P\Delta V$ and the entropy term $T\Delta S$ will determine the stability of a system in the free energy landscape. In case of the multicomponent (CaCoFeMgNi)-oxide single solid solution phase

formation would definitely increase the configurational entropy, however, the positive contribution from the strain energy component would nullify the energetic advantage in the free energy landscape. So, the multicomponent oxide compositionally segregates in order to strike a trade-off between entropy and strain energy. Further, oriented growth of solid solution phase, spinel phase and hexagonal phase with coherent and semi-coherent interfaces reduces the positive contribution of the strain energy in order to achieve further advantage in the free energy landscape. The formation of compositionally modulated helical structures in the (CoMgNi)-oxide solid solution phase after long time sintering proves that within the helical structures the distribution of the cations is still macroscopically random, hence configurational entropy remains high. However, compositional modulation and the relative rotation among the domains reduces the strain energy. Through this arrangement, the system is able to maximize the negative contribution of the entropy term, however, in turn it reduces the positive contribution of the strain energy term. Thus, it is able to maximize its energetic advantage in terms of free energy. It is clearly seen that the stability of this multicomponent oxide is a trade-off between entropy and strain energy. Widely believed entropy stabilization in this class of materials should be thoroughly reinvestigated in the light of the possible trade-off between entropy and strain energy. It should be noted that in this qualitative explanation only configurational entropy has been considered, other entropy contribution should also be taken into account in order to arrive at a more accurate analysis of the stability of phases in this class of materials.

3.5. Conclusions

I. Two chemically segregated regions; one enriched in Ca and Fe ions and another in Co, Mg, Ni ions is produced in the microstructure of quinary equimolar multicomponent (CaCoFeMgNi)-oxide upon sintering at 1523 K for different lengths of time followed by water quenching. In the Co, Mg, Ni rich region ternary

solid solution of (CoMgNi)-oxide with cubic rocksalt structure with ~4.21 Å lattice parameter is observed. In the Ca, Fe ion rich regions, three phases namely; CaO based solid solution phase with cubic rocksalt structure with ~4.78 Å lattice parameter, a cubic spinel phase with ~8.41 Å lattice parameter and a hexagonal phase with a = 2.94 Å and c = 5.28 Å lattice parameter are observed. Ordering of cations and vacancy takes place in the octahedral voids of the hexagonal phase.

II. Ternary (CoMgNi)-oxide and quaternary (CaCoMgNi)-oxide, derivative of the original quinary equimolar multicomponent (CaCoFeMgNi)-oxide, after sintering at 1523 K for different lengths of time followed by quenching produces the same solid solution phases with cubic rocksalt structure as obtained in the quinary equimolar oxide. Intermediate mechanical alloying before sintering does not alter the phase and microstructure evolution in the quinary and its ternary and quaternary derivative oxides.

III. In the (CoMgNi)-oxide solid solution phase after sintering the quinary oxide for 100 h at 1523 K followed by quenching, mutually rotated cubic domains with rocksalt structure is observed. Chemical modulation and mutual rotation among the domains leading to helical structure is likely to reduce lattice and interface strain arising out of different cation radii and incoherency at the interfaces.

IV. In the Ca and Fe ion rich regions in the quinary oxide, after sintering at 1523 K for different lengths of time, highly oriented growth of the solid solution phase with rocksalt structure, cubic spinel phase and hexagonal phase is observed. The interfaces of these phases are either coherent or semi-coherent. It is due to the tendency of the quinary oxide to reduce its strain energy of the interfaces.

V. The orientation relationship of the cubic solid solution phase with rocksalt structure with the cubic spinel phase and with the hexagonal phase are $[\bar{1}11]_{RS} \parallel [\bar{1}11]_S$ and $(220)_{RS} \parallel (2\bar{2}4)_S$; $[2\bar{1}\bar{1}0]_H \parallel [\bar{1}11]_{RS}$ and $(0002)_H \parallel (\bar{2}02)_{RS}$; and $[2\bar{1}\bar{1}0]_H \parallel [\bar{1}11]_S$ and $(0002)_H \parallel (\bar{4}\bar{2}\bar{2})_S$ (RS: Rocksalt, S: Spinel; H: Hexagonal phase).

VI. Extensive compound deformation twins with $s = (2\bar{1}\bar{1}0)$, $K_1 = (0002)$, $\eta_1 = [0\bar{1}10]$, $K_2 = [10\bar{1}0]$ and $\eta_2 = [01\bar{1}1]$ as twin variants are observed along with anti-phase boundaries (APBs) in the hexagonal phase. Ordering and twinning in the hexagonal phase takes place in a bid to relax its lattice strain.

VII. Configurational entropy is not the sole stabilizing factor in the quinary oxide. It is a trade-off between the configurational entropy and the strain energy that stabilises the phases by minimizing its free energy.

3.6. Reference

1. Z. Lun, B. Ouyang, D. H. Kwon, Y. Ha, E. E. Foley, T. Y. Huang, Z. Cai, H. Kim, M. Balasubramanian, Y. Sun, J. Huang, Y. Tian, H. Kim, B. D. McCloskey, W. Yang, R. J. Clement, H. Ji, G. Ceder, Cation-disordered rocksalt-type high-entropy cathodes for Li-ion batteries, Nature Mater., 2021, Vol. 20, 214-221.
2. A. Sarkar, Q. Wang, A. Schiele, M. R. Chellali, S. S. Bhattacharya, D. Wang, T. Brezesinski, H. Hahn, L. Velasco, B. Breitung, High-entropy oxides: fundamental aspects and electrochemical properties, Adv. Mater., 2019, 1806236 (9 pages).
3. C. Oses, C. Toher, S. Curtarolo, High-entropy ceramics, Nature Rev. Mater., 2020, Vol. 5, 295-309.

4. Y. Gu, A. Bao, X. Wang, Y. Chen, L. Dong, X. Liu, H. Pan, Y. Li, X. Qi, Engineering the oxygen vacancies of rocksalt-type high-entropy oxides for enhanced electrocatalysis, Nanoscale, 2022, Vol. 14, 515-524.
5. M. P. Jimenez-Segura, T. Takayama, D. Berardan, A. Hoser, M. Reehuis, H. Takagi, N. Dragoe, Long-range magnetic ordering in rocksalt-type high-entropy oxide, Appl. Phys. Lett., 2019, Vol. 114, 122401 (5 pages).
6. B. L. Musico, D. Gilbert, T. Z. Ward, K. Page, E. George, J. Yan, D. Mandrus, V. Keppens, The emergent field of high entropy oxides: design, prospect, challenges and opportunities for tailoring material properties, APL Mater., 2020, Vol. 8, 040912 (16 pages)
7. H. Jia, M. Horton, Y. Wang, S. Zhang, K. A. Persson, S. Meng, M. Liu, Persona of transition metal ions in solids: a statistical learning on local structures of transition metal oxides, Adv. Sci., 2022, 220756 (9 pages).
8. D. Berardan, S. Franger, A. K. Meena, N. Dragoe, Room temperature lithium superionic conductivity in high entropy oxide, J. Mater. Chem. A, 2016, Vol. 4, 9536-9541.
9. W. Steurer, Single-phase high entropy alloys: a critical update, Mater. Char., 2020, Vol. 162, 110179 (17 pages).
10. B. Cantor, I. T. H. Chang, P. Knight, A. J. B. Vincent, Microstructural development in equiatomic multicomponent alloys, Mater. Sci. Eng. A, 2004, Vol. 375-377, 213-218.
11. J. W. Yeh, S. K. Chen, S. J. Lin, J. Y. Gan, T. S. Chin, T. T. Shun, C. H. Tsau, S. Y. Chang, Nanostructured high-entropy alloys with multiple principal elements: novel alloy design concepts and outcomes, Adv. Eng. Mater., 2004, Vol. 6 (5), 299-303.

12. K. C. Pitike, K. C. Santosh, M. Eisenbach, C. A. Bridges, V. R. Cooper, Predicting the phase stability of multicomponent high-entropy compounds, Chem. Mater., 2020, Vol. 32, 7507-7515.
13. M. Fracchia, M. Coduri, M. Manzoli, P. Ghigna, U. A. Tamburini, Is configurational entropy the main stabilizing term in rock-salt $Mg_{0.2}Co_{0.2}Ni_{0.2}Cu_{0.2}Zn_{0.2}O$ high entropy oxide?, Nature Comm., 2022, Vol. 13, 2977 (4 pages).
14. C. M. Rost, E. Sachet, T. Borman, A. Moballegh, E. C. Dickey, D. Hou, J. L. Jones, S. Curtarolo, J. P. Maria, Entropy-stabilized oxide, Nature Comm., 2015, Vol. 6, 8485 (8 pages).
15. Y. Zhang, T. T. Zuo, Z. Tang, M. C. Gao. K. A. Dahmen, P.K.Liaw, Z. P. Lu, Microstructure and properties of high-entropy alloys, Prog. Mater. Sci., 2014, Vol. 61, 1-93.
16. G. Anand, A. P. Wynn, C. M. Handley, C. L. Freeman, Phase stability and distortion in high entropy oxides, Acta Mater., 2018, Vol. 146, 119-125.
17. D. Ma, B. Grabowski, F. Kormann, J. Neugebauer, D. Raabe, *Ab initio* thermodynamics of CoCrFeMnNi high entropy alloy: importance of entropy contributions beyond the configurational one, Acta Mater., 2015, Vol. 100, 90-97.
18. S. J. McCormack, A. Navrotsky, Thermodynamics of high entropy oxides, Acta Mater. 2021, Vol. 202, 1-21.
19. O. N. Senkov, J. D. Miller, D. B. Miracle, C. Woodward, Accelerated exploration of multi-principal element alloys with solid solution phases, Nature Comm., 2015, Vol. 6, 6529 (10 pages).
20. D. B. Miracle, O. N. Senkov, A critical review of high entropy alloys and related concepts, Acta Mater., 2017, Vol. 122, 448-511.

21. D. Berardan, A. K. Meena, S. Franger, C. Herrero, N. Dragoe, Controlled Jahn-Teller distortion in (MgCoNiCuZn)O-based high entropy oxides, J. Alloys Comp., 2017, Vol. 7, 693-700.
22. C. M. Rost, Z. Rak, D. W. Brenner, J. P. Maria, Local structure of the $Mg_xNi_xCo_xCu_xZn_xO$ (x = 0.2) entropy stabilized oxide: EXAFS study, J. Am. Ceram. Soc., 2017, Vol. 00, 1-7.
23. A. Sarkar, R. Djenadic, N. J. Usharani, K. P. Sanghvi, V. S. K. Chakravadhanula, A. S. Gandhi, H. Hahn, S. S. Bhattacharya, Nanocrystalline multicomponent entropy stabilized transition metal oxides, J. Eu. Ceram. Soc., 2017, Vol. 37, 747-754.
24. C. B. Carter, M. G. Norton, Ceramic Materials Science and Engineering, Spinger, 2nd Edition, New York 2013
25. Y. M. Chiang, D. P. Birnie, W. D. Kingery, Physical Ceramics: principles for ceramic science and engineering, Wiley Publication, 1997, USA.
26. J. Basu, R. Divakar, In-situ electron microscopy investigation of reduction-induced microstructural changes in NiO, Ceram. International, 2015, Vol. 41(10), 12658-12667.
27. N. Zhou, S. Jiang, T. Huang, M. Qin, T. Hu, J. Luo, Single-phase high-entropy intermetallic compounds (HEICs): bridging high-entropy alloys and ceramics, Sci. Bulletin, 2019, Vol. 64, 856-864.
28. T. H. Chou, J. C. Huang, C. H. Yang, S. K. Lin, T. G. Nieh, Consideration of kinetics on intermetallics formation in solid-solution high entropy alloys, Acta Mater., 2020, Vol. 195, 71-80.
29. J. Basu, S. Ranganathan, Glass-forming ability and stability of ternary Ni-early transition metal (Ti/Zr/Hf) alloys, Acta Mater. 2008, Vol. 56, 1899-1907.

30. A. Inoue, Stabilization of metallic supercooled liquid and bulk amorphous alloys, Acta Mater., 2000, Vol. 48, 279-306.
31. J. Basu, S. Ranganathan, Bulk metallic glasses: a new class of engineering materials, Sadhana, 2003, Vol. 28, 783-798.
32. V. Shivam, J. Basu, R. Manna, N. K. Mukhopadhyay, Local composition migration induced microstructural evolution and mechanical properties of non-equiatomic $Fe_{40}Cr_{25}Ni_{15}Al_{15}Co_5$ medium entropy alloy, Met. Mater. Trans. A, 2021, Vol. 52, 1777-1789.
33. A. S. Pal, A. K. L. Das, A. Singh, K. M. Knowles, Md. I. Ahmad, J. Basu, Evolution of self-assembled chessboard nanostructure spinel in a CoFeGaMnZn multicomponent oxide, Philos. Mag., 2022, Vol. 102(12), 1121-1135.
34. A. S. Pal, A. K. L. Das, K. Gururaj, M. Sadhasivam, K. M. Knowles, Md. I. Ahmad, K. G. Pradeep, J. Basu, Nanoarchitectonics of self-assembled chessboard-like structures by recurrent phase separation and coalescence of nano domains in CoFeMn oxide, Acta Mater., 2023, Vol. 242, 118423 (12 pages).
35. V. M. Talanov, V. B. Shirokov, Tilting structures in spinels, Acta Cryst., 2012, Vol. A68, 595-606.
36. B. G. Hyde, A. N. Bagshaw, S. Andersson, M. O'Keeffe, Some defect structures in crystalline solids, Annu. Rev. Mater. Sci., 1974, Vol. 4, 43-92.
37. A. Singh, S. Yasui, A. S. Pal, L. A. Bendersky, I. Takeuchi, R. K. Mandal, J. Basu, Structure and interfaces of compositionally graded $Li(Ni, Mn)_xO_y$ cathodes on (111) Nb-doped $SrTiO_3$, Philos. Mag., 2022, Vol. 102(16), 1547-1579.
38. P. Duwez, Metastable phases obtained by rapid quenching from the liquid state, Prog. Solid State Chem., 1967, Vol. 3, 377-400.

39. B. S. Murty, S. Ranganathan, Novel materials synthesis by mechanical alloying/milling, Int. Mater. Rev., 1998, Vol. 43, 101-141.
40. M. Brahlek, M. Gazda, V. Keppens, A. R. Mazza, S. J. McCormack, A. M. Gryn, B. Musico, K. Page, C. M. Rost, S. B. Sinnott, C. Toher, T. Z. Ward, A. Yamamoto, What is in a name: defining “high entropy” oxides, APL Mater. 2022, Vol. 10, 110902 (12 pages).

CHAPTER – 4

LOCAL COMPOSITION MODULATION AND ORIENTED INTER-GROWTH INDUCED STRAIN MINIMIZATION IN ENTROPY STABILIZED (CoCuMgNiZn) OXIDE

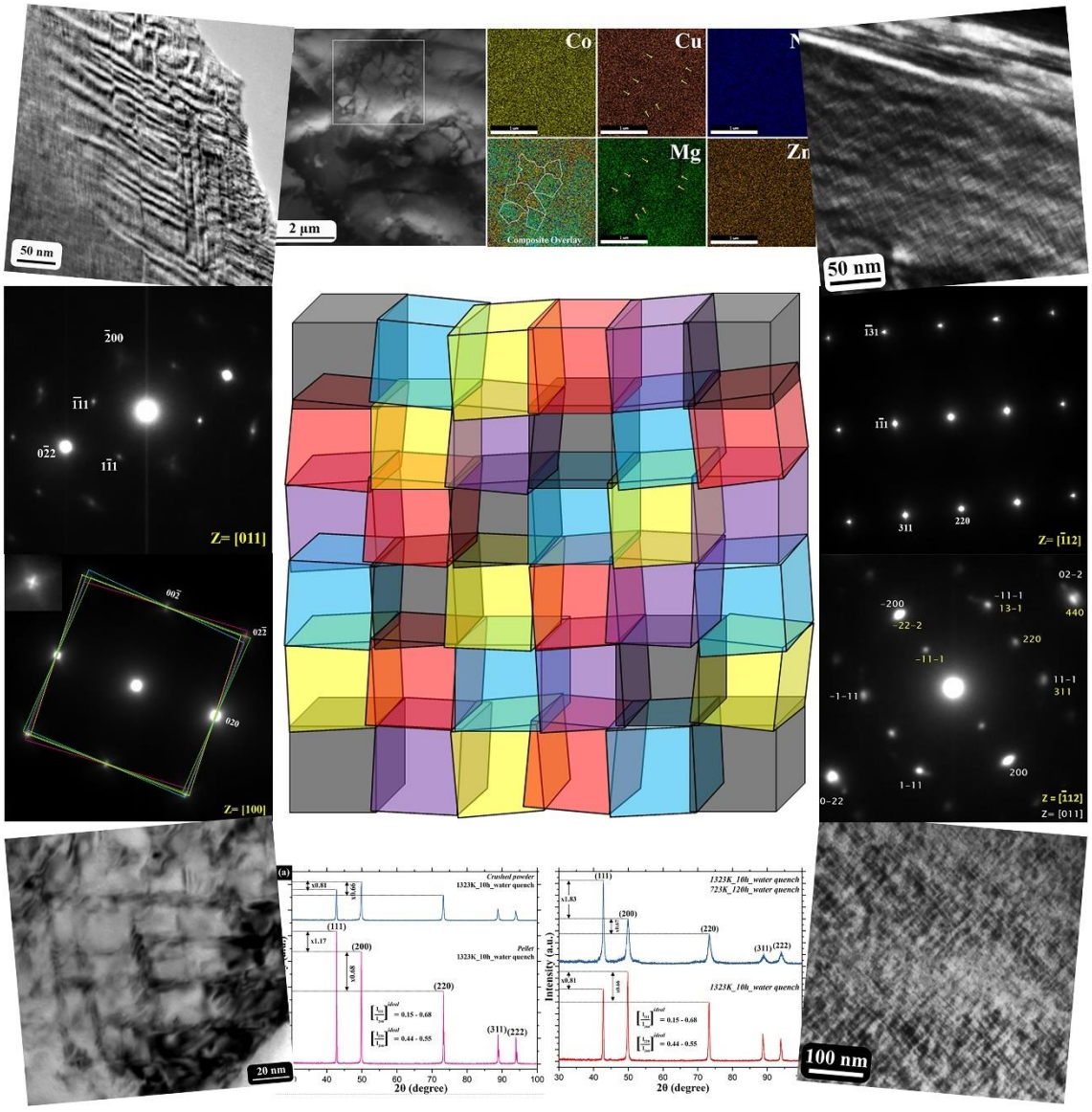

4.1. Introduction

High entropy materials/ceramics (HEMs/HECs) [1-2] have emerged over the last decade as a potential candidate for catalysis, electrochemical energy conversion and storage [3-7]. High entropy oxides (HEOs) [8-9] are one of the important members in the family of HEMs/HECs. They differ from high entropy alloys (HEAs) [10-11], as in case of HECs/HEOs, there are distinct sublattices for cations and anions [12-14]. The entropy of the materials may be made high either by the substitution of cations or anions or both in their respective sublattices in equimolar or near equimolar proportions [15]. As a result, the calculation of total entropy is also done separately for cation and anion sublattice for HEOs/HECs. It is also believed that little difference in the ionic sizes coupled with negative enthalpy of mixing and isostructuralism of most of the precursors are promoting factors for synthesis of stable, single-phase HEOs/HECs [16]. Presence of multiple ions in the cation or anion sublattice makes the configurational entropy so high that this class of materials are always stabilized by entropy, which has led to the derivation of their new name as entropy stabilized materials (ESMs) [12].

(CoCuMgNiZn) high entropy oxide is the first known ESO in this class, which is stabilized in a cubic rocksalt structure [12, 17]. A good volume of data has been reported on the synthesis and functional properties of this ESO [18-20]. However, its mechanism of entropic stabilization, distribution of cations, stability in the time-temperature space and tailoring of novel properties upon further substitution has received relatively less attention [13, 15, 21-22]. An atomistic picture that combines its structure, stability and properties is still missing.

The present work has been taken up to synthesize single-phase ESO in equimolar (CoCuMgNiZn) system and study its local structure, chemistry and stability in the time-temperature space so that the atomic scale mechanisms behind the evolution of novel

properties may be deciphered and tailored further. It is observed that the ESO forms a cubic rocksalt structure globally. However, there are modulated domains within the structure and there is a definite tendency of the ESO to minimize its volumetric, lattice and interfacial strain through the formation of tweeds, domains and inter-growth of structurally correlated phases, which is presented in the subsequent sections of the communication.

4.2. Materials & methods

Multicomponent, equimolar (CoCuMgNiZn) entropy stabilized oxide has been prepared through solid state synthesis route pertaining to the ease of materials handling and probability of success. High purity metal oxide; Co(II, III)O (>99.8 at%), CuO (>99.9 at%), MgO (>99.95 at%), NiO (>99.9 at%) and ZnO (>99.95 at%) were procured from either Sigma Aldrich or Alfa Aesar. Metal oxides in stoichiometric proportions were mixed thoroughly in a mortar and pestle. The mixed powder was compacted in a uniaxial hydraulic press with 4T load to form the green compacted pellets of ~12 mm diameter and ~4-5 mm thickness. The green compacted pellets were sintered in a high temperature tube furnace in air to obtain the entropy stabilized (CoCuMgNiZn) oxide. In order to maintain perfect stoichiometry and avoid contamination, a number of green compacted pellets were vertically stacked in a platinum crucible with the lid on. The sintered pellet from the center of the stack, in all the heat treatments, was taken for further studies. Four different heat treatment schedules for sintering the green compacted pellets to form the entropy stabilized (CoCuMgNiZn) oxide was followed. Those are; sintering at 1323 K for 10 h followed water quenching, sintering at 1323 K for 100 h followed by water quenching, sintering at 1323 K for 10 h followed by furnace cooling to room temperature at ~3 ^{o}C/min and sintering at 1323 K for 10 h followed by ageing at 723 K for 120 h and subsequent water quenching.

Phase evolution in the sintered samples in pellet and powder form were studied by x-ray diffraction (XRD) in a Malvern Panalytical Empyrean high-resolution x-ray diffractometer

with Cu-K_α (λ= 1.54 Å) and Co-K_α (λ= 1.79 Å) radiation. The diffractometer was operated at 40 kV operating voltage with 40 mA tube current. Prior to the x-ray diffraction experiments of the pellets, both sides of the pellet were polished in a conventional way. Microstructure and chemistry of the sintered pellets were studied in a FEI Quanta 200F scanning electron microscope (SEM) operated with an accelerating voltage of 30 kV. For SEM studies the sintered, aged and quenched pellets were metallographically polished and ultrasonicated in ethanol. X-ray energy dispersive spectroscopy (XEDS) mapping of the samples was done at the regions of interest in order to understand the distribution of the ions. The sintered, aged and quenched samples of the entropy stabilized (CoCuMgNiZn) oxide were studied in a FEI Tecnai G2 T20 transmission electron microscope (TEM) under 200 kV accelerating voltage. For TEM observation, the sintered, aged and quenched samples were cut into thin slices by using a low-speed diamond saw, then they were polished to a minimal thickness of ~100 μm, dimple ground to ~30 μm and then they were thinned to electron transparency by PIPS II Gatan ion mill.

The simulation of x-ray diffraction patterns was done by indigenously developed code and JEMS software was used for simulation of electron diffraction patterns. VESTA software was used for development of crystal structure models.

4.3. Results

X-ray diffraction (XRD) patterns with Co-K_α (λ= 1.79 Å) radiation from the (CoCuMgNiZn) entropy stabilized oxide (ESO) after sintering at 1323 K for 10 h followed by water quenching are given in Figure 4.1a. The XRD pattern (in pink) from the sintered quenched pellet shows sharp 111, 200, 220, 311 and 222 peaks corresponding to a rocksalt structure with *a~4.24 Å* lattice parameter. The sharp diffraction peaks are indicative of strain free grains with large grain size. In this diffraction pattern shouldering of the 220, 311 and 222 peaks can be observed. Shouldering of the peaks in an ESO with exactly similar composition has been observed before, which has been attributed to the diffraction by $K_{\alpha II}$ radiation of the target material [17]. However, it could be due to the introduction of tetragonality in the otherwise (CoCuMgNiZn) ESO with cubic rocksalt structure or local modulation in the d-spacings in the crystal. It has also been investigated with electron diffraction and will be discussed later in this communication. The XRD pattern (in blue) from the sintered, quenched (1323 K for 10 h) and powdered sample shows similar diffraction peaks with minor right shift, which can be indexed to a rocksalt phase with *a~4.23 Å* lattice parameter. In this sample, the diffraction peaks are quite sharp indicative of large strain free crystals in the microstructure. In this diffraction pattern also shouldering of the peaks at higher angle could be observed. In comparison to the diffraction pattern from the pellet (in pink), the diffraction peaks from the powder sample are relatively broad. Additionally, a reversal in the total integrated intensity of 111 and 200 peaks in the pellet and the powder sample is easily discerned. In the pellet (in pink), the total integrated intensity of the 111 peak is ~1.17 times of that of the 200 peak. However, the total integrated intensity of the 111 peak in the powder sample (in blue) is ~0.81 times of the 200 peak.

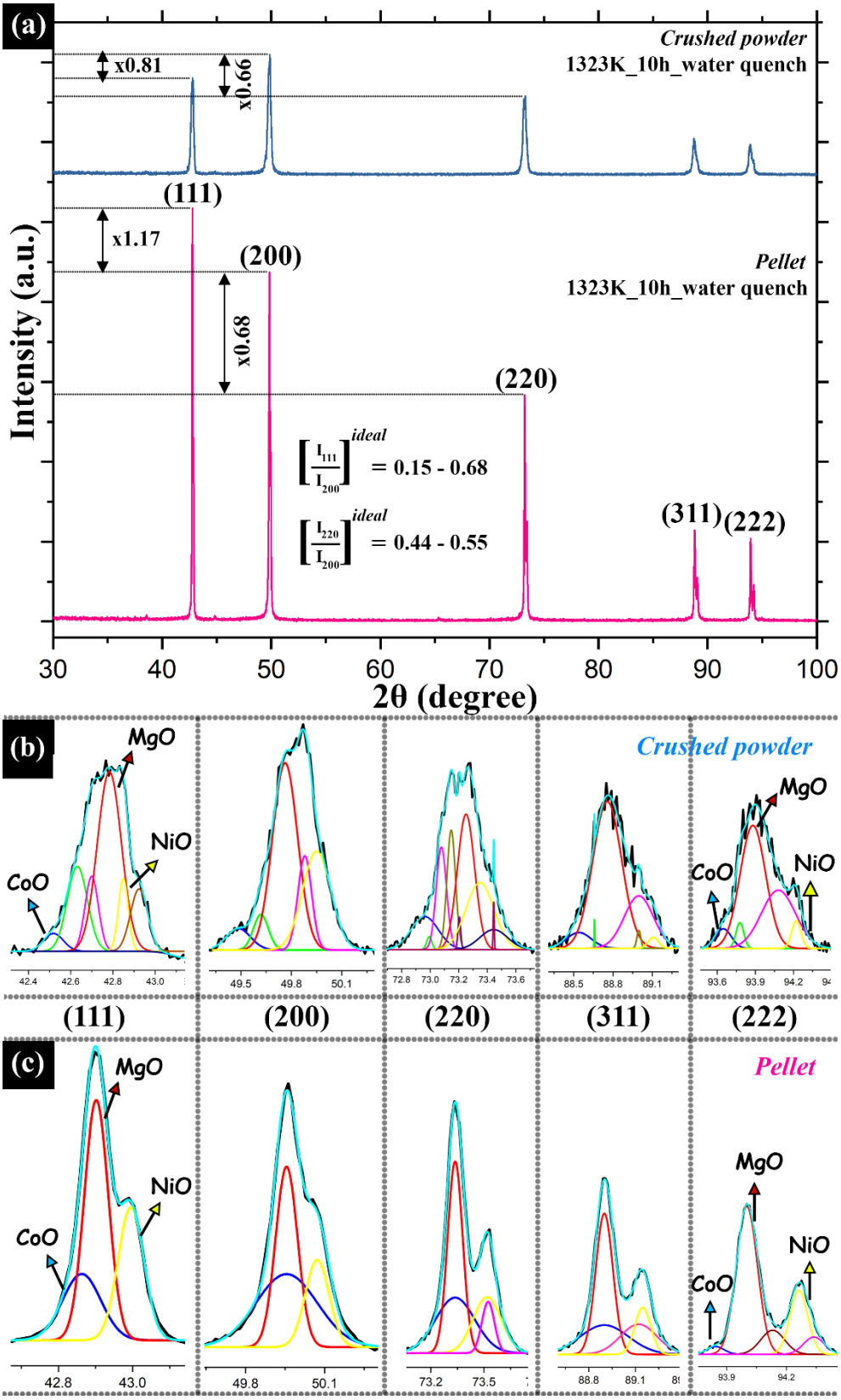

Figure 4.1: (a) X-ray diffraction (XRD) patterns of (CoCuMgNiZn) ESO after sintering at 1323 K for 10 h followed by water quenching. The diffraction pattern in pink is from the sintered and quenched pellet and the pattern in blue is from its crushed powder. (b) Deconvolution of the XRD peaks from the crushed powder and (c) deconvolution of the XRD peaks from the pellet. Deconvoluted peaks can be matched with CoO, MgO and NiO.

The ideal intensity ratio of 111 and 200 diffraction peak from a typical rocksalt structure should be ~0.15-0.68 (as obtained from simulation and reported JCPDS data cards), which is closely observed in the powder. In fact, it is worth mentioning that none of the intensity ratios in the diffraction pattern from the pellet and the powder match with the ideal intensity ratios for a cubic rocksalt structure. The reversal in intensity in case of the pellet may be attributed to the development of a weak surface texture. It is also reported that in this ESO, reversal of intensity may appear due to the distortion in the structure induced by Jahn-Teller distortion and processing history [23, 24]. The departure of the diffraction patterns from the ideal diffraction pattern of a cubic rocksalt structure is indicative of the presence finer structural modulations, which is worth probing further.

In order to probe the presence of finer structural details in the sintered and quenched (1323 K for 10 h) (CoCuMgNiZn) ESO, all the XRD peaks from the powder and the pellet have been deconvoluted (Figure 4.1(b-c)) and each of the deconvoluted peaks has been matched against individual oxide precursors used for the synthesis of the ESO. The XRD peaks from the powder sample (Figure 4.1b) are relatively broad with several discontinuities. All the diffraction peaks may be deconvoluted to several major and minor peaks with the left most one (blue), middle one (red) and right most one (yellow) matching with CoO, MgO and NiO respectively. Similar trend is observed in the XRD peaks from the pellet sample. The XRD peaks from the pellet may be deconvoluted (Figure 4.1c) to three major peaks; the left most (blue), middle (red) and right most (yellow) may be indexed with the corresponding d-spacings of CoO, MgO and NiO respectively. Deconvolution of the XRD peaks and its similarity with the corresponding d-spacings of the pure precursor oxides hints at local composition variation that may exist in this otherwise cubic rocksalt based ESO. It may further be inferred that local modulation of the structure, caused by local composition variation, is very much akin to the rocksalt structures of CoO, MgO and NiO.

Copper and zinc ions are incorporated into the local structure. Introduction of copper and zinc may further introduce distortion and Jahn-Teller effect, which is manifested by the presence of shouldering and non-ideal intensity distribution in the XRD pattern.

XRD patterns of the (CoCuMgNiZn) ESO pellet after sintering at 1323 K for 10 h followed by water quench, sintering at 1323 K for 100 h followed by water quench and

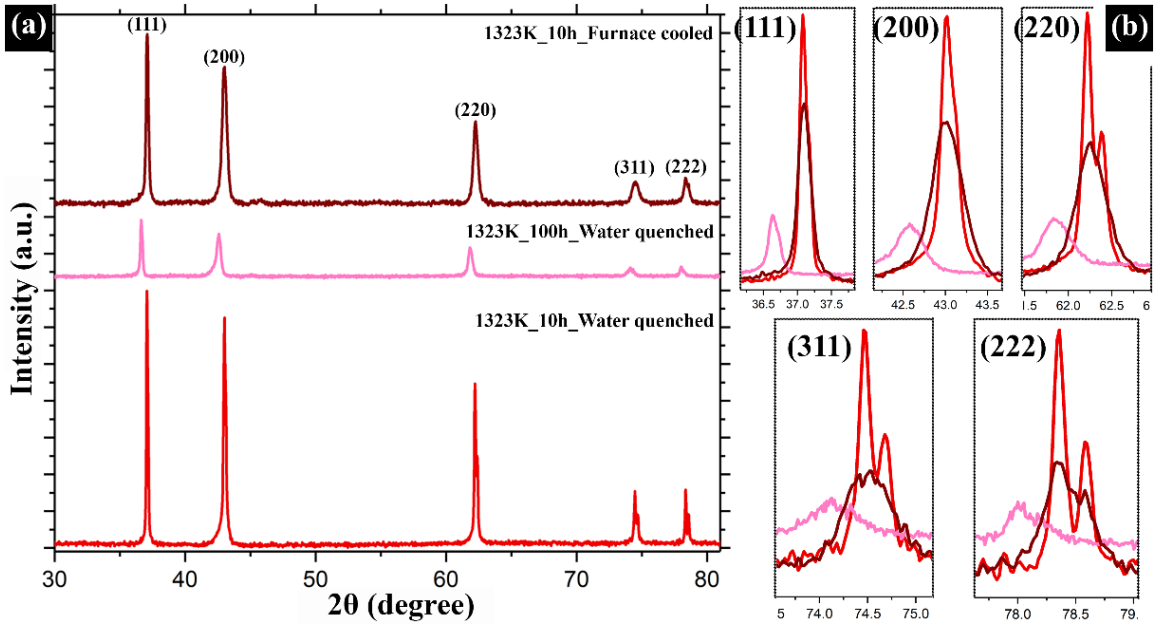

Figure 4.2: (a) X-ray diffraction patterns (XRD) of (CoCuMgNiZn) ESO pellet after sintering at 1323 K for 10 h followed by water quenching (red), after sintering at 1323 K for 100 h followed by water quenching (pink) and after sintering at 1323 K for 10 h followed by furnace cooling (brown). (b) Superimposition of XRD peaks after three different thermal treatments. Long h of exposure at high temperature leads to a systematic left shift coupled with broadening and reduction in total integrated intensity.

sintering at 1323 K for 10 h followed by furnace cooling at ~3°C/min are given in Figure 4.2a. The x-ray diffraction experiments were conducted by Cu-K_α radiation ($\lambda_{Cu\ K\alpha}$ = 1.54 Å). All the diffraction patterns may be indexed with cubic rocksalt structure with subtle differences. In the diffraction pattern from the pellet after sintering at 1323 K for 10 h sharp peaks with clear shouldering in the higher angle peaks could be observed. However, in the diffraction patterns, after sintering for 100 h followed by water quenching and sintering for 10 h followed by furnace cooling, shouldering is not clearly visible and the diffraction

peaks have broadened instead. Broadening of the diffraction peaks after longer h of sintering and after furnace cooling is counter-intuitive as longer h of exposure at high temperature should release the strain in the sample and corresponding grain growth should result in sharpening of the peaks. In order to rationalize this observation, the diffraction peaks after three heat treatment cycles are superimposed (Figure 4.2b). It is observed that for samples after sintering at 1323 K for 10 h the diffraction peaks (in red) are the most intense ones. After sintering at 1323 K for 10 h followed by furnace cooling there is no shift in peak position (in brown), however there is a broadening induced reduction in the peak intensity. This observation indicates that longer h of exposure at high temperature results in more variation in the d-spacings of the same crystal structure, which is intuitively indicative of a local fine scale composition modulation that is likely to induce a change in the structure parameters of the crystal. It will be probed further in the later sections of the communication. A clear left shift in the peak positions along with broadening induced reduction in total intensity of the peaks (in pink) is observed after sintering the ESO at 1323 K for 100 h. Broadening of the peaks with associated reduction in the total intensity may be explained by the local fine scale composition modulation induced structural changes leading to a wider variation in the d-spacings. However, the left shift of the peaks indicates an additional increase in the average cell parameter and the cell volume. Increase in average cell parameter and its volume may be directly correlated with reduction in the volumetric strain in the crystal as the increase in the crystal volume necessarily means increase in size of the octahedral voids and easier accommodation of the cations in there in an ideal rocksalt structure. It will be discussed further and will be associated with the stabilization of the ESO in later part of the communication.

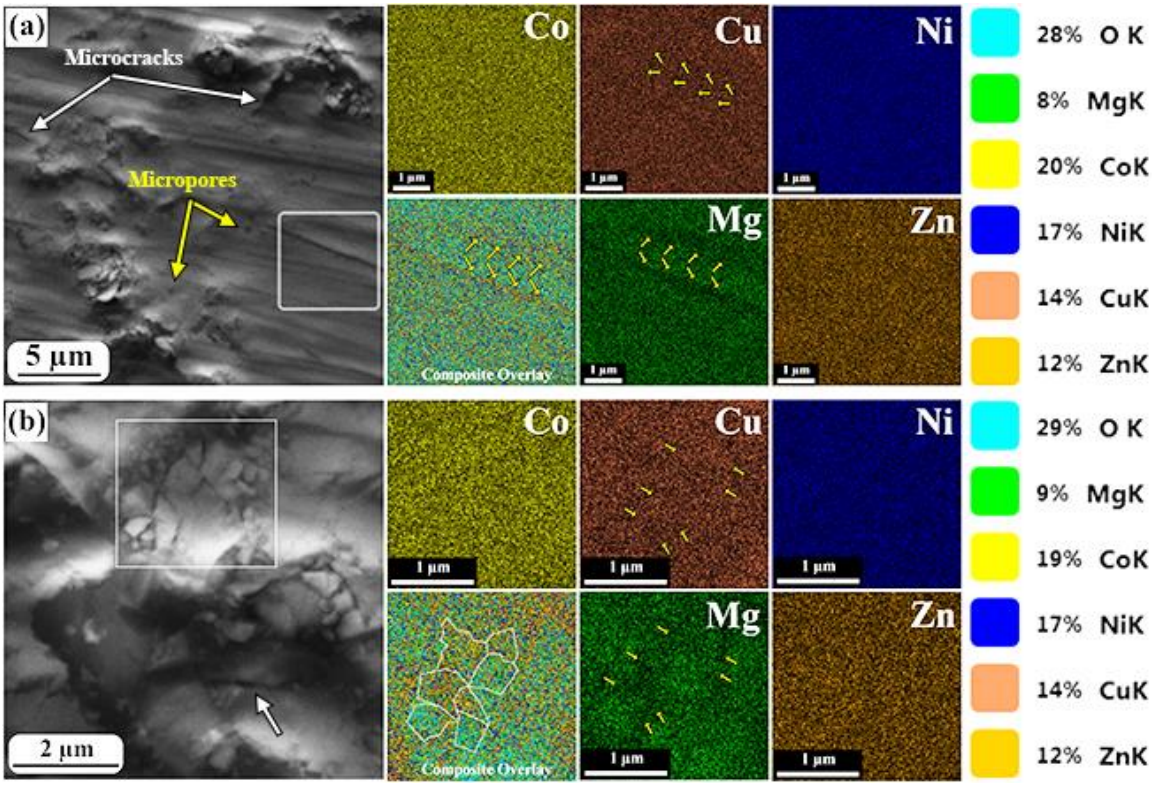

Figure 4.3: Scanning electron microscope (SEM) image and XEDS chemical maps of Co, Cu, Mg, Ni, Zn and the composite map of (CoCuMgNiZn) ESO pellet after (a) sintering at 1323 K for 10 h and (b) 1323 K for 100 h followed by water quenching. Fine scale segregation of Cu and Mg ions is evident in the maps. It is marked with arrows and delineated with dotted boundaries.

Secondary electron image and X-ray energy dispersive spectroscopy (XEDS) maps of all the ions in the (CoCuMgNiZn) ESO after sintering at 1323 K for 10 h and 100 h are given in Figure 4.3(a-b) respectively. In the secondary electron image of the ESO after sintering at 1323 K for 10 h (Figure 4.3a), uniformly sintered grains with varying grain sizes is observed. In the image, a few scattered pores and microcracks (marked with arrows) are also observed. In the XEDS maps, Co, Ni and Zn ions are uniformly distributed. However, local segregation of Cu and Mg is easily discerned (marked with arrows). The Cu ion enriched regions are depleted in Mg ions and vice versa. In the composite map of all the ions, clearly delineated colour distribution indicates that microscale chemical segregation of Cu and Mg takes place after 10 h of sintering at 1323 K in this ESO. (CoCuMgNiZn) ESO has been reported to form chemically homogeneous single phase [12, 17]. However,

microscale chemical segregation is clearly evident in this system. The same ESO after sintering at 1323 K for 100 h (Figure 4.3b) continues to maintain the grainy morphology with a wide variation in grain size. In the XEDS maps, a fairly uniform distribution of Co, Ni and Zn ions can be readily discerned over a large scale. However, there are isolated regions (marked with arrows) where Cu and Mg ions are preferentially segregated at sub-micron length scales. In the composite map, sub-grain boundaries have been delineated, where sub-grains preferentially enriched in Cu or Mg ions are observed. This observation, contrary to published literature reports [12, 17], proves that chemical segregation takes place in this ESO and the segregated regions grow in size with the time of sintering. However, the kinetics of chemical segregation and grain growth appears to be quite sluggish.

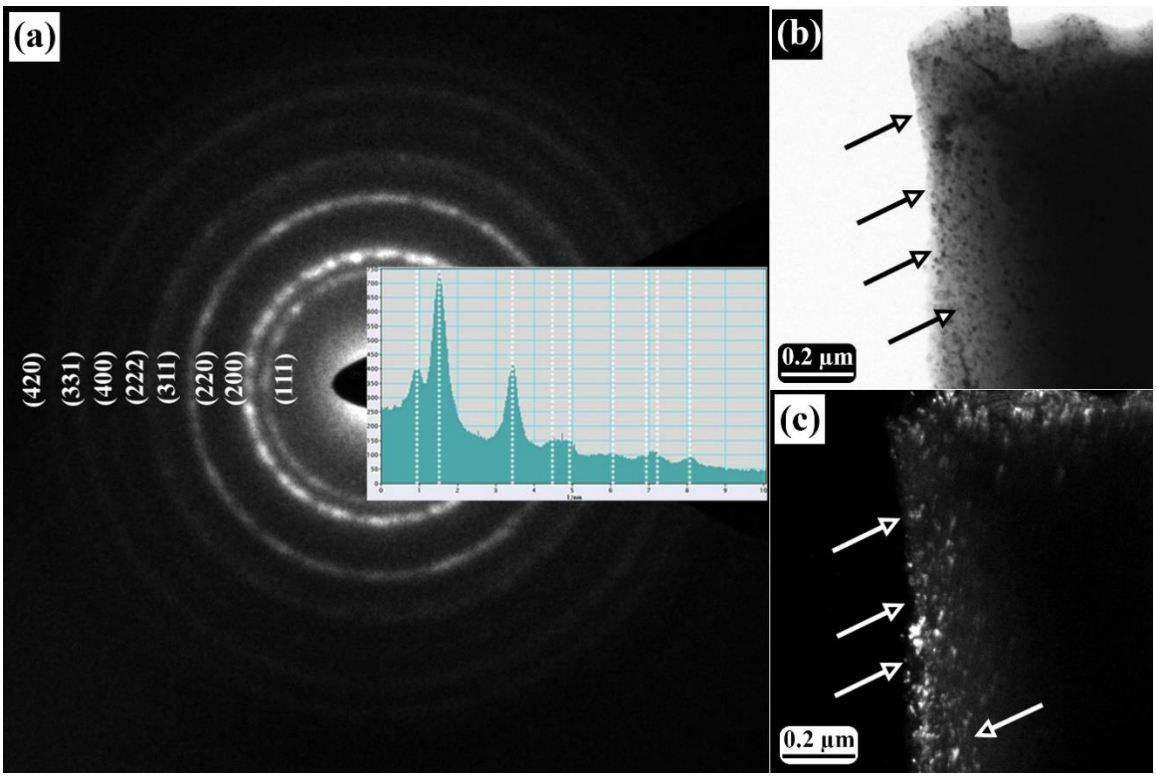

Figure 4.4: Sintered and quenched equimolar quinary (CoCuMgNiZn)ESO exhibiting (a) Polycrystalline electron diffraction pattern with spotty rings which can be indexed to a FCC phase with a~4.23 Å lattice parameter whereas (b) and (c) are the corresponding BF-DF pair showing nano-crystallites of the rocksalt phase. It was recorded from the periphery of the sample after ion-milling, making it necessary to revisit and optimize the electron thinning parameters to avoid such process-induced particle size refinement.

Selected area electron diffraction pattern with its corresponding bright field and complimentary dark field images of the sintered and quenched (CoCuMgniZn) ESO is shown in Figure 4.4(a-c). The diffraction pattern brings out the polycrystalline nature of the ESO, which shows concentric spotty rings that may be indexed to a FCC structure with *a~4.2 Å* (marked in Figure 4.4a). The intensity line profile when plotted along the radius of the circles, gives rise to all the allowed reflections of the cubic rocksalt phase. Corresponding BF/DF pair shows the presence of nano-crystallites of the rocksalt phase, which undergoes reversal of contrast from dark spots in BF to illuminated bright spots in the complimentary DF image (marked with arrows in Figure 4.4b-c). However, in order to probe single-crystal diffraction patterns for further insights, the ion-milling parameters were optimized to reduce such process-induced particle size refinement.

Bright field TEM images and selected area electron diffraction patterns from different zone axes of the (CoCuMgNiZn) ESO after sintering at 1323 K for 10 h followed by water quenching are given in Figure 4.5(a-f). The electron diffraction patterns (Figure 4.5(a-d)) may be indexed to a cubic rocksalt structure with *a~4.22 Å*, which is in agreement with the lattice parameter value as obtained from the XRD patterns. Some of the diffraction spots are diffused, streaked and occasionally a shape is observed (marked by dotted circles in Figure 4.5(a-d)). In the bright field image (Figure 4.5e) large faceted grains with fringe contrast at the grain boundaries is observed. However, within the grain a tweed like contrast is observed, which is not expected in single-phase materials with uniform chemistry. Higher magnification image (Figure 4.5f) of the grain body shows an inter-weaved pattern. The size of the inter-weaved regions is ~5-15 nm. However, there are regions in the grain body, which are free from such tweed-like structures. It is marked with a faceted boundary structure. The tweeds are wavy and the tweed boundaries are not perpendicular to one another (Figure 4.5f).

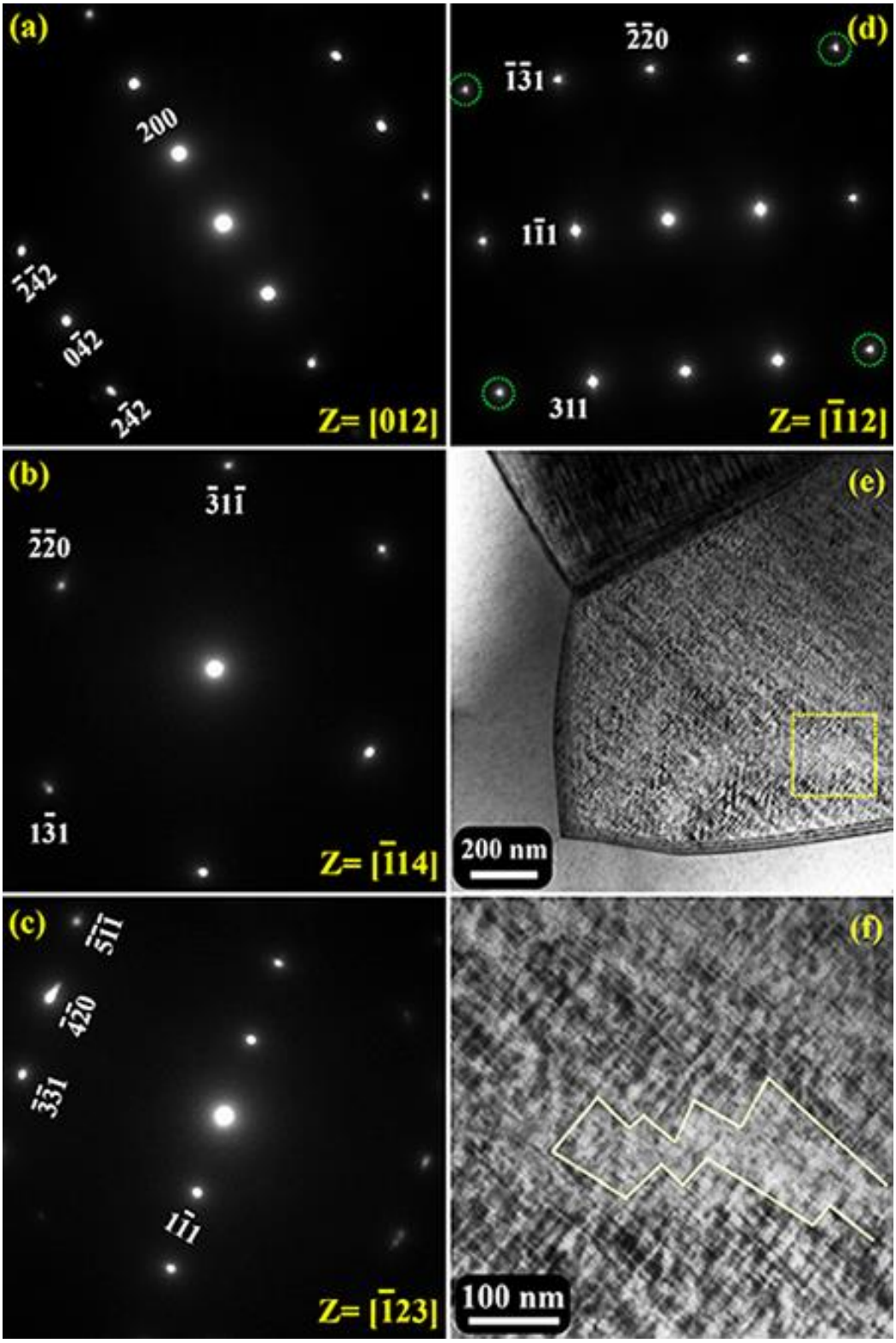

Figure 4.5: (a-d) Electron diffraction patterns of (CoCuMgNiZn) ESO after sintering at 1323 K for 10 h followed by water quenching. The electron diffraction patterns are from (a) z=[012], (b) z=[$\bar{1}$14], (c) z=[$\bar{1}$23], (d) z=[$\bar{1}$12]. In the bright field image in (e) tweed contrast within the grain body and fringe contrast at the grain boundaries is observed. (f) Magnified image of the region marked with dotted square in (e). Tweed free region is marked with yellow lines.

The origin of this inter-woven tweed morphology could be due to the oriented growth of polymorphically related structures within the same grain with or without any modulation in chemistry. However, in the secondary electron images and in the XEDS chemical maps, fine scale chemical segregation has been observed (Figure 4.3). It is expected that the tweed morphology evolves out of a fine scale chemical modulation induced polymorphic transformations within the grain body. It requires further investigation and it will be reported in subsequent sections of the communication.

Selected area electron diffraction pattern from one large and faceted grain of (CoCuMgNiZn) ESO after sintering at 1323 K for 10 h followed by water quenching may be indexed to a [100] zone axis pattern of a cubic rock salt structure with *a~4.22 Å* lattice parameter (Figure 4.6a). However, there are finer details in the pattern, e. g. 020 type spots are streaked along two almost perpendicular directions and there is diffuseness around the spots. The 022 type of spots show intensity modulation along two almost perpendicular directions and there is diffused streaking around it (Figure 4.6a inset). Intensity modulation leading to a particular shape of the diffraction spots and diffused streaking clearly indicates local modulation in d-spacings in the crystal. In order to rationalize the observation, extreme ends of the intensity modulations are joined together with dotted coloured lines (Figure 4.6a), which bring out the [100] zone axis symmetry shapes of a cubic rocksalt structure, however mutually rotated with respect to one another. Individual differently coloured [100] zone axis symmetry shapes are given in Figure 4.7a. The symmetry shapes may be divided into two sets (blue, pink form one set and green, yellow form another set), in each set the symmetry shapes are rotated in opposite sense, however by varying degrees. From each of these symmetry shapes, when 002 and 020 type vectors are plotted (Figure 4.7b), it appears that the magnitude of ratio of 002 and 020 vectors for the blue and pink pair is ~1, however the same ratio is ~1.02 for the green and

yellow pair. This definitely indicates that there could be local composition modulation induced distortions in the crystal. To support this point further the angular relationships between the 002 and 020 type vectors have been looked at and it has been found to be not exactly 90°.

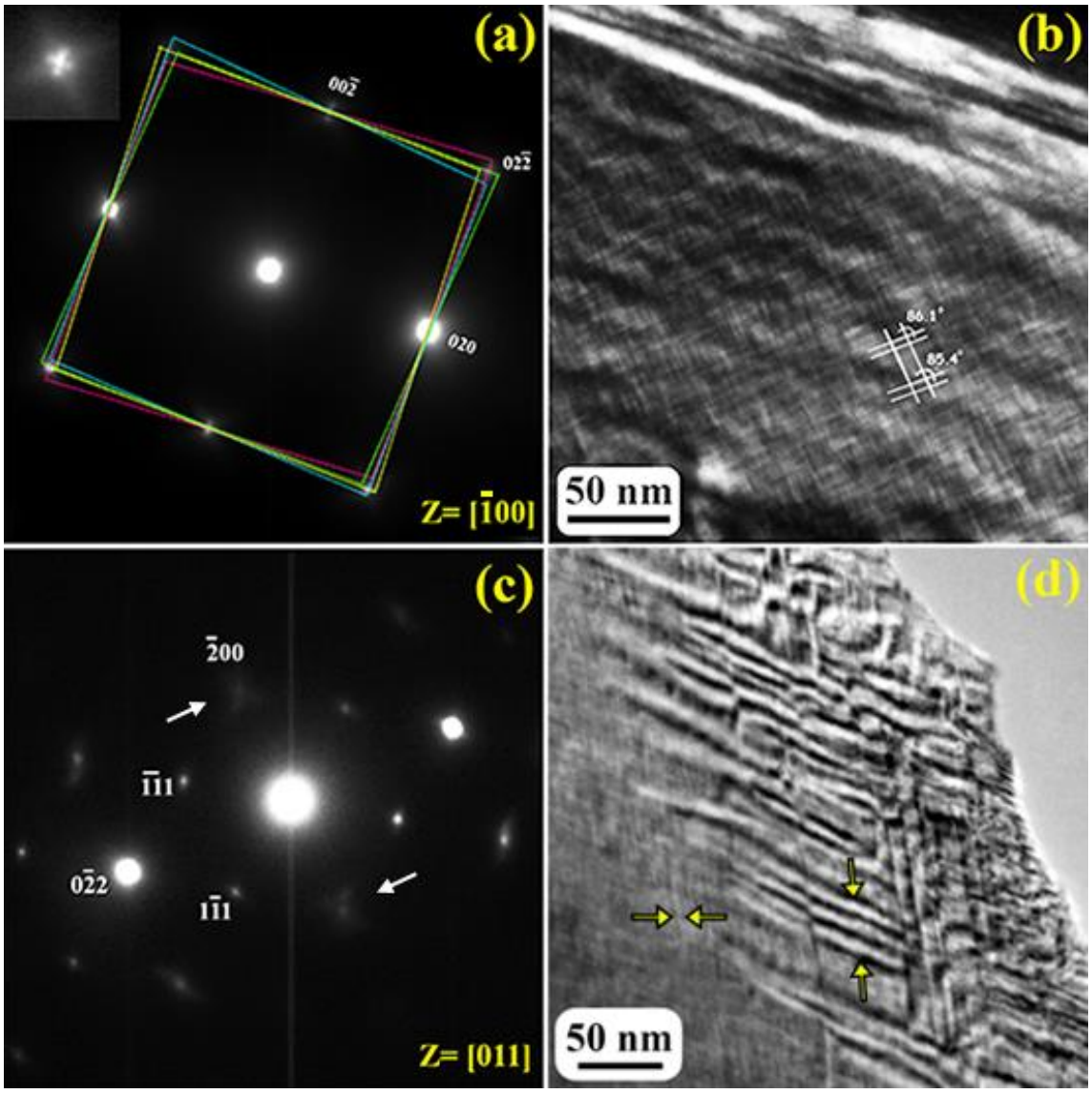

Figure 4.6: (a-d): Electron diffraction patterns, bright and dark field images of (CoCuMgNiZn) ESO after sintering at 1323 K for 10 h followed by water quenching. The diffraction pattern in (a) corresponds to z=[$\bar{1}$00] zone axis pattern of a cubic rocksalt structure. Diffused scattering, streaking and shape evolution (inset) of 02$\bar{2}$ type spot is observed. Extreme ends of the modulated spots are joined together to reveal the mutually rotated symmetry shapes. In the dark field image in (b) mutually intersecting non-orthogonal tweeds are observed. The electron diffraction pattern in (c) is from z=[011] zone axis of the same grain, where streaking and diffused intensity of the spots is observed. The bright field image in (d) shows the inter-penetrating tweeds.

This further indicates that local composition fluctuation induced non-cubic distortions take place in the crystal, and that in turn leads to shape evolution in the diffracted spots. The size of the modulated domains is so small that it gives birth to streaking in perpendicular directions. The structure of this phase largely remains to be cubic rocksalt globally, when such fine details in the diffraction pattern are ignored. However, such fine scale modulations are definitely present in the crystal and they manifest themselves in terms of shape evolution of the diffracted spots. When individual and differently coloured [100] symmetry shapes with their relative rotation and distortion are superimposed (Figure 4.7c), it gives rise to the experimentally observed diffraction pattern in Figure 4.6a. It is worth noting at this point that, such kind of composition modulation may not be detected by high resolution chemical mapping as chemically modulated domains are randomly distributed in the crystal and even fine probe techniques will not be able to detect the small variations in local chemistry within the individual domains due to the finite thickness of the crystal.

Dark field TEM image from the grain body (Figure 4.6b) with the 020 spot in the diffraction pattern in Figure 4.6a clearly brings out the tweed contrast in the grain interior. The individual tweeds are wavy but continuous and they do not intersect each other in exactly perpendicular orientation (marked by the traces in Figure 4.6b). This perfectly corroborates the experimentally observed diffraction pattern (Figure 4.6a) and its theoretical interpretation (Figure 4.7). Selected area electron diffraction pattern from the same grain along [011] zone axis (Figure 4.6c) exhibits similar shape evolution and streaking of 200, 022 and 222 type of spots. Similar wavy and mutually intersecting tweeds are observed in the bright field image (Figure 4.6d). Similar and mutually corroborating evidence in real and reciprocal space from two different major zone axis directions of the same grain definitely proves local composition modulation and distortion in the crystal after sintering and quenching.

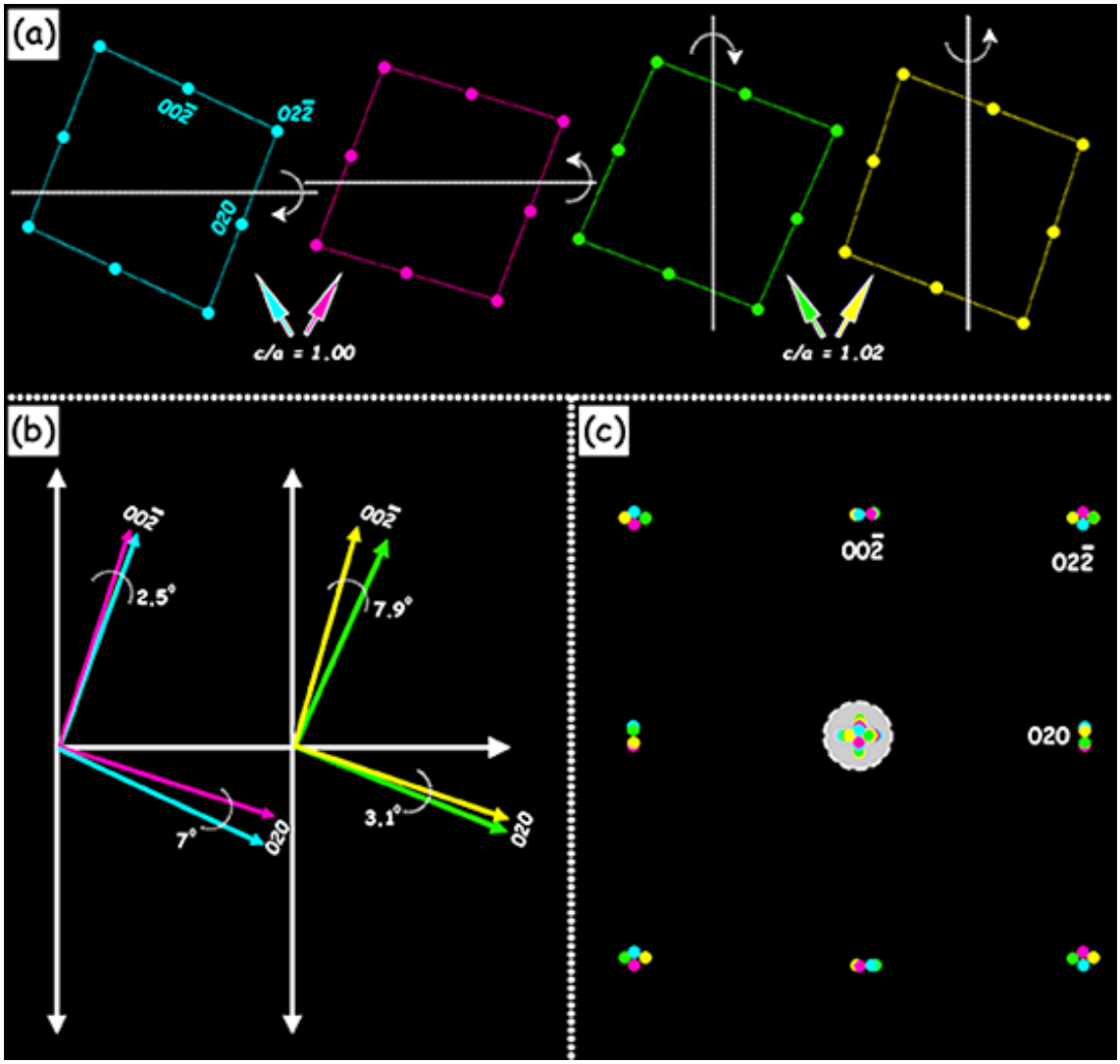

Figure 4.7: (a) Mutually rotated symmetry shapes as obtained from the electron diffraction pattern in Figure 5(a). The symmetry shapes may be separated into two groups with mutual relative rotation and with different c/a ratios. (b) Principal vectors from the symmetry shapes in (a) are plotted to reveal their relative rotation. (c) Mutually rotated symmetry shapes in (a) are superimposed to schematically generate the electron diffraction pattern in Figure 5(a).

Selected area electron diffraction patterns and corresponding bright field images from a different region of the (CoCuMgNiZn) ESO after sintering at 1323 K for 10 h followed by water quenching are given in Figure 4.8(a-d). The diffraction pattern in Figure 4.8a, may be indexed to a [100] zone axis pattern of a cubic rocksalt structure with *a~4.23 Å* lattice parameter, which is exactly similar to the lattice parameter as obtained from the XRD studies. However, in the diffraction pattern, the 002 type of spots are elongated and the 220

type of spots are arced with a definite intensity modulation. The two extreme ends of the arced reflections are connected by dotted cyan and yellow lines, which bring out two mutually rotated symmetry shapes of [100] zone axis of a cubic rocksalt structure. Similar such symmetry shapes may be generated by connecting all the in between spots of the arced 220 type of reflections. It may be inferred from this observation that several cubic domains with mutual in-plane rotation gives birth to such arced reflection in the diffraction pattern. In the corresponding bright field image (Figure 4.8b) mottled contrast with parallel linear fringes (marked with arrows) may be observed. Combined observation of arcing in the diffraction pattern (Figure 4.8a) and mottled contrast with linear fringes in the bright field image (Figure 4.8b) corroborates to the fact that several mutually rotated domains exist in the grain. In order to reduce the interfacial strain, the domains rotate with respect to one another. Selected area diffraction pattern from the same grain but along [$\bar{1}$12] zone axis (Figure 4.8c) exhibits similar elongation and arcing of the diffraction spots with definite intensity modulation. When the extreme ends of the arced spots are connected together by dotted cyan and yellow lines, mutually rotated symmetry shapes of [$\bar{1}$12] axis are observed. In the corresponding bright field image (Figure 4.8d) mottled contrast with linear fringes is observed. It further reinforces the fact that mutually rotated cubic domains do exist in the ESO. As arcing is observed from two not mutually perpendicular zone axes, it is confirmed that the domains are having both in-plane and out-of-plane rotation. It arises out of the tendency of the material to reduce strain, which will be elucidated further in the discussion section.

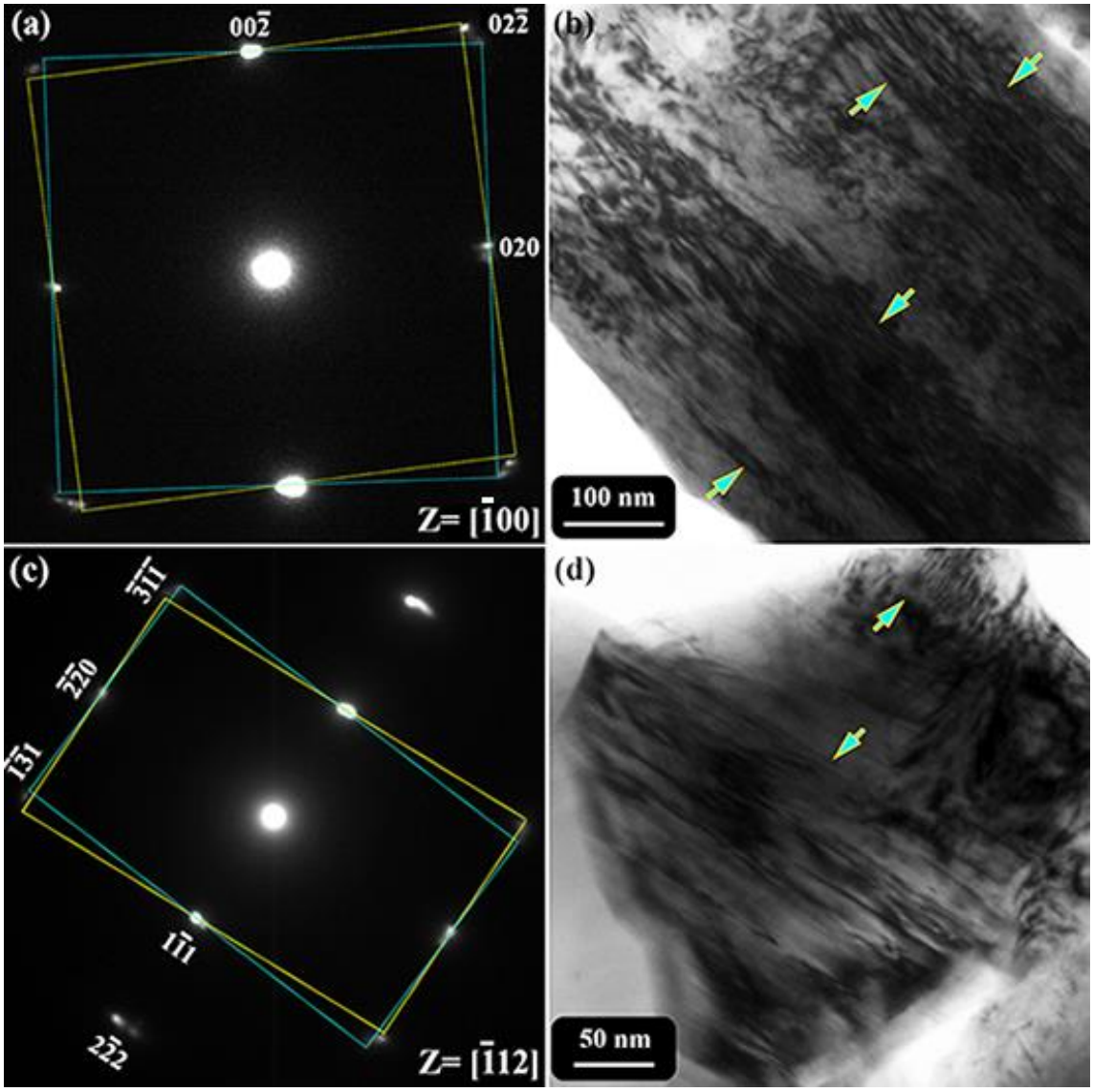

Figure 4.8: (a-d): Electron diffraction patterns and TEM bright field images of (CoCuMgNiZn) ESO after sintering at 1323 K for 10 h followed by water quenching. Arcing in (a) z=[$\bar{1}$00] and (c) z=[$\bar{1}$12] electron diffraction patterns is associated with the mutual in-plane and out-of-plane rotation of domains. Intensity modulated arcs in each of the diffraction patterns are connected with dotted lines to reveal the symmetry shapes of the corresponding zone axes. Fringe contrast is observed in corresponding bright field images in (b) and (d). The fringes are marked with arrows.

XRD pattern of the (CoCuMgNiZn) ESO powder after sintering at 1323 K for 10 h followed by water quenching (in red) and the same powder after sintering at 1323 K for 10 h followed by ageing at 723 K for 120 h followed by water quenching (in blue) are given in Figure 4.9. The x-ray diffraction experiments were conducted by Co-K_α radiation ($\lambda_{Co\ K\alpha}$ = 1.79 Å). As observed previously, in the XRD pattern of the sintered and quenched ESO

powder the diffraction peaks are sharp and they may be indexed to a cubic rocksalt structure with *a~4.23 Å* lattice parameter. Minor shouldering is observed in the diffraction peaks, which may be attributed to local composition modulation induced variation of d-spacings or introduction of tetragonality in the crystal. The ratio of the integrated intensity of 111 and 200 peaks is ~0.81, which is close to the ideal value. In the XRD pattern of the same ESO powder after ageing at 723 K for 120 h, similar peaks corresponding to a cubic rocksalt structure are observed. However, the peaks are broad, which is counter intuitive. The broadening of the peaks may be attributed to the development of a wider variation in d-spacings in the crystal upon ageing. It has been investigated further by electron diffraction and diffraction contrast imaging. After ageing the sample, reversal of 111 and 200 peak intensities is observed. The integrated intensity ratio of 111 and 200 peak after ageing the ESO turns out to be ~1.83. Reversal in intensity ratio in ESOs has been attributed to the processing history and active interplay of Jahn-Teller distortion [23]. The microstructural effect of this has been investigated by diffraction contrast imaging.

Selected area electron diffraction pattern from [100] zone axis of the (CoCuMgNiZn) ESO after sintering at 1323 K for 10 h followed by ageing at 723 K for 120 h and water quenching (Figure 4.10a) shows spot splitting and asymmetric diffused scattering. Spot splitting and diffused scattering clearly indicates the formation of structurally related domains with possible minor rotation among them. The diffraction pattern may be indexed as a whole to a cubic rocksalt structure with *a~4.23 Å* lattice parameter. However, it is not possible to determine the variation in crystal structure and lattice parameter of individual domains with accuracy. In the corresponding bright field image (Figure 4.10b) interpenetrating boundaries leading to a domain-like structure are observed. In the higher magnification image of the same area (Figure 4.10c) almost square domains of ~15-25 nm size are observed.

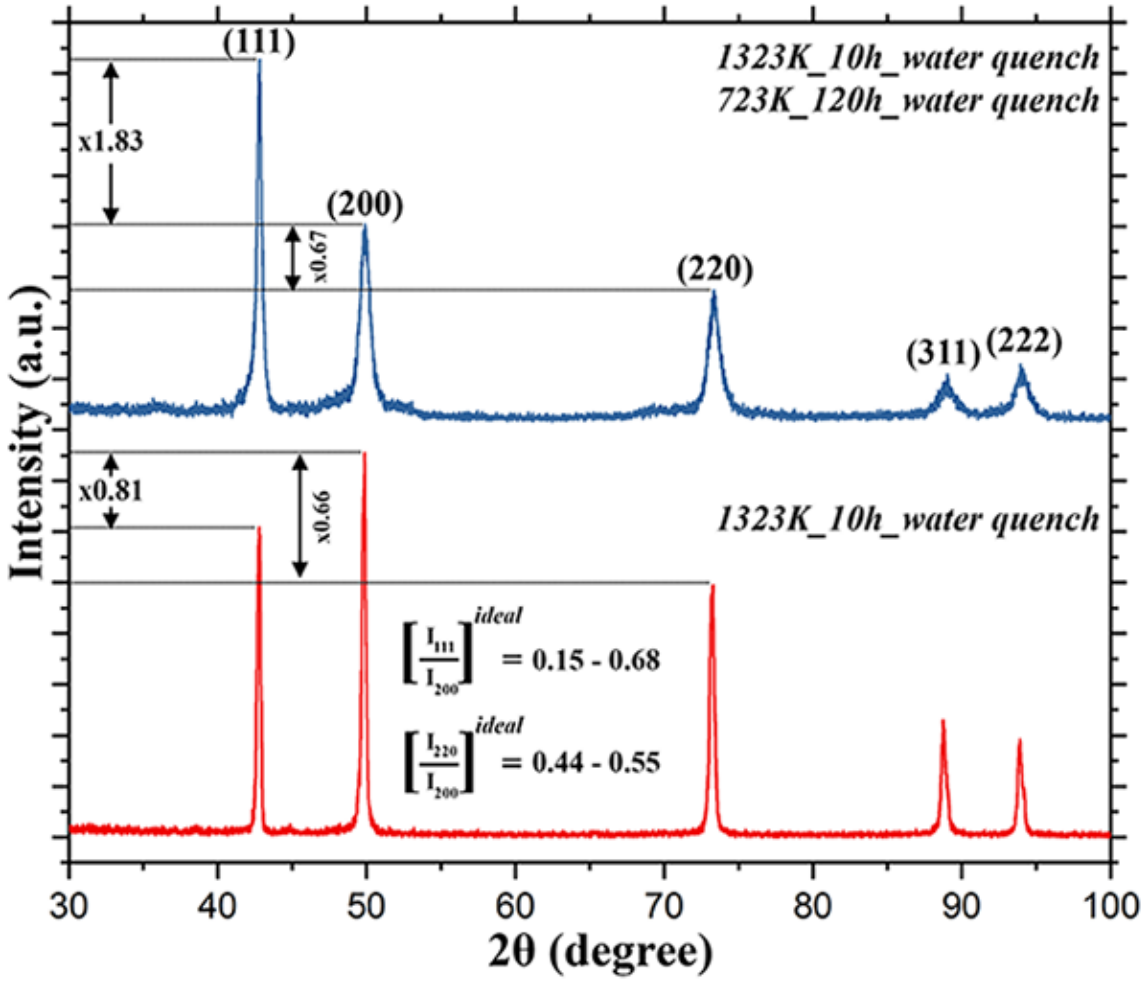

Figure 4.9: XRD patterns of (CoCuMgNiZn) ESO after sintering at 1323 K for 10 h followed by water quenching (in red) and after sintering at 1323 K for 10 h followed by ageing at 723 K for 120 h followed by water quenching (in blue). Anomalous intensity distribution and broadening of diffraction peaks after ageing is evident in the ESO.

The domain boundaries are thick and appearance of δ-fringes at the boundaries indicates that the domain walls are tilted with respect to the electron beam. The domains are formed after ageing and they grow to a size of ~15-25 nm after 120 h of holding, which clearly indicates that the growth kinetics of such domains is quite sluggish. In the dark field image (Figure 4.10d) with 020 spot lights up some of the boundaries. The domain wall boundaries are likely to be a variant of 020 type of planes. The growth of such domain walls, its implication on the stability of the single cubic rocksalt phase of this ESO will be discussed in the discussion section.

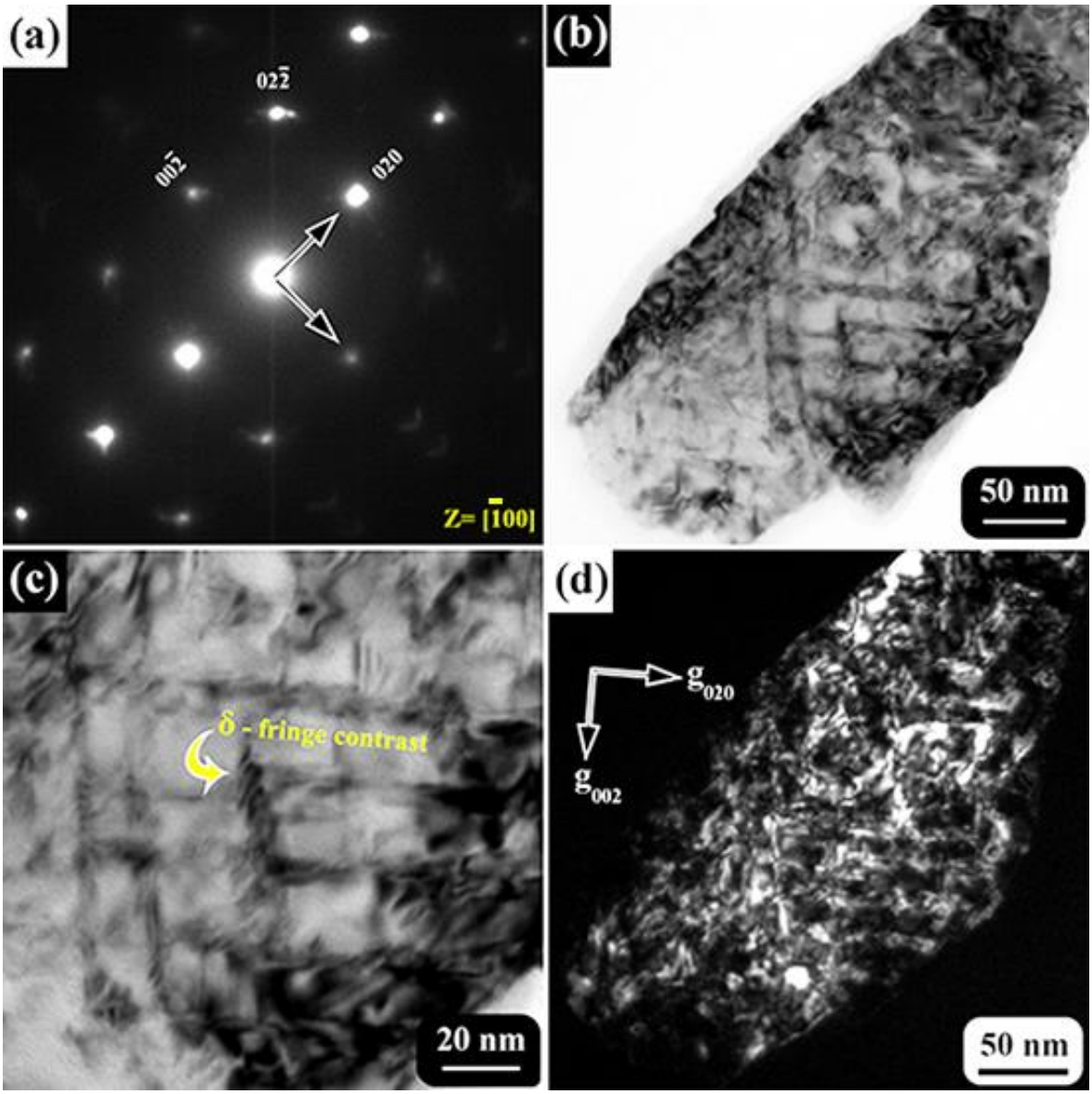

Figure 4.10: (a) z=[1̄00] electron diffraction pattern, TEM (b-c) bright field images and (d) dark field image of (CoCuMgNiZn) ESO after sintering at 1323 K for 10 h, subsequent ageing at 723 K for 120 h followed by water quenching. In the diffraction pattern in (a), asymmetrical diffused streaking of spots, splitting of spots is observed. In the bright field images (b-c) domain like structure with domain wall boundaries are observed. The domain wall boundaries are lightened up in the dark field image in (d) with g=020 diffraction spot.

Selected area electron diffraction pattern from a different region of the (CoCuMgNiZn) ESO after sintering at 1323 K for 10 h followed by ageing at 723 K for 120 h and water quenching is given in Figure 4.11(a-b). Both the diffraction patterns in Figure 4.11 are one and the same, however, one is inverted with respect to the other. In the diffraction pattern, modulation of intensity of the spots with occasional diffuseness is observed. All the principal reflections, their corresponding d-spacings, angular relations and the ratio of the principal vectors are given in Figure 4.11a. The diffraction pattern cannot be indexed consistently only with a cubic rocksalt phase with disordered cation distribution. The reflections connected with green dotted lines in the shape of a distorted hexagon corresponds to the [011] zone axis pattern of a cubic rocksalt phase with *a~4.22 Å* lattice parameter. In that case, the rocksalt phase is ordered along [200] and [022] type of directions. However, extra diffused intensity of 200 and 022 type of spots indicates that there is a likelihood of another correlated phase being present. The reflections connected with dotted yellow line in the form of a rectangle may be indexed to $[\bar{1}12]$ zone axis pattern of a cubic spinel phase with *a~8.15 Å* lattice parameter. In that situation, there is a specific orientation relationship between the cubic rocksalt phase and the cubic spinel phase with random cation distribution. The orientation relationships are $[\bar{1}12]_{Spinel} \parallel [011]_{Rocksalt}$ and $[220]_{Spinel} \parallel [0\bar{2}2]_{Rocksalt}$. There is a possibility that the cubic rocksalt phase is ordered and/or cubic spinel phase has grown locally with a specific orientation relationship with the rocksalt phase. The structural and thermodynamic implication of such observation will be discussed in the discussion section.

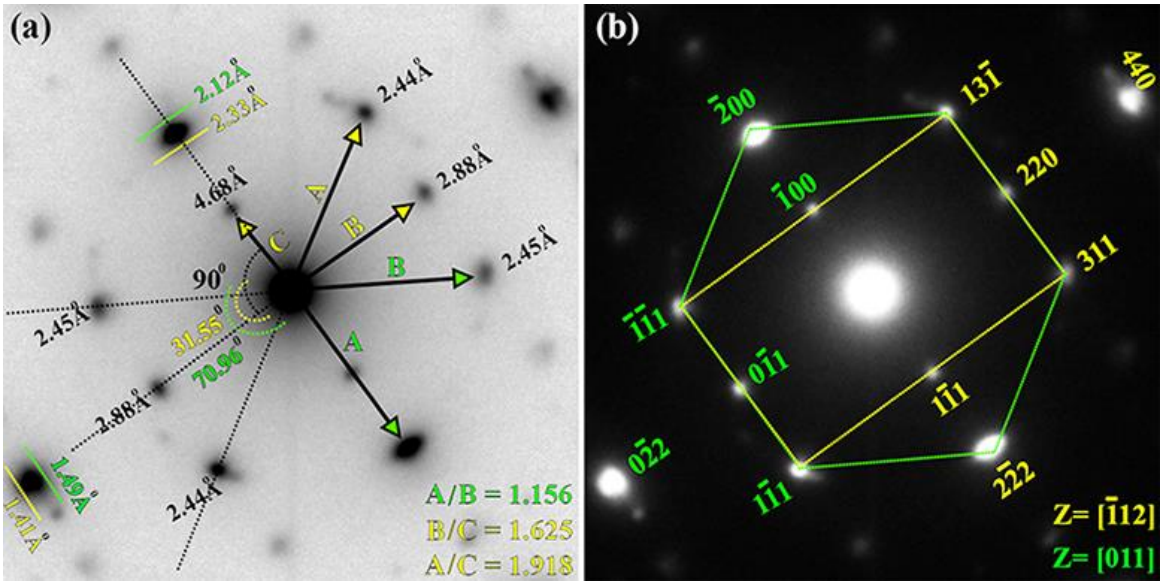

Figure 4.11: (a-b) Electron diffraction patterns from a different region of (CoCuMgNiZn) ESO after sintering at 1323 K for 10 h, subsequent ageing at 723 K for 120 h followed by water quenching. The diffraction pattern in (a) is inverted with respect to the diffraction pattern in (b). The patterns may be indexed with co-existent rocksalt phase and a spinel phase with a definite orientation relationship. The d-spacings, angular relationships and ratio of principal vectors are marked in (a). In (b) the diffraction spots corresponding to a rocksalt phase and a spinel phase are marked with different colours. The diffraction spots are connected with differently coloured dotted lines to bring out the zone axes symmetry shapes.

4.4. Discussion

Equimolar (CoCuMgNiZn) ESO is the first ever reported high entropy oxide in this class of new engineering materials, which is known to be stable in single phase rocksalt structure with random cation distribution and uniform chemistry [12]. The novel properties of this class of materials are sensitive to the structure and chemistry at the atomic scale [17, 25]. The properties have been explored with a general assumption that the structure and chemistry is uniform with absolutely random cation distribution. In the present study, the ESO has been systematically explored by XRD and electron microscopy in order to revisit its stability in the temperature-composition space. The evidences, when jotted down together, brings out a unified picture that clearly indicates the presence of very small structural domains with subtle variation of chemistry and oriented intergrowth of phases. It

may be directly related to the thermodynamic stability, kinetics of evolution of the microstructure, which will be discussed in the following sections.

4.4.1. Single phase and uniform chemistry of (CoCuMgNiZn) ESO

Over the last decade several high entropy oxides with multiple cation or anion disordering in their respective sublattices have been reported in literature [1-2, 26]. Single phase cubic rocksalt structure with uniform chemistry in (CoCuMgNiZn) ESO was the first ever high entropy oxide synthesized and characterized that initiated the excitement in this field [12]. Through XRD studies, the cubic rocksalt phase in this ESO has been reported. The shouldering or splitting that is observed in the XRD pattern has been attributed to the diffraction of Cu-$K_{\alpha I}$ and Cu-$K_{\alpha II}$ radiation [17]. In the present study, (CoCuMgNiZn) ESO after sintering at 1323 K for 10 h in pellet and powder form has been characterized by XRD with Co-K_{α} radiation. The diffraction pattern (Figure 4.1a) may be indexed to a cubic rocksalt structure with *a~4.24 Å* lattice parameter. The shouldering may be attributed to the diffraction by Co-$K_{\alpha I}$ and Co-$K_{\alpha II}$ radiations. However, similar shouldering or splitting may also arise due to polymorphic transformation or local variation of chemistry. In order to explore the possibility of diffraction by Co-$K_{\alpha I}$ and Co-$K_{\alpha II}$ radiations, experimentally observed split between the peaks has been compared with the theoretically expected split between the peaks, which is given in Table 4.1. It is consistently observed for all allowable reflections that the experimentally observed split between the peaks is ~1.5-2.0 times higher than the theoretically expected separation between the peaks. Similar experiments have been done for the same ESO after sintering at 1323 K for 10 h, 100 h followed by water quenching and sintering at the same temperature followed by furnace cooling. However, for these samples, XRD experiments have been done with Cu-K_{α} radiation. In conformity with the earlier publications [17], shouldering and peak splitting is observed in these experiments also (Figure 4.2). However, the experimentally observed split between

the peaks is consistently ~1.5-2.5 times higher than the theoretically expected split due to the diffraction by Cu-$K_{\alpha I}$ and Cu-$K_{\alpha II}$ radiations (Table 4.1). It may be concluded from this experimental observation and theoretical calculation that the shouldering and splitting in the XRD pattern is not likely due to the diffraction either by Co-K_α or Cu-K_α doublets. The possibility of local polymorphic transformation with or without associated local modulation of chemistry should be explored.

Table 4.1: Theoretically calculated peak positions, the expected separation between $K_{\alpha I}$ and $K_{\alpha II}$ peaks and their relative comparison with the experimentally observed split between the peaks in (CoCuMgNiZn) ESO. The values are truncated after 3rd place of decimal without approximation.

$\lambda_{Co\ K\alpha I}$ = 1.789 Å, $\lambda_{Co\ K\alpha II}$ = 1.792 Å; $\lambda_{Cu\ K\alpha I}$ = 1.541 Å, $\lambda_{Cu\ K\alpha II}$ = 1.544 Å

Plane	d-spacing (Å)		$2\theta_B$ (°)		$2\theta_B$ (°)		$2\Delta\theta_B$ (°)			
	Co K_α	Cu K_α	Co $K_{\alpha I}$	Cu $K_{\alpha I}$	Co $K_{\alpha II}$	Cu $K_{\alpha II}$	Experimental		Theoretical	
(111)	2.445	2.447	42.919	36.623	42.995	36.745	0.107	0.122	0.076	0.074
(200)	2.117	2.12	49.988	42.551	50.078	42.761	0.129	0.21	0.090	0.086
(220)	1.497	1.497	73.386	61.825	73.530	62.065	0.202	0.24	0.144	0.134
(311)	1.277	1.276	88.930	74.082	89.118	74.365	0.261	0.283	0.188	0.168
(222)	1.223	1.222	94.008	77.966	94.213	78.291	0.284	0.325	0.205	0.182

There are several indirect evidences in the XRD patterns of the ESO after different types of thermal treatments that polymorphic transformation associated with local compositional modulations leads to the broadening, shouldering and splitting of peaks with non-ideal intensity ratio. In the XRD pattern with Co-K_α radiation of the pellet and the powder of (CoCuMgNiZn) ESO after sintering at 1323 K for 10 h followed by water quenching, non-

ideal intensity ratio has been observed (Figure 4.1a). Similar non-ideal intensity ratio with Cu-K_α radiation has been observed in the same ESO after different thermal treatments (Figure 4.2 and Figure 4.9). In earlier literature departure from ideal intensity ratio of the diffraction peaks has been attributed to the thermal history of the ESO along with Jahn-Teller distortion induced changes in the structure [23-24].

In the present study, in the SEM-XEDS maps (Figure 4.3) local variation of chemistry associated with the enriched and depleted regions of Mg and Cu has been observed. This further reinforces the idea of local polymorphic transformations with associated chemical modulation in this ESO. The XRD peaks of ESO after sintering at 1323 K for 10 h followed by water quenching (Figure 4.1(b-c)) may be deconvoluted to a number of peaks, which resemble after the d-spacings of the precursor oxides. Similar observation holds good for all other XRD patterns of the ESO with different thermal history. Moreover, longer h of exposure at high temperature (Figure 4.2 and Figure 4.9) leads to the reduction in total integrated intensity of the XRD peaks along with broadening. This observation is counter intuitive so far grain growth and stress relaxation in the grains is concerned. However, it definitely points to the formation of local structural domains with or without variation in chemistry. This statement may further be supported by the observation of tweeds within the grain body of the ESO along with shape evolution and diffused streaking of the diffraction spots (Figure 4.5 and Figure 4.6).

4.4.2. Structural modulation induced tweed formation and strain minimization

In the bright field images of the ESO, after sintering at 1323 K for 10 h, tweed formation within the grain body is observed. The tweeds are discontinuous that form ~5-15 nm domains (Figure 4.5). The corresponding electron diffraction patterns conform to a cubic

rocksalt structure with *a~4.23 Å* lattice parameter. However, diffused intensity around the spots with diffused streaking, spot splitting and evolution of shapes with modulation of intensity may be observed (Figure 4.6). When the extreme ends of the intensity modulated diffraction spots are connected with dotted lines, approximately [100] zone axis symmetry shapes of a cubic rocksalt structure are observed (Figure 4.6a). It may further be deduced that the symmetry shapes belong to two groups with different *c/a* ratios, which are rotated with respect to one another (Figure 4.7a). Experimentally observed diffraction pattern in Figure 4.6a may be generated schematically by superimposing the symmetry shapes in Figure 4.7a. Combined observation of this diffraction pattern along with tweed formation within the grain body clearly indicates the formation of local structural domains within the ESO. Structural domains may be associated with local variation of chemistry. However, it cannot be confirmed as the chemical variation may be random and finite thickness of the sample renders it impossible to associate one domain with a particular chemistry even by a fine probe technique as domains with different chemistry are stacked together along the thickness of the sample.

In a different region of the ESO, after sintering at 1323 K for 10 h, arcing of spots with finite intensity modulation is observed (Figure 4.8). It may further be deduced from the diffraction patterns that structural domains are formed with mutual in-plane and out-of-plane rotation that leads to the arcing of the diffraction spots. In the corresponding bright field images linear fringe contrast is observed (Figure 4.8). After ageing the ESO for long h, growth of such domains with clear domain walls is observed (Figure 4.10). Similar domain formation with in-plane and out-of-plane rotation leading to a helical structure of domains has been observed in (CaCoFeMgNi) multicomponent oxide [27].

Mutually rotated domain formation that appears as tweed or two-dimensional fringes is schematically presented in Figure 4.12a. In this figure, local composition modulation has

been assumed to be the driving mechanism that leads to local structural variation. Local structural variation helps in relaxing the lattice strain that is manifested due to the presence of multiple cations in the same lattice. However, in order to minimize the interfacial strain, the local structurally modulated domains rotate with respect to one another.

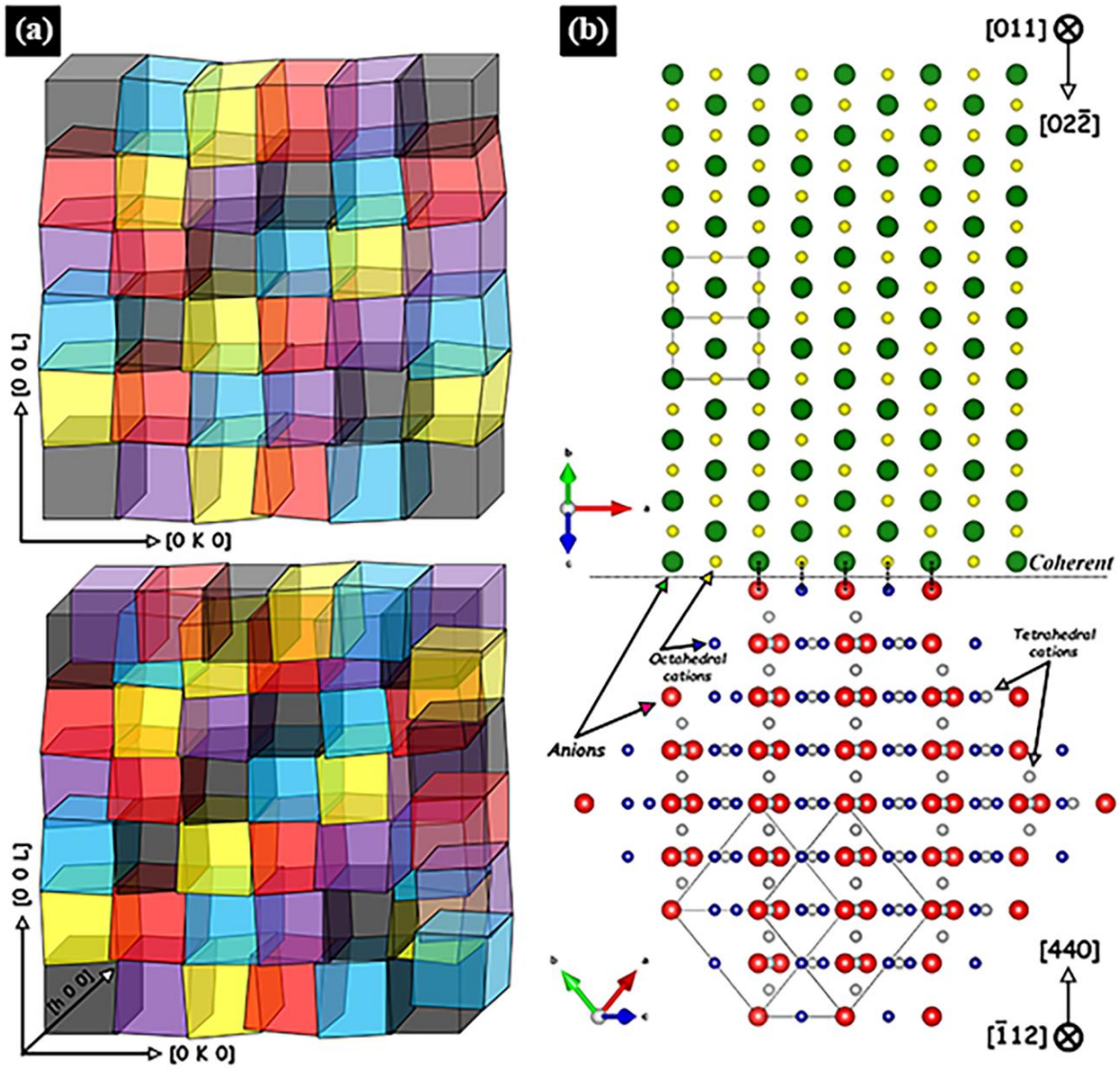

Figure 4.12: (a) Schematic representation of structurally modulated domains in 2D and in 3D in the (CoCuMgNiZn) ESO. Structural modulation may be initiated with the chemical modulation in individual domains, which are represented with different colours. Structural modulation in 3D makes the ESO appear as uniform in chemistry due to the overlap of domains with different chemistry. (b) Schematic representation of oriented growth of rocksalt phase and a spinel phase. The interface is coherent.

The assumed local chemical variation leading to local structural modulation is presented with different colours of the domains in the schematic in Figure 4.12a. Such domains grow further with ageing. However, the growth kinetics is sluggish. Chemical modulation of such domains is quite difficult, if not impossible, to capture through fine probe imaging and spectroscopy techniques as the domains are randomly distributed and due to the finite thickness of the sample, domains with different chemistry may stack up one on the top of other. As the interaction volume of the probe is not restricted within one domain, the domains will always reveal uniform average chemistry of the ESO.

The (CoCuMgNiZn) ESO after sintering at 1323 K for 10 h followed by ageing at 723 K for 120 h and quenching shows oriented growth of spinel domains in the rocksalt structure (Figure 4.11). There is a possibility of cation ordering in the rocksalt structure along <200> and <022> type directions. There is a specific orientation relationship between the rocksalt phase and the spinel phase. Rocksalt and spinel phase are structurally quite correlated as in the rocksalt phase all the octahedral voids are filled out and in the spinel phase only alternate octahedral voids are filled out. There is a good possibility that spinel phase grows within the rocksalt phase locally in an oriented manner. The interface structure of the rocksalt phase with the spinel phase with the observed orientation relationship is schematically presented in Figure 4.12b. It is observed from the crystal structure diagram that the interface between the rocksalt phase and the spinel phase is coherent that assures minimal interface strain. Similar coherent and semi coherent interface formation through oriented growth of phases has been observed in (CaCoFeMgNi) multicomponent oxide after different heat treatments [27].

It is worth pointing out that the (CoCuMgNiZn) ESO after sintering at 1323 K for 10 h, 100 h followed by water quenching and furnace cooling shows definite changes in the XRD patterns (Figure 4.2). There is a reduction in the total integrated intensity of the peaks with

finite broadening after longer h of heat treatment, which might be associated with the local chemical variation leading to a modulation in d-spacings. A finite leftward shift of the peaks is also observed after longer h of heat treatment. Left shift of the peaks indicates increase in the d-spacings and increase in the lattice parameter and volume of the crystal. This may be associated with the volumetric stress relaxation of the crystal with longer h of exposure at high temperature. The structure of the ESO is cubic rocksalt with *a~4.22 Å* lattice parameter. In the rocksalt structure, oxygen ions form the FCC lattice and the cations are octahedrally located. Assuming [110] direction to be the closest packed direction, the relationship between the lattice parameter *'a'* and the radius of the oxygen ion *'r'* is $4r=\sqrt{2}a$ and the size of the octahedral void V_r may be written as $V_r= (\sqrt{2}-1)r$. Based on this calculation, the maximum size of cation that may be accommodate in the octahedral void is ~62 pm. However, the size of Co^{2+}, Cu^{2+}, Mg^{2+}, Ni^{2+}, Zn^{2+} at octahedral coordination are ~75 pm, ~73 pm, ~72 pm, ~69 pm and ~74 pm respectively. Size of the octahedral cations being larger than the octahedral size, accommodation of the cations in the octahedral voids leads to the generation of volumetric stress. High temperature exposure for longer time provides the required stimuli to release the volumetric stress by increasing the average lattice parameter of the crystal and the volume. Further, local modulation helps in reducing the lattice strain.

It may be summed up from the above discussion that the ESO with random distribution of cations always attempts to reduce its strain field provided an external energy stimulus is obtained. Local chemical modulation, variation in d-spacings and increase in lattice parameter helps in reducing the volumetric stress and lattice strain, which is manifested in broadening of x-ray diffraction peaks, diffused intensity around the electron diffraction spots and its shape evolution, arcing of the diffracted spots and tweed/domain formation in the grain body. Local structural variation induced by local chemical modulation leads to

the formation of interfacial strain between the tweeds and the domains. Mutual rotation, interpenetration of domains/tweeds and oriented growth of correlated phases with coherent/semi-coherent boundaries helps in accommodating the interfacial strain. Very similar observation in case of (CaCoFeMgNi) multicomponent oxide [27] further reinforces the mechanism of strain minimization in multicomponent ESOs.

4.4.3. Thermodynamic implications of strain minimization and stability of ESO

High entropy oxide (HEO), an important member in the family of high entropy materials (HEMs), is said to be entropy stabilized by random distribution of cations in the cation sublattice [2, 15, 22]. It is believed that random distribution of five or more cations increases the configurational entropy so much that free energy of the system is always dominated by the entropic contribution irrespective of enthalpy of formation of such oxides [28]. This has led to the new name of this class of materials as entropy stabilized oxide (ESO) [12]. Equimolar (CoCuMgNiZn) oxide is the first ever reported high entropy oxide that is believed to be stabilized in a cubic rocksalt structure in the time-temperature space. It is also widely reported that the presence of five cations makes the lattice quite strained [15].

In the present study, fine scale composition segregation between Cu and Mg ions has been observed in a subtle way. Additionally, the tendency of the system to reduce its volumetric strain, lattice strain and interfacial strain has been observed through the formation of tweeds, inter-grown domains and oriented growth of structurally correlated phases with or without compositional modulation. Though entropy remains to be the single most dominating factor in deciding the stability of the phase in time-temperature space, other

factors should also be taken into account in order to understand the thermodynamic stability issue of the material.

Change in Gibbs free energy is given by $\Delta G = \Delta H - T\Delta S$, where the symbols have their usual meaning. Further, $\Delta H = \Delta U + P\Delta V$ for a constant pressure process. The term $P\Delta V$ may be considered to be the change in the mechanical energy in the process. A qualitative look in the above equations indicates that the presence of five or more cations in the same sublattice will make the configurational entropy very high. However, it will definitely increase the strain energy in the crystal. $-T\Delta S$ term will always have a negative contribution and the strain energy term ($P\Delta V$) will always have a positive contribution to the Gibbs free energy change. Formation of local compositionally modulated domains will reduce the negative contribution of $-T\Delta S$ term, however, the reduction of volumetric strain, lattice strain and interfacial strain through the formation of tweeds, inter-grown domains and oriented growth of structurally correlated phases will reduce the positive contribution of the $P\Delta V$ term. Combined interplay of these two terms should negatively maximize the change in Gibbs free energy. It is understood that the stability of such multicomponent oxides is not solely determined by the entropy. However, it is a combined interplay of entropy and strain energy. Similar behaviour has been observed in case of (CaCoFeMgNi) multicomponent oxide [27].

4.5. Conclusions

It may be concluded from the present study that first ever reported (CoCuMgNiZn) ESO forms a cubic rocksalt structure with *a~4.22 Å* lattice parameter. However, the shouldering or splitting of peaks in XRD, hitherto which has been understood as the diffraction from Cu-K_α or Co-K_α doublets, may not be correct. The shouldering, splitting and non-ideal intensity distribution should be attributed to local structural modulation in the ESO, accompanied with local compositional variation. The rocksalt phase in the ESO reduces its

volumetric strain, lattice strain and interfacial strain by tweed formation and sluggish growth of the tweeds in the form of domains that separates several structurally modulated domains within the rocksalt phase. Oriented growth of structurally correlated phases with coherent/semi-coherent interfaces further reduces the strain in the ESO. The stability of the ESO is not solely determined by the maximization of configurational entropy. However, it is the trade-off between the configuration entropy and different types of strain energy that determines the stability of the phase in time-temperature space.

4.6. Reference

1. C. Oses, C. Toher, S. Curtarolo, High-entropy ceramics, Nat. Rev. Mater., 2020, 5, 295-309.
2. M. Brahlek, M. Gazda, V. Keppens, A. R. Mazza, S. J. McCormack, A. Mielewczyk-Gryn, B. Musico, K. Page, C. M. Rost, S. B. Sinnott, C. Toher, T. Z. Ward, A. Yamamoto, What is in a name: Defining “high entropy” oxides, APL Mater., 2022, 10, 110902-11.
3. Z. Lun, B. Ouyang, D. H. Kwon, Y. Ha, E. E. Foley, T. Y. Huang, Z. Cai, H. Kim, M. Balasubramanian, Y. Sun, J. Huang, Y. Tian, H. Kim, B. D. McCloskey, W. Yang, R. J. Clement, H. Ji, G. Ceder, Cation-disordered rocksalt-type high-entropy cathodes for Li-ion batteries, Nat. Mater., 2021, 20, 214-221.
4. Q. Wang, A. Sarkar, Z. Li, Y. Lu, L. Velasco, S. S. Bhattacharya, T. Brezesinski, H. Hahn, B. Breitung, High entropy oxides as anode material for Li-ion battery applications: A practical approach, Electrochemistry Communications, 2019, 100, 121-125.
5. D. Berardan, S. Franger, A. K. Meena, N. Dragoe, Room temperature lithium superionic conductivity in high entropy oxides, J. Mater. Chem. A, 2016, 4, 9536-9541.
6. A. Sarkar, L. Velasco, D. Wang, Q. Wang, G. Talasila, L. de Biasi, C. Kubel, T. Brezesinski, S. S. Bhattacharya, H. Hahn, B. Breitung, High entropy oxides for reversible energy storage, Nature Communications, 2018, 9, 3400 (9 pages).
7. M. V. Kante, M. L. Weber, S. Ni, I. C. G. van den Bosch, E. van der Minne, L. Heymann, L. J. Falling, N. Gauquelin, M. Tsvetanova, D. M. Cunha, G. Koster, F.

Gunkel, S. Nemsak, H. Hahn, L. V. Estrada, C. Baeumer, A high-entropy oxide as high activity electrocatalyst for water oxidation, ACS Nano, 2023, 17, 5329-5339.

8. A. Sarkar, Q. Wang, A. Schiele, M. R. Chellali, S. S. Bhattacharya, D. Wang, T. Brezesinski, H. Hahn, L. Velasco, B. Breitung, High-entropy oxides: Fundamental aspects and electrochemical properties, Adv. Mater., 2019, 31, 1806236 (9 pages).
9. S. H. Albedwawi, A. Aljaberi, G. N. Haidemenopoulos, K. Polychronopoulou, High entropy oxides-exploring a paradigm of promising catalysts: A review, Materials and Design, 2021, 202, 109534 (27 pages).
10. S. Maiti, W. Steurer, Structural-disorder and its effect on mechanical properties in single-phase TaNbHfZr high-entropy alloy, Acta Mater., 2016, 106, 87-97.
11. Y. Zhang, T. T. Zuo, Z. Tang, M. C. Gao, K. A. Dahmen, P. K. Liaw, Z. P. Lu, Microstructures and properties of high-entropy alloys, Prog. Mater. Sci., 2014, 61, 1-93.
12. C. M. Rost, E. Sachet, T. Borman, A. Moballegh, E. C. Dickey, D. Hou, J. L. Jones, S. Curtarolo, J. P. Maria, Entropy-stabilized oxides, Nature Communications, 2015, 6, 8485 (8 pages).
13. G. Anand, A. P. Wynn, C. M. Handley, C. L. Freeman, Phase stability and distortion in high-entropy oxides, Acta Mater., 2018, 146, 119-125.
14. K. C. Pitike, K. C. Santosh, M. Eisenbach, C. A. Bridges, V. R. Cooper, Predicting the phase stability of multicomponent high-entropy compounds, Chem. Mater., 2020, 32, 7507-7515.
15. S. J. McCormack, A. Navrotsky, Thermodynamics of high entropy oxides, Acta Mater., 2021, 202, 1-21.
16. A. Sarkar, R. Djenadic, N. J. Usharani, K. P. Sanghvi, V. S. K. Chakravadhanula, A. S. Gandhi, H. Hahn, S. S. Bhattacharya, Nanocrystalline multicomponent entropy stabilized transition metal oxides, J. Eu. Ceram. Soc., 2017, 37, 747-754.
17. C. M. Rost, Z. Rak, D. W. Brenner, J. P. Maria, Local structure of the $Mg_xNi_xCo_xCu_xZn_xO$ (x=0.2) entropy-stabilized oxide: An EXAFS study, J. Am. Ceram. Soc., 2017, 100, 2732-2738.
18. Y. Gu, A. Bao, X. Wang, Y. Chen, L. Dong, X. Liu, H. Pan, Y. Li, X. Qi, Engineering the oxygen vacancies of rocksalt-type high-entropy oxides for enhanced electrocatalysis, Nanoscale, 2022, 14, 515-524.

19. Z. Grzesik, G. Smola, M. Stygar, J. Dabrowa, M. Zajusz, K. Mroczka, M. Danielewski, Defect structures and transport properties in (Co, Cu, Mg, Ni, Zn)O high entropy oxide, J. Eu. Ceram. Soc., 2019, 39, 4292-4298.
20. W. Hong, F. Chen, Q. Shen, Y. H. Han, W. G. Fahrenholtz, L. Zhang, Microstructural evolution and mechanical properties of (Mg, Co, Ni, Cu, Zn)O high-entropy ceramics, J. Am. Ceram. Soc., 2019, 102, 2228-2237.
21. A. D. Dupuy, M. R. Chellali, H. Hahn, J. M. Schoenung, Nucleation and growth behavior of multicomponent secondary phases in entropy-stabilized oxides, J. Mater. Res., 2023, 38, 198-214.
22. M. Fracchia, M. Coduri, M. Manzoli, P. Ghigna, U. A. Tamburini, Is configurational entropy the main stabilizing term in rock-salt $Mg_{0.2}Co_{0.2}Ni_{0.2}Cu_{0.2}Zn_{0.2}O$ high entropy oxide, Nature Communications, 2022, 13, 2977 (4 pages).
23. D. Berardan, A. K. Meena, S. Franger, C. Herrero, N. Dragoe, Controlled Jahn-Teller distortion in (MgCoNiCuZn)O-based high entropy oxide, J. Alloys Comp., 2017, 704, 693-700.
24. Z. Rak, J. P. Maria, D. W. Brenner, Evidence for Jahn-Teller compression in the (Mg, Co, Ni, Cu, Zn)O entropy-stabilized oxide: A DFT study, Mater. Lett., 2018, 217, 300-303.
25. C. M. Rost, D. L. Schmuckler, C. Bumgardner, M. S. B. Haque, D. R. Diercks, J. T. Gaskins, J. P. Maria, G. L. Brennecka, X. Li, P. E. Hopkins, On the thermal and mechanical properties of $Mg_{0.2}Co_{0.2}Ni_{0.2}Cu_{0.2}Zn_{0.2}O$ across the high entropy to entropy-stabilized transition, APL Mater., 2022, 10, 121108 (6 pages).
26. B. L. Musico, D. Gilbert, T. Z. Ward, K. Page, E. George, J. Yan, D. Mandrus, V. Keppens, The emergent field of high entropy oxides: Design, prospects, challenges and opportunities for tailoring material properties, APL Mater., 2020, 8, 040912 (16 pages).
27. S. Mukherjee, N. K. Mukhopadhyay, J. Basu, Composition modulation, strain minimization and oriented growth of phases in equimolar (CaCoFeMgNi) multicomponent oxide, Acta Mater., 2025, 285, 120621 (12 pages).
28. M. Fracchia, M. Coduri, P. Ghigna, U. A. Tamburini, Phase stability of high entropy oxides: A critical review, J. Eu. Ceram. Soc., 2024, 44, 585-594.

Chapter – 5

Structural modulation, oriented intergrowth of rocksalt and spinel in equimolar multicomponent {Co(Cr/Mg)FeMnNi}-oxide and its derivatives

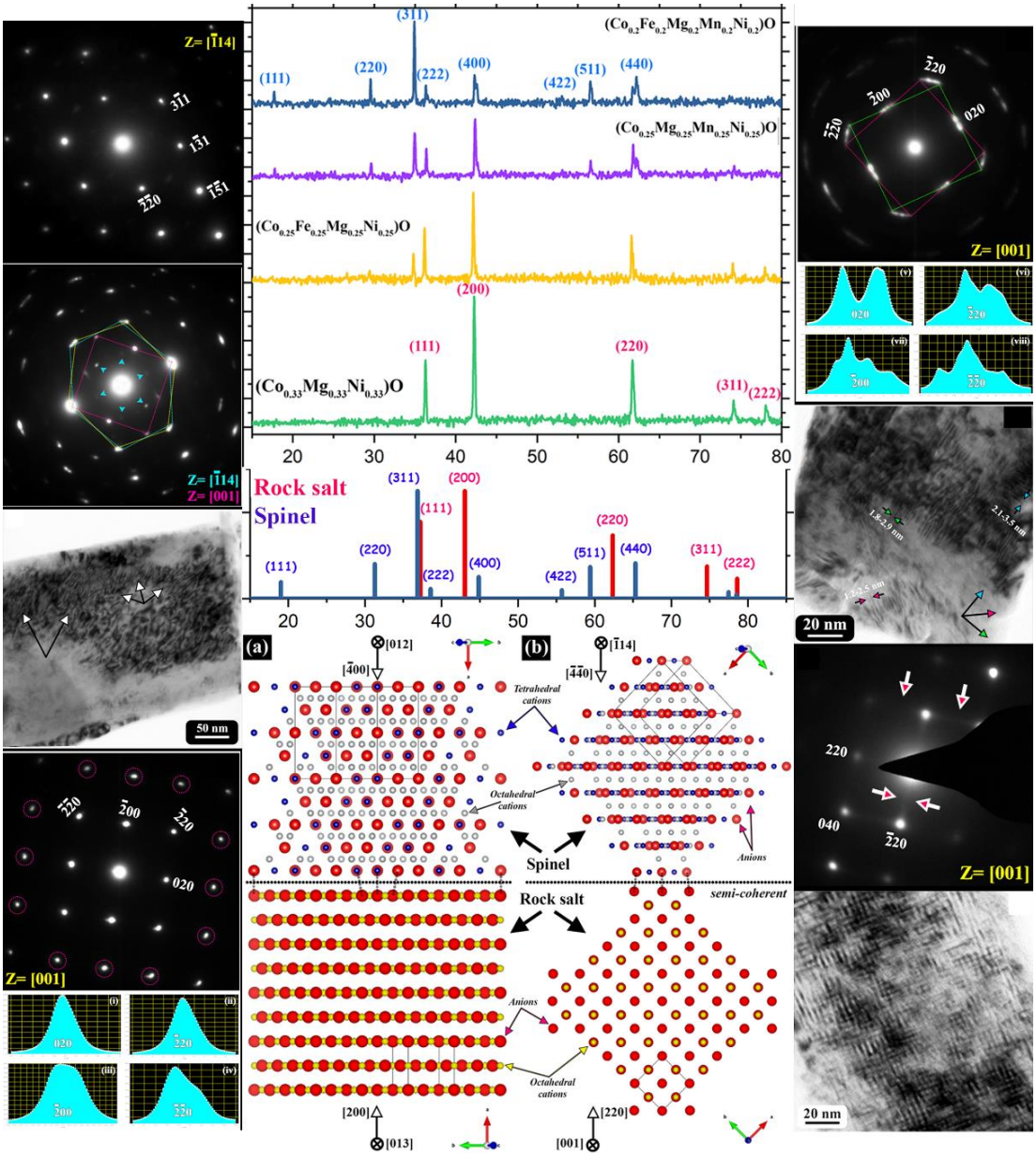

5.1. Introduction

Spinel and rocksalt forming high entropy oxides (HEOs)/ multicomponent oxides (MCOs) have garnered tremendous attention in the recent past owing to their favourable properties making it frontrunner candidates for their use in the field of energy conversion, storage and catalysis [1-7]. Right after the discovery of rocksalt HEO in (CoCuMgNiZn)O, less than a decade ago [8], successful synthesis of phase-pure spinel forming HEO in $(CoCrFeMnNi)_3O_4$ was reported a few years later [9], and subsequently a plethora of other HEO forming compositions were reported from each family of ceramic crystal structure [10,11]. A lot of groups have investigated these two special compositions since then, with primary focus on their functional properties [12-15]. Several substitutions to explore the composition-phase space have also been reported [16,17]. However, phase stability, microstructural evolution and the mechanism behind synergistic effect of entropic stabilization in these HEOs has been comparatively less explored [18-20]. There are couple of major schools of thought regarding the phase formation and stability of such multicomponent metallic oxides. The overwhelming belief that stabilization of a homogeneous disordered single-phase solid-solution stems from the dominance of configurational entropy of mixing in HEOs, sits on one hand [21, 22]. On the other hand, enthalpic penalties induced precipitation of related multicomponent secondary phases and/or defect microstructure formation has also been explored by a few research groups [23,24]. However, direct experimental evidences for such deviations are scarce. Additionally, the spinel crystal structure is relatively more complex than rocksalt counterpart owing to the degrees of freedom of void filling by cations, rendering it amenable to ordering, phase separation or distortions [25-30].

The current work has been carried out to understand the stability and phase-pure nature of the original spinel forming HEO. In order to arrive at satisfactory conclusions from

previously unreported experimental evidences, it is necessary to accumulate findings from its derivative lower-order oxides. It has been found out that equimolar ternary (CoMgNi)-oxide with rocksalt structure gives rise to phase-pure spinel structure upon partial substitution by Mn- and Fe-ions. This gives rise to $(CoFeMgMnNi)_3O_4$ single-phase spinel forming MCO, which is being reported for the first time. However, structural modulation and oriented inter-growth of related phases sharing coherent/semi-coherent boundaries in both the ternary and quinary MCO and HEO respectively can be discerned, which was previously not envisaged. Furthermore, phase separation event along specific crystallographic directions, although at its nascent stage, is found to influence the microstructural formation in the first ever reported $(CoCrFeMnNi)_3O_4$ spinel HEO.

5.2. Materials and methods

Multicomponent, equimolar oxides of (CoFeMgMnNi), (CoCrFeMnNi) and its binary, ternary and quaternary derivatives i. e. (MgNi)-oxide, (CoNi)-oxide, (CoMgNi)-oxide, (CoFeMgNi)-oxide and (CoMgMnNi)-oxide have been synthesized by solid-sate synthesis route due to the ease of materials handling and probability of success. Starting precursor oxides i. e. Co(II,III)O, Cr(III)O, Fe(II,III)O, MgO, Mn(III)O and NiO (>99.8 at% purity) were procured from either Alfa Aesar or Sigma Aldrich. The oxides in powder form were mixed in stoichiometric proportions for all the binary, ternary, quaternary and quinary compositions before they were mixed thoroughly in a mortar and pestle. Mixed equimolar ternary oxide of (CoMgNi) was further ball milled for 40 h in a Retsch PM400 planetary ball mill in dry environment using zirconia vial and balls at 200 rpm with 10:1 ball to powder ratio. During ball milling, the milling process was paused for 30s after every 60s of milling to avoid dynamic recrystallization. In order to study the phase evolution in the mixed powder, samples were collected after 5h, 15h and 40h of milling. The collected samples were characterized by X-ray diffraction (XRD) in a Rigaku MiniFlex600 table top

X-ray diffractometer with Cu-K_α (λ= 1.54 Å) radiation operated at 40 kV accelerating voltage with 15 mA tube current.

Precursor oxides, mixed in stoichiometric proportions, for all the binary, ternary, quaternary and quinary compositions were compacted in a uniaxial hydraulic press with 4T load to produce the green compacted pellets of ~12 mm diameter with ~4-5 mm thickness. The green compacted pellets were sintered at ~1473 K for 10 h in air before they were water quenched. Quinary (CoFeMgMnNi)-oxide was also sintered at 1473 K for 100 h, in addition to the 10 h sintering and it was then water quenched. Additionally, the ternary (CoMgNi)-oxide was aged at 723 K for 120 h in air and the it was water quenched. Sintering and ageing treatments were carried out in a platinum crucible with the lid on. In order to maintain perfect stoichiometry and avoid contamination, a number of pellets with identical composition were stacked together in the platinum crucible and the pellet from the centre of the stack was taken for further studies. Sintered, quenched and aged multicomponent oxides were characterized by XRD using a Malvern Panalytical high-resolution X-ray diffractometer with Cu-K_α (λ= 1.54 Å) and Co-K_α (λ= 1.79 Å) radiations. The diffractometer was operated 40 kV accelerating voltage with 40 mA tube current. The as-synthesized and aged multicomponent oxides were studied in a Tecnai G2 T20 transmission electron microscope (TEM). For TEM observation, thin slices were obtained from sintered, quenched and aged pellets by cutting the pellets with a low-speed saw. A slice from the center of the pellet was crushed to powder. The crushed powder was suspended in ethanol and was ultrasonicated for 15 minutes before it was drop-cast onto a carbon coated copper grid of ~3mm diameter. The XRD patterns were simulated by indigenously developed code and the structural models were developed by Vesta^{TM} software.

5.3. Results

In the XRD pattern of the as mixed equimolar mixture of Co(II,III)O, MgO and NiO (Figure 5.1a), individual diffraction peaks of the precursor oxide phases could be easily discerned. The Co(II,III)O exists both in spinel and rocksalt structures as evident from the XRD peaks marked by blue solid triangles and hollow open circles in red. MgO and NiO exist exclusively in rocksalt structure as marked by red close circles and black filled close circles respectively. The diffraction peaks of MgO and NiO are almost overlapping, which may be justified by the nearly similar lattice parameter and structure of the two oxides. The diffraction peaks of CoO with rocksalt structure appears very close to the MgO and NiO diffraction peaks due to its similar structure, however with a slightly larger lattice parameter. The experimentally observed diffraction patterns (Figure 5.1a) show excellent match with the simulated diffraction patterns (Figure 5.1b) of rocksalt and spinel structures with $a_{spinel} \sim 8.1$ Å *and* $a_{rocksalt} \sim 4.2$ Å. The lattice parameters of MgO, NiO and CoO are *a~4.21 Å, a~4.15 Å and a~4.26 Å* respectively. However, the lattice parameter of Co_3O_4 with spinel structure is *a~8.08 Å*, which is almost double (lattice parameter ratio~ 1.89) of the lattice parameter of the rocksalt phase. The structural relationship between the rocksalt phase and the spinel phase will be discussed in terms of their nature of void filling and ionic radii in the discussion section of the communication.

After 5h of milling, the XRD peaks (Figure 5.1a) becomes broad due to the refinement of particle size and accumulation of strain in the lattice of the crystals. The peaks corresponding to the spinel phase continue to exist. There is a sharp reduction in the intensity of the peaks corresponding to the rocksalt phase and the peaks corresponding to the CoO rocksalt phase cannot be distinctly observed. It appears as a shoulder to the peaks corresponding to the NiO and MgO rocksalt phases. It may be inferred that solid solutioning starts at the initial stages of milling. NiO and MgO acts as the host lattice in which CoO

with rocksalt structure starts getting incorporated. After 15h of milling, the peaks (Figure 5.1a) are further broadened with reduction of intensity as strain continues to get accumulated with simultaneous reduction in the particle size. The peaks corresponding to the CoO phase with rocksalt structure are completely merged with the peaks of the NiO and MgO phases. After 40h of milling, only the spinel phase is observed distinctly and the rocksalt phase is observed as a shoulder to the spinel phase.

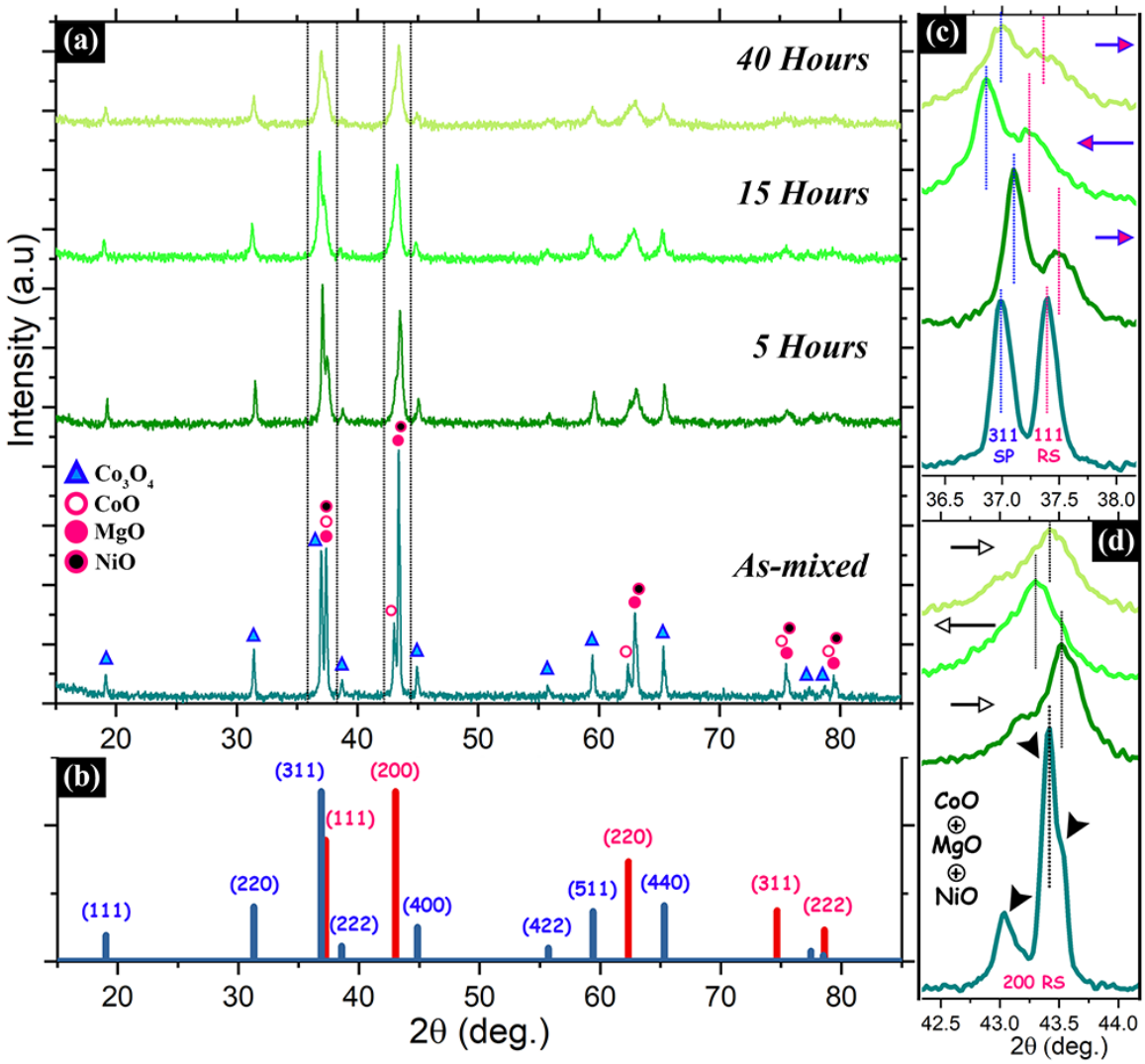

Figure 5.1: (a) X-ray diffraction (XRD) patterns of equimolar (CoMgNi)-oxide powder in the as-mixed condition and after 5h, 15h, 40h of ball milling. (b) Simulated XRD pattern of cubic rocksalt (a ~ 4.2 Å) in red and cubic spinel (a ~ 8.1 Å) in blue respectively. (c) Magnified view of 311 peak of cubic spinel and 111 peak of cubic rocksalt in as-mixed condition and after 5h, 15h and 40h of ball milling (d) Magnified view of the evolution of 200 peak of cubic rocksalt phase in the as-mixed condition and after 5h, 15h and 40h of ball milling.

It may be inferred that after 40h of milling solid solution phase consisting of spinel and rocksalt is formed in the initial stoichiometric mix of the elemental oxide powder. A magnified view of the evolution of the 311 peak of the spinel phase and the 111 peak of the rocksalt phase with the progress of milling is given in Figure 5.1c. As stated earlier, with the progress of milling both the peaks are broadened and they start to merge with one another. However, there is a slight rightward shift of the peaks after 5h of milling, which becomes a net leftward shift after 15h of milling and again a slight rightward shift after 40h of milling. Change in d-spacing due to progressive solid solutioning is expected to be uni-directional in nature. In this case, switching of the shift direction may be attributed to the change in d-spacings and cell volume due to the accumulation of strain and vacancies in the lattice of the spinel and rocksalt based solid solution phases and the attempt of the phase mixture to optimize its vacancy concentration, composition etc. Likewise, the magnified view of the 200 peak of the rocksalt-based CoO, MgO and NiO phases (Figure 5.1d) shows initiation of peak merger after 5h of milling. After 15h of milling, individual peaks of CoO, MgO and NiO phases are not observed indicating that the process of solid solution phase formation is mostly complete after 15h of milling. However, along with the peak broadening, a slight rightward shift after 5h of milling, a net leftward shift after 15h of milling and a slight rightward shift after 40h of milling is observed. This may also be attributed to the accumulation of strain, increase in vacancy concentration in the rocksalt based solid solution phase and the attempt of the phase to optimize its strain, vacancy concentration and composition. It will be substantiated further in the discussion section in terms of ionic radii of the species and the structural similarity between rocksalt and spinel phases.

XRD patterns of equimolar binary (MgNi)-oxide (in red), (CoNi)-oxide (in blue) and ternary (CoMgNi)-oxide (in green) powder after sintering at 1473 K for 10 h are given in

Figure 5.2. In the binary (MgNi)-oxide exclusively rocksalt phase with *a~4.21 Å* lattice parameter is observed. In the binary (CoNi)-oxide cubic rocksalt phase with *a~4.20 Å* and a cubic spinel phase with *a~8.25 Å* lattice parameters are observed. In the ternary (CoMgNi)-oxide only cubic rocksalt phase with *a~4.20 Å* lattice parameter is observed. In the diffraction pattern of this ternary oxide a small undulation corresponding to the 220 peak of a spinel phase is observed. However, the undulation is so small, it may not be used as a confirmation for the existence of the spinel phase.

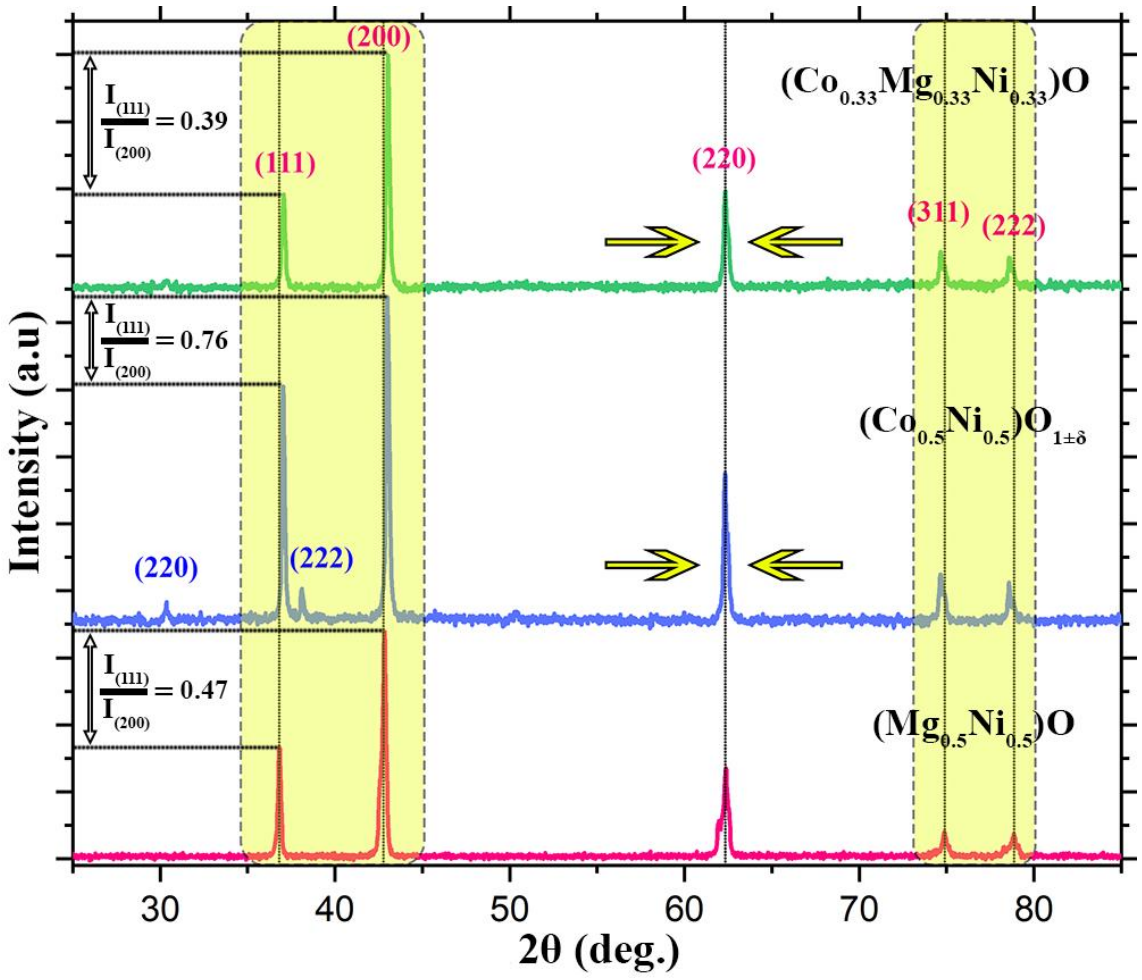

Figure 5.2: X-ray diffraction (XRD) patterns of equimolar binary (MgNi)-oxide, (CoNi)-oxide and ternary (CoMgNi)-oxide powder after sintering at 1473 K for 10h followed by water quenching. In all three compositions cubic rocksalt phase forms as the major phase, however, with varying intensity ratios of 111 and 200 diffraction peaks.

In order to further investigate the existence of the spinel phase, XRD patterns of the (CoMgNi)-oxide after sintering at 1473 K for 10h in the pellet and powder form has been compared (Figure 5.3a). In the XRD pattern of the pellet, a distinct 220 peak for spinel has been observed and other spinel peaks overlap with the peaks of the rocksalt phase. It may be due to the low volume fraction of the spinel phase and its oriented growth with the rocksalt phase. It is noteworthy that the lattice parameter of the spinel phase is almost double of the rocksalt phase as stated earlier. The normalized intensity plot of the experimental XRD patterns of the pellet and the crushed powder as shown in Figure 5.3a are given in Figure 5.3b. It is confirmed that the Compton inelastic background of the powder after crushing the sintered and quenched pellet is higher than the sintered and quenched pellet itself. Due to the high Compton background in the XRD pattern of the crushed powder of the sintered and quenched pellet, the low intensity 220 peak of spinel may remain invisible. It is understandable that crushing of the pellet introduces strain that increases the Compton background scattering in the crushed powder. It may be inferred that low volume fraction of the spinel phase, its oriented growth with the rocksalt phase and concomitant increase in the Compton background scattering leads to the almost invisibility of the low intensity 220 peak of the spinel phase in the crushed powder. Similar changes in XRD patterns in entropy stabilized oxides (ESOs) depending on processing conditions has been reported before.

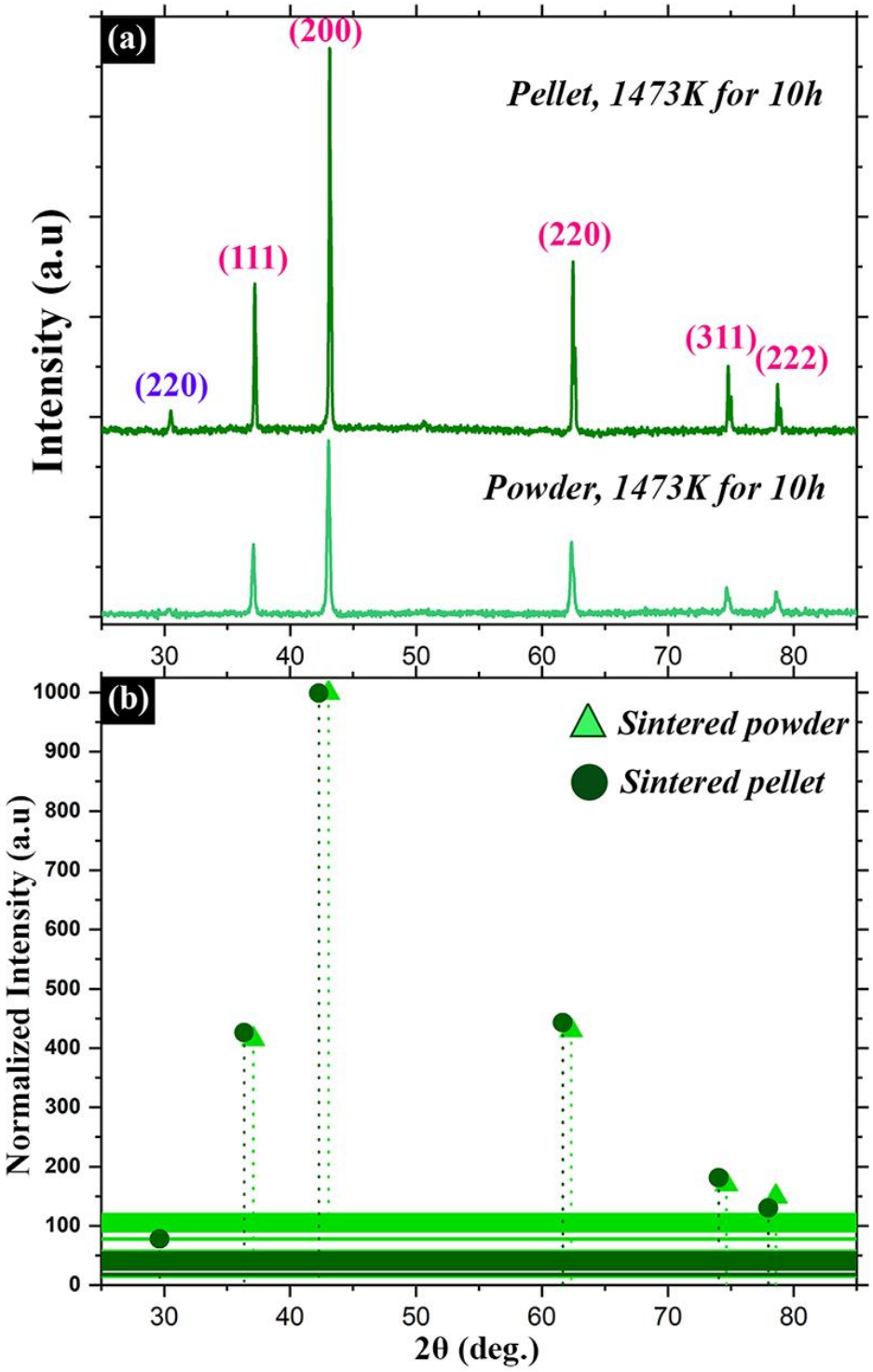

Figure 5.3: (a) X-ray diffraction (XRD) patterns of equimolar ternary (CoMgNi)-oxide powder (light green) and pellet (dark green) after sintering at 1473 K for 10h followed by water quenching. In the pellet, signature of cubic spinel phase is observed, which is absent in the powder. (b) Normalized intensity plots from the experimental XRD patterns of the powder (light green) and pellet (dark green). Compton modified scattering background is represented as bands with respective colours. Compton modified background for the powder being high, the low intensity spinel peak gets suppressed in the powder.

TEM bright field image (BF) and electron diffraction patterns of (CoMgNi)-oxide after sintering at 1473 K for 10h followed by water quenching are given in Figure 5.4(a-d). In the BF image (Figure 5.4c) mottled contrast indicating the presence of residual strain is observed. The corresponding diffraction patterns from z=[011] (Figure 4a), z=[125] (Figure 5.4b) and z=[013] (Figure 5.4d) may be indexed to a cubic rocksalt phase with *a~4.2 Å* lattice parameter. It is noteworthy that the diffraction patterns from a cubic spinel phase with double the lattice parameter will appear to be very similar from similar zone axes as will be demonstrated later in this communication. However, in case of a spinel phase some systematic extra spots should be observed, which are not present in the diffraction patterns. As the selected area diffraction patterns are obtained from very localized regions, the signature of cubic spinel phase is absent. This perfectly corroborates the XRD results, where it has been stated that the spinel phase is present in a very small volume fraction. Around the diffraction spots, diffuse scattering is observed (Figure 5.4a and 5.4d) and in some of the diffraction spots, geometric shape evolution and splitting is observed (Figure 5.4a and 5.4b). It will be discussed further in the subsequent sections. TEM DF image (Figure 5.4e) and its corresponding BF pair (Figure 5e inset) after ageing the sintered and quenched sample at 723K for 120h shows extensive fringe contrast along with the mottled contrast. Magnified version of the BF image in Figure 5.4e (inset) is given in Figure 5.4f. The fringe contrast is clearly visible in the image. The fringes are marked with arrows in the image. The spacing between consecutive fringe ranges from ~1.5-3.5 nm. In the diffraction pattern from the same region (Figure 5.5b) along z=[001], extensive splitting and arcing of spots with intensity modulation is observed. Different points in the diffracted arcs may be systematically joined together to bring out the symmetry shape corresponding to the four-fold [001] zone axis pattern of a cubic rocksalt phase with *a~4.2 Å* lattice parameter.

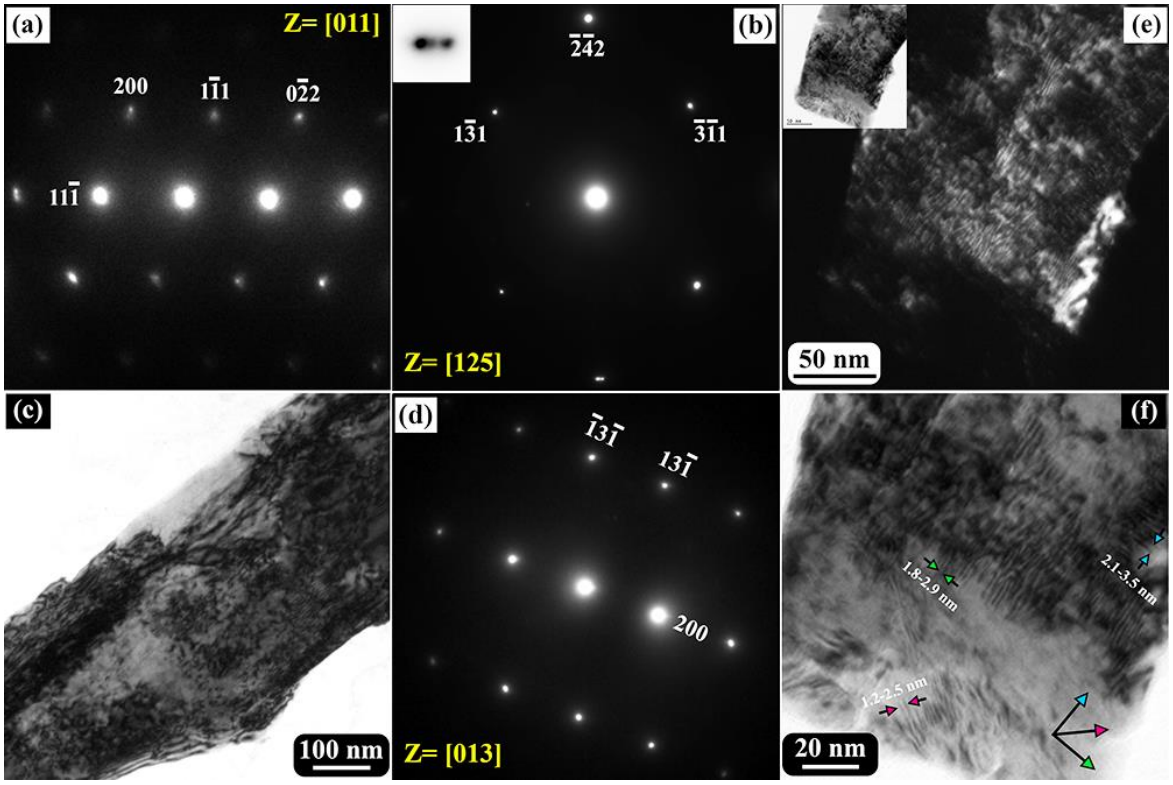

Figure 5.4: (a-d) Bright field image and selected area diffraction patterns along z=[011], z=[125] and z=[013] zone axes from ternary equimolar (CoMgNi)-oxide after sintering at 1473 K for 10 h followed by water quenching. The diffraction patterns may be indexed to a cubic rocksalt phase (a ~ 4.2 Å) with diffuseness and occasional spot splitting. Mottled contrast associated with strain fields is observed in the bright field image. (e) Centred dark field image and complementary bright field image (inset) from the same ternary equimolar (CoMgNi)-oxide after sintering at 1473 K for 10 h followed by ageing at 723 K for 120 h, in which parallel fringe with alternating contrast is observed. (f) Magnified bright field image of (e) showing multiply oriented fringes with ~1.5-3.5 nm spacing between them.

Two such symmetry shapes by joining the extreme ends of the arcs are shown in the figure with coloured dotted lines. It is observed that the symmetry shapes are rotated with respect to one another. Mutual rotation between two symmetry shapes formed by joining the extreme ends of the arcs is ~20°. It may be inferred that cubic rocksalt domains with mutual rotation among them do exist in the aged sample. It can be substantiated that the mutually rotated domains are developed during ageing by comparing a similar diffraction pattern along z=[001] from the sintered and quenched sample in Figure 5.5a. The diffraction pattern from the sintered and quenched sample (Figure 5.5a) along z=[001] may be indexed

to a cubic rocksalt phase with *a~4.2 Å* lattice parameter. However, the arcing, splitting and modulation of intensity is absent in the lower order spots. Minor arcing and spot splitting are observed in the higher order spots (circled in the diffraction pattern in Figure 5.5a). This necessarily means that ternary, equimolar oxide tends to form a domain structure from the very beginning. However, there is a kinetics of such mutually rotated domain formation, due to the paucity of time this did not develop during sintering and quenching. It is further evidenced, when the intensity distribution of the lower order spots perpendicular to the individual g-vectors is plotted in one dimension. Intensity distribution plots are given below the corresponding diffraction patterns in Figure 5.5. The intensity distribution plots of the g-vectors for the sintered and quenched sample are mostly symmetric with a very minor skewness for the $\bar{2}\bar{2}0$ type spots. In comparison to that the intensity distribution plots of the diffraction spots for the sintered, quenched and aged sample shows multiple maxima with finite skewness. Formation of mutually rotated domains in sintered, quenched and aged sample manifests itself in the form of wavy fringe contrast in the BF and DF images as has been observed in Figure 5.4e and 5.4f. Formation of such mutually rotated domains leading to a fringe contrast and tweed morphology has been observed after long h of sintering and ageing in (CaCoFeMgNi)-oxide and (CoCuMgNiZn)-oxide respectively. It is understood that such tweed structures form in multicomponent oxide after long h of sintering and ageing in a bid to minimize its strain. It will be discussed further in the discussion section.

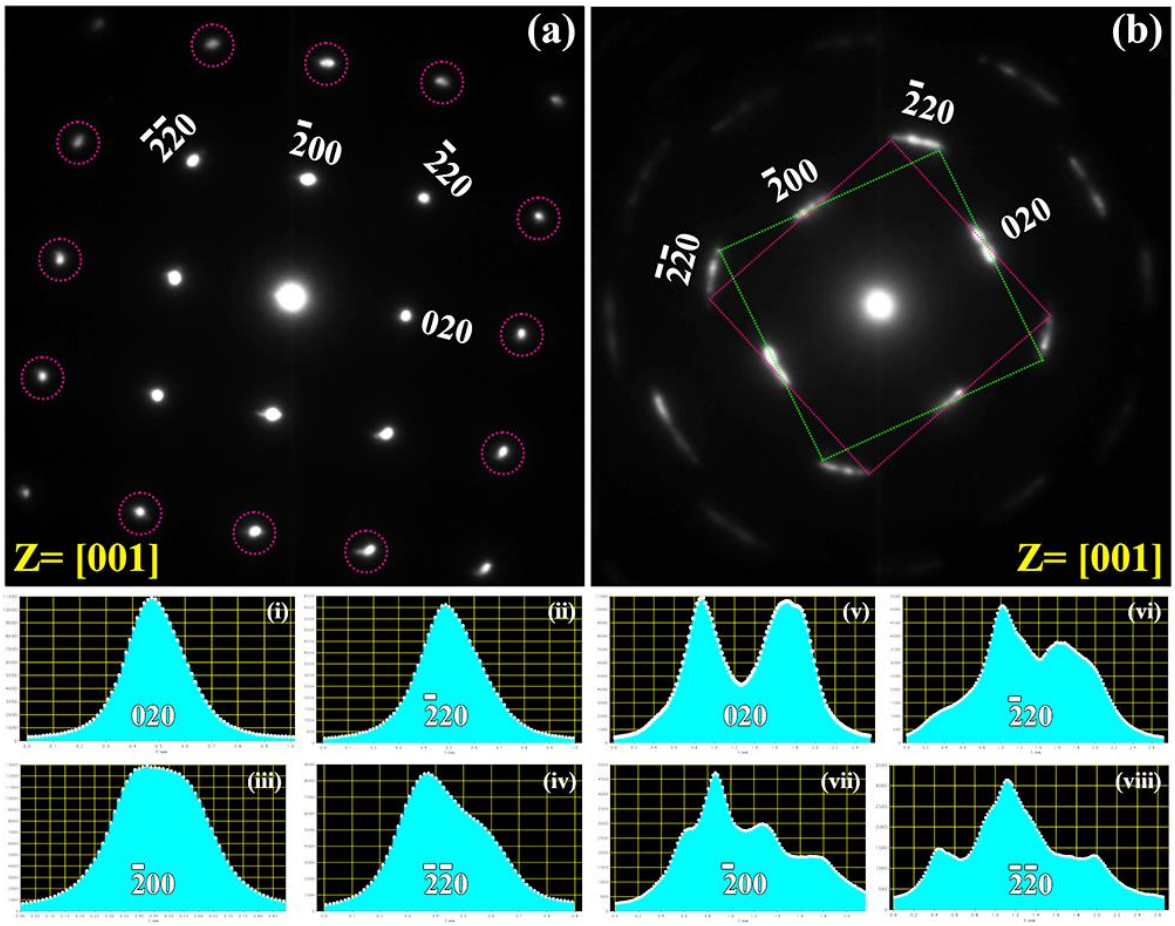

Figure 5.5: (a) Selected area electron diffraction pattern along z=[001] zone axis of (CoMgNi)-oxide after sintering at 1473 K for 10h followed by water quenching. Onset of splitting in the higher order spots (marked by dotted circles) is observed. (i-iv) Intensity distribution plots of 200 and 220 type spots are almost symmetrical. (b) Selected area electron diffraction pattern along z=[001] zone axis of (CoMgNi)-oxide after sintering at 1473 K for 10h, ageing at 723 K for 120h followed by water quenching. The diffraction spots are split and arced with modulation of intensity distribution. (v-viii) Intensity distribution plots of 200 and 220 type spots are not symmetrical with several maxima.

Ternary equimolar (CoMgNi)-oxide has been partially substituted with Fe-ion, Mn-ion and both Fe-, Mn-ion to form equimolar quaternary (CoFeMgNi)-oxide, (CoMgMnNi)-oxide and equimolar quinary (CoFeMgMnNi)-oxide. XRD patterns of the quaternary and quinary derivative oxides after sintering at 1473 K for 10h followed by water quenching is given in Figure 5.6. As reported earlier, (CoMgNi)-oxide after sintering and quenching forms cubic rocksalt phase with *a~4.2 Å* lattice parameter. Upon systematic addition of Fe-ions, in the quaternary (CoFeMgNi)-oxide after sintering at 1473 K for 10h followed by water

quenching the cubic rocksalt phase with *a~4.2 Å* lattice parameter continues to exist. However, the most intense 311 peak of a spinel phase with *a~8.4 Å* lattice parameter appears. Upon systematic addition of Mn-ions, coexistence of two-phase mixture of a cubic rocksalt with *a~4.2 Å* lattice parameter and a cubic spinel with *a~8.4 Å* lattice parameter is observed in the quaternary sintered and quenched (CoMgMnNi)-oxide. In the quinary (CoFeMgMnNi)-oxide, after sintering and quenching, predominantly a spinel phase with *a~8.38 Å* lattice parameter is observed. It is worth mentioning that the diffraction peaks of a cubic rocksalt phase with *a~4.2 Å* (half the lattice parameter of the cubic spinel phase) lattice parameter will overlap with the diffraction peaks of the spinel phase. It is further evidenced by the presence of shoulders in the 222, 400 and 440 diffraction peaks of the spinel phase. It should be noted that, to the best of the knowledge of the authors, quinary multicomponent (CoFeMgMnNi)-oxide has not been reported before. It has been investigated further by electron diffraction after sintering for different lengths of time, which will be reported in the subsequent sections.

TEM BF images and corresponding electron diffraction patterns from the same region of (CoFeMgMnNi)-oxide after sintering at 1473 K for 10h are given in Figure 5.7(a-d). In the BF images extensive mottled contrast is observed and the electron diffraction patterns along z=[001] and z=[$\bar{1}$14] may be indexed to a cubic spinel phase with *a~8.38 Å* lattice parameter. It is noteworthy that in the BF image in Figure 5.7d localized fringe contrast is observed. Magnified view of the fringe contrast is given in Figure 5.7d (inset). Existence of this linear Moire fringe contrast is indicative of two crystals with similar or nearly similar d-spacing are juxtaposed over one another with or without minor tilting [33]. As it has been stated earlier, the structure of spinel and rocksalt phase are quite similar. It may be the juxtaposition of a cubic rocksalt phase over a cubic spinel phase. However, due to the paucity of the diffraction evidence, it may not be confirmed at this stage.

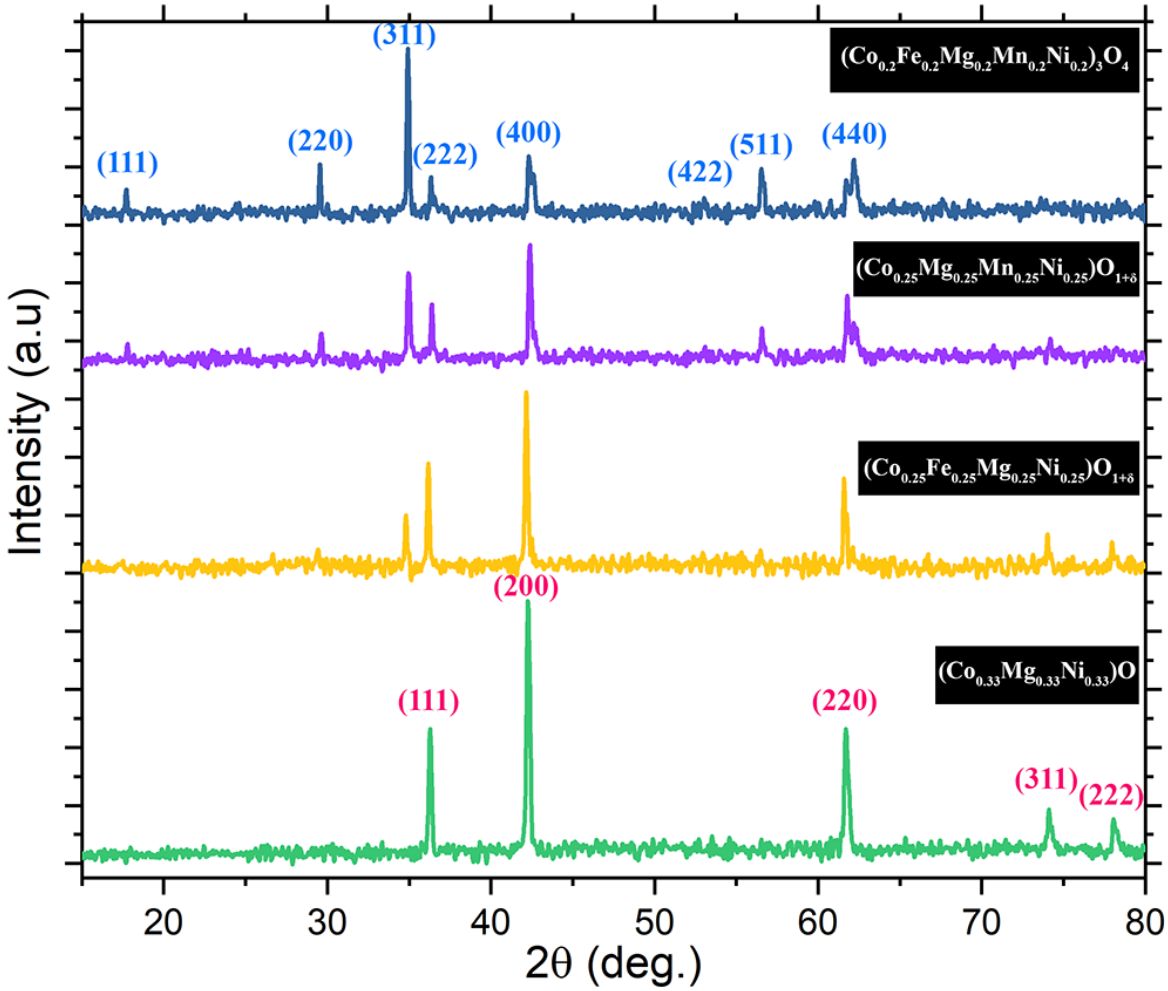

Figure 5.6: X-ray diffraction (XRD) patterns of (CoMgNi)-oxide with systematic addition of Fe- and Mn-ions after sintering at 1473 K for 10h followed by water quenching. With systematic addition of Fe- and Mn-ions the major phase in the equimolar multicomponent oxide changes from cubic rocksalt phase to cubic spinel phase.

TEM BF images from different regions, corresponding electron diffraction patterns and their inverted versions with the indexing for (CoFeMgMnNi)-oxide after sintering at 1473 K for 100 h followed by water quenching are given in Figure 5.8(a-f). In the BF image in Figure 5.8c, mottled and irregular fringe contrast is observed. Existence of such contrast may indicate presence of localized residual strain and structural modulation in the material. Corresponding electron diffraction pattern (Figure 5.8a), shows extensive spot splitting,

arcing and intensity modulation. The inverted version of the diffraction pattern is given in Figure 5.8b. The diffraction pattern may be indexed to a cubic spinel phase with *a~8.33 Å* lattice parameter and a cubic rocksalt phase with *a~ 4.15 Å* lattice parameter. The diffraction vectors for the cubic spinel phase and the cubic rocksalt phase along with their angular relationships and the ratios of the principal vectors are marked in Figure 5.8b in cyan and magenta colour respectively. The diffraction pattern may be indexed to a z=[$\bar{1}$14] zone axis pattern of a cubic spinel phase. It is noted that the first order reflections in this zone axis are weak (marked by cyan arrows in Figure 5.8a and dotted circles in Figure 5.8b) and the second order reflections are strong. The second order reflections are strong as they are common to both the spinel and the rocksalt phase. In addition, arcing, splitting and intensity modulation in the second order spots are observed. When the second order spots are systematically joined together with dotted lines (Figure 5.8a), it clearly brings out the two-fold symmetry shape corresponding to z=[$\bar{1}$14] zone axis of a cubic spinel phase, however, rotated with respect to one another. This clearly indicates that the spinel phase forms structurally modulated domains, which are rotated with respect to one another. Formation of such rotated domains has been reported for quinary (CaCoFeMgNi)-oxide and (CoCuMgNiZn)-oxide after long h of sintering or ageing. It will be discussed further in the discussion section. There are some additional diffraction spots in the diffraction pattern in Figure 5.8a and its inverted version in Figure 5.8b. Those spots are marked in magenta along with the ratio of the principal vectors. The spots are joined together with magenta dotted lines (Figure 5.8a), that brings out a four-fold symmetry shape. The additional spots may be indexed to a cubic rocksalt phase along z=[001] zone axis *a~ 4.15 Å* lattice parameter. It is due to the simultaneous presence of a cubic spinel phase with the rocksalt phase intensity modulation is observed in the diffraction pattern.

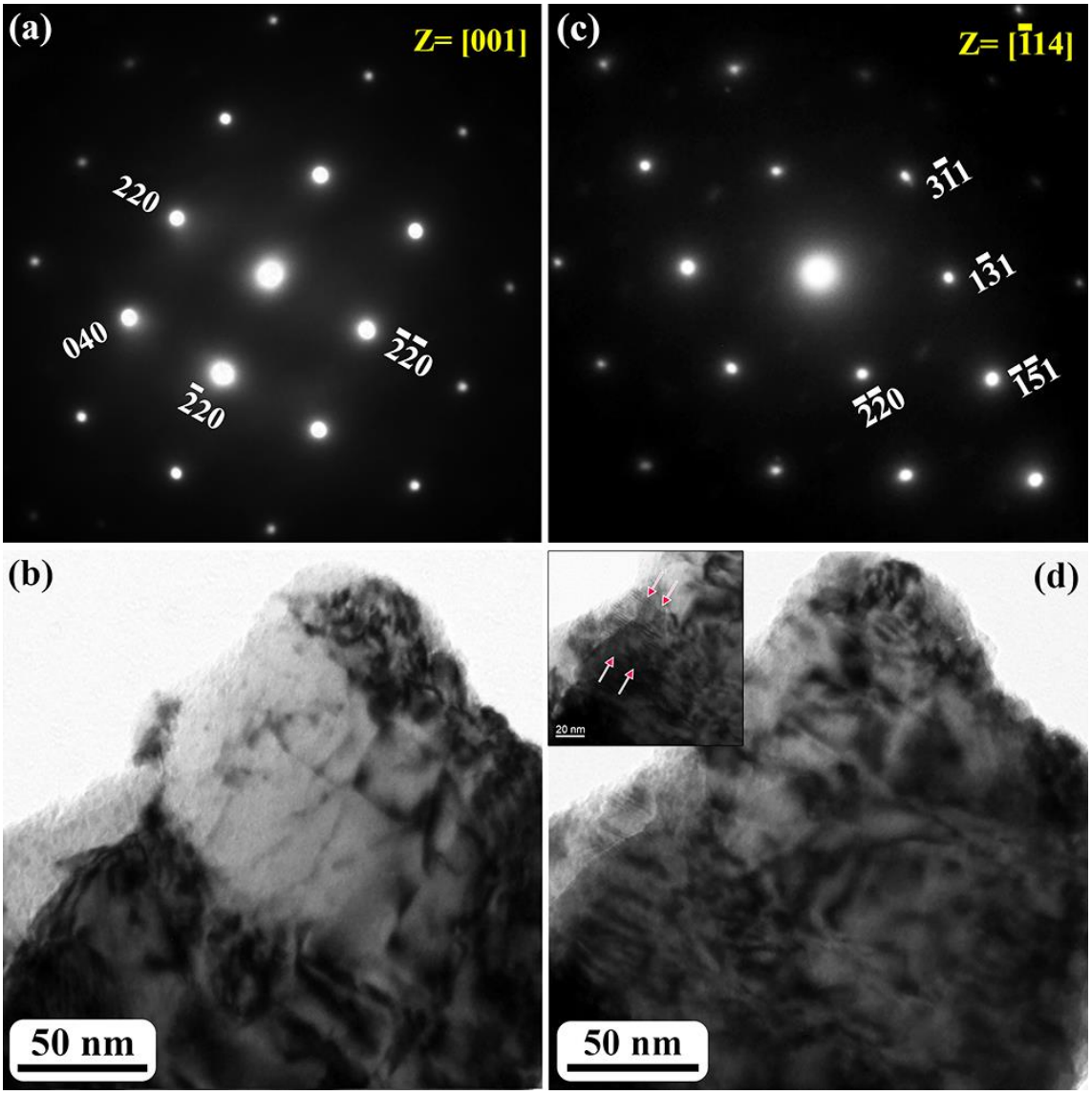

Figure 5.7: (a, c) Selected area electron diffraction patterns along z=[001] and z=[$\bar{1}$14] zone axes respectively and (b, d) bright field images of the multicomponent equimolar (CoFeMgMnNi)-oxide after sintering at 1473 K for 10h followed by water quenching. Electron diffraction patterns are indexed to a cubic spinel phase (a~8.38 Å). In the bright field images mottled contrast with occasional fringe contrast (Figure 7d inset) is observed.

It is noteworthy that there is an orientation relationship between the rocksalt phase and the spinel phase, which may be written as $[\bar{1}14]_{Spinel} \parallel [001]_{Rocksalt}$ and $(440)_{Spinel} \parallel (\bar{2}\bar{2}0)_{Rocksalt}$. BF image from a different region (Figure 5.8d) shows a domain like contrast in addition to the irregular fringe contrast. The corresponding electron diffraction pattern and its inverted version are given in Figure 5.8e and Figure 5.8f respectively. In this diffraction pattern also

modulation of intensity is observed and it may be indexed to z=[012] zone axis of a cubic spinel phase and z=[013] of a cubic rocksalt phase. The spots corresponding to the spinel phase, rocksalt phase, their principal vectors and their ratios are marked in cyan and magenta respectively. Similar orientation relationship is evident in this diffraction pattern. The orientation relationship is $[012]_{Spinel} \parallel [013]_{Rocksalt}$ and $(400)_{Spinel} \parallel (\bar{2}00)_{Rocksalt}$.

Effect of substitution of Cr-ions in place of Mg-ions in the quinary equimolar (CoFeMgMnNi)-oxide after sintering followed by quenching, which results into an equimolar quinary (CoCrFeMnNi)-oxide, has been studied by XRD and TEM. It is noteworthy that equimolar (CoCrFeMnNi)-oxide is the first ever reported single-phase spinel forming high entropy oxide (HEO). It is also the oxide form of the first reported high entropy Cantor alloy. In the XRD pattern of the sintered and quenched (CoFeMgMnNi)-oxide (Figure 5.9), cubic spinel phase with *a~8.38 Å* lattice parameter and cubic rocksalt phase with *a~4.2 Å* in minor proportion are observed. In the XRD pattern of the (CoCrFeMnNi)-oxide after sintering at 1473 K for 10h, cubic spinel phase with *a~8.36 Å* lattice parameter is predominantly observed. However, shoulders are observed in 222, 400 and 440 peaks, which can be directly indexed as the 111, 200 and 220 peak of a cubic rocksalt phase with half the lattice parameter. The XRD patterns of the same oxide after sintering and quenching, in pellet and powder form (Figure 5.9), have been compared and they do not show any significant difference except peak broadening and concomitant reduction in peak intensity. It may be inferred that in (CoCrFeMnNi)-oxide after sintering and quenching cubic spinel phase forms predominantly. However, there might be a possibility of oriented growth of cubic rock phase with half the lattice parameter within the spinel phase.

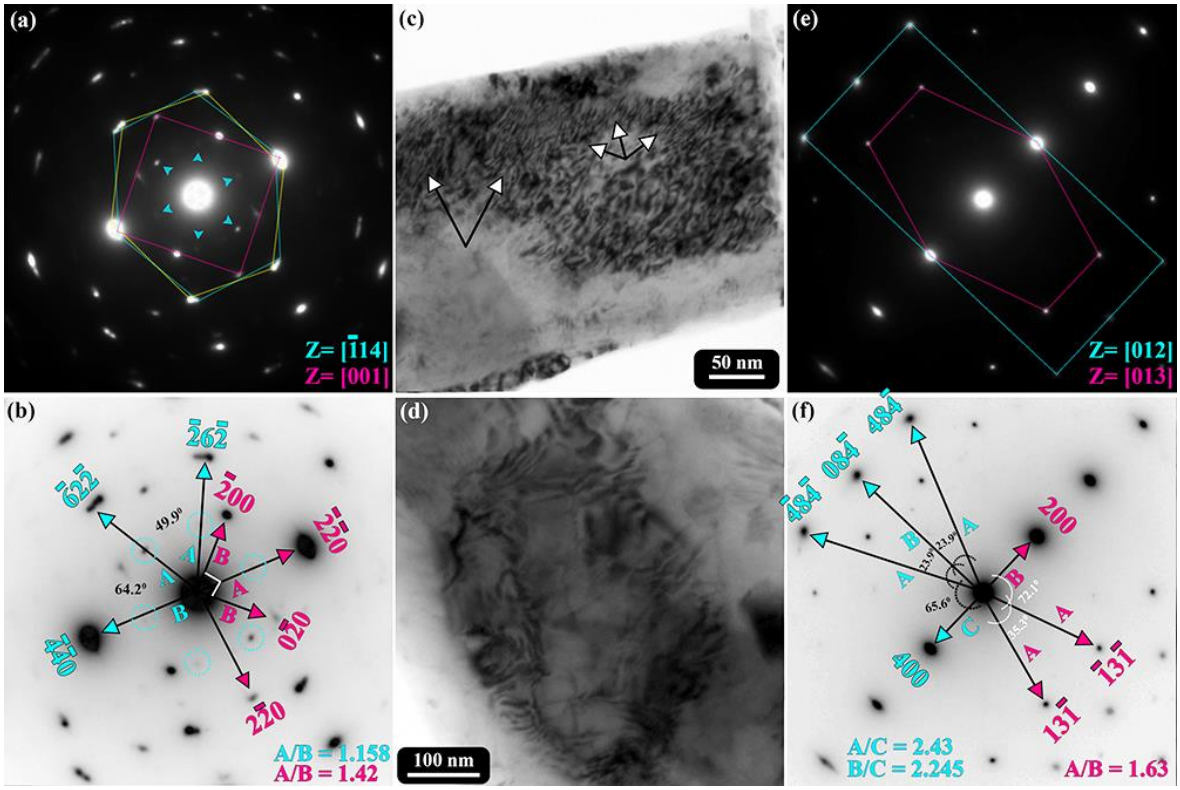

Figure 5.8: Selected area electron diffraction patterns and bright field images of (CoFeMgMnNi)-oxide after sintering at 1473 K for 100h followed by water quenching. The diffraction pattern in (a) is indexed to a cubic spinel phase, z=[$\bar{1}$14] zone axis along with a coexistent rocksalt phase, z=[001] zone axis. Indices of the diffraction spots, their angular relationships and ratios of principal vectors are given in (b), which is inverted with respect to (a). In the corresponding bright field image in (c), extensive fringe contrast (marked by arrows) within the mottled contrast is observed. The diffraction pattern in (e) is indexed to the same cubic spinel phase, z=[012] zone axis along with the coexistent cubic rocksalt phase, z=[013] zone axis. Indices of the diffraction spots, their angular relationships and the ratios of the principal vectors are given in (f), which is inverted with respect to (e). The corresponding bright field image in (d) shows domain like structure along with fringe contrast. Orientation relationship between the cubic spinel phase and the cubic rocksalt phase is evident.

TEM images and corresponding electron diffraction patterns of (CoCrFeMnNi)-oxide after sintering at 1473 K for 10h followed by quenching are given in Figure 5.10(a-f). In the electron diffraction pattern (Figure 5.10c) along z=[001], clear four-fold symmetry of the zone axis is observed. The diffraction pattern may be indexed to a cubic spinel phase with *a~8.36 Å* lattice parameter. It is noteworthy that the diffraction spots are diffused and a continuous streaking along 220 type vectors is observed.

It necessarily indicates the presence of continuous structural modulation in the multicomponent oxide. In the BF image (Figure 5.10a), a fine scale modulation is observed. In the magnified version of the BF image, given in Figure 5.10d, coexistence of structural modulation along two perpendicular directions is observed. The existence of such structural modulations leads to the formation of a domain morphology (marked in Figure 5.10d), which are ~5nm X 5nm is size. In the centred DF image (Figure 5.10b) with 220 spot under multibeam excitation, similar modulation is observed. The domains with alternate bright and dark contrast are marked in Figure 5.10b.

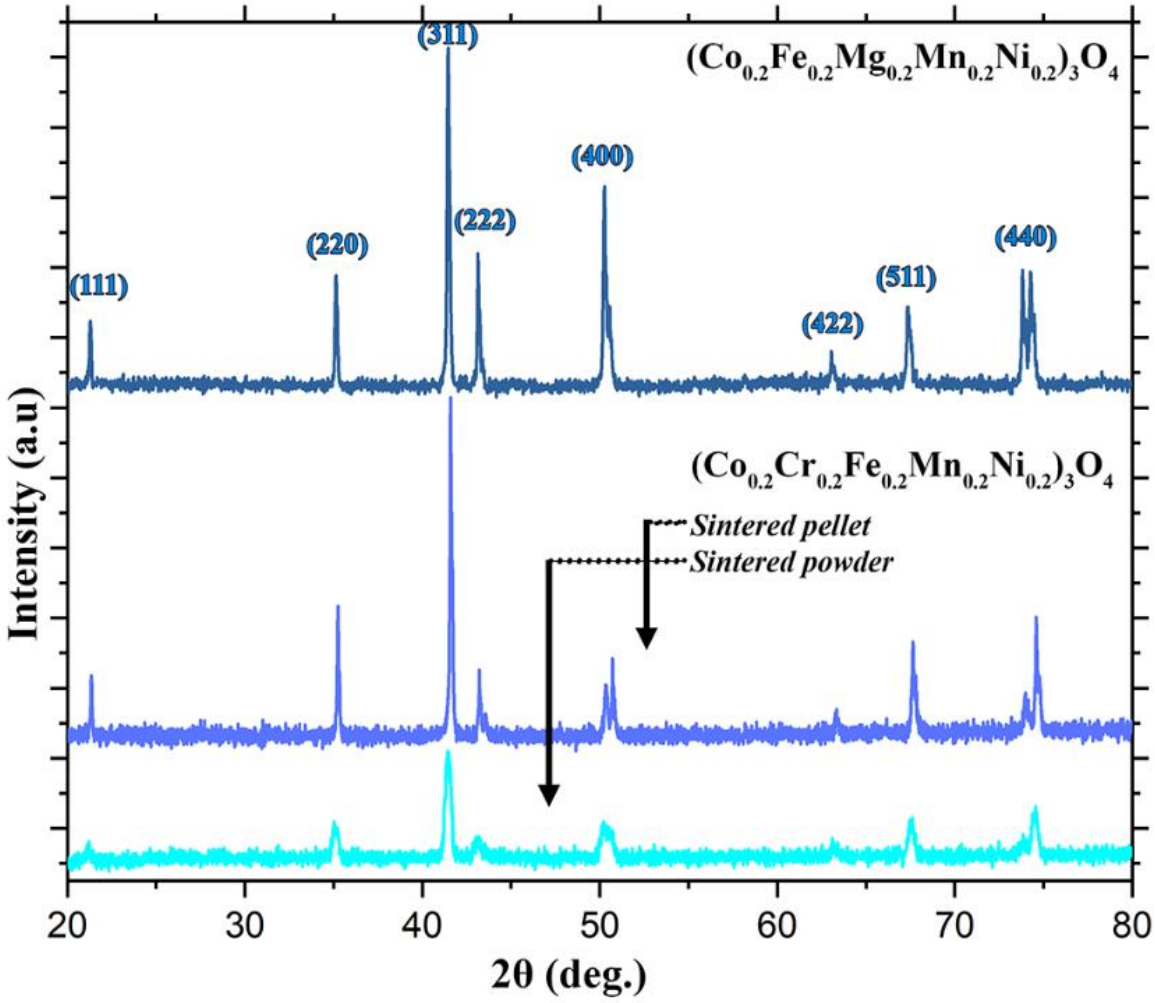

Figure 5.9: X-ray diffraction (XRD) patterns of (CoFeMgMnNi)-oxide and (CoCrFeMnNi)-oxide after sintering at 1473 K for 10h followed by water quenching. In both of the multicomponent oxides cubic spinel phase is observed to be the predominant phase with systematic peak splitting and shouldering.

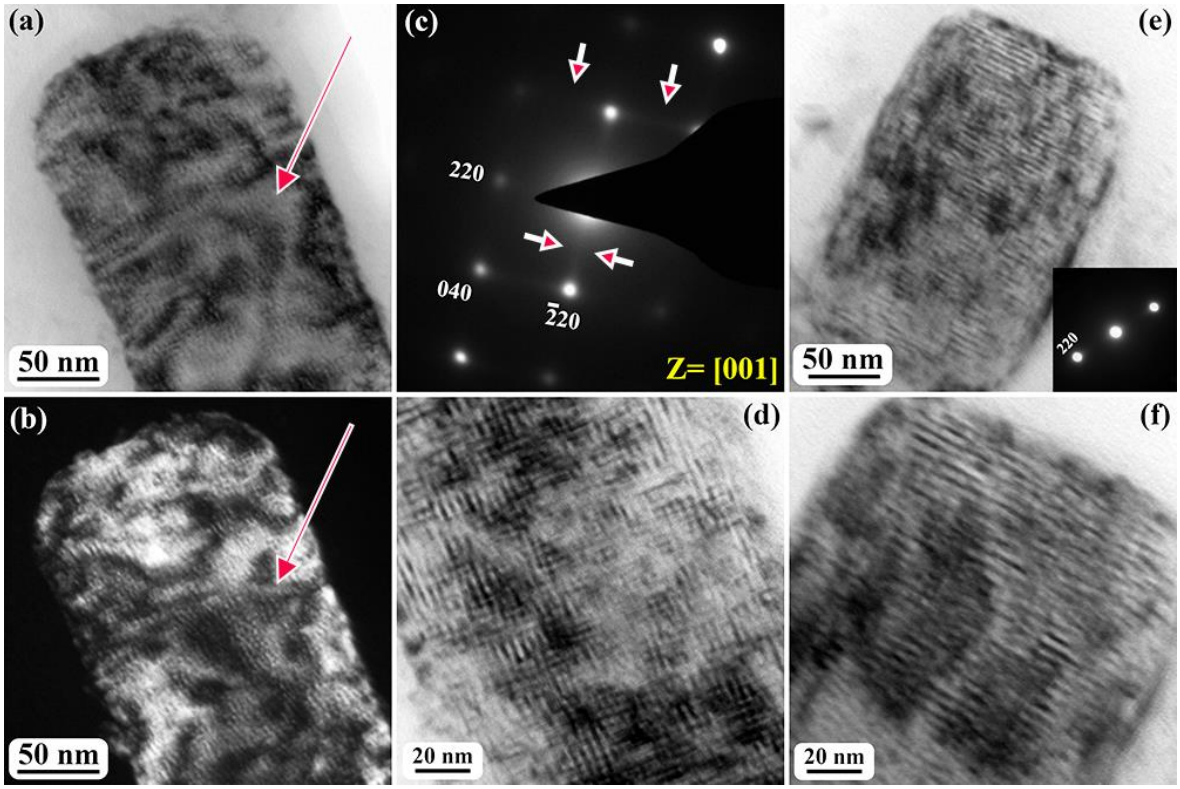

Figure 5.10: (a-f) Bright field, centred dark field and selected area electron diffraction patterns of (CoCrFeMnNi)-oxide after sintering at 1473 K for 10h followed by water quenching. The diffraction pattern in (c) is indexed to a cubic spinel phase, z=[001] zone axis. The diffraction spots are diffused with streaking along mutually perpendicular 220 type directions (marked with arrows). In the bright field image in (a) and corresponding centred dark field image in (b) modulation and formation of nanodomains are observed (marked with arrows). In two-beam bright field image in (e) and in (f) modulation along 220 direction is observed. Corresponding two beam diffraction pattern is given in the inset of (e). Cross penetration of modulation leading to the formation of domains is shown in the high magnification image in (d).

BF image of the same region with only 220 row of spots excited (Figure 5.10e) shows the modulation in only one direction perpendicular to the 220 reciprocal lattice vectors. The magnified version of the same region (Figure 5.10f) shows the modulation perpendicular to 220 type directions with modulation wavelength of ~5nm giving birth to a lamellar appearance. It may be inferred that the modulation develops in the spinel phase along 220 type directions. It will be discussed in detail in the discussion section.

5.4. Discussion

Systematic synthesis followed by XRD and TEM experimentations of quinary equimolar (CoFeMgMnNi)-oxide, (CoCrFeMnNi)-oxide and its binary, ternary quaternary derivative oxides establish a pattern in terms of evolution of cubic spinel and rocksalt phases, their orientation relationship and microstructural growth during sintering and ageing at different temperatures over varying lengths of time. Quinary multicomponent oxides and its derivatives are metastable in nature, which keep on changing their phase fraction, structural modulation and microstructural growth. A bird eye view of the fundamental nature of these equimolar multicomponent oxides is discussed in the following sections.

5.4.1. Phase evolution and structural correlation between spinel and rock salt

Ternary equimolar mixture of Co(II,III)O, MgO and NiO upon dry milling for 40 h results in a phase mixture of cubic spinel and rocksalt phases. The lattice parameter of the resulting spinel phase is almost double of the rocksalt phase. Initially NiO and MgO oxide act as the host lattice for rocksalt structure, in which CoO is incorporated. In the same line, Co_3O_4 phase with spinel structure acts as the host lattice for the spinel phase in which Ni- and Mg-ions are incorporated. It is further observed that with the progress of milling and solid solution formation, strain induced broadening of diffraction peaks takes place with a concomitant shift in its mean position (Figure 5.1). Shift in the peak position is not uni-directional. Shift in the peak position may directly be associated with the change in d-spacings, lattice parameter and cell volume. It is understood that with the progress of milling, vacancy concentration in the lattice continues to increase. Continuous change in the vacancy concentration in the spinel and in the rocksalt phase is one of the reasons behind the change in the d-spacings, lattice parameter and the cell volume. As the spinel and the rocksalt phases are associated through the vacancy concentration, the relative phase

fraction of spinel and the rocksalt phases changes that leads to a shift in the mean position of the peak. In this connection it is important to explain the structural correlation between the spinel phase and the rocksalt phase. In both the phases, oxygen forms the FCC lattice, in case of the rocksalt phase all the octahedral voids are filled up with cations and in case of the spinel phase half the octahedral voids are filled with cations. This explains that the rocksalt phase may transform to a spinel phase when vacancy concentration is changed and vice versa. After sintering the mixed powder, similar spinel and rocksalt phases are observed in the pellet. On addition of Fe- and Mn-ions in the ternary (CoMgNi)-oxide, i. e. in the quaternary (CoFeMgNi)-oxide and in the (CoMgMnNi)-oxide also similar phase mixture of rocksalt and spinel is observed. However, in quinary (CoFeMgMnNi)-oxide and (CoCrFeMnNi)-oxide predominantly spinel is observed. Predominant spinel phase formation in the quinary oxide may be attributed to the multiple oxidation states of Fe, Cr and Mn and related Jan Teller distortions in the lattice.

5.4.2. Oriented growth of spinel, rocksalt phases and its interface structure

In the (CoMgNi)-oxide after sintering at 1473 K for 10 h, predominantly rocksalt phase with *a~4.2 Å* lattice parameter is observed. In the electron diffraction pattern of the rocksalt phase diffuseness in the primary diffraction spots and minor arcing and split in the higher order spots is observed (Figure 5.4(a-d) and Figure 5.5a). Diffuseness in the primary diffraction spots and split in the higher order spots may be attributed to the residual strain in the rocksalt crystal due to the presence of multiple cations in the phase. Mottled contrast in the BF image (Figure 5.4c) confirms the presence of residual strain the crystal. However, ageing at 723 K for 120 h, results in arcing in the diffraction spots (Figure 5.5b). It may be explained by the formation of structurally modulated domains in the rocksalt phase and a continuous relative rotation between the domains. Structurally modulated domain

formation and relative rotation between them takes place in order to reduce the lattice strain in the crystal. In the corresponding TEM images (Figure 5.4(e-f)) formation of irregular fringe contrast is observed. Inter-fringe spacing may directly be correlated with the stacking of domains with relative in-plane and out-of-plane rotation. Similar domain formation, relative rotation between them has been observed in (CaCoFeMgNi)-oxide and (CoCuMgNiZn)-oxide before.

In quinary (CoFeMgMnNi)-oxide after sintering at 1473 K for 10 h, spinel phase forms predominantly. In the electron diffraction pattern of the spinel phase similar diffuseness in the diffraction spots is observed (Figure 5.7a and Figure 5.7c). When the quinary oxide is sintered for 100 h at 1473 K, modulation of intensity in the diffraction pattern and systematic appearance of extra spots are observed (Figure 5.8a and Figure 5.8e) and it may be directly correlated to the oriented growth of a rocksalt phase within the spinel phase with almost half the lattice parameter of the spinel phase. The interface diagram of the spinel phase with the rocksalt phase has been presented schematically in Figure 5.11. The interface is semi-coherent. It is understood that such orientation relationship develops in a bid to reduce the interface strain through continuous reconstructive transformations at the interfaces. In a similar way, in the (CoCrFeMnNi)-oxide after sintering at 1473 K for 10 h structurally modulated domains (Figure 5.10a-f) are observed with continuous diffuse streaking in the diffraction pattern along 220 type directions. Structural modulations in multicomponent oxides appears to be a common phenomenon which takes place in order to reduce strain in the crystal. The structural and compositional modulations grow with time as has been reported in (CoFeMn)-oxide before [30].

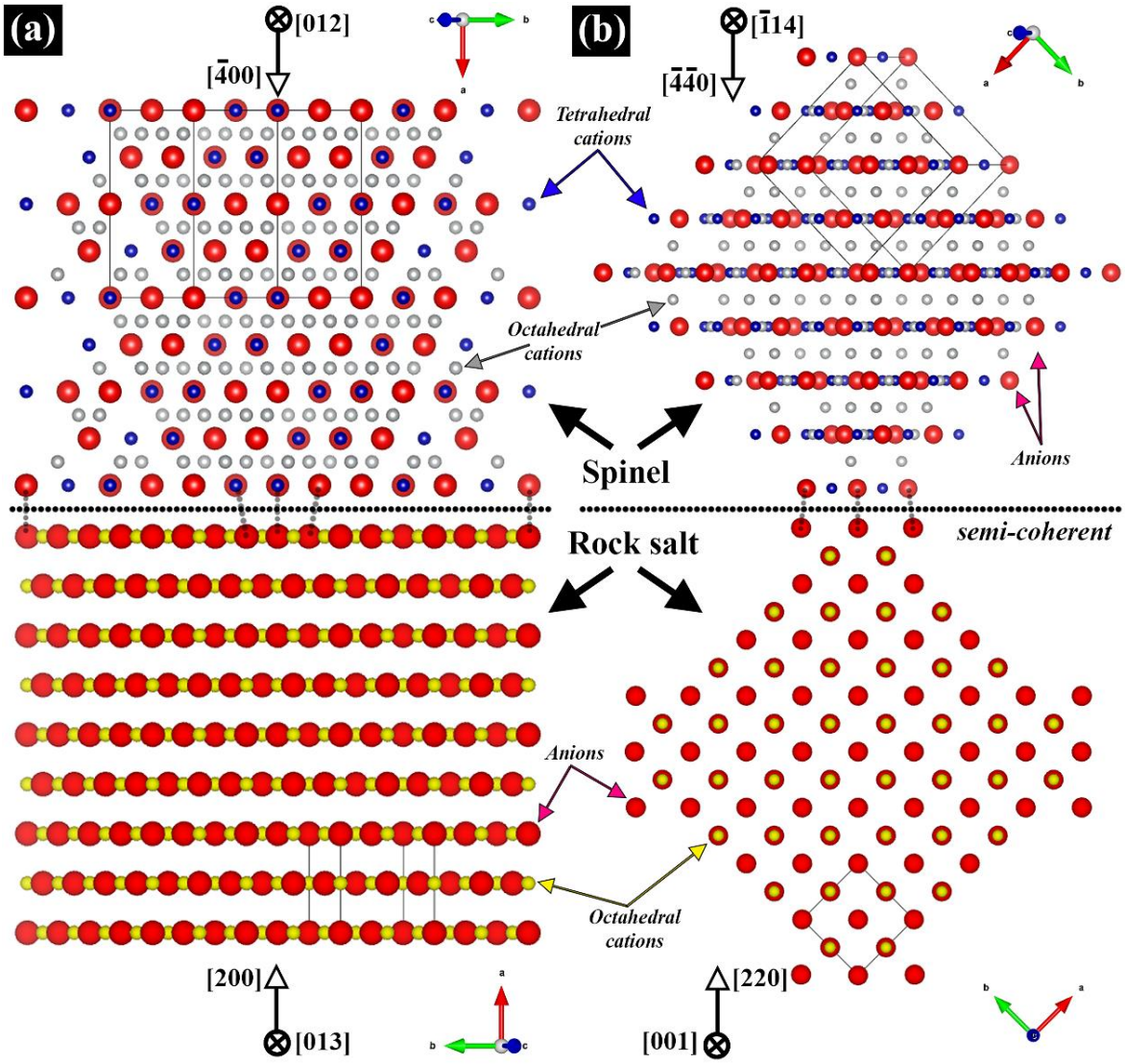

Figure 5.11: Projected interface structure diagram between cubic spinel phase and cubic rocksalt phase. The interface structure diagram has been developed based on the experimentally observed orientation relationship between the cubic spinel phase and the cubic rocksalt phase. The interfaces are semi-coherent in nature.

5.4.3 Stabilization through energy minimization

In the multicomponent quinary (CoFeMgMnNi)-oxide and (CoCrFeMnNi)-oxide, spinel phase forms after sintering. However, with prolonged sintering or ageing oriented growth of rocksalt phase and development of structural modulation is clearly visible. It is also understood that oriented growth and structural modulation takes place in order to minimize strain in the crystal. Quinary multicomponent oxides are metastable and with energy impetus from outside in the form of prolonged exposure at higher temperature, these oxides

try to reduce their energy through minimization of strain in the crystal, which manifests itself as domain formation, their relative rotation, coherent/semi-coherent interface formation etc. Similar trend has been observed for (CaCoFeMgNi)-oxide and (CoCuMgNiZn)-oxide. Multicomponent oxides are believed to be entropy stabilized. However, the authors have noted a complex interplay between entropy and strain energy that leads to the energy minimization. Gibbs free energy may be written as $\Delta G = \Delta H - T\Delta S$, where the symbols have their usual meaning. Further, $\Delta H = \Delta U + P\Delta V$ for a constant pressure process. Combining both the equations, Gibbs free energy equation may be written as $\Delta G = \Delta U + P\Delta V - T\Delta S$. The term $P\Delta V$ represents mechanical energy associated with the transformation. In a multicomponent oxide, due to the presence of several cations in the lattice, configurational entropy is high that maximizes the negative contribution of the $T\Delta S$ term. However, maximizing the entropy comes with a cost of enhanced strain the lattice, which is reflected by the $P\Delta V$ term. In order to make the Gibbs free energy component optimally negative, the system tries to modulate itself compositionally and structurally that reduces the negative contribution of the entropy term. However, through structural and compositional modulations it forms coherent/semi-coherent interfaces and reduces the lattice strain. That is how it reduces the positive contribution of the $P\Delta V$ term. It is a trade-off between the entropy and the strain energy that minimizes the Gibbs free energy of the system. The authors would tend to believe that in multicomponent systems, it is not only the entropy that determines the stability. It is a trade-off between entropy and strain energy that determines the stability of the system.

5.5. Conclusions

High-energy ball-milling sets up a competition between rocksalt and spinel phases which is driven by the build-up of vacancies and its varying concentration in the phases, which keeps on changing with milling time. Equimolar ternary (CoMgNi)-oxide, previously

anticipated as the host structure for the stabilization of quinary phase-pure (CoCuMgNiZn)-oxide with rocksalt structure, co-exists with small volume fraction of spinel phase. Furthermore, it is metastable with respect to intermediate temperature ageing heat treatment, and microstructural features appear due to the formation of intergrown domain structure arising out of successive mutual in-plane and out-of-plane rotations.

Systematic substitution of Mn- and Fe-ions in (CoMgNi)-oxide transforms the global average single-phase with rocksalt structure to a global average single-phase with spinel structure in equimolar (CoFeMgMnNi)-oxide, being reported for the first time. Prolonged exposure to high temperature in (CoFeMgMnNi)-oxide leads to precipitation of a rocksalt phase of half the lattice parameter, which develops according to definite orientation relationships with its parent spinel phase sharing semi-coherent boundaries between them. Structural modulation observed in sintered and quenched equimolar (CoCrFeMnNi)-oxide along <220> crystallographic directions was previously unanticipated. Furthermore, local composition modulation induced formation of nanometer-sized domains, which in turn brings out the shortcomings of the high entropy effect.

5.6. Reference

[1] W. Bian, H. Li, Z. Zhao, H. Dou, X. Cheng, X. Wang, Entropy stabilization effect and oxygen vacancy in spinel high-entropy oxide promoting sodium ion storage, Electrochimica Acta, 2023, 447, 142157 (10 pages)

[2] F. Zhai, X. Zhu, W. Zhang, G. Cao, H. Zhang, Y. Xing, Y. Xiang, S. Zhang, Insight of the evolution of structure and energy storage mechanism of $(FeCoNiCrMn)_3O_4$ spinel high entropy oxide in life-cycle span as lithium-ion battery anode, J. Power Sources, 2024, 603, 234418 (11 pages)

[3] D. Berardan, S. Franger, D. Dragoe, A.K. Meena, N. Dragoe, Colossal dielectric constant in high entropy oxides, Phys. Status Solidi RRL, 2016, 10, 328-333

[4] H. Wu, Q. Lu, Y. Li, J. Wang, Y. Li, R. Jiang, J. Zhang, X. Zheng, X. Han, N. Zhao, J. Li, Y. Deng, W. Hu, Rapid joule-heating synthesis for manufacturing high entropy oxides as efficient electrocatalysts, Nano Lett., 2022, 22, 6492-6500

[5] J. Zhang, J. Yan, S. Calder, Q. Zheng, M.A. McGuire, D.L. Abernathy, R. Ren, S.H. Lapidus, K. Page, H. Zheng, J.W. Freeland, J.D. Budai, R.P. Hermann, Long-range antiferromagnetic order in a rocksalt high entropy oxide, Chem. Mater., 2019, 31, 3705-3711

[6] H. Yang, Q. Chen, J. Zhu, G. Jiang, L. He, N. Qiu, Y. Wang, Selective construction of amorphous/crystalline heterostructure high entropy oxide for Li-ion batteries, J. Alloys Comp., 2024, 986, 174140 (9 pages)

[7] M.P.J. Segura, T. Takayama, D. Berardan, A. Hoser, M. Reehuis,H. Takagi, N. Dragoe, Long-range magnetic ordering in rocksalt-type high-entropy oxides, Appl. Phys. Lett., 2019, 114, 122401-5

[8] C. M. Rost, E. Sachet, T. Borman, A. Moballegh, E.C. Dickey, D. Hou, J.L. Jones, S. Curtarolo, J.P. Maria, Entropy-stabilized oxides, Nat. Commun., 2015, 6, 9485 (8 pages)

[9] J. Dabrowa, M. Stygar, A. Mikula, A. Knapik, K. Mroczka, W. Tejchman, M. Danielewski, M. Martin, Synthesis and microstructure of the $(Co,Cr,Fe,Mn,Ni)_3O_4$ high entropy oxide characterized by spinel structure, Mat. Lett., 2018, 216, 32-36

[10] L. Lin, K. Wang, R. Azmi, J. Wang, A. Sarkar, M. Botros, S. Najib, Y. Cui, D. Stenzel, P.A. Sukkurji, Q. Wang, H. Hahn, S. Schweidler, B. Breitung, Mechanochemical synthesis: route to novel rock-salt-structured high-entropy oxides and oxyfluorides, J. Mater. Sci., 2020, 55, 16879-89

[11] B.L. Musico, D. Gilbert, T.Z. Ward, K. Page, E. George, J. Yan, D. Mandrus, V. Keppens, The emergent field of high entropy oxides: Design, prospects, challenges and opportunities for tailoring material properties, APL Mater., 2020, 8, 040912 (17 pages)

[12] R. J. Clement, Z. Lun, G. Ceder, Cation-disordered rocksalt transition metal oxides and oxyfluorides for high-energy lithium-ion cathodes, Energy Environ. Sci., 2020, 13, 345 (29 pages)

[13] C.M. Rost, D.L. Schmuckler, C. Bumgardner, M.S.B. Hoque, D.R. Diercks, J.T. Gaskins, J.P. Maria, G.L. Brennecka, X. Li, P.E. Hopkins, On the thermal and mechanical properties of $Mg_{0.2}Co_{0.2}Ni_{0.2}Cu_{0.2}Zn_{0.2}O$ across the high-entropy to entropy-stabilized transition, APL Mater., 2022, 10, 121108 (7 pages)

[14] W. Hong, F. Chen, Q. Shen, Y.H. Han, W.G. Fahrenholtz, L. Zhang, Microstructural evolution and mechanical properties of (Mg,Co,Ni,Cu,Zn)O high-entropy ceramics, J. Am. Ceram. Soc., 2019, 102, 2228-2237

[15] J. Lu, K.S. Lee, Spinel cathodes for advanced lithium ion batteries: a review of challenges and recent progress, Mater. Technology, 2016, 1208957 (15 pages)

[16] N.J. Usharani, R. Shringi, H. Sanghavi, S. Subramanian, S.S. Bhattacharya, Role of size, alio-/multi-valency and non-stoichiometry in the synthesis of phase-pure high entropy oxide (Co,Cu,Mg,Ni,Na,Zn)O, Dalton Trans., 2020, 49, 7123 (10 pages)

[17] H. Yang, L. He, Z. Yang, Q. Chen, G. Jiang, J. Zhu, R. Xue, N. Qiu, Y. Wang, Design optimization of spinel-rocksalt intergrown high entropy oxide structure for enhanced electrochemical properties, J. Alloys Comp., 2023, 968, 172135 (12 pages)

[18] A.D. Dupuy, M.R. Chellali, H. Hahn, J.M. Schoenung, Nucleation and growth behaviour of multicomponent secondary phases in entropy-stabilized oxides, J. Mater. Res., 2023, 38, 198-214

[19] A.D. Dupuy, I.T. Chiu, P. Shafer, E. Arenholz, Y. Takamura, J.M. Schoenung, Hidden transformations in entropy-stabilized oxides, J. Eu. Ceram. Soc., 2021, 41, 6660-6669

[20] Z. Rak, J.P. Maria, D.W. Brenner, Evidence for Jahn-Teller compression in the (Mg,Co,Ni,Cu,Zn)O entropy-stabilized oxide: A DFT study, Mat. Lett., 2018, 217, 300-303

[21] M. Frachhia, M. Coduri, M. Manzoli, P. Ghigna, U.A. Tamburini, Is configurational entropy the main stabilizing term in rock-salt $Mg_{0.2}Co_{0.2}Ni_{0.2}Cu_{0.2}Zn_{0.2}$ high entropy oxide, Nat. Commun., 2022, 13, 2977 (4 pages)

[22] G. Anand, A.P. Wynn, C.M. Handley, C.L. Freeman, Phase stability and distortion in high-entropy oxides, Acta Mater., 2018, 146, 119-125

[23] Z. Grzesik, G. Smola, M. Stygar, J. Dabrowa, M. Zajusz, K. Mroczka, M. Danielewski, Defect structure and transport properties in (Co,Cu,Mg,Ni,Zn)O high entropy oxide, J. Eu. Ceram. Soc., 2019, 39, 4292-4298

[24] J. Baek, M.D. Hossain, P. Mukherjee, J. Lee, K.T. Winther, J. Leem, Y. Jiang, W.C. Chueh, M. Bajdich, X. Zheng, Synergistic effects of mixing and strain in high entropy spinel oxides for oxygen evolution reaction, Nat. Commun., 2023, 14, 5936 (11 pages)

[25] A. Navrotsky, O.J. Kleppa, The thermodynamics of cation distributions in simple spinels, J. Inorg. Nucl. Chem., 1967, 29, 2701-2714

[26] Y. Horibe, S. Takeyama, S. Mori, Large-scale phase separation with nano-twin domains in magnetite spinel $(Co,Fe,Mn)_3O_4$, AIP conf. Proc., 2016, 1763, 050005 (5 pages)

[27] P.K. Davies, M. Akaogi, Phase intergrowths in spinelloids, Nature, 1983, 305, 788-790

[28] K. E. Sickafus, J.M. Wills, N.W. Grimes, Spinel compounds: Structure and property relations, J. Am. Ceram. Soc., 1999, 82, 3279-92

[29] A. Singh, S. Yasui, A.S. Pal, L.A. Bendersky, I. Takeuchi, R.K. Mandal, J. Basu, Structure and interfaces of compositionally graded $Li(Ni,Mn)_xO_y$ cathodes on (111) Nb-doped $SrTiO_3$, Philosophical Magazine, 2022, 102, 1547-1579

[30] A.S. Pal, A.K.L. Das, K. Gururaj, M. Sadhasivam, K.M. Knowles, Md. I. Ahmad, K.G. Pradeep, J. Basu, Nanoarchitectonics of self-assembled chessboard-like structures by recurrent phase separation and coalescence of nano domains in CoFeMn oxide, Acta Mater., 2023, 242, 118423 (12 pages)

[31] D. Berardan, A. K. Meena, S. Franger, C. Herrero, N. Dragoe, Controlled Jahn-Teller distortion in (MgCoNiCuZn)O-based high entropy oxides, J. Alloys Comp., 2017, 704, 693-700

[32] S. Mukherjee, N.K. Mukhopadhyay, J. Basu, Local composition modulation and oriented inter-growth induced strain minimization in entropy stabilized (CoCuMgNiZn) oxide [Communicated]

[33] S. Mukherjee, N.K. Mukhopadhyay, J. Basu, Composition modulation, strain minimization and oriented growth of phases in equimolar (CaCoFeMgNi) multicomponent oxide, Acta Mater., 2025, 285, 120621 (12 pages)

[34] B. Cantor, I. T. H. Chang, P. Knight, A. J. B. Vincent, Microstructural development in equiatomic multicomponent alloys, Mater. Sci. Eng. A, 2004, 375-377, 213-218

[35] A. S. Pal, A. K. L. Das, A. Singh, K. M. Knowles, M. I. Ahmad, J. Basu, Evolution of a self-assembled chessboard nanostructure spinel in a CoFeGaMnZn multicomponent oxide, Philos. Mag., 2022, 102(12), 1121-1135

Chapter – 6

Structure-activity relationship for electrocatalysis in rocksalt and spinel based multicomponent oxides and its derivatives

6.1. Introduction

The accelerated depletion of fossil fuel reserves coupled with rapidly changing geo-political scenario has put alternative energy sources, its conversion and storage at the forefront of research activities globally [1-3]. Renewable-energy based economy is driving the modern society away from fossil-fuel based economy slowly and steadily [4-6]. However, the age-old tradition of producing hydrogen using coal or natural gas is still prevalent, continuously degrading the environment in the process and is likely to be ceased as an option in the near future [4,5]. In this context, production, storage and transportation of hydrogen has emerged as the new energy currency [6-8]. However, most renewable sources of energy are intermittent and spurious, which calls for material containers for efficient energy storage and conversion techniques [9,10]. Thus, the ability to split water efficiently and effectively to produce clean hydrogen plays a vital role in energy sciences with the potential to help decarbonize the global energy harvesting system [6-8]. There are three broad ways of splitting water to obtain clean hydrogen i.e. thermochemical, electrochemical and photochemical methods which produces oxygen through oxygen evolution reaction (OER) at the anode and hydrogen through hydrogen evolution reaction (HER) at the cathode as redox pairs [11]. The major bottleneck in electrochemical water-splitting experiments is the high activation barrier for a 4-electron transfer process for efficient OER and HER making it kinetically extremely sluggish, requiring very high input energy as overpotential to break the O-H bonds [12]. Thus, developing efficient electrocatalysts and understanding the properties in relation to its composition, phase(s) and structure promises the way forward [13-15]. Noble metal oxides IrO_2 and RuO_2 remains to be the state-of-the-art electrocatalysts, however, their extremely high cost and scarcity has led to a resurgence of developing multicomponent oxides in the last few decades [15].

Moreover, there is a dearth of literature so far, the structure-property correlation of high entropy oxides or multicomponent oxides (HEOs/MCOs) are concerned. The current work has been carried out to understand the factors affecting the electrocatalytic performances of phase pure rocksalt and spinel HEOs, two-phase mixture of rocksalt and spinel along with multi-phase MCOs. The compositions have been tested against linear sweep voltammetry (LSV), cyclic voltammetry (CV) and obtained Tafel slopes along with overpotential values. The results have been correlated with the experimental findings from SEM, XRD and TEM studies in an attempt to understand the relationship between electrocatalytic activity and phase, microstructure and chemistry.

6.2. Sample preparation and experimental setup

Precursor metal oxides Co(II,III)O, Cr(III)O, Cu(II)O, Fe(II,III)O, MgO, Mn(III)O, NiO and ZnO of high purity (>99.8%) were procured from either Alfa Aesar or Sigma Aldrich. Weighed powder in stoichiometric proportions were taken and mixed thoroughly in a mortar and pestle. Mixed powders of different equimolar compositions i.e. (CoMgNi)-oxide, (CoMgMnNi)-oxide, (CoCaFeMgNi)-oxide, (CoCuMgNiZn)-oxide and (Co(Mg/Cr)FeMnNi)-oxide were green compacted in an uniaxial hydraulic press under 4T load. The green compacted pellets were sintered at either 1323K or 1473K for 10 h followed by water quenching in an air-atmosphere tube furnace. Moreover, sintered pellet from couple of compositions were further subjected to ageing treatment at 723K for 120 h.

Electrocatalytic activity for efficient catalysis in OER experiments were carried out on an Electrochemical workstation (CORRTEST CS 350) using CS Studio. A three-electrode setup has been used with glassy carbon as working electrode, Ag/AgCl as reference electrode, graphite rod as counter electrode and 1M KOH solution as electrolyte. The glassy

carbon electrode was cleaned and polished (mirror finish) using high purity alumina and "ink" of each composition was drop-cast onto the glassy carbon electrode (0.071 cm^2 surface area). For preparing the ink, thin slices were cut from the sintered pellets of various compositions and it was ground into powder by mortar and pestle after which 1 mg of the specimen powder was mixed with 10 μL of 5wt% Nafion solution and 350 μL of ethanol in a vial. The vial was then ultrasonicated for sufficient time before ~ 7 μL of the ink was pipetted out on to the glassy carbon electrode. After the setup was complete, linear sweep voltammetry (LSV), cyclic voltammetry (CV) and electron impedance spectroscopy (EIS) was carried out multiple times on each of the compositions for reproducibility of results. For phase and microstructural characterization, standard metallographic procedure was carried out before its examination by XRD, SEM and TEM as mentioned in chapters 3, 4 and 5. Finally, an attempt has been made to correlate the electrocatalytic activity of the multicomponent oxides in relation to its phase, crystal structure, microstructure and chemistry.

6.3. Results and Discussion

All the sintered, quenched, aged equimolar multicomponent oxides (MCOs) and high entropy oxides (HEOs) were tested for linear sweep voltammetry (LSV) response at a scan rate of 10 mV/sec under alkaline condition. The current density (J) vs reduced hydrogen potential (RHE) plots of sintered and quenched (CaCoFeMgNi)-oxide, (CoFeMgMnNi)-oxide, (CoCuMgNiZn)-oxide and (CoCrFeMnNi)-oxide are given in Figure 6.1. The respective trends have been colour coded as well as marked by arrows. For reproducibility of results, three data sets were recorded from each of the oxides and the best one plotted, which has less than 1% difference in values from the rest. It is evident from Figure 6.1 that sintered and quenched (CaCoFeMgNi)-oxide performs the least well, followed by (CoFeMgMnNi)-oxide. So far as (CoCuMgNiZn)-oxide is concerned, it yields the

maximum current density per incremental increase in voltage, however, (CoCrFeMnNi)-oxide outperforms the rest in terms of earliest onset to oxygen evolution reaction (OER). It may be discerned from the x-axis offsets from which the curves start rising with positive slopes (Figure 6.1). It is a common practice to provide some sort of activation to the specimen ink coated electrode, before recording the LSV response. This is usually done to coat the working electrode with oxide and hydroxide products on the surface, which is responsible for enhanced electrocatalytic activities. Surface oxygenation of active metal sites is believed to be key for evaluating catalytic response. Even if the specimen ink is not activated before the LSV response is recorded, analytical equations may be fitted from open circuit potential values or by IR (product of current and resistance) correction method post experiment. Subtraction of the solvent resistance effect and non-activation effect from the obtained plots is often done. These refinements in essence makes the LSV curves rise very steeply and sharply from the onset of OER overpotential. However, in the set of experiments discussed throughout this chapter, neither prior activation was provided nor post-mortem IR correction has been employed. Figure 6.1 depicts the raw response of the MCOs/HEOs and an attempt has been made to understand their trends from subsequent characterization of phase, microstructure and chemical distribution. They will be discussed in the subsequent sections. Figure 6.1 inset compares the LSV responses from equimolar quinary (CoCuMgNiZn)-oxide and its derivative equimolar ternary (CoMgNI)-oxide, in both sintered and quenched condition as well as sintered, quenched and aged condition. Both the current density response as well as overpotential response is better for higher-order oxide than its derivative lower order oxide.

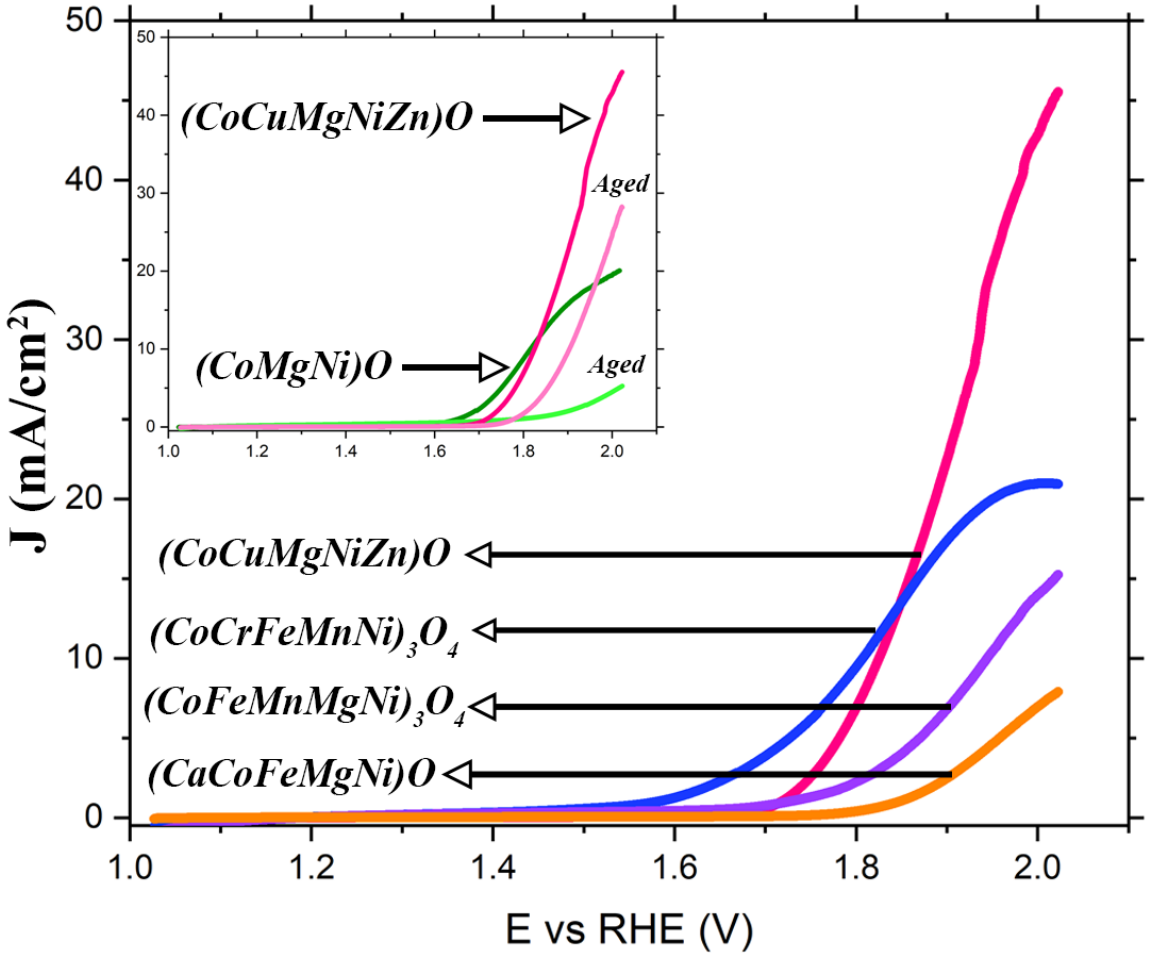

Figure 6.1: LSV plots recording the current density as a function of applied voltage, calibrated against reduced hydrogen electrode. The response from each oxide is colour coded. The inset compares the electrocatalytic response from (CoCuMgNiZn)-oxide and its derivative (CoMgNi)-oxide after sintering and ageing heat treatments.

Moreover, in both the ternary and quinary oxides, it is evident that with ageing heat treatment of the same compositions, a consistent deterioration of the electrocatalytic activity may be discerned (Marked in inset). The reasons for such performances and trends have been investigated through the systematic characterization and will be discussed subsequently.

Phase evolution of the respective MCOs and HEOs after solid-state synthesis, sintering and quenching are represented in the XRD patterns of Figure 6.2. It is observed that equimolar ternary (CoMgNi)-oxide crystallizes in a phase-pure rocksalt structure (a~4.22Å). The

major FCC peaks 111, 200, 220, 311 and 222 have been marked with filled circles. The ratio of the total integrated intensity of the 111 and 200 peaks also matched with simulated results. However, presence of very small volume fraction of a spinel phase (a~8.1Å) has been previously reported in this composition [16]. Partial substitution of Mn-ions in the ternary oxide yielded equimolar quaternary (CoMgMnNi)-oxide. Quaternary equimolar (CoMgMnNi)-oxide formed a mixture of two phases namely, rocksalt phase (a~4.22Å) and spinel phase (a~8.4Å) of roughly ~39% and 61% phase fraction respectively.

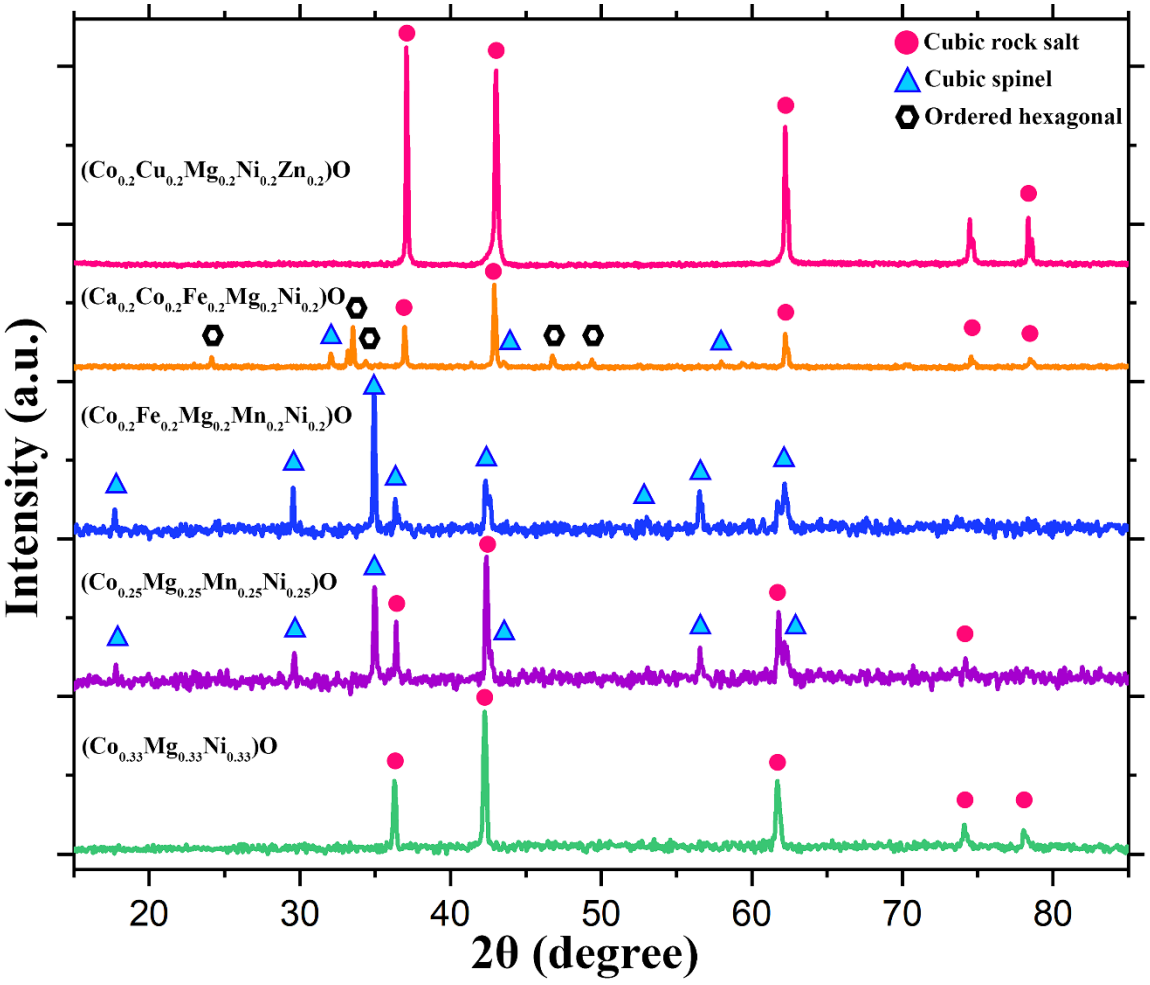

Figure 6.2. Experimental XRD patterns from sintered and quenched equimolar, ternary (CoMgNi)-oxide (green), quaternary (CoMgMnNi0-oxide (purple), quinary (CoFeMgMnNi)-oxide (blue), (CaCoFeMgNi)-oxide (orange) and (CoCuMgNiZn)-oxide (magenta). Respective phases have been marked with different coloured symbols.

Higher 2θ peaks of the rocksalt phase are absent, and shouldering of 200 and 220 peaks may be discerned, which may be indexed to 400 and 440 peaks of the spinel phase. Systematic addition of Fe-ions to the quaternary equimolar mixture of (CoMgMnNi)-oxide produced equimolar quinary (CoFeMgMnNi) HEO. It forms a single-phase spinel structure (a~8.38Å) globally, although systematic peak splitting and shouldering is observed. The XRD signature from sintered and quenched equimolar (CoCrFeMnNi) HEO also produced very similar pattern to that of (CoFeMgMnNi) HEO, as reported previously, and therefore it has not been shown in Figure 6.2 for the purpose of clarity [16]. Replacement of Mn-ions with Ca-ions in equimolar proportion produced quinary (CoFeMgMnNi)-oxide. It showed a complex diffraction pattern with several peaks. The major rocksalt phase (a~4.15Å) could easily be discerned, however, simulation methods had to be employed to retrieve the minor phases accurately, which has been reported elsewhere [17]. It has been found out that apart from a disordered rocksalt major phase, significant phase fraction of an ordered hexagonal phase (a~2.94Å, c~5.28Å) exists along with minor phase fraction of another rocksalt phase (a~4.78Å) and spinel phase (a~8.35Å) respectively. The approximate phase fractions were computed to be ~48%, ~35%, ~11% and 5% respectively. Finally, equimolar quinary (CoCuMgNiZn)-entropy stabilized oxide (ESO) crystallizes in a phase-pure rocksalt structure (a~4.23Å) on a global average. In its diffraction pattern, significant non-ideal intensity distribution between the 111 and 200 peaks may be discerned, along with systematic shouldering. It is envisaged that local composition modulation or Jahn-Teller induced local structural modulation or both may substantiate the experimental deviations from ideal structure, as has been reported earlier [18].

In order to rationalize the LSV behaviours of the four quinary MCOs/HEOs from Figure 6.1, microstructural characterization of the sintered and quenched pellets of the respective oxides have been carried out (Figure 6.3) by SEM and TEM techniques. Representative

SEM-SE images at two different magnifications, TEM BF/DF image and corresponding electron diffraction patterns have been shown for each of the four compositions in Figure 6.3. The common characteristic from all the SEM images is the uniform sintering of the pellets, which is estimated to be very close to its theoretical density, with minimal porosity observed. The sintered and quenched (CaCoFeMgNi)-oxide shows grainy morphology of varying size distribution and contrast (Figure 6.3-a1). The average grain size lies in the range of ~5-10 μm. Grains of dark contrast phase are occasionally engulfed by lighter contrast agglomerate phase (figure 6.3-a1(inset)). It has been confirmed earlier that the dark contrast phase is preferentially enriched in Co-, Ni- and Mg-ions while light contrast phase is enriched in Ca- and Fe-ions preferentially [17]. While the major rocksalt phase is found in (Co,Mg,Ni)-enriched areas, the minor phases of an ordered hexagonal structure, cubic rocksalt structure and cubic spinel structure are often found to coexist together in the (Ca,Fe)-enriched regions. They are found to share definite orientation relationship with one another, while sharing coherent/semi-coherent interphase interfaces among each other. A selected area electron diffraction pattern corroborating the same is given in Figure 6.3-a2. The three phases are marked in different colours, with their zone axis and principal vectors marked. Figure 6.3-a3 is dark field (DF) image from the ordered hexagonal phase, which is often found to exist independently from the other minor phases. Bands of alternating contrast may easily be discerned in the DF image, which are compound type of twins. The electron diffraction pattern clearly brings out systematic splitting of higher order spots, maintaining an angle of ~5.2 degrees (Figure 6.3-a3(inset)). The SEM-SE image from sintered and quenched (CoFeMgMnNi)-oxide in Figure 6.3-b1 shows bimodal grain size distribution with larger grains (~25 μm) surrounded by agglomerates of much finer grains (~3 μm). Porosity is also observed in between the grain size distribution.

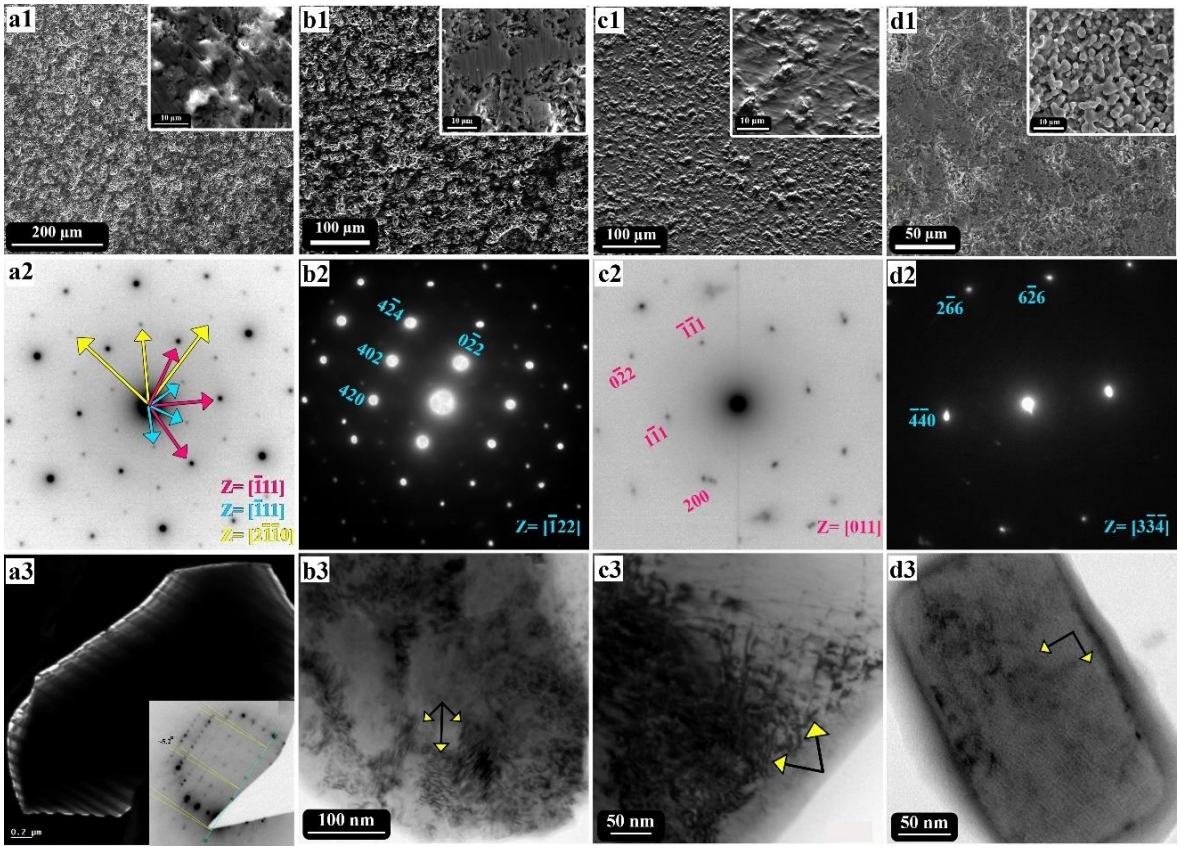

Figure 6.3: SEM-SE micrographs, selected area diffraction pattern and TEM bright field/dark field images from sintered and quenched (a1-a3) (CaCoFeMgNi)-oxide, (b1-b3) (CoFeMgMnNi)-oxide, (c1-c3) (CoCuMgNiZn) ESO and (d1-d3) (CoCrFeMnNi) HEO respectively. The microstructural features are marked with arrows and indexing of diffraction patterns have been done employing different colour schemes.

Fine sub-micron bands of dark contrast may be discerned within the larger grains (Figure 6.3-b1(inset)). The selected area diffraction pattern may be indexed to a z=[$\bar{1}$22] zone axis of a cubic spinel phase (Figure 6.3-b2). However, clear modulation of intensity and bulging of the first order spots may be discerned. The corresponding bright field image shows mottled contrast in the single crystal grain body, with occasional fringe contrast, which are marked by arrows (Figure 6.3-b3). The SEM image in Figure 6.3-c1 of (CoCuMgNiZn) ESO shows uniform grain size distribution with finer agglomerates. The sub-grain structure is visible within the agglomerate clusters, with minimal porosity (Figure 6.3-c1(inset)). Selected area diffraction pattern from z=[011] zone axis confirms a global average single-

phase rocksalt structure, however with shape evolution and splitting of spots (Figure 6.3-c2). The corresponding BF image in Figure 6.3-c3 shows fringe contrast along with domain structure (marked with arrows). The SEM image from a region of interest in sintered and quenched (CoCrFeMnNi) HEO again shows uniform sintering with bimodal grain size distribution (Figure 6.3-d1). The finer colonies have roughly spherical shaped particles of ~2μm, interconnected with one another (Figure 6.3-d1(inset)). A representative electron diffraction pattern from the average single-phase with spinel structure is depicted in Figure 6.3-d2. It conforms to the z=[33$\bar{4}$] zone axis single crystal pattern, however, bulging and onset of splitting of the 440 type of spots may be seen. The corresponding bright field image in Figure 6.3-d3 shows fine nano-domain contrast, which are arranged mutually perpendicular to each other (marked with arrows). It has been previously shown that they are interweaved fringes, with in between domain size of ~5-10 nm [16]. It may be concluded from the above observations combined, that local structural modulation within a global average single-phase in quinary ESO/HEO enhances the electrocatalytic performance in contrast to phase-pure ternary or multi-phase quinary oxides.

In order to rationalize the drop in electrocatalytic activity with ageing, SEM-XEDS maps have been collected from both equimolar ternary (CoMgNi)-oxide as well as (CoCuMgNiZn) ESO (Figure 6.4(a-b)). Elemental mapping has been carried out on pellets of the same composition (a1,a2 and b1,b2), one after sintering at 1323K for 10h followed by water quenching (a1,b1) and the other one after sintering followed by ageing at 723K for 100h (a2,b2).

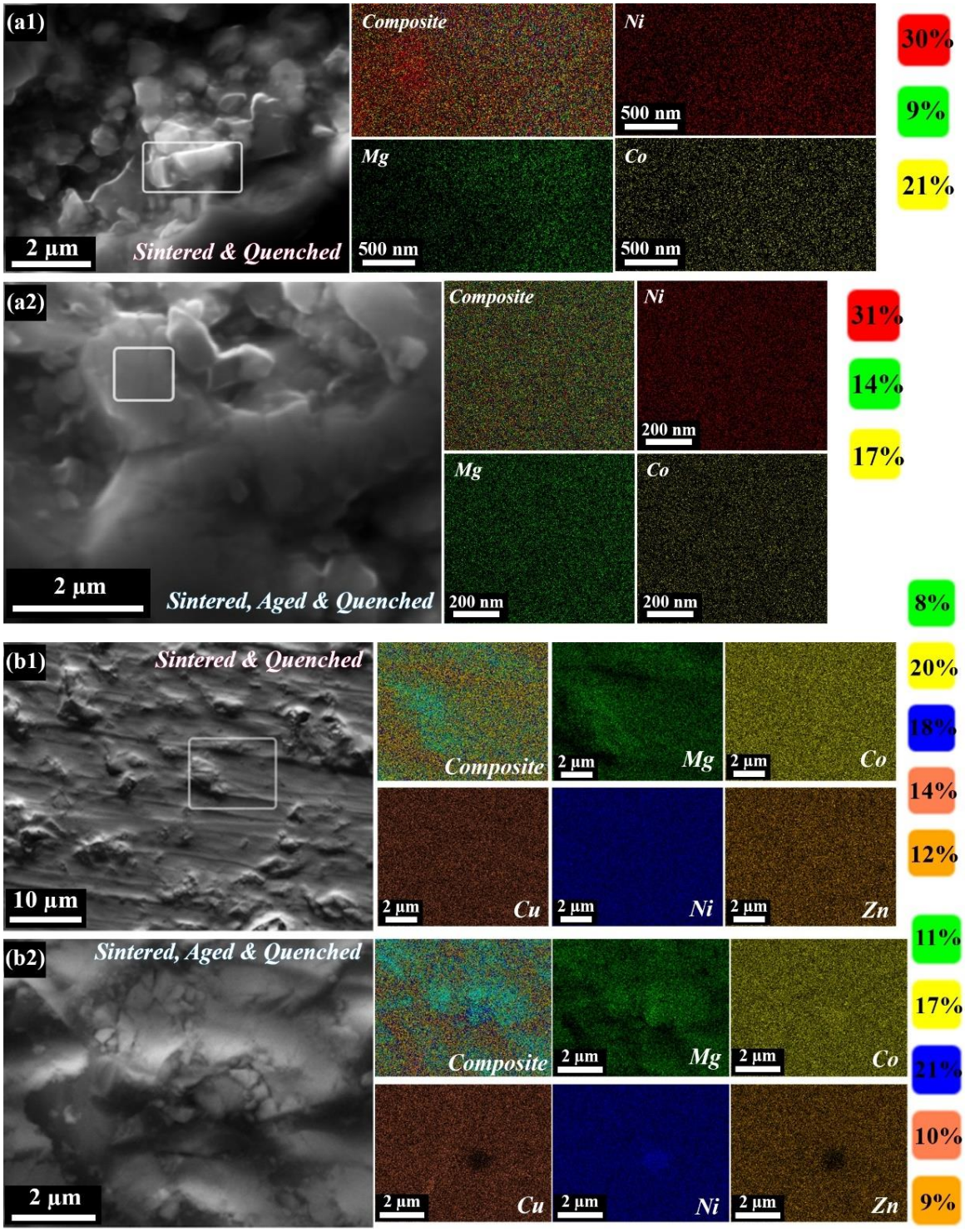

Figue 6.4: SEM-XEDS chemical mapping from (a1) sintered and quenched (CoMgNi)-oxide, (a2) sintered, aged and quenched (CoMgNi)-oxide, (b1) sintered and quenched (CoCuMgNiZn) ESO and (b2) sintered, aged and quenched (CoCuMgNiZn) ESO respectively. The quantification of the cation weight % has been provided in coloured boxes adjacent to the respective maps.

It may be easily discerned from the chemical quantification of the respective cation K-shell excitations in both the oxides, that the surface composition gets altered after ageing heat treatment. The ternary (CoMgNi)-oxide shows a significant enrichment of Mg-ions after ageing, however with a depletion of Co-ions and similar concentration of Ni-ions (Figure 6.4a1-a2). Similarly, in (CoCuMgNiZn) ESO after ageing, a significant depletion of Co-, Cu- and Zn-ions may easily be discerned, with enrichment in Mg- and Ni-ions (Figure 6.4b1-b2). Preferential micro-segregation of ionic species may be seen in SEM-XEDS composite maps. Since surface composition, especially the concentration of redox active cation sites determines the electrocatalytic activity, the drop in performance after ageing heat treatment becomes clear from the chemical distribution maps.

The current density (J) has been plotted against the reduced hydrogen potential (RHE) for equimolar quaternary (CoMgMnNi)-oxide in Figure 6.5a. For reproducibility of results, three linear sweep voltammetry (LSV) curves have been plotted. It shows the best electrocatalytic activity among all the other HEO/ESO or multicomponent oxides reported in this chapter. Equimolar quaternary (CoMgMnNi)-oxide records the steepest slope among the rest, which points to the enhanced conductivity of the multicomponent oxide. It has also recorded the highest current density along with the lowest overpotential to achieve 10 mA/cm^2. The cyclic voltammetry (CV) test was carried out on the same composition at different scan rates and is plotted in Figure 6.5b. It is seen that with progressively higher scan rates, the area under the hysteresis loop keeps on increasing. This points to the enhanced efficiency of redox reaction rates. However, no significant oxidation and reduction peaks could be discerned in the CV curves. It is recalled that equimolar quaternary (CoMgMnNi)-oxide shows a two-phase mixture of spinel and rocksalt phases (Figure 6.2 in purple).

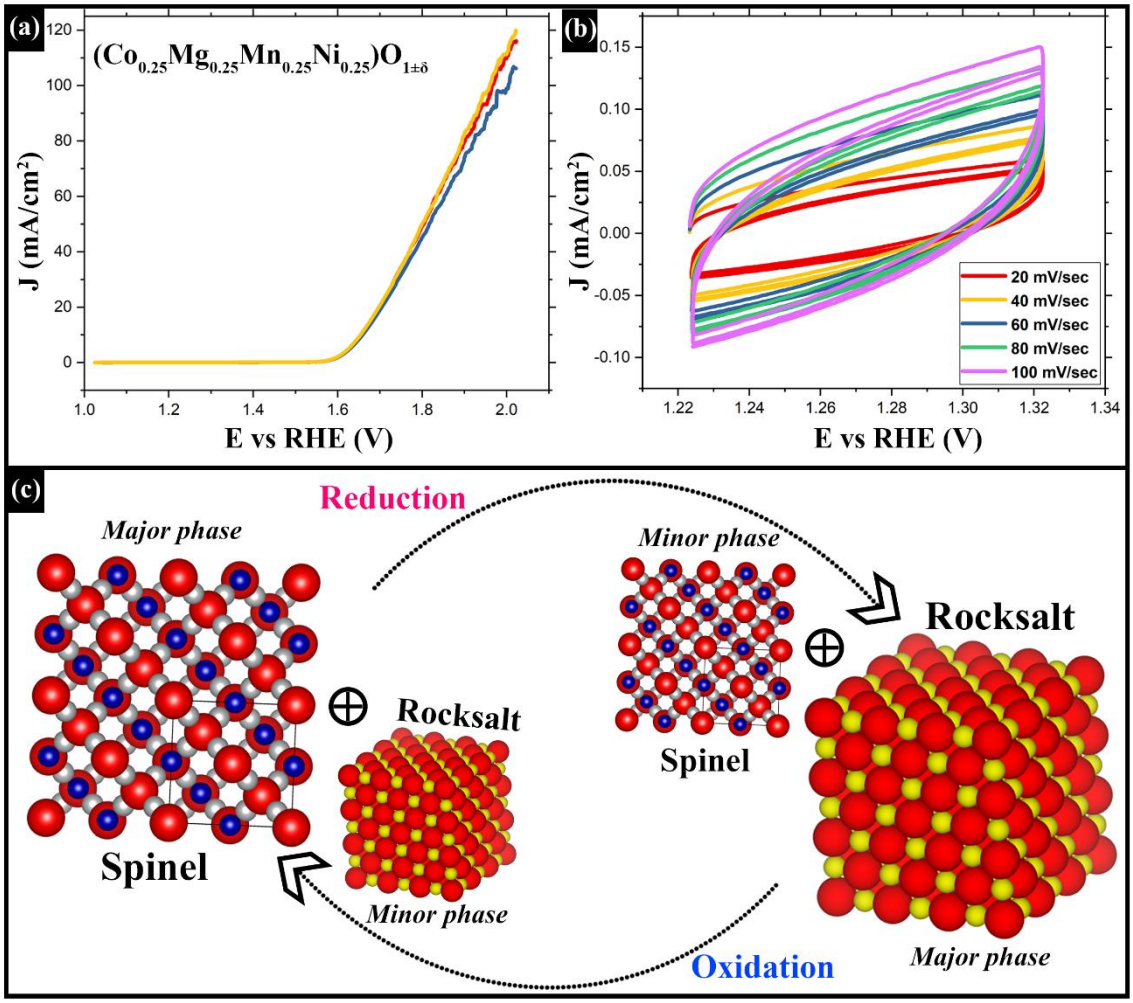

Figure 6.5: (a) LSV response from sintered and quenched equimolar (CoMgMnNi)-oxide, (b) CV plots from the same oxide under varying scan rates and (c) schematic representing possible mechanism behind enhanced electrocatalytic activity in the dual-phase oxide.

It is also previously reported that dual-phase (CoFeMgMn)-oxide drastically lowers the temperature of a two-step thermochemical water-splitting via interconversion of rocksalt and spinel phases during heating and cooling [19]. In order to rationalize the superior performance of sintered and quenched (CoMgMnNi)-oxide based on the current observations and the school of thought proposed earlier, a schematic representation has been depicted in Figure 6.5c. The possible interconversion between spinel and rocksalt phases in varying phase fractions during oxidation and reduction cycles is thought to enhance the electrocatalytic activity in this multicomponent oxide [19]. In this process, the

thermodynamic cycle becomes essentially a redox heat engine due to the continuous exchange of oxygen. The lattice oxygen mechanism (LOM) is more likely to be operational.

The overpotential plots and the Tafel slopes of all the oxides have been plotted in Figure 6.6a-b. Figure 6.6a represents the bar diagram of the overpotential required to cross current density of 5 mA/cm^2 for the respective oxides. The overpotential values at 1 mA/cm^2 and at 10 mA/cm^2 is reported in white and black respectively. The equimolar quaternary (CoMgMnN)-oxide shows the least overpotential values at all possible current densities, followed by singl-phase spinel structured (CoCrFeMnNi) HEO followed by phase-pure rocksalt structured (CoCuMgNiZn) ESO. It is also to be noted that the spread in the recorded overpotential values to achieve 1, 5 and 10 mA/cm^2 current density respectively, is quite high for most of the oxides barring quaternary (CoMgMnNi)-oxide. This further validates the solvent resistance and non-activation effect of the specimen inks. Multi-phase (CaCoFeMgNi)-oxide and single-phase (CoMgNi)-oxide shows the highest overpotential values and performs the poorest. Correspondingly, the Tafel slope is the lowest for (CoMgMnNi)-oxide while it is the highest for (CaCoFeMgNi)-oxide (Figure 6.6b).

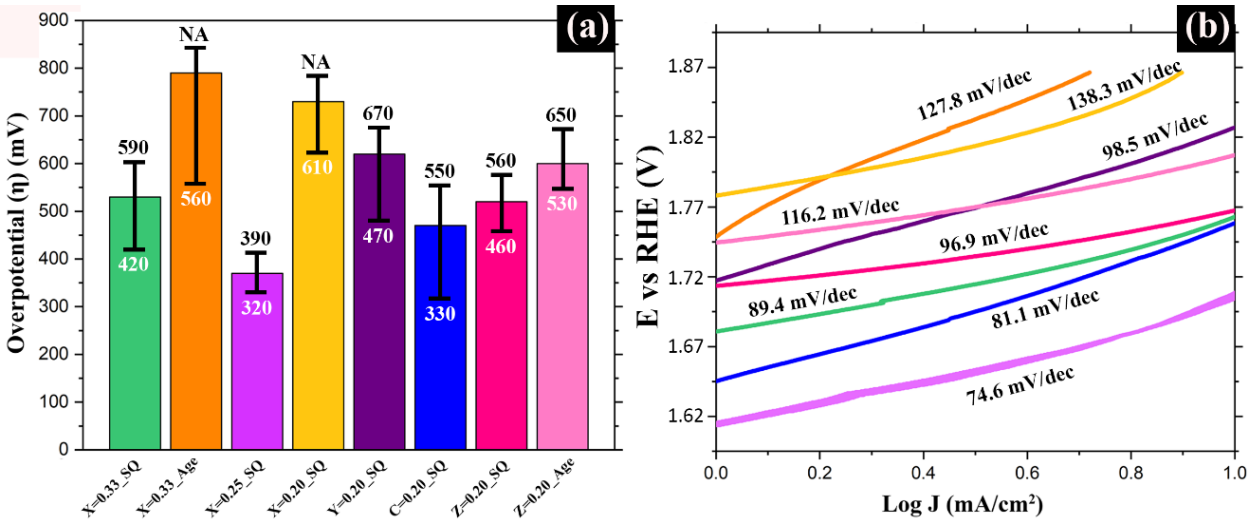

Figure 6.6: (a) Overpotential plots for all the respective multicomponent oxides at 5 mA/cm^2 and (b) Tafel slopes for the same oxides. The histogram is accompanied with computed overpotential values at 1 mA/cm^2 (in white) and at 10 mA/cm^2 (in black). The Tafel slopes are marked over each oxide.

6.4. Conclusions

It may be concluded from the present study that equimolar quaternary (CoMgMnNi)-oxide is a potential candidate for efficient electrocatalysis, recording a low overpotential of 390 mV to achieve a current density of 10 mA/cm^2 with a Tafel slope of ~74.6 mV/dec. It is thought that the possible interconversion between spinel and rocksalt phases in varying phase fractions during oxidation and reduction cycles enhances the redox activity of the material. It thus becomes likely that the lattice oxygen mechanism (LOM) becomes operative over and above adsorbate evolution mechanism (AEM) during the interconversion between spinel and rocksalt phases. Equimolar quinary (CaCoFeMgNi)-oxide performs the poorest as electrocatalyst, owing to large scale chemical segregation and multi-phase nature. Both the (CoCrFeMnNi) HEO characterized by spinel structure and (CoCuMgNiZn) ESO characterized by rocksalt structure show encouraging electrocatalytic performance, which scope for further enhancement. This is attributed to the local structural modulation in both the compositions, with or without associated fine-scale compositional modulation. Moreover, lower order derivative oxides perform poorer compared to similar structured higher order oxide. Furthermore, probable change in bulk chemistry and a definite change in surface chemistry in the multicomponent oxides occurs during ageing treatment, which in turn affects the electrocatalytic activity for the worse. While Co-, Ni-, Fe-, Mn-ions are known to enhance the conductivity of the catalysts, enrichment of Mg-ions is known to stabilize a particular kind of phase and hence reduce the catalytic response.

6.5. Reference

1. C. Liu, F. Li, L. P. Ma, H. M. Cheng, Advanced materials for energy storage, Adv. Mater., 2010, 22, E28-E62
2. B. C. H. Steele, A. Heinzel, Materials for fuel-cell technologies, Nature, 2001, Vol. 414, 345-352
3. X. Yu, Z. Tang, D. Sun, L. Ouyang, M. Zhu, Recent advances and remaining challenges of nanostructured materials for hydrogen storage applications, Prog. Mater. Sci., 2017, Vol. 88, 1-48
4. A. S. R. Bati, M. Batmunkh, J. G. Shapter, Emerging 2D layered materials for perovskite solar cells, Adv. Energy Mater., 2019, 1902253 (21 pages)
5. J. Knaster, A. Moeslang, T. Muroga, Materials research for fusion, Nature Physics, 2016, Vol. 12, 424-434
6. J. Baek, M. D. Hossain, P. Mukherjee, J. Lee, K. T. Winther, J. Leem, Y. Jiang, W. C. Chueh, M. Bajdich, X. Zheng, Synergistic effects of mixing and strain in high entropy spinel oxides for oxygen evolution reaction, Nat. Commun., 2023, Vol. 14 (5936), 1-11
7. L. Sharma, N. K. Katiyar, A. Parui, R. Das, R. Kumar, C. S. Tiwary, A. K. Singh, A. Halder, K. Biswas, Low-cost high entropy alloy (HEA) for high-efficiency oxygen evolution reaction (OER), Nano Research, 2022, Vol. 15 (6), 4799-4806
8. D. Wang, C. Duan, Y. Yu, X. Li, Z. Wang, Y. Liu, C. Liu, Co-regulation of anion-cation in transition metal high entropy oxide for outstanding OER electrocatalytic performance, Journal of Alloys and Compounds, 2023, Vol. 967, 171758
9. Y. Liu, X. Zhang, Metamaterials: a new frontier of science and technology, Chem. Soc. Rev., 2011, Vol. 40, 2494-2507
10. N. I. Zheludev, Y. S. Kivshar, From metamaterials to metadevices, Nature Materials, 2012, Vol. 2, 917-924

11. J. B. Goodenough, Perspective on engineering transition-metal oxides, Chemistry of Materials, 2014, Vol. 26, 820-829
12. M. Anandkumar, E. Trofimov, Synthesis, properties, and applications of high-entropy oxide ceramics: Current progress and future perspectives, Journal of Alloys and Compounds, 2023, Vol. 960, 170690
13. D. Berardan, S. Franger, D. Dragoe, A. K. Meena, N. Dragoe, Colossal dielectric constant in high entropy oxides, Phys. Status Solidi RRL, 2016, Vol. 10 (4), 328-333
14. D. Berardan, S. Franger, A. K. Meena, N. Dragoe, Room temperature lithium superionic conductivity in high entropy oxides, J. Mater. Chem. A, 2016, Vol. 4, 9536
15. Z. Y. Liu, Y. Liu, Y. Xu, H. Zhang, Z. Shao, Z. Wang, H. Chen, Novel high-entropy oxides for energy storage and conversion: From fundamentals to practical applications, Green Energy and Environment, 2023, Vol. 8, 1341-1357
16. S. Mukherjee, N. K. Mukhopadhyay, J. Basu, Structural modulation and oriented growth of rocksalt and spinel phases in equimolar multicomponent {Co(Cr/Mg)FeMnNi}-oxide and its derivatives, J. Am. Ceram. Soc., 2025, e20619 (15 pages)
17. S. Mukherjee, N.K. Mukhopadhyay, J. Basu, Composition modulation, strain minimization and oriented growth of phases in equimolar (CaCoFeMgNi) multicomponent oxide, Acta Mater., 2025, 285, 120621 (12 pages)
18. S. Mukherjee, N.K. Mukhopadhyay, J. Basu, Local composition modulation and oriented inter-growth induced strain minimization in entropy stabilized (CoCuMgNiZn) oxide [Communicated]
19. S. Zhai, J. Rojas, N. Ahlborg, K. Lim, M. F. Toney, H. Jin, W. C. Chueh, A. Majumdar, The use of ply-cationic oxide to lower the temperature of two-step thermochemical water-splitting, Energy & Environmental Science, 2018, Vol. 11, 2172-2178

CHAPTER – 7

A UNIFIED PICTURE

7.1 Thesis conclusion

The research work carried out throughout the thesis concludes the following:

- Multicomponent metal oxides have inherently much higher molecular weights and mass absorption coefficients than their metallic alloys counterpart. This essentially increases the inelastic component of scattering during x-ray diffraction (XRD) experiments and raises the Compton modified background level. It has been demonstrated in the case of equimolar quinary (CoCuMgNiZn) ESO (Chapter 4) where a prominent reversal of intensity is observed between the two most intense peaks of an average cubic rocksalt phase. Moreover, sintered and quenched equimolar ternary (CoMgNi) MCO reveals a prominent spinel 220 peak, which is present in the sintered pellet but it is found to be absent in its crushed powder (Chapter 5). Hence the commonplace practice of characterizing such complex chemistry metal oxides in its powder form, established in literature (owing to the brittle nature of the sintered pellets), may be interpreted with caution.
- Cubic rocksalt and cubic spinel phases have highly correlated crystal structure. Both the phases are FCC derivative structures with anions decorating the close-packed lattice. However, in the rocksalt phase, the cations fill out all the four octahedral voids and forms six-fold coordination polyhedras with neighbouring anions while in the spinel phase, cations in their +2 oxidation states fill out half of the octahedral voids whereas remaining cations in their +3 oxidation states occupy one-eighth of the tetrahedral voids. Hence geometric frustration in the lattice (high entropy composition) coupled with external stimulus (temperature, pressure) can bring about interconversion between rocksalt and spinel phases through diffusional reconstructive transformation. It has been shown in Chapters 3, 4 and 5 where local spinel domains inside major rocksalt phase and local rocksalt domains inside major spinel phase are found to coexist, sharing

definite orientation relationship with coherent/semi-coherent interphase interfaces between them.

- ❖ Processing parameters like sintering temperature, holding time and subsequent ageing heat treatment play a crucial role in phase formation and its stability. It has been demonstrated in Chapters 3, 4 and 5 that prolonged exposure to high temperatures not only forces non-isostructural phases to combine with the major phase but also possible rearrangement in crystal structure with successive in-plane and out-of-plane rotations. Such arrangement ensures maximum randomness along individual atom-columns (high entropy effect) while also relieving the lattice strain (enthalpic penalty) at the same time. This observation also explains the randomly mixed column chemistry frequently encountered in ESOs/HEOs using high-resolution fine-probe techniques like STEM-XEDS and APT.
- ❖ Both the rocksalt forming (CoCuMgNiZn)-ESO (Chapter 4) and spinel forming (CoCrFeMnNi)-HEO (Chapter 5) tends to form nano interweaved modulated microstructure. However, in the former scenario 200-type planes (rocksalt) take part in the process of structural modulation whereas 220-type of planes (spinel) becomes operative in the later. The structurally modulated domains may or may not be associated with chemical modulation. Although the fundamental reason behind such observation remains unanswered at the moment, however, it perhaps explains the oriented growth of spinel 220 type reflection in otherwise phase-pure rocksalt structure of ternary (CoMgNi)-oxide (Chapter 5).
- ❖ Iron (II,III) oxide (predominantly in the +3 state) forms an ordered hexagonal phase (hR10; R -3 c prototype) with planar defect-structure in presence of larger ionic radii Ca^{+2} cations and exsolves out of the major rocksalt phase in (CaCoFeMgNi)-oxide (Chapter 3). However, in the presence of similar cationic radii Mn^{+3}, it helps to stabilize

the average cubic spinel structure (cF56; F d -3 m prototype) in (CoFeMgMnNi)-oxide (Chapter 5). Therefore, the same cation in presence of different species is amenable to hop along local minima in the energy landscape and change its coordination environment, in order to stabilize a particular kind of ordered/disordered structure (Chapters 3 and 5). This observation further brings out the enthalpic penalties in highly concentrated compositions and the importance of fluctuation in oxidation states, coordination environment and consequently ionic radii.

- Ternary phase-pure (CoMgNi)-oxide with average rocksalt structure relieves its lattice strain by forming a helical domain structure with small amount of correlated spinel phase formation (Chapter 5). However, quinary phase-pure (CoCuMgNiZn)-ESO with global average rocksalt crystal structure and single-phase (Co(Cr/Mg)FeMnNi)-HEO with global average spinel crystal structure tends to form tweed microstructure with structural modulation. It also hints at non-random distribution of multiple cations and therefore to the presence of short-range order (SRO) domains. The tweeds may act as template for subsequent phase separation to form self-assembled microstructure over large length scales. Further geometric frustration due to disproportionate differences in ionic sizes, leads to chemical segregation along with structural modulation and/or formation of planar fault dominated defect microstructure.
- Equimolar quaternary (CoMgMnNi)-oxide outperforms its quinary HEO counterparts as electrocatalyst for OER activity having a two-phase rocksalt plus spinel structure. This observation leads to the importance of phase-fractions, related crystal structures and their reversible interconversion during oxidation and reduction cycles, bringing out excellent match with a recent model proposed in literature (Chapter 6).

7.2 Scope for further research

Since no scientific research is truly exhaustive, the scope of further research along the lines of this thesis may be summarized as follows:

- Employing high-energy ball-milling on sintered and quenched pellets of MCOs/HEOs/ESOs to refine the particle size and promote inter-mixing of phases. The refinement of crystallite size is bound to enhance the OER activities manifold as established in literature, whereas the effect of forced inter-mixing after sintering can be studied for the first time.
- Exploring domain chemistry and fine structure of such materials through XPS and STEM-EELS spectroscopic techniques and 4D-STEM datasets respectively. Since transition metal oxides are amenable to switch their oxidation states, such experiments may shed further insights regarding phase formation and microstructural evolution. Furthermore, TEM in-situ experiments inside a gas-cell with regulated oxidizing/reducing environment are bound to provide with novel atomistic mechanisms of structural phase transformation.

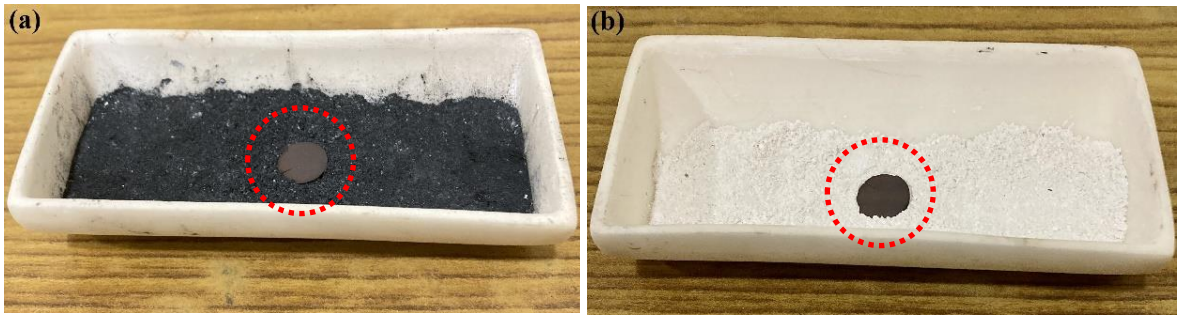

Figure 7.1: Sintered and quenched pellet of equimolar ternary (CoMgNi)-oxide placed on an alumina tray filled with a mixture of alumina and graphite powder (a) before ageing treatment and (b) after ageing treatment. The obvious change in colour of the powder bed and not the pellet, may easily be discerned.

- Enhancing phase separation events through prolonged holding time at low to intermediate temperatures (to overcome kinetic barrier) in order to navigate the energy landscape of the material systems and its manifestation on microstructural evolution.
- Exploration of MCOs/HEOs/ESOs as possible candidates for effective carbon capture, either from environment or industries. In an accidental trial of ageing a sintered pellet placed on a mixture of graphite and alumina powder inside an alumina crucible, it has been seen that the greyish white mixture turns clear white after ageing treatment. The brownish sintered pellet showed no change in colour nor XRD signature when compared to the same composition pellet after ageing without the graphite plus alumina bed.

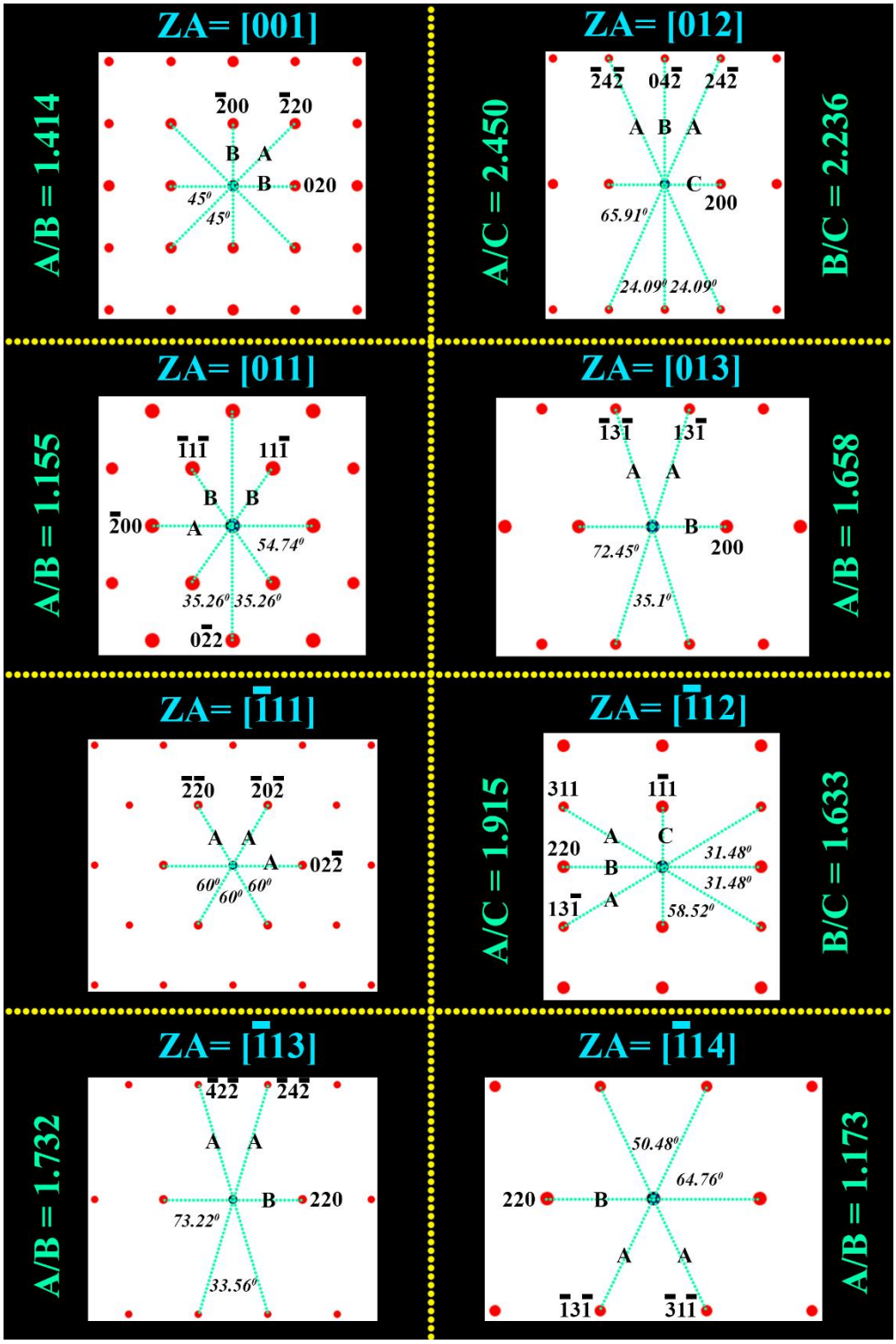

Figure A.1: *Single-crystal spot electron diffraction patterns from several zone axis of a FCC structure ($u^2+v^2+w^2<22$). The patterns have been simulated with the help of JEMS software. The respective zone axis directions are marked as "ZA" on top of each pattern. The ratio of the principal vectors along with the interplanar angles are marked in the respective patterns.*

Appendix-II: Python code for XRD pattern simulation

Excerpt from the python code for simulation of x-ray diffraction (XRD) patterns:

```
 "cell_type": "code",
 "execution_count": 226,
 "id": "abc88470-a468-4a2e-be0e-482a5c05390e",
 "metadata": {},
 "outputs": [],
 "source": [
  "material ='w-Ti'\n",
  "lattice_type='hexagonal'\n",
  "wavelength=1.54\n",
  "a=4.6\n",
  "b=4.6\n",
  "c=2.82\n",
  "\n",
  "alpha= 90\n",
  "beta= 90\n",
  "gamma=90\n",
  "alpha_rad = math.radians(alpha)\n",
  "beta_rad = math.radians(beta)\n",
  "gamma_rad = math.radians(gamma)\n",
  "lattice={}\n",
  "\n",
  "motifs = {\n",
  "    #\"Al\": np.array([[0.0, 0.0, 0.0],[0.5,0.5,0.0],[0.5,0.0,0.5],[0.0,0.5,0.5]]),\n",
  "    #\"Mn\": np.array([[0.5, 0.5, 0.5],[0.0,0.0,0.5],[0.0,0.5,0.0],[0.5,0.0,0.0]]),\n",
  "                                                                    #\"Cu\":
np.array([[1/4,1/4,1/4],[3/4,3/4,3/4],[3/4,3/4,1/4],[3/4,1/4,3/4],[1/4,3/4,3/4],[1/4,1/4,3/4
],[1/4,3/4,1/4],[3/4,1/4,1/4]])\n",
```

```
    "    #\"Cu\": np.array([[0.5,0.0,0.5],[0.0,0.5,0.5]])\n",
    "                                    #\"Si\":  np.array([[0.0,  0.0,
0.0],[0.5,0.5,0.0],[0.5,0.0,0.5],[0.0,0.5,0.5],[1/4,1/4,1/4],[3/4,3/4,1/4],[3/4,1/4,3/4],[1/4,
3/4,3/4]]),\n",
    "    #\"As\": np.array([[1/3, 2/3, 1/4],[2/3,1/3,3/4]])\n",
    "    \"Ti\": np.array([[0.0, 0.0, 0.0], [1/3, 2/3, 1/2],[2/3,1/3,1/2]])\n",
    "    #\"Sn\": np.array([[0.0,0.0,0.0],[0.5, 0.5, 0.5],[0.0,1/2,1/4],[1/2,0.0,3/4]])\n",
    "    \n",
    "   }\n",
    "   \n",
    "   #motifs = np.array([[0.0, 0.0, 0.0], [0.0, 0.5, 0.5],[0.5, 0.0, 0.5],[0.5, 0.5, 0.0]])\n",
    "   #motifs = np.array([[0.0, 0.0, 0.0], [0.5, 0.5, 0.5]])\n",
    "   #motifs = np.array([[0.0, 0.0, 0.0], [2/3, 1/3, 1/2]])\n",
    "   #motifs = np.array([[0.0, 0.0, 0.0]])\n",
    "   \n",
    "   peak_positions = []\n",
    "   peak_intensity=[]\n",
    "   df=pd.read_csv(\"atomic scattering factor.csv\")\n",
    "   df_raw = pd.read_excel(\"lorentz polarization factor.xlsx\", header=0)"
  ]
 },
 {
  "cell_type": "code",
  "execution_count": 228,
  "id": "b8079682-aa88-4ae7-bbcb-7ec852f5dcfb",
  "metadata": {},
  "outputs": [
   {
    "name": "stdout",
    "output_type": "stream",
    "text": [
```

```
    "rounded 0.4\n",
    "10.9\n"
   ]
  }
 ],
 "source": [
  "def find_fo(h,k,l,element):\n",
  "    s11 = b**2 * c**2 * math.sin(alpha_rad)**2\n",
  "    s22=  a**2 * c**2 * math.sin(beta_rad)**2\n",
  "    s33=  a**2 * b**2 * math.sin(gamma_rad)**2\n",
  "        s12 = a * b * c**2 * (math.cos(alpha_rad) * math.cos(beta_rad) - math.cos(gamma_rad))\n",
  "        s23 = c * b * a**2 * (math.cos(beta_rad) * math.cos(gamma_rad) - math.cos(alpha_rad))\n",
  "        s13 = a * c * b**2 * (math.cos(gamma_rad) * math.cos(alpha_rad) - math.cos(beta_rad))\n",
  "    v = a * b * c * math.sqrt((1 - math.cos(alpha_rad)**2 - math.cos(beta_rad)**2 - math.cos(gamma_rad)**2 + 2 * math.cos(alpha_rad) * math.cos(beta_rad) * math.cos(gamma_rad)))\n",
  "    \n",
  "\n",
  "    numerator = s11 * h**2 + s22 * k**2 + s33 * l**2 + 2 * s12 * h * k + 2 * s23 * k * l + 2 * s13 * l * h\n",
  "    d = v / math.sqrt(numerator)\n",
  "    d=round(d,2)\n",
  "    theta = np.arcsin(wavelength / (2 * d))\n",
  "    theta=round(theta,2)\n",
  "    position= round(np.degrees(2*theta),2)\n",
  "\n",
  "    temp= (math.sin(math.radians(position/2)))/wavelength\n",
  "    rounded_temp = round(temp, 1)\n",
  "    value=1\n",
```

```
  "    print(\"rounded\",rounded_temp)\n",
  "    try:\n",
  "        value = df.loc[df['Element'] == element, str(rounded_temp)].values[0]\n",
  "    except KeyError:\n",
  "        value=1\n",
  "    return value\n",
  "print(find_fo(0,0,2,'Ti'))\n"
 ]
},
```

LIST OF PUBLICATIONS

1. *Saptarshi Mukherjee*, N.K. Mukhopadhyay, Joysurya Basu, Composition modulation, strain minimization and oriented growth of phases in equimolar (CaCoFeMgNi) multicomponent oxide, Acta Mater., 2025, 285, 120621 (12 pages)

2. *Saptarshi Mukherjee*, N.K. Mukhopadhyay, Joysurya Basu, Structural modulation and oriented growth of spinel and rocksalt phases in equimolar (Co(Cr/Mg)FeMnNi) multicomponent oxide and its derivatives, J. Am. Ceram. Soc., 2025, e20619 (15 pages)

3. *Saptarshi Mukherjee*, Sandip Bysakh, N.K. Mukhopadhyay, Joysurya Basu, Local composition modulation and oriented inter-growth induced strain minimization in entropy stabilized (CoCuMgNiZn)-oxide [Communicated]

4. *Saptarshi Mukherjee,* Shivank Shukla, Chanchal Ghosh, N.K. Mukhopadhyay, Joysurya Basu, Phase Stability and microstructural evolution in vanadium-titanium alloys with oxygen dissolution and varying titanium-content, Microscopy and Microanalysis, 2020, Vol. 26 (S2), 2086-2088

5. *Saptarshi Mukherjee*, Rajdeep Chatterjee, Urwashi Gupta, B. Mukherjee N.K. Mukhopadhyay, Joysurya Basu, Structure-activity relationship for electrocatalysis in rocksalt and spinel based multicomponent oxides and its derivatives [To be communicated]

6. *Saptarshi Mukherjee*, N.K. Mukhopadhyay, Joysurya Basu, Revisiting the aspects of phase formation, microstructural evolution and its stability in rocksalt and spinel forming high entropy oxides [To be communicated]

List of conference presentations

1. Oral presentation at the National Student's Seminar on Metallurgy and Materials Science **(BTTD-2024)**, by IIM (Jamshedpur chapter) in association with CSIR-NML and Tata Steel Ltd. during June 19-21st, 2024.
   Recipient of Best Oral Presentation Award

2. Oral and poster presentation at the International Conference on Electron Microscopy **(EMSI-2024)**, by IIT Bombay during May 16-18th, 2024.
   Recipient of Best Poster Presentation Award

3. Oral presentation at the National Symposium of Research Scholars **(NSRS-2024)** on Metallurgy and Materials, by IIT Kanpur during March 9-10th, 2024.
   Recipient of Best Oral Presentation Award

4. Poster presentation at the 20th International Microscopy Congress **(IMC20)** in Busan, Republic of Korea during September 10-15th, 2023.
   Recipient of Travel Bursary Awards from RMS, UK and EMSI, India

5. Poster presentation at the International Conference on Electron Microscopy **(EMSI-2023)** in Delhi, during February 8-10th, 2023.

6. Oral presentation at Microscopy and Microanalysis **(M&M-2020)**, Milwaukee during August 3-7th, 2020.

7. Oral presentation at the Early Career European Microscopy Congress **(EMC-2020)**, Copenhagen during November 24-26th, 2020.

8. Poster presentation at the 12th Asia-Pacific Microscopy Conference **(APMC-2020)**, Hyderabad during February 3-7th, 2020.